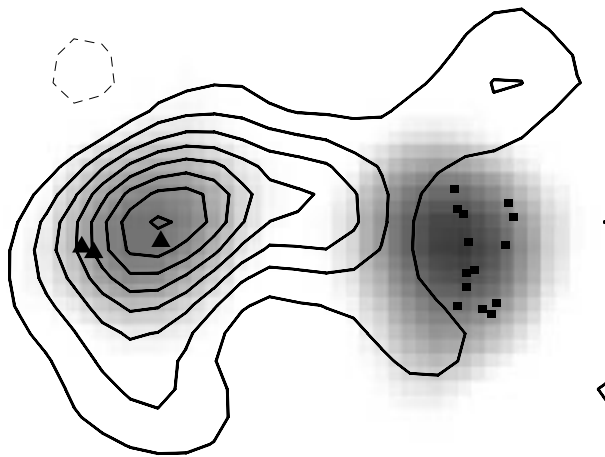


Radio observations of high mass
star forming regions:
hot cores and photon dominated regions



Inaugural-Dissertation
zur
Erlangung des Doktorgrades
der Mathematisch-Naturwissenschaftlichen Fakultät
der Universität zu Köln

vorgelegt von

Friedrich Wyrowski
aus Duisburg

Köln 1997

Berichtersteller: Prof. Dr. G. Winnewisser
Prof. Dr. H. Heintzmann

Tag der mündlichen Prüfung: 9. Dezember 1997

Zusammenfassung — Summary in German

Massereiche Sterne entstehen im Inneren von dichten Molekülwolken. In dieser Arbeit wird der Einfluß massereicher Sterne während ihres Entstehungsprozesses auf ihre molekulare Umgebung untersucht. Dazu wurden radioastronomische Messungen mit Einzelteleskopen und Interferometern im Zentimeter bis Submillimeter Wellenlängenbereich durchgeführt. Die sogenannte “Hot Core”-Phase, in der gerade entstandene junge, massereiche Sterne ihre elterlichen Molekülwolken aufheizen und es zur Ausbildung von heißen ($T \sim 200$ K) Wolkenkernen kommt, wird unter verschiedenen Aspekten analysiert:

Die physikalischen Bedingungen der Molekülwolken, in denen die heißen Wolkenkerne eingebettet sind, wurden mit Hilfe des seltenen $C^{17}O$ Isotopomers in 16 Quellen untersucht. Die typische Ausdehnung dieser Wolken ist 1 pc mit mittleren Dichten von 10^5 cm^{-3} und Temperaturen von 25 K. Die abgeleiteten Massen der Wolken liegen im Bereich von 10^3 bis $5 \cdot 10^4 M_{\odot}$ und die meisten der Wolken sind im Virialgleichgewicht.

Der mit dem ultrakompakten HII Gebiet G10.47+0.03 assoziierte heiße Wolkenkern wird detailliert mit Hilfe von $^{15}NH_3$ als optisch dünner Indikator hoher Dichten analysiert. Die Rotationstemperatur zwischen den beobachteten metastabilen Niveaus ist 185 ± 20 K und entspricht im Vergleich mit Strahlungstransportmodellen einer kinetischen Temperatur von 240 ± 40 K. Aus der schwachen Besetzung des nicht metastabilen (4,3) Niveaus ergibt sich $5 \cdot 10^7 \text{ cm}^{-3}$ als obere Grenze für die Dichte.

Um die Infrarotfelder im Inneren der heißen Wolkenkerne zu studieren, sind eine Reihe von Molekülen in vibrationsangeregten Zuständen beobachtet worden. Eine der beobachteten Quellen, G10.47+0.03, stellt sich als bisher einzigartig im Hinblick auf hochangeregte molekulare Linienemission heraus. Die Anregungstemperaturen für die strahlungsgepumpten Linien liegen im Bereich von 175–300 K. In dieser Studie werden eine Reihe von vibrationsangeregten Zuständen von HC_3N zum ersten Mal im interstellaren Raum nachgewiesen und die besondere Rolle dieses Moleküls zur Überdeckung eines großen Bereichs von Rotations- sowie Vibrationsanregung gezeigt.

Die Säulendichten der komplexen Moleküle CH_3CH_2CN , CH_2CHCN , CH_3OCH_3 , $HCOOCH_3$, CH_3CH_2OH und CH_3CHO wurden in einer Reihe von heißen Wolkenkernen bestimmt, wodurch eine wertvolle Datenbasis für theoretische Studien der Chemie der heißen Wolkenkerne bereitgestellt wird. Im Vergleich mit chemischen Modellen läßt sich eine Zeitspanne von $5 \cdot 10^4$ Jahren seit dem Einsetzen einer Heizquelle im Inneren der Wolkenkerne abschätzen.

Das Entstehungsgebiet massereicher Sterne W3(OH) wurde eingehend mit Hilfe des IRAM Interferometers untersucht. Mit hoher räumlicher Auflösung (0.016 pc) wurden die $J=1-0$ und $J=2-1$ Linien von $C^{17}O$ sowie die Kontinuumsstrahlung bei 112 und 225 GHz kartiert. Der mit Wassermasern assoziierte heiße Wolkenkern zeigt bei beiden Frequenzen

kompakte Kontinuummmission von heißem Staub mit einem Spektralindex von 3.6. Die $C^{17}O$ Karten zeigen den heißen Wolkenkern tief eingebettet im molekularen Gas, während sich das ultrakompakte HII Gebiet am Rand der dichten Molekülwolke befindet. Staub- und Linienstrahlung des heißen Wolkenkerns sind konsistent mit einer Masse von $10 M_{\odot}$. Überdies wurden Linien einer Vielzahl von komplexen Molekülen beobachtet, die klar die chemischen Unterschiede zwischen dem heißen Wolkenkern und dem ultrakompakten HII Gebiet zeigen. Orientierung und räumliche Ausdehnung der Maseremission aus der W3(OH) Region stimmen mit der beobachteten thermischen Emission überein. Diese Analyse macht deutlich, daß Interferometrie bei 1.3 mm einer der besten Wege ist, um die physikalischen und chemischen Bedingungen in Entstehungsgebieten massereicher Sterne zu studieren.

Neben den heißen Wolkenkernen werden in dieser Arbeit photonendominierte Gebiete (PDR) in Sternentstehungsgebieten massereicher Sterne untersucht. Der Schwerpunkt liegt dabei auf der Analyse der physikalischen Bedingungen und Morphologie des teilweise ionisierten Gases, in dem vor allem Kohlenstoff ionisiert vorliegt. Dazu wurde die Kohlenstoff-Rekombinationslinie verwendet. Neue Nachweise dieser Linie in NGC 7023 und S 106 mit dem 100-m Effelsberg Teleskop werden vorgestellt und die physikalischen Bedingungen in den PDR durch Vergleich mit Messungen der [C II] $158 \mu\text{m}$ Feinstrukturlinie mit der von Natta et al. (1994) vorgeschlagenen Methode bestimmt. Eine umfangreiche Analyse der PDR assoziiert mit NGC 2023 wurde, basierend auf Messungen der Kohlenstoff-Rekombinationslinie und $C^{18}O$, durchgeführt. Diese Daten deuten auf Dichten von 10^5 cm^{-3} im ionisierten, sowie im molekularen Material hin.

Vom Orion Nebel wurden Beobachtungen der $C91\alpha$ Rekombinationslinie mit dem Very-Large-Array, sowie $C65\alpha$ Beobachtungen mit dem 100-m Teleskop durchgeführt. Diese Ergebnisse – mit der besten bisher erreichten räumlichen Auflösung (0.02 pc) der C^+ Verteilung in einer PDR — zeigen, daß sich ionisierter Kohlenstoff in der mit dem “Orion Bar” assoziierten PDR in einer dünnen, klumpigen Schicht zwischen der Ionisationsfront und dem molekularen Gas befindet. Die beobachtete Linienbreite führt zu einer oberen Grenze für die Temperatur in der C^+ Schicht, und die Linienintensität weist auf Dichten zwischen $5 \cdot 10^4$ und $2.5 \cdot 10^5 \text{ cm}^{-3}$ hin. Diese Studie zeigt, daß die Kohlenstoff-Rekombinationslinie ein momentan einzigartiges Werkzeug zur Analyse von teilweise ionisiertem Gas mit hoher räumlicher und spektraler Auflösung darstellt.

ABSTRACT

This thesis investigates the impact of high mass star formation on its molecular environment by means of radio astronomical observations using single dish telescopes and interferometers in the centimeter to sub-millimeter wavelength range. The hot core phenomenon, in which newly formed high mass (proto) stars interact with their molecular surroundings is studied in various aspects:

Physical parameters of the molecular cloud cores, in which hot cores are embedded, are studied on basis of $C^{17}O$ measurements towards a sample of 16 sources. The $C^{17}O$ emitting clumps typically have sizes of 1 pc, average densities and temperatures of 10^5 cm^{-3} and 25 K, respectively. Clump masses from 10^3 to $5 \cdot 10^4 M_{\odot}$ are found and most of the clumps are virialised.

The hot core associated with the ultracompact HII region G10.47+0.03 is analyzed in detail using $^{15}NH_3$ as an optically thin high density tracer. The rotational temperature between metastable levels is found to be 185 ± 20 K. In comparison with an LVG model a kinetic temperature of 240 ± 40 K is deduced. The non-detection of $^{15}NH_3(4,3)$ allows to set an upper limit of $5 \cdot 10^7 \text{ cm}^{-3}$ to the molecular hydrogen density in the hot core.

To probe the infrared field in hot cores, a variety of molecules in vibrationally excited states were observed. One of the observed sources, G10.47+0.03, has shown to be a unique source in terms of high excitation molecular lines. The derived excitation temperatures are 175–300 K for the radiatively pumped lines. In this study many vibrationally excited states of HC_3N have been detected for the first time in interstellar space, showing the particular usefulness of this molecule to trace a wide range of rotational *and* vibrational excitation.

In addition, column densities of the complex molecules CH_3CH_2CN , CH_2CHCN , CH_3OCH_3 , $HCOOCH_3$, CH_3CH_2OH , and CH_3CHO were determined towards several hot cores which provide a valuable data base for theoretical studies of hot core chemistry. Comparison with chemical models lead to a chemical time scale of $5 \cdot 10^4$ years after onset of the heating sources.

The IRAM Interferometer was used to map the $J=1-0$ and $J=2-1$ lines of $C^{17}O$ as well as the continuum at 112 and 225 GHz of the W3(OH) region. Towards the hot core at the position of the water masers W3(H_2O) compact continuum emission was observed at both frequencies with spectral index of 3.6 from hot dust emission. The $C^{17}O$ maps show more extended gas with the most massive molecular clump towards W3(H_2O) and none towards W3(OH) itself. Dust continuum and molecular line fluxes are both consistent with a mass of $10 M_{\odot}$. Moreover, lines from several complex molecules are detected which show chemical differences between hot core and UC HII. Orientation and spatial extends of masers coincide with the observed thermal emission. This study shows that 1.3 mm interferometry is very appropriate to trace the physical and chemical conditions of the sites of high mass star formation.

To study the photon dominated regions of high mass star forming clouds, in particular their ionized carbon content, the utility of carbon recombination lines is investigated. New detections of carbon recombination lines are reported from NGC 7023 and S 106 using the 100-m telescope. The physical parameters of the PDRs are determined by comparisons with the [C II] 158 μm fine structure lines using the method of Natta et al. (1994). A detailed study of the PDR associated with NGC 2023 is presented basing on carbon recombination and carbon monoxide observations. The data suggest densities of 10^5 cm^{-3} for both the ionized and molecular gas.

VLA D-array observations of the C91 α carbon recombination line as well as Effelsberg 100-m observations of the C65 α line were carried out towards the Orion Nebula with spatial resolutions of 10'' and 40'', respectively. The results show the ionized carbon in the PDR associated with the Orion Bar to be in a thin, clumpy layer sandwiched between the ionization front and the molecular gas. From the observed line widths one gets an upper limit on the temperature in the C⁺ layer of 1500 K and from the line intensity a hydrogen density between $5 \cdot 10^4$ and $2.5 \cdot 10^5 \text{ cm}^{-3}$ for a homogeneous medium. This analysis shows that carbon recombination lines offer, up to now, a unique tool to study partially ionized gas with high spatial and angular resolution.

Contents

1	Introduction	1
1.1	Ultracompact HII regions	2
1.2	Hot cores	3
1.3	Photon dominated regions	4
1.4	Outline	5
I	Hot cores	7
2	C¹⁷O towards hot cores	9
2.1	Introduction	9
2.2	KOSMA observations	10
2.3	Estimation of source sizes	13
2.4	Temperatures from Boltzmann plots	14
2.5	Physical properties of the molecular cores	17
2.6	Conclusions	20
3	¹⁵NH₃ in the hot core associated with G10.47+0.03	22
3.1	Introduction	22
3.2	100-m observations of ¹⁵ NH ₃	23
3.3	Results	23
3.4	Analysis	25

3.5	Statistical Equilibrium results	26
3.5.1	Kinetic temperature estimates	27
3.5.2	The excitation of non-metastable levels of $^{15}\text{NH}_3$	28
3.6	Discussion	29
3.7	Conclusions	31
4	Probing the IR-field of hot cores	33
4.1	Introduction	33
4.2	Observations	34
4.3	Vibrationally excited cyanoacetylene	36
4.3.1	Frequencies of vibrationally excited states	36
4.3.2	The whole sample	39
4.4	HC_3N in G10.47+0.03	40
4.4.1	The identifications	40
4.4.2	The level population	45
4.4.3	The excitation of the lines	49
4.5	Other radiatively excited molecules	51
4.5.1	Vibrationally excited hydrogen cyanide	51
4.5.2	Vibrationally excited ammonia	53
4.5.3	Isocyanic acid	53
4.5.4	Vibrationally excited vinyl cyanide	55
4.6	Characteristics of the IR source	56
4.7	Conclusions	57
5	The chemical state of hot cores	59
5.1	Introduction	59
5.2	Determination of molecular abundances	61
5.3	Discussion of the observed molecular species	62

5.3.1	CH ₃ CH ₂ CN—Ethyl cyanide	62
5.3.2	CH ₂ CHCN—Vinyl cyanide	65
5.3.3	HCOOCH ₃ —Methyl formate	66
5.3.4	CH ₃ OCH ₃ —Dimethylether	67
5.3.5	CH ₃ CH ₂ OH—Ethanol	68
5.3.6	CH ₃ CHO—Acetaldehyde	69
5.3.7	Deuterated molecules	71
5.4	The chemical age of hot cores	72
5.5	Conclusions	74
6	An interferometer study of gas and dust in W3(OH)	76
6.1	Introduction	76
6.2	Observations and data reduction	78
6.3	The millimeter continuum emission	79
6.3.1	Results	79
6.3.2	The radio continuum spectrum	80
6.3.3	Mass estimates from the dust emission	82
6.4	C ¹⁷ O emission	82
6.4.1	Gas mass distribution	83
6.4.2	Hot core mass	84
6.5	Complex molecules in W3(OH)	85
6.5.1	Identification and morphology	85
6.5.2	Analysis	88
6.6	The relation between thermal and masering gas	93
6.7	Conclusions	95

II	Photon dominated regions	97
7	The carbon recombination line in selected star forming regions	99
7.1	Introduction	99
7.2	History and theory	99
7.3	Ionized carbon in models of PDRs	102
7.4	Observations	103
7.5	Results and discussion	103
7.5.1	S 140	103
7.5.2	S 106	105
7.5.3	NGC 7023	106
7.5.4	DR 21	107
7.5.5	IC 63 and RMC	107
7.6	Conclusions	108
8	A detailed study of the PDR associated with NGC 2023	110
8.1	Introduction	110
8.2	Observations	112
8.2.1	C91 α 100-m observations	112
8.2.2	C ¹⁸ O KOSMA observations	112
8.3	Observational results	113
8.3.1	C91 α	113
8.3.2	C ¹⁸ O	114
8.3.3	Comparison of C91 α with molecular tracers in NGC 2023	116
8.4	Physical parameters of the NGC 2023 PDR	117
8.4.1	Face-on homogeneous PDR models	119
8.4.2	Edge-on homogeneous models	120
8.4.3	Clumpy models	122

8.4.4	Effect of “interstellar abundances” on inferred densities	125
8.5	Characteristics of the molecular core in NGC 2023	125
8.6	Discussion and conclusions	128
9	Carbon radio recombination lines towards the Orion Nebula	131
9.1	Introduction	131
9.2	Observations	132
9.2.1	C65 α observations of Orion with the Effelsberg 100-m telescope . . .	132
9.2.2	C91 α observations of the Orion Bar with the VLA	132
9.3	Observational results	133
9.3.1	Morphology of carbon radio line emission	133
9.3.2	Level populations in the C91 α emitting region	136
9.3.3	Comparison with molecular hydrogen emission	137
9.3.4	Physical parameters in the C91 α emitting region	138
9.4	Conclusions	138
III	Conclusions and prospects	141
A	30-m line parameters	145

Chapter 1

Introduction

With the discovery of nuclear reactions as energy generating process in stars (Bethe 1939), it became clear that luminous massive stars use their nuclear fuel at such high rates that their total lifespan is only of order $10^6 - 10^7$ yrs, short compared to galactic timescales. Therefore their very existence is evidence for ongoing star formation. This is further supported by the observations of only loosely bound associations of massive stars with dynamical ages short in comparison to the age of the Galaxy (Ambartsumian 1947). They are always associated with interstellar matter (Blaauw 1964) and the proximity is decreasing with their evolutionary stage suggesting a slow drift from their birthplaces. The advent of radio and infrared observations about 25 years ago then revealed cold and dusty molecular clouds with luminous embedded infrared sources as the sites of high mass star formation (Zuckerman & Palmer 1974; Becklin & Neugebauer 1967).

The influence of high mass stars on the interstellar medium is tremendous: during their process of formation they are sources of luminous, bipolar outflows (Shepherd & Churchwell 1996), their strong ultraviolet and far-ultraviolet radiation fields give rise to bright HII and photon-dominated regions, and during their whole lifetime powerful stellar winds interact with the surroundings. In the course of time, this leads to the destruction of the parental cloud. Finally, their short life ends culminating in a violent supernova explosion, injecting heavy elements into the interstellar medium and possibly triggering further star formation with the accompanying shocks (Herbst & Assousa 1977). All these points together underline the importance of formation and evolution of massive stars also for the understanding of galaxies as a whole.

The current picture of the process of star formation has mainly emerged from the study of regions of low mass star formation. This is understandable in view of the smaller distances to low mass star forming regions (100-200 pc, in contrast to at least 450 pc for high mass star forming regions) and the existence of a so-called isolated mode of star formation where individual stars form relatively undisturbed in individual molecular cores

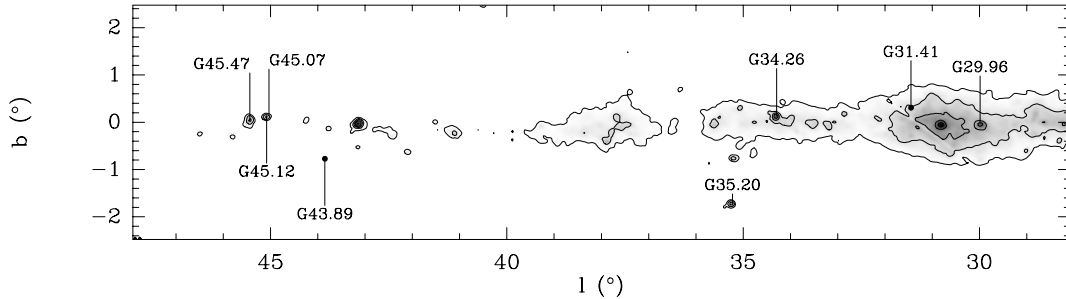


Fig. 1.1.— Sites of high mass star formation in the Galaxy traced by $100\ \mu\text{m}$ emission from the IRAS sky survey (Beichmann et al. 1985). We marked all sources observed in this thesis. Other bright HII region complexes seen in the map: W43 ($30.8^\circ, 0^\circ$), W49 ($43.1^\circ, 0.2^\circ$).

(Lada 1991; Shu et al. 1996). The dominant mode for massive star formation is the so-called clustered mode in which low and high mass stars form together leading to the creation of OB associations. A further complication is the above mentioned strong influence of already formed high mass stars on new generations of forming stars altering the conditions for star formation in a complicated fashion. Therefore it is the aim of this thesis to study the impact of high mass star formation on its molecular environment.

1.1. Ultracompact HII regions

One important difference between low and high mass star formation is that for the latter the lifespan of a hydrostatic core before the onset of hydrogen burning is shorter than the free-fall timescale of the envelope. High mass objects are therefore in their youngest phases still deeply embedded in their parental molecular cloud cores. Evidence for these early cocoon phases is given by ultracompact (UC) HII regions. These small ($\sim 0.1\ \text{pc}$) and dense ($n_e \sim 10^5\ \text{cm}^{-3}$) ionized fingerprints of recent massive star formation are only accessible by radio and IR observations.

The first observations of UC HII regions were made at the end of the 1960s (see Habing & Israel 1979 for a short history) and soon they were recognized also as strong emitters in the infrared due to radiation from their warm dust cocoons. A comprehensive review of properties of UC HIIs considering also newer results is given by Churchwell (1991). The galactic distribution of UC HII regions is discussed by Wood & Churchwell (1989a). They found these embedded objects to be located close to the Galactic plane with an angular scale height of only 0.6° . Due to their strong FIR radiation, compact HII regions are easily recognized in the IRAS sky survey (Beichmann et al. 1985): to illustrate their galactic distribution a part of the first quadrant of the Galaxy is shown in Figs. 1.1 and 1.2 where sources which will be discussed in this thesis are marked.

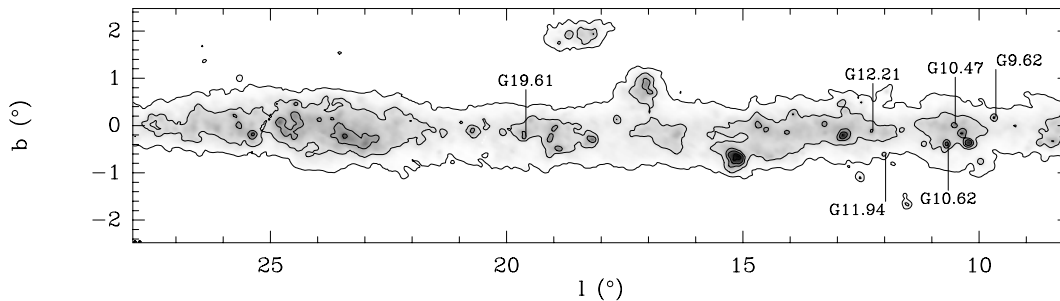


Fig. 1.2.— Same as Fig. 1.1. Other bright HII region complexes seen in the map: W33 ($12.7^\circ, -0.2^\circ$), M17 ($15.0^\circ, -0.7^\circ$).

Comparison with the number of optically visible O stars led Wood & Churchwell to the conclusion that they spend 10% to 20% of their lifetime embedded in their natal molecular clouds. But this timescale of roughly 10^5 yrs is incompatible with the short dynamical timescales for expansion of the UC HIIs ($10^3 - 10^4$ yrs). Several authors discussed possible causes for this discrepancy: the cometary morphology of about 20% of the UC HIIs (Wood & Churchwell 1989b) is suggestive of bow shocks caused by supersonic movement of the embedded O stars relative to the surrounding molecular clouds (van Buren et al. 1990) maintaining compactness of the HII region for typical cloud crossing timescales of 10^5 yrs; however, to account for the cometary morphology other explanations are also possible, such as champagne flows, but the exact nature of their shape is still debatable. Other scenarios are that photo evaporation of circumstellar disks leads to high electron densities close to the star for timescale longer than the dynamical timescale (Hollenbach et al. 1994) or that the UC HIIs are confined by the turbulent pressure of the ambient gas (Xie et al. 1996).

1.2. Hot cores

While studying the molecular environments of ultracompact HII regions, it became clear that a large number of them are associated with hot (> 100 K), dense ($\sim 10^7$ cm^{-3}) and small (~ 0.1 pc) molecular gas clumps and water masers which are believed to be a signpost of recent star formation (see Churchwell et al. 1990, Cesaroni et al. 1992 for single dish observations, and Walmsley & Schilke 1993 for a review). These properties are reminiscent of the archetypical Orion Hot Core, and the hot regions are therefore named hot cores. With follow-up observations using interferometers with high angular resolution (e.g. Cesaroni et al. 1994; Hofner & Churchwell 1996) it was found that the hot cores are in most cases offset from the HII regions, which therefore cannot account for the heating of the cores, and that the water masers are in general associated with the hot cores and not with the UC HIIs. It is therefore believed that hot cores are an evolutionary stage of high mass star formation prior to formation of an HII region; the knowledge of massive star formation therefore strongly demands for a detailed understanding of the hot core phenomenon.

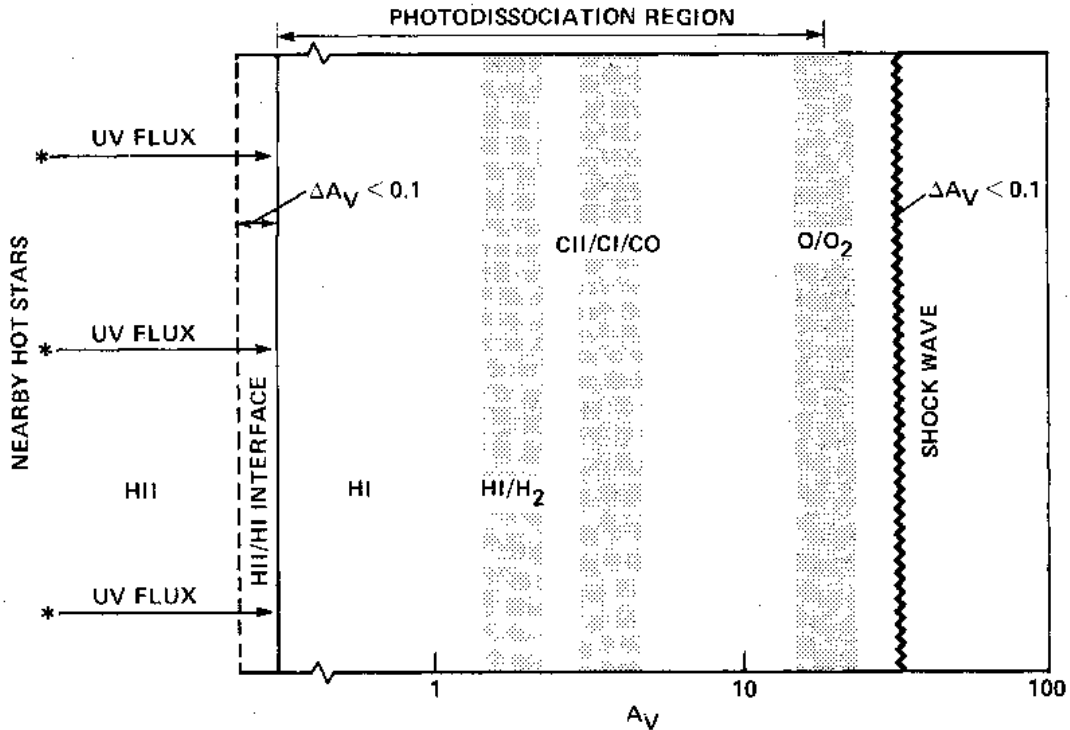


Fig. 1.3.— Scheme of a photon dominated region taken from Tielens & Hollenbach (1985). FUV radiation of nearby massive stars penetrate deeply into adjacent molecular clouds leading to the indicated different surface layers.

1.3. Photon dominated regions

Newly formed massive stars inject large amounts of energy into their surroundings in form of ionizing radiation. Besides the ionization of bright HII regions, intense far-ultraviolet (FUV) radiation with energies smaller than the Lyman limit can penetrate deeply into adjacent molecular clouds leading to so-called photon dominated or photodissociation regions (PDRs, for a recent review see Hollenbach & Tielens 1997) in which heating and chemistry is dominated by FUV photons. A sketch of a PDR is shown in Fig. 1.3: all the Lyman continuum photons are absorbed in a thin transition zone from ionized to atomic hydrogen, but FUV photons penetrate further into the cloud photoionizing carbon and photodissociating oxygen up to certain depths into the cloud. The FUV photons are mainly absorbed by grains leading to intense continuum FIR radiation from the PDRs. Some of the absorption events give rise to the ejection of photoelectrons which subsequently heat the gas; most of the electrons in the PDR, however, are due to the photoionization of carbon. The main gas cooling mechanisms are via emission of [C II] $158 \mu\text{m}$ and [O I] $63 \mu\text{m}$ fine structure lines.

The fractional ionization of a molecular cloud, at least at moderate depth into the cloud, is therefore governed by the influence of FUV radiation. But charged particles in conjunction with a magnetic field lead to a support of a cloud against gravitational

collapse. It has been suggested that the rate of star formation could be coupled to FUV photoionization leading to the model of photoionization-regulated star formation (McKee 1989; Bertoldi & McKee 1996). Therefore, also in the context of star formation, it is of major importance to examine PDRs, in particular to study their dominant ion C^+ .

1.4. Outline

The first part of this thesis is dedicated to the study of the hot core phenomenon in a variety of approaches:

In Chapter 2 the scene is set by a study of the global molecular environment in which current high mass star formation takes place. This is done with observations of optically thin rotational lines of $C^{17}O$ towards a sample of UC HII regions. More local physical conditions of one of these objects are analyzed in Chapter 3 where again an optically thin tracer, the rare ^{15}N isotopomer of ammonia, is used which has a much higher critical density than CO. It therefore traces the very dense parts of the molecular cloud core, i.e. the hot core itself. Chapter 4 examines the use of vibrationally excited molecules to probe the infrared field in the interior of hot cores and presents the most extensive coverage of vibrationally excited cyanoacetylene to date. Hot cores as chemical factories are then discussed in Chapter 5 and estimates of the chemical age of hot cores are given in comparison to chemical models. All these studies have been made by single dish telescopes and therefore suffered from the unknown detailed morphologies of the star formation regions. This is attacked in Chapter 6 where a comprehensive high resolution interferometer study is presented towards the high mass star forming region W3(OH). There, many aspects of the previous chapters are revisited, but now with the additional high resolution information.

In the second part of this thesis ionized carbon in photon dominated regions is investigated using the carbon recombination line:

Chapter 7 gives some introductory explanation for the use and interpretation of the carbon recombination line. It also presents some new detections of this line towards star formation regions. A detailed discussion of the PDR of the reflection nebula NGC 2023 using the carbon recombination lines together with new carbon monoxide observations towards this source, is found in Chapter 8. In Chapter 9 the mapping of the carbon recombination line using the Very Large Array towards the nearest accessible HII region/molecular cloud complex Orion A is reported. These observations reveal the distribution of ionized carbon in the Orion Bar PDR with the best spatial resolution to date.

REFERENCES

- Ambartsumian V.A. 1947, "Stellar Evolution and Astrophysics", Armenian Acad. of Sci., 1947
- Becklin E.E., Neugebauer G. 1967, ApJ 147, 799
- Beichmann C.A., Neugebauer, G., Habing, H.J., Clegg, P.E., Chester, T.J. 1985, IRAS Explanatory Supplement
- Bertoldi F., McKee C. 1996, in "Amazing light", ed. R.Y. Chiao p.41, Springer, New York
- Bethe H. 1939, "Energy Production in Stars", Phys. Rev. 55, 434
- Blaauw A. 1964, ARAA 2, 213
- Cesaroni R., Walmsley C.M., Churchwell E. 1992, A&A, 256, 618
- Cesaroni R., Churchwell E., Hofner P., Walmsley C.M., Kurtz S. 1994, A&A, 288, 903
- Churchwell E., Walmsley C.M., Cesaroni R. 1990, A&AS, 83, 119
- Churchwell E. 1991, in "The physics of star formation and early stellar evolution", eds. C.J. Lada & N.D. Kylafis, Kluwer, Dordrecht
- Habing H.J., Israel F.P. 1979, ARAA 17, 345
- Herbst W., Assousa G.E. 1977, ApJ 217, 473
- Hofner, P., Churchwell E. 1996, A&AS 120, 283
- Hollenbach D.J., Johnstone D., Lizano S., Shu F. 1994, ApJ 428, 654
- Hollenbach D.J., Tielens A.G.G.M. 1997, ARAA 35, 179
- Lada C.J. 1991, in "The physics of star formation and early stellar evolution", eds. C.J. Lada & N.D. Kylafis, Kluwer, Dordrecht
- McKee C.F. 1989, ApJ 345, 782
- Shepherd D.S., Churchwell E. 1996, ApJ 472, 225
- Shu F., Najita J., Galli D., Ostriker E. 1996, in:"Protostars and planets III" p. 3
- Tielens A. , Hollenbach D. 1985, ApJ 291, 722
- Van Buren D., Mac Low M., Wood D.O.S., Churchwell E. 1990, ApJ 353, 570
- Walmsley C.M., Schilke P. 1993, in:"Dust and chemistry in astronomy", eds. T.J. Millar & D.A. Williams, Institute of Physics Publishing, Bristol & Philadelphia
- Wood D.O.S., Churchwell E. 1989a, ApJ 340, 265
- Wood D.O.S., Churchwell E. 1989b, ApJS 69, 831
- Xie T., Mundy L.G., Vogel S.N., Hofner P. 1996, ApJ 473, L131
- Zuckerman B., Palmer P. 1974, ARAA 12, 279

Part I

Hot cores

Chapter 2

C¹⁷O towards hot cores

2.1. Introduction

Essential to the understanding of the formation of massive stars is the knowledge of the environment in which they are born and spend their earliest evolutionary phases. It is now generally accepted that giant molecular clouds, or more specifically, dense condensations within them, are the birthplaces of massive stars. Optically thin lines of CO, such as C¹⁷O, allow us to estimate fundamental physical properties of these molecular cores, such as their column densities, total masses, and average temperatures. For a comparison of this tracer with sub-millimeter continuum emission from dust grains as a probe of the physical conditions of the clouds see Goldsmith et al. (1997).

The first systematic study of molecular gas associated with ultracompact (UC) HII regions has been a survey of water and ammonia emission towards a sample of 84 sources by Churchwell et al. (1990). However, the problem with using ammonia to determine masses is that the abundance of this species is clearly enhanced by an uncertain amount. Follow up ¹³CO observations by Churchwell et al. (1992) suffered from the high optical depths, evident from strong self-absorption features in the spectra. This allows only a very coarse estimate of the column densities towards these sources. Cesaroni et al. (1991) used the optically thin density tracer C³⁴S to determine density, mass, and size of several sources and found dense clumps ($\sim 10^6 \text{ cm}^{-3}$) with masses of about 2000 M_⊙ and an average size of 0.4 pc.

We already carried out a small survey (16 sources) of C¹⁷O in its (1–0) and (2–1) rotational transitions towards ultracompact HII regions using the 30-m telescope (Hofner et al. 1997, in prep.). However, excitation analysis on the basis of only two transitions is very uncertain, and therefore we decided to use the 3-m KOSMA telescope for additional observations of the (3–2) transitions. Since the (2–1) transition can be observed simultaneously, we can also check for more extended gas in the larger KOSMA beam.

Table 2.1: Observed Sources. The distances are taken from Churchwell et al. (1990).

Source	$\alpha(1950)$ h m s	$\delta(1950)$ ° ' "	d kpc
W3(OH)	02 23 16.5	61 38 57	2.2 ^a
G9.62+0.19	18 03 16.2	-20 32 03	5.7 ^b
G10.47+0.03	18 05 40.3	-19 52 21	5.8
G10.62-0.38	18 07 30.7	-19 56 29	6.0 ^c
G11.94-0.62	18 11 04.4	-18 54 20	4.2
G12.21-0.10	18 09 43.7	-18 25 09	13.5
G19.61-0.23A	18 24 50.3	-11 58 33	4.5
G29.96-0.02	18 43 27.1	-02 42 36	7.4
G31.41+0.31	18 44 59.2	-01 16 07	7.9
G34.26+0.15	18 50 46.1	01 11 12	4.0
G35.20-1.74	18 59 14.0	01 09 02	3.1
G43.89-0.78	19 12 02.8	09 17 19	4.2
G45.07+0.13	19 11 00.4	10 45 43	6.0
G45.12+0.13	19 11 06.2	10 48 25	6.9
G45.47+0.05	19 12 04.3	11 04 11	6.0
G75.78-0.34	20 19 52.0	37 17 02	4.1

^a Humphreys (1978)

^b Hofner et al. (1994)

^c Keto & Ho (1988)

2.2. KOSMA observations

Simultaneous observations of C¹⁷O (2-1) and (3-2) were carried out in February and March 1996 with the KOSMA 3-m telescope (see Winnewisser et al. 1990 for a detailed description of the instrument) on the Gornergrat in conjunction with the Cologne dual channel SIS receiver system. The half-power beamwidths of the telescope at the frequencies of C¹⁷O (2-1) and (3-2) are 112'' and 75'', respectively. Pointing was checked on Jupiter and is thought to be accurate to within 30''. The receivers were operated in double sideband mode and calibration was carried out using the usual chopper calibration technique (Kutner & Ulrich 1981). The calibration stability was checked by regular observations of the strong source G34.26 which results in an RMS scatter of 20% at both frequencies. We used the facility acousto-optical spectrometers with spectral resolutions of 0.2 and 0.6 km s⁻¹ and bandwidths of 287 and 1388 MHz at 220 and 330 GHz, respectively, average system temperatures were 390 and 510 K. To obtain main beam brightness temperature as intensity scale, the antenna temperature was divided by the forward spillover and scattering efficiency (0.7 at 230 GHz and 0.51 at 345 GHz) which was measured by Kramer (1992) on Jupiter. An overview of the observed sources is given in Table 2.1.

Table 2.2: KOSMA 3-m line parameters

Source	Transition	T_{MB} (K)	$\int T_{\text{MB}} dv$ (K km s ⁻¹)	v_{LSR} (km s ⁻¹)	FWHM (km s ⁻¹)
W3(OH)	C ¹⁷ O 2-1	0.44	2.3	-47.2	4.9
	C ¹⁷ O 3-2	1.1	4.7	-47.9	3.9
G9.62+0.19	2-1	0.76	4.2	3.9	5.2
	3-2	0.7	4.1	3.6	5.2
G10.47+0.03	2-1	0.44	3.4	67.7	7.3
	3-2	0.5	3.7	67.4	6.6
G10.62-0.38	2-1	1.7	9.8	-2.8	5.5
	3-2	2.7	16.4	-3.6	5.7
G11.94-0.62	2-1	0.67	3.3	37.6	4.7
	3-2	0.8	4.3	37.7	5.0
G12.21-0.10	2-1	0.41	2.9	25.3	6.7
	3-2	0.5	4.6	25.4	9.2
G19.61-0.23	2-1	0.31	2.1	42.9	6.4
	3-2	0.5	2.6	43.9	5.3
G29.96-0.02	2-1	0.54	3.3	98.2	5.8
	3-2	0.7	4.5	97.5	6.1
G31.41+0.31	2-1	0.70	3.7	97.3	4.9
	3-2	0.6	2.8	97.2	4.6
G34.26+0.15	2-1	1.41	7.9	58.1	5.3
	3-2	2.5	13.3	57.7	4.9
G35.20-1.74	2-1	0.46	2.4	42.7	4.9
	3-2	1.0	4.5	42.8	4.2
G43.89-0.78	2-1	0.39	1.5	54.3	3.7
	3-2	0.4	1.4	53.4	3.4
G45.07+0.13	2-1	0.24	1.5	58.7	5.8
	3-2	0.24	1.7	57.9	6.7
G45.12+0.13	2-1	0.37	2.4	58.5	6.0
	3-2	0.8	3.5	57.9	4.3
G45.47+0.05	2-1	0.26	1.8	59.0	6.5
	3-2	0.27	1.9	59.3	6.6
G75.78-0.34	2-1	0.40	2.0	-0.3	4.6
	3-2	0.6	2.8	-0.2	4.3

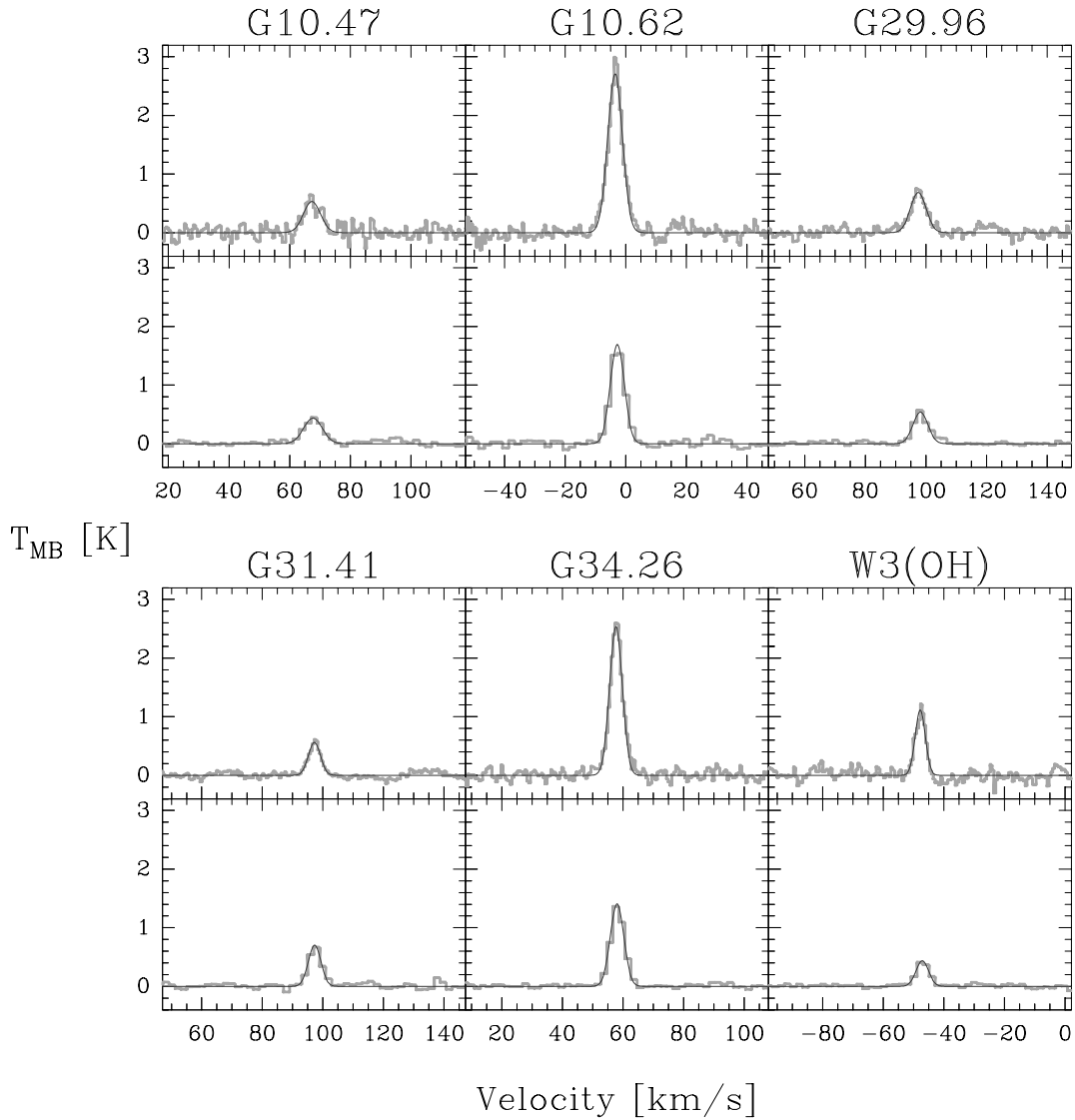


Fig. 2.1.— C^{17}O (2–1) (lower panels) and (3–2) (upper panels) KOSMA spectra towards a subset of the observed ultracompact HII regions. Gaussian fits have been applied to the spectra.

Spectra of a subset of the observed sources which will be relevant in other chapters of this thesis are shown in Fig. 2.1. The line parameters were obtained from Gaussian fits and are listed in Table 2.2. In addition to the single pointing observations, we observed a small map in $\text{C}^{17}\text{O}(2-1)$ towards W3(OH). These results will be discussed in Chapter 6.

Since we will use the KOSMA observations in conjunctions with recent results of IRAM 30-m observations of the same sources (Hofner et al. 1997), their main observing parameters are reviewed: observations of $\text{C}^{17}\text{O}(1-0)$ and (2–1) are obtained in Summer 1995 of the sources given in Table 2.1 with a half-power beamwidth of $22''$ and $11''$, respectively. Besides single pointing spectra, also 3×3 maps with $20''$ spacing were obtained.

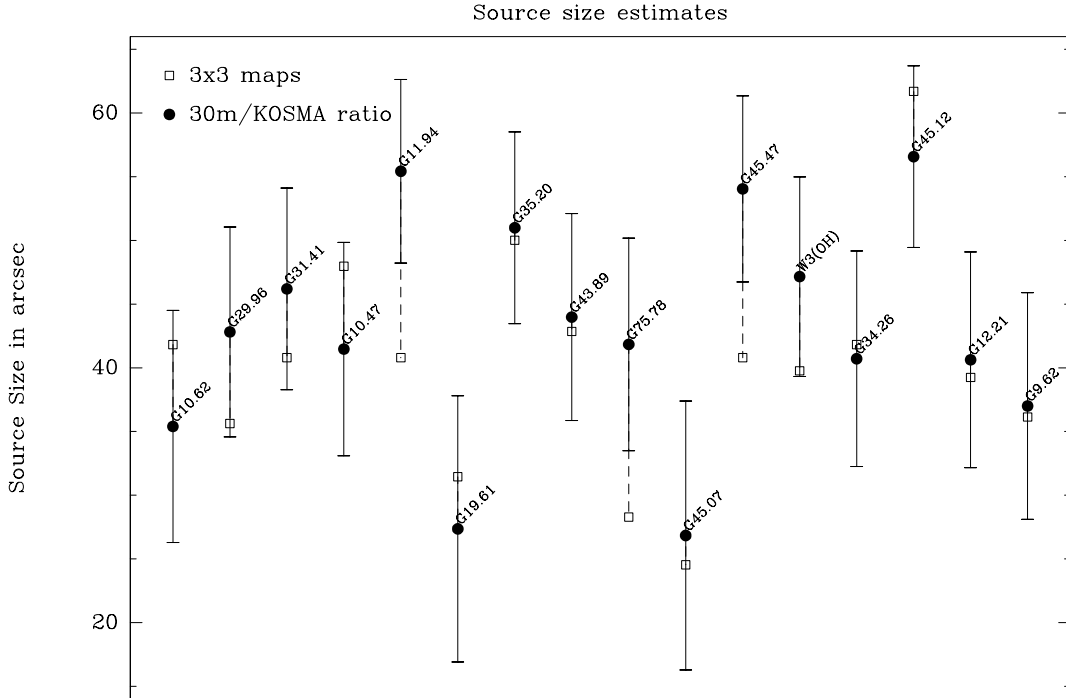


Fig. 2.2.— Source size estimates using two independent methods: a) from the $\text{C}^{17}\text{O}(2-1)$ ratio, and b) from the 3×3 30-m maps.

2.3. Estimation of source sizes

To determine integral properties of the molecular surroundings of the UC HII region, a proper knowledge of the spatial extend of the molecular gas is necessary. This can also be used to correct our observations for different beam sizes.

A first estimate of the size of the C^{17}O emitting region can be made by comparison of measured KOSMA and 30-m $\text{C}^{17}\text{O}(2-1)$ line intensities. In the case of Gaussian intensity distributions of a source the intrinsic intensity is modified by the beam filling factor:

$$T_L = T_S \frac{\theta_S^2}{\theta_S^2 + \theta_B^2} \quad (2.1)$$

where T_L denotes the measured intensity, T_S the intrinsic intensity of the source, and θ_S and θ_B source and beam diameter, respectively. Combining this equation for both telescopes, one gets the source diameter as a function of the line ratio $R = T_{30\text{m}}/T_{\text{KOSMA}}$:

$$\theta_S^2 = \theta_{30\text{m}}^2 \frac{(\theta_{\text{KOSMA}}/\theta_{30\text{m}})^2 - R}{R - 1} \quad (2.2)$$

From small 3×3 point maps done with the 30-m, covering a $40''$ square per source, we can also determine the source sizes. For that purpose we fit 2-dimensional Gaussians to

the observed intensity distributions and deconvolved beam and source using $\theta_{\text{obs}}^2 = \theta_{\text{S}}^2 + \theta_{\text{B}}^2$. This method cannot account for more extended gas which would be prominent in the 112'' KOSMA beam. Therefore it is important to check both methods for consistency (Fig. 2.2). We assumed errors of 20% on every intensity measurement and neglected the much smaller errors of the Gaussian fits. The agreement between the determined sizes is remarkably good (the average deviation is only 6'') and confirms our assumption of Gaussian intensity distributions for the observed sources. Only the sources G11.94, G45.47, and G75.78 show deviations larger than the error bars of more than 10''. For these sources this could be evidence for a halo or another confusing source seen in the KOSMA beam and indeed, CO observations of Hunter (1997) show in the cases of G45.47 and G75.78 molecular emission towards G45.45 and G75.76, respectively, both in a distance of about 1'. The average source size is $42 \pm 8''$, and from the 30-m data the typical elongation (ratio of major to minor axis) is 1.2 ± 0.15 . We can compare this with the source sizes determined with other tracers: Cesaroni et al. (1991) used C^{34}S to estimate masses of eight molecular clumps associated with UC HII regions. Their source size estimates are roughly only one half of the sizes seen in C^{17}O . Since the critical density for CS is higher, this can be interpreted as a density gradient to the inside of the clump. Also Hunter (1997) found on the average source sizes smaller by about 50% using broadband continuum imaging at 350 and 450 μm with the CSO. This emission is a function of both the dust column density and the temperature. We can therefore expect also an increase of the temperature to the inside which will become more evident in the next section.

The obtained apparent angular source sizes can be converted to linear sizes once the distances are known. In most cases we used the kinematic distances given by Churchwell et al. (1990) which are based on the velocities v_{LSR} of the sources and the rotational curve from Brand (1986). One should note that these distances could be in the worst cases in error by about a factor of two. The distances are quoted in Table 2.1 as long as no other reference is given.

In the following sections we will use the average of the source sizes obtained from the discussed methods. In the cases of large deviations between them (see Fig. 2.2), we will use the size from the 30-m maps to avoid confusion by nearby sources.

2.4. Temperatures from Boltzmann plots

With the help of the estimated source sizes we can now determine intrinsic C^{17}O intensities, i.e. intensities corrected for the beam-source coupling. We do not have to take the hyperfine structure of the C^{17}O lines into consideration, which is smaller than the observed line widths, since we are only interested in the integral of the optical thin emission. If for simplicity we assume LTE, the kinetic temperature is equal to the rotational temperature, which we fit to the population of the observed levels in Fig. 2.3 for a subset

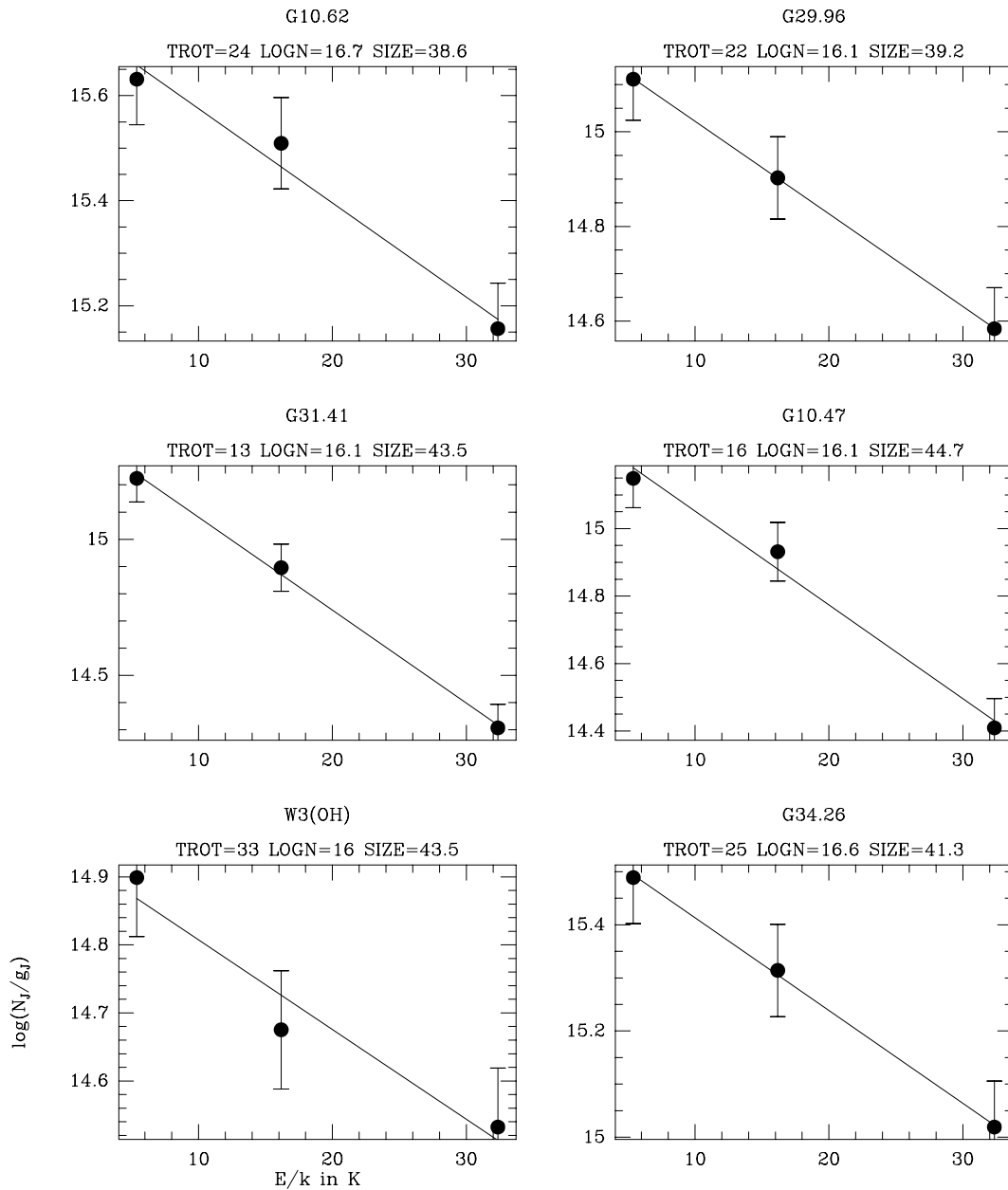


Fig. 2.3.— $C^{17}O$ Boltzmann plots for a subset of the observed sources with source averaged column densities using the source sizes of Table 2.3. The (1–0) and (2–1) lines at upper energies of 5.4 and 16.2 K are the 30-m data, the (3–2) lines at 32.4 K the KOSMA data.

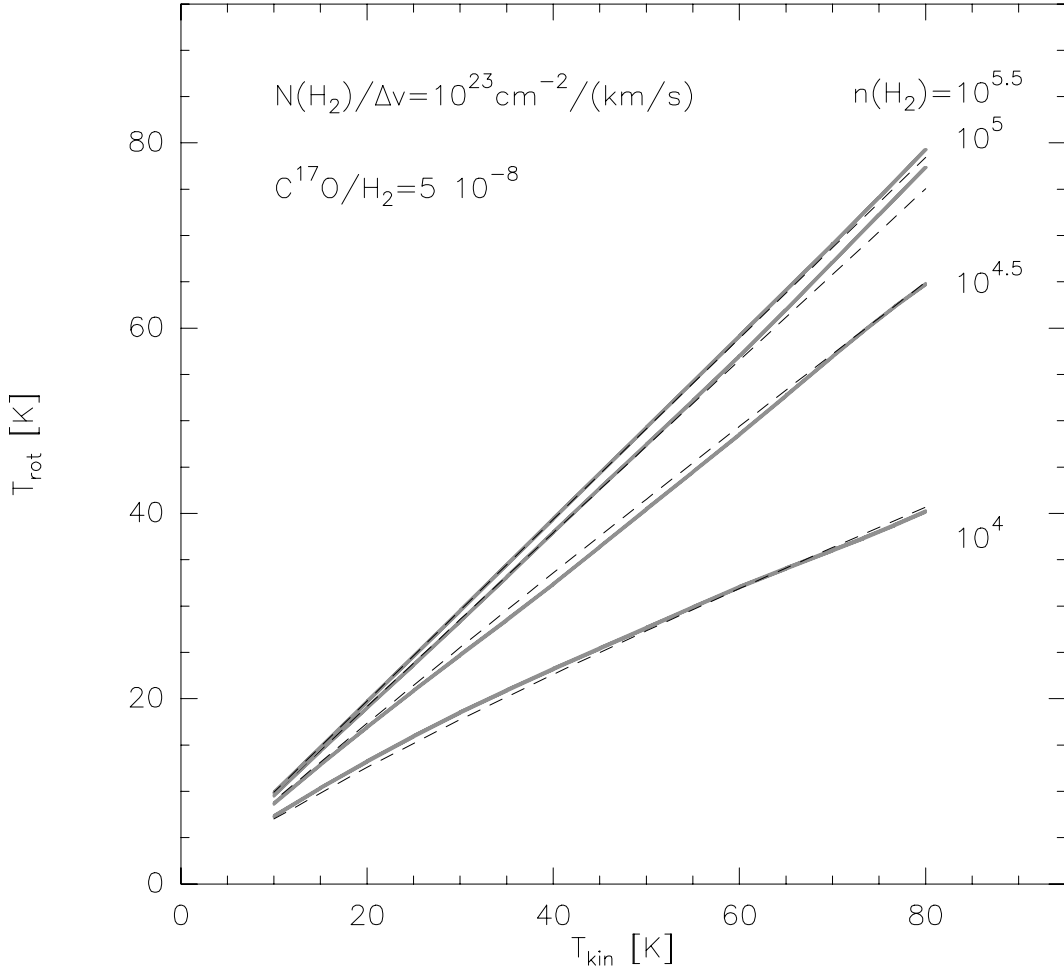


Fig. 2.4.— Statistical equilibrium results for the population of the $C^{17}O$ $J=1,2,3$ levels, described by T_{rot} , as a function of density and kinetic temperature. Fits to the results are shown as dashed lines.

of the sources (see Sect. 5.2 for details). The source averaged total column densities is here given by the intersection of the fit with the ordinate axis. Within the assumed 20% errors in the intensity measurements, they all can be fitted with one temperature. Small deviations, which are visible in, e.g. G10.62 and W3(OH), can be due to excitation effects or due to non-Gaussian intensity distributions. The average rotational temperature of all observed sources is 22 ± 8 K.

To analyze the usefulness of the rotational temperature as kinetic temperature estimate, we ran large velocity gradient (LVG) models in which we solved the statistical equilibrium equations for the CO level population using the LVG (Sobolev) approximation (de Jong et al. 1975) for the radiative transfer. The collisional rates used are those calculated by Flower & Launay (1985). These models depend on the parameters $n(\text{H}_2)$, T_{kin} , and $N(\text{mol})/\Delta v$. In the case of optically thin lines, the dependence on the last parameter $N/\Delta v$ is removed to first order by analyzing only line ratios. Rotational temperatures were derived from the

calculated population in the $J=1,2,3$ levels and their dependence on the parameters are shown in Fig. 2.4. For a relatively low density of 10^4 cm^{-3} the level population is subthermal ($T_{\text{ex}} < T_{\text{kin}}$), leading to a considerable underestimate of the kinetical temperature. At about a density of $10^{5.5} \text{ cm}^{-3}$ all three levels are fully thermalized and $T_{\text{rot}} = T_{\text{kin}}$. The relation between rotational and kinetic temperature is fitted for different temperatures with

$$\begin{aligned} T_{\text{rot}} &= T_{\text{kin}}^\alpha \\ \alpha &= 1 - 0.0045 \exp(-2.36(\log(n) - 5.5)). \end{aligned} \quad (2.3)$$

We estimated the given expression for α numerically for the statistical equilibrium results found in the range shown in Fig. 2.4. Hence, if one knows the density, the correction given in Eq. 2.3 can be applied to obtain the kinetic temperature. This is done for our sources in the next section.

2.5. Physical properties of the molecular cores

In this section, we estimate the physical parameters density, temperature, and mass of the molecular cores. We assume homogeneous, spherical cores and therefore the density can be obtained from dividing the column density by the source size which both have been derived before. The results are shown in Table 2.3 with densities in the range from 2×10^4 to $3 \times 10^5 \text{ cm}^{-3}$ averaged over the source. In contrast to this estimate the C^{34}S observations of Cesaroni et al. (1991) lead to densities of order 10^6 cm^{-3} which again argues for a strong density gradient to the inside of the clumps.

With the help of these densities, we can apply corrections to the rotational temperature to account for subthermal population of rotational levels at low densities as discussed in the last section. The result is an average kinetic temperature of $24 \pm 8 \text{ K}$ for our sample. This may be compared with temperature estimates from other surveys towards massive star forming regions: Chini et al. (1986) observed the 1.3 mm continuum of 57 strong FIR sources, all identified as compact HII regions, with a $90''$ beam and estimated the average dust temperature from the 1.3 mm to $100 \mu\text{m}$ ratio to be 25 K. The analysis of Churchwell et al. (1990) of ammonia (1,1) and (2,2) emission of 75 UC HII region with a $40''$ beam lead to a peak of their temperature distribution at about 20 K. Higher temperatures are found by the analysis of the FIR and sub-mm continuum emission towards 17 UC HII region by Hunter (1997). His sample shows an average dust temperature of $40 \pm 10 \text{ K}$. As discussed above, the source sizes observed in his study are significantly lower which suggest that his observations trace the hotter inner parts of the molecular clumps.

If we integrate the column densities found in the last section over the whole clump, assumed as Gaussian, we get an estimate of the total clump gas mass:

$$M(\text{H}_2) = \frac{\pi D^2}{4 \ln 2} \frac{N(\text{C}^{17}\text{O})}{X} m_{\text{H}_2} \quad (2.4)$$

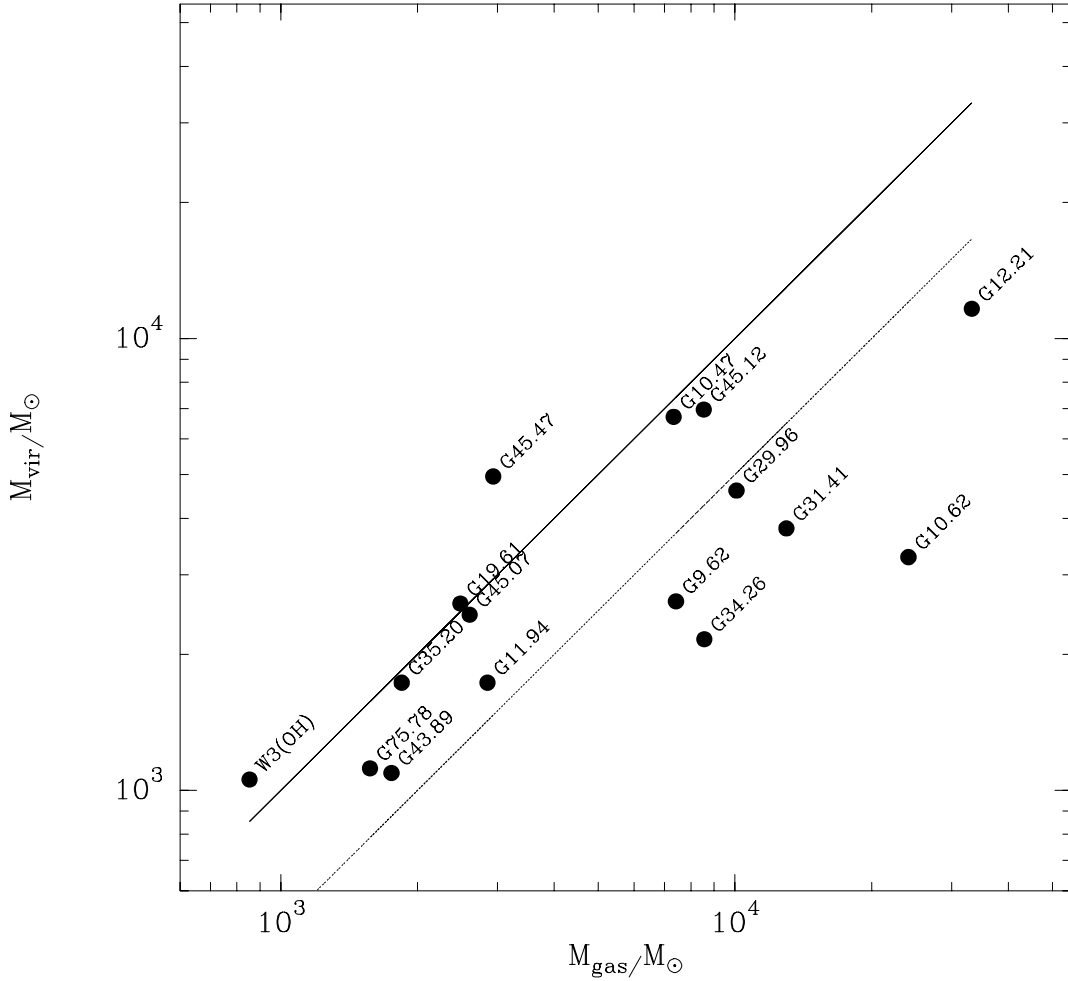


Fig. 2.5.— Comparison of virial and gas masses for the molecular cores of our sample. The solid diagonal line is the locus of equal virial and gas masses, and the dotted line represents gas masses twice the dynamical masses.

Here D denotes the source size, N the total column density, $X = 5 \cdot 10^{-8}$ the C^{17}O abundance, and m_{H_2} the mass of a hydrogen molecule. The observed masses of the cores are in the range from 10^3 to $5 \times 10^4 M_{\odot}$.

Another mass estimate can be obtained from the C^{17}O line width by applying the virial theorem (Rohlfs & Wilson 1996):

$$\frac{M}{M_{\odot}} = 125 \left(\frac{\Delta v}{\text{km s}^{-1}} \right)^2 \left(\frac{D}{\text{pc}} \right) \quad (2.5)$$

We choose to use the width of the $\text{C}^{17}\text{O}(2-1)$ KOSMA lines since in the KOSMA beam the whole clumps are included and the signal-to-noise is still sufficient to estimate reliable spectral line widths. Now we have to take also the hyperfine structure of C^{17}O into consideration. For this purpose we calculated the superposition of the different hyperfine components, assuming the optically thin case, for given intrinsic line widths between 3 and

Table 2.3: Derived physical parameters

Source	Size (pc)	$N(\text{H}_2)$ (10^{23} cm^{-2})	$n(\text{H}_2)$ (10^4 cm^{-3})	T_{kin} (K)	$M(\text{H}_2)$ ($10^3 M_{\odot}$)	M_{vir} ($10^3 M_{\odot}$)
W3(OH)	0.5	2.2	15.4	34	0.9	1.1
G9.62+0.19	1.0	4.0	12.9	16	7.4	2.6
G10.47+0.03	1.3	2.6	6.6	17	7.3	6.7
G10.62-0.38	1.1	10.6	30.6	25	24.1	3.2
G11.94-0.62	0.8	2.3	8.9	25	2.9	1.7
G12.21-0.10	2.6	2.7	3.3	31	33.2	11.6
G19.61-0.23	0.6	3.4	16.9	17	2.5	2.6
G29.96-0.02	1.4	2.8	6.5	24	10.1	4.6
G31.41+0.31	1.7	2.6	5.0	14	13.0	3.8
G34.26+0.15	0.8	7.4	30.0	25	8.6	2.2
G35.20-1.74	0.8	1.8	7.6	36	1.8	1.7
G43.89-0.78	0.9	1.2	4.6	14	1.8	1.1
G45.07+0.13	0.7	2.6	11.2	19	2.6	2.4
G45.12+0.13	2.0	1.2	2.0	31	8.5	7.0
G45.47+0.05	1.2	1.2	3.2	22	2.9	5.0
G75.78-0.34	0.6	2.8	15.9	42	1.6	1.1

7 km s^{-1} and fitted Gaussians to these artificial lines to estimate their effective linewidths. The following relations between intrinsic and observed linewidths were found for the (1-0) and (2-1) transitions:

$$\Delta v_{\text{obs}}(1-0) = 1.9 + \Delta v_{\text{int}}^{0.9} \quad (2.6)$$

$$\Delta v_{\text{obs}}(2-1) = 0.3 + \Delta v_{\text{int}} \quad (2.7)$$

For the (3-2) lines the hyperfine splitting is too small to have an observable influence on the lines. The calculated virial masses, with the correction for the hyperfine splitting applied, are given in Table 2.3 and in Fig. 2.5 they are plotted against the gas masses: within a factor of two there is agreement between these masses for most sources implying that the clumps are virialised. In some cases there is a trend to higher gas than virial mass suggesting an unstable, collapsing state of the cloud. This has actually been observed for G10.62 (Ho & Haschick 1986) which is the most extreme case in our sample and W3(OH) and G34.26 were found by Keto et al. (1987) to be two further collapse candidates. A rough estimate of the collapsing timescale is $t_C \approx R/\Delta v$ which is for the sources with $M_{\text{vir}} < M(\text{H}_2)/2$ between $1-3 \times 10^5$ yr in accordance with the lifetimes of UC HII's estimated by Wood & Churchwell (1989).

In the previous discussion we excluded magnetic fields which in principle can support molecular clouds against collapse (see the review of McKee & Zweibel 1996) and then the net magnetic energy has to be included into the virial theorem. For simplicity we

assumed equipartition between dynamical and magnetic energy by drawing the dotted line in Fig. 2.5 which gives the loci of $M_{\text{gas}} = 2M_{\text{dyn}}$ where we now interpreted the mass from the observed linewidth as dynamical mass. It seems to be a better fit to the data but would imply magnetic fields of $B = 2.5 \times N_{21} \mu\text{G} \approx 250 - 2500 \mu\text{G}$ (McKee & Zweibel 1996). Evidence for such high values of magnetic field strength towards UC HII/hot core sources is the observation of the Zeeman splitting of thermal OH towards W3(OH) leading to about 3 mG (Güsten et al. 1994).

2.6. Conclusions

We performed observations of the $\text{C}^{17}\text{O}(2-1)$ and $(3-2)$ lines towards a sample of 16 ultracompact HII regions, that are embedded in dense molecular gas, using the 3-m KOSMA telescope. Together with the results of a survey of the $(1-0)$ and $(2-1)$ lines with the 30-m, we derived the physical conditions of the molecular gas. The average sizes of the C^{17}O emitting clumps are found to be 1 pc and the densities averaged over the sources are of order 10^5 cm^{-3} . We performed LVG calculations to demonstrate the relation between rotational and kinetic temperature, and an average kinetic temperature of 25 K is found. These density and temperature estimates are lower than results of CS and sub-mm continuum surveys, suggesting an increase of these quantities to the inside of the clumps. Clump masses from 10^3 to $5 \times 10^4 M_{\odot}$ are found and most of the clumps are virialised.

REFERENCES

- Brand J. 1986, Ph.D Thesis, Leiden University
 Cesaroni R., Walmsley C.M., Kömpe C., Churchwell E. 1991, A&A 252, 278
 Chini R., Kreysa E., Mezger P.G., Gemünd H.-P. 1986, A&A 154, L8
 Churchwell E., Walmsley C.M., Cesaroni R. 1990, A&AS 83, 119
 Churchwell E., Walmsley C.M., D.O.S. Wood 1992, A&A 253, 541
 de Jong T., Dalgarno A., Chu S. 1975, ApJ 199, 69
 Flower D.R., Launay J.M. 1985, MNRAS 214, 271
 Goldsmith P.F., Bergin E.A., Lis D.C. 1997, ApJ accepted
 Güsten R., Fiebig D., Uchida K.I. 1994, A&A 286, L51
 Ho P.T.P., Haschick A.D. 1986, ApJ 304, 501
 Hofner P., Kurtz S., Churchwell E., Walmsley C.M., Cesaroni R. 1994, ApJ 429, L85
 Hofner P., Wyrowski F., Walmsley C.M., Churchwell E., in prep.
 Humphreys R.H. 1978, ApJS 38, 309
 Hunter T. 1997, Ph.D. Thesis, California Institute of Technology, Pasadena
 Keto E.R., Ho P.T.P. 1988, ApJ 324, 920
 Keto E.R., Ho P.T.P., Reid M.J. 1987, ApJ 323, L117

- Kramer C. 1992, Ph.D. Thesis, Universität zu Köln
- Kutner M.L., Ulrich B.L. 1981, ApJ 250, 341
- McKee C.F., Zweibel E.G. 1996, in: "Protostars and planets III" p. 327
- Rohlfs K., Wilson T. 1996, "Tools of Radio Astronomy", Springer
- Winnewisser G., Zimmermann P., Hernichel J., Miller M., Schieder R. 1990, A&A 230, 248
- Wood D.O.S., Churchwell E. 1989, ApJ 340, 265

Chapter 3

$^{15}\text{NH}_3$ in the hot core associated with G10.47+0.03

3.1. Introduction

The molecular surroundings of hot cores have been studied in the last chapter using C^{17}O . If one aims to study properties of the hot core alone with a single dish telescope, one has to separate emission from the the hot core and the surroundings. This can be done by using emission from molecules with higher dipole moment and accordingly higher critical density (e.g. NH_3 and CH_3CN).

One of the problems encountered has been the high optical depth found in these lines. For example, a series of studies has been carried out using ammonia and methyl cyanide observations to determine the temperature (e.g. Churchwell et al. 1990; Cesaroni et al. 1992; Olmi et al. 1993; Cesaroni et al. 1994). Towards G10.47+0.03 (Cesaroni et al. 1994), the optical depth in the $\text{NH}_3(4,4)$ line approaches 100. This complicates the interpretation in that optically thick transitions are sensitive to surface effects and to temperature gradients along the line of sight. The intensity of an optically thin line by contrast reflects an average over the cores. This is often more useful if one's aim is to understand the energetics of the gas where star formation is currently taking place.

With this in mind, we have undertaken a study of the ^{15}N isotope of ammonia towards a sample of galactic hot core regions (Wyrowski 1994; Wyrowski & Walmsley 1996). Here we want to describe the results of the observations towards G10.47+0.03.

The local isotopic abundance ratio is $[\text{}^{14}\text{N}]/[\text{}^{15}\text{N}] = 300$ and thus, as long as the NH_3 optical depths are less than 300, one can expect $^{15}\text{NH}_3$ to be thin. However, at least in

The results of this chapter are published in Astronomy and Astrophysics 314, 265 (1996) in collaboration with C.M. Walmsley.

Table 3.1: Center frequencies of $^{15}\text{NH}_3$ lines (from Hermsen et al. 1985, see also for a discussion of the hyperfine structure.)

line	ν (MHz)
(1,1)	22624.930
(2,2)	22649.843
(3,3)	22789.422
(4,3)	21673.91
(4,4)	23046.016
(5,5)	23421.982
(6,6)	23922.313

one case — towards the UC HII region NGC 7538 — the $^{15}\text{NH}_3(3,3)$ line is known to be a weak maser (Mauersberger et al. 1986; Schilke et al. 1992). Strong departures from LTE complicate the interpretation if one attempts to deduce the kinetic temperature based upon the relative intensities of $^{15}\text{NH}_3$ lines. Hence the use of $^{15}\text{NH}_3$ as a temperature probe depends partly on the degree to which the processes which lead to non-LTE population in NGC 7538 influence other sources and transitions. However, the $^{15}\text{NH}_3$ study of Orion by Hermsen et al. (1985) showed no clear signs of non-LTE behavior.

3.2. 100-m observations of $^{15}\text{NH}_3$

The observations were carried out with the Effelsberg 100-m telescope in three sessions (Mar. 1994, Mar. and Apr. 1995). The receiver was the facility 1.3 cm K-band maser receiver with an effective noise temperature on the sky from 120 to 450 K depending on weather and elevation. Our spectrometer was a 1024 channel autocorrelator which we used with a 12.5 MHz bandwidth. The resulting spectral resolution was 0.15 km/s and the beam at the frequencies of the $^{15}\text{NH}_3$ lines (see Table 3.1) was about $40''$. Pointing was checked at roughly hourly intervals by means of continuum scans through G10.62. We found the pointing to be accurate to within $4''$. Our calibration was based upon continuum scans through NGC 7027, assuming a flux density of 5.83 Jy corresponding to a main-beam brightness temperature of 8.37 K. We also corrected for telescope gain changes with elevation and checked the calibration accuracy by measuring the scatter in the flux density found in continuum scans on G10.62 which results in a calibration uncertainty of 20%.

3.3. Results

In G10.47+0.03, all metastable transitions of $^{15}\text{NH}_3$ from (1,1) to (6,6) were detected and the spectra are shown in Fig. 3.1. In Table 3.2, we list the line parameters (determined by Gaussian fits) of all observed transitions. $\Delta v_{1/2}$ is the line FWHM. For non-detections

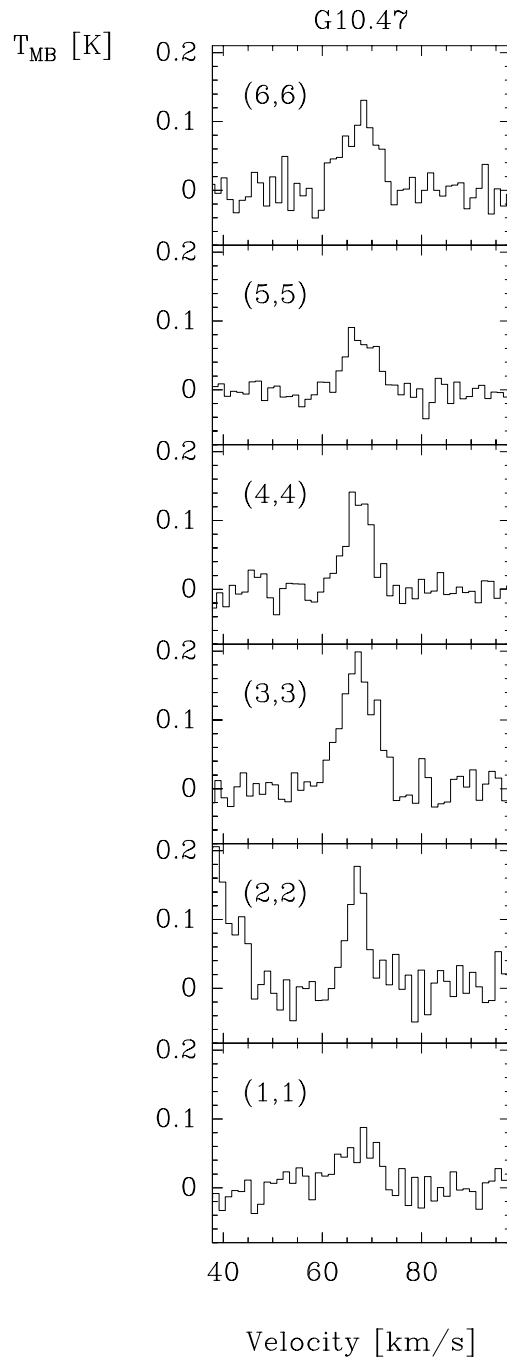


Fig. 3.1.— $^{15}\text{NH}_3$ (1,1) to (6,6) inversion transitions detected towards G10.47. All lines are on the same scale. The (2,2) spectrum shows at velocities below 45 km s^{-1} the red wing of the $\text{NH}_3(5,4)$ line.

Table 3.2: Line parameters derived from Gaussian fits for $^{15}\text{NH}_3$. For non-detections the noise levels (1σ) are given.

Source	(J,K)	T_{MB} (K)	V_{LSR} (km s $^{-1}$)	$\Delta v_{1/2}$ (km s $^{-1}$)
G10.47	(1,1)	0.06 ± 0.03	67.1 ± 0.8	9.1 ± 1.8
	(2,2)	0.17 ± 0.13	67.0 ± 0.9	4.5 ± 2.4
	(3,3)	0.18 ± 0.02	67.1 ± 0.2	8.0 ± 0.4
	(4,4)	0.14 ± 0.03	67.2 ± 0.2	5.5 ± 0.6
	(5,5)	0.08 ± 0.02	67.6 ± 0.3	7.0 ± 0.7
	(6,6)	0.11 ± 0.03	67.7 ± 0.4	7.3 ± 0.8
	(4,3)	< 0.02		

the noise levels (1σ) are given. We searched for the $^{15}\text{NH}_3(4,3)$ line and obtained an upper limit (1σ) of 20 mK.

3.4. Analysis

We were able to derive rotational temperatures for the ortho and para species separately. When considering the Boltzmann plot for $^{15}\text{NH}_3$ in G10.47 (Fig. 3.2), one should be aware that the assumption of isothermality is likely quite inaccurate. Moreover, we do *not* expect precise LTE between metastable levels. Such effects are likely to lead to curvature in Fig. 3.2 and indeed we see an indication of this in the (1,1) column density which may also have a contribution from more extended lower density material than that responsible for the emission seen at higher J. Therefore we excluded the (1,1) transition in the fit. We find $T_{\text{rot}}(\text{ortho}) = 202 \pm 17$ K and $T_{\text{rot}}(\text{para}) = 172 \pm 20$ K. These values are marginally larger than the temperature derived from the VLA observations of Cesaroni et al. (1994, $T(\text{VLA})=165$ K). As a check on our uncertainties, we fit all lines with a constant average linewidth of 6.9 km s^{-1} which leads to $T_{\text{rot}}(\text{ortho}) = 210 \pm 15$ K and $T_{\text{rot}}(\text{para}) = 140 \pm 20$ K.

The beam averaged $^{15}\text{NH}_3$ column density can be derived from the fit to the Boltzmann plot as the sum of all metastable lines using the fit parameters and is $(6.2 \pm 0.7) \times 10^{13} \text{ cm}^{-2}$. For a $^{14}\text{N}/^{15}\text{N}$ ratio of 300, the NH_3 source averaged column density

$$N(\text{NH}_3) = 300 \cdot \frac{40''^2 + \theta_S^2}{\theta_S^2} \cdot N_{\text{TOT}} \quad (3.1)$$

is $5 \times 10^{18} \text{ cm}^{-2}$ using the source sizes $\theta_S=2.4''$ from the interferometer observations of $\text{NH}_3(4,4)$ of Cesaroni et al. (1994). On basis of their data, they estimated a NH_3 column density of $1.4 \times 10^{19} \text{ cm}^{-2}$.

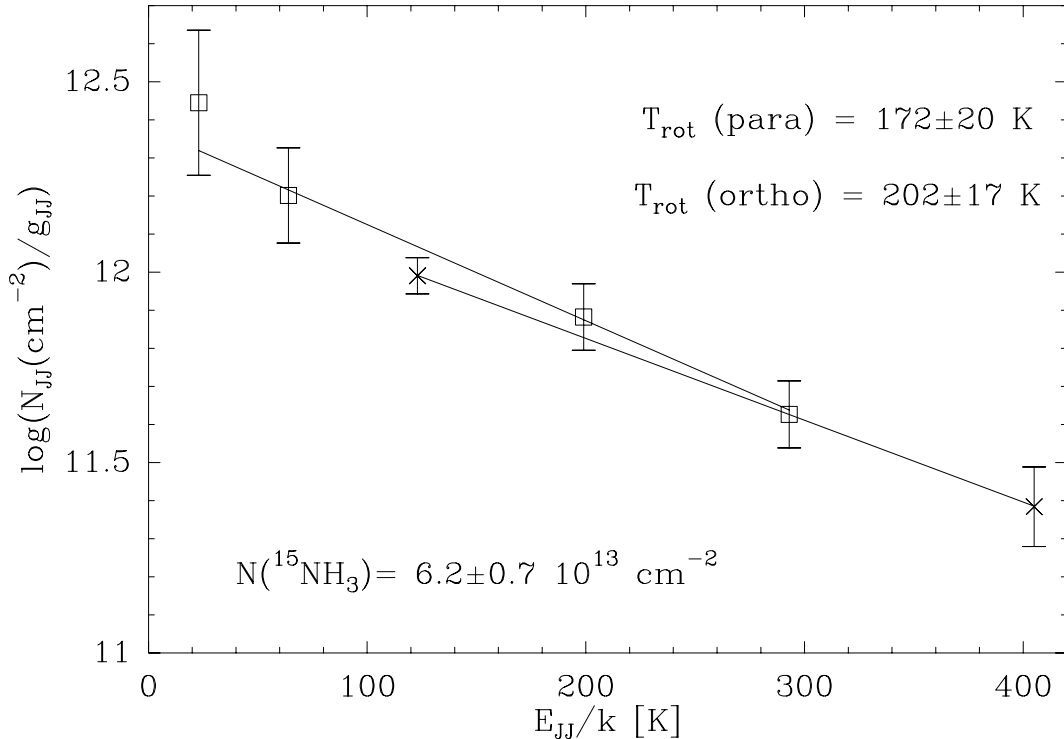


Fig. 3.2.— Boltzmann plot for G10.47. Ortho (crosses) and para (squares) transitions are fit separately. The given column density is sum of all metastable lines using the fit parameters.

3.5. Statistical Equilibrium results

In this section, we compare our observations with predictions of a statistical equilibrium program for ammonia level populations. We consider first the relationship of the rotational temperature which we have derived (Sect. 3.4) and the kinetic temperature in the hot core. Then we discuss what limits we can place on the density and dust radiation field in G10.47 based upon our upper limit for $^{15}\text{NH}_3(4,3)$. We also use the model to check the errors in NH_3 column density determination which arise from the assumption that only metastable levels in $^{15}\text{NH}_3$ are populated.

A description of the statistical equilibrium program used here has been given by Hermsen et al. (1988). Collisional rates are taken from Danby et al. (1988) using a rather arbitrary extrapolation to deal with rotational levels outside the range for which the rates have been calculated. The radiation field at the ammonia line frequencies is calculated using the LVG escape probability for a spherical flow (de Jong et al. 1975). While this may not be valid, we do not know the real geometry and velocity fields in these sources and hence more refined schemes do not seem necessary. Parameters of the model are $n(\text{H}_2)$, T_{kin} and $n(\text{NH}_3)/(dv/dr)$, which is equivalent to the ratio of column density to line width. Far infrared radiation from dust can be included with the parameters dust temperature T_{dust} —

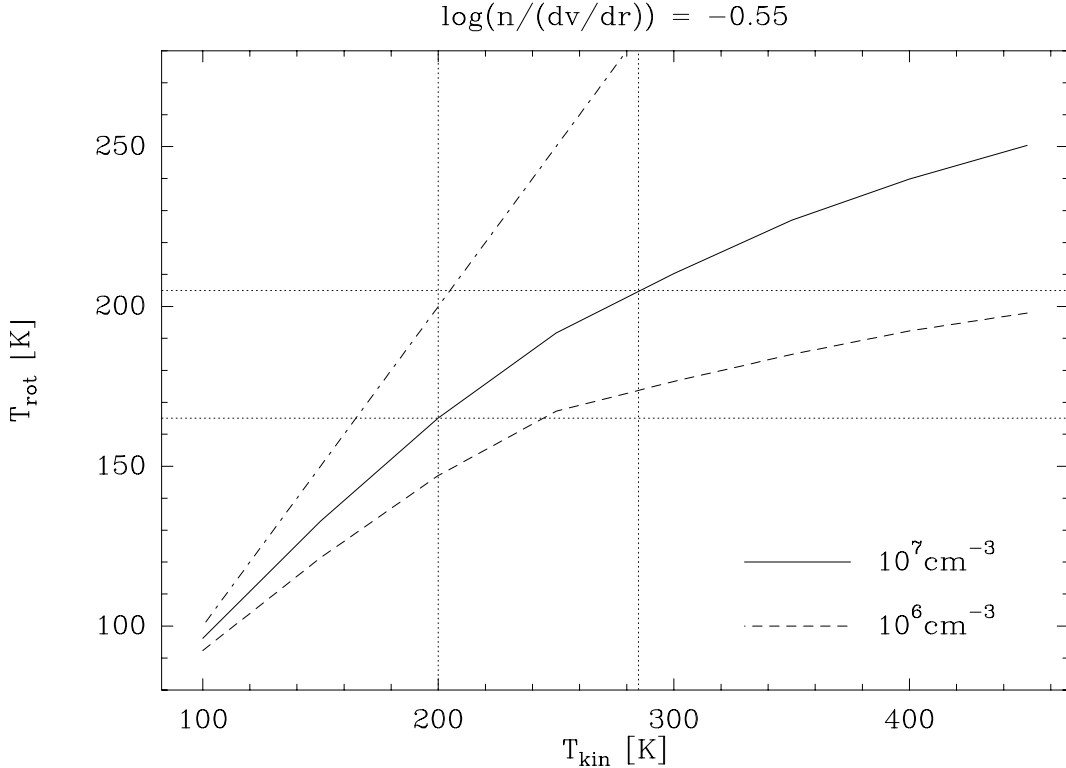


Fig. 3.3.— Predictions of statistical equilibrium model for $n(\text{NH}_3)/(dv/dr) = 0.28 \text{ cm}^{-3}/(\text{km s}^{-1}\text{pc}^{-1})$. The fitted T_{rot} is shown as a function of kinetic temperature T_{kin} for models with H_2 densities of 10^7 cm^{-3} (full line) and 10^6 cm^{-3} (dashed line). Dotted lines show the observational limits based upon our results (1σ errors).

assumed equal to the gas temperature — and the optical depth of the dust at 50 microns $\tau(50\mu\text{m})$ (Deguchi 1981; Hermsen et al. 1988). A geometrical dilution factor of unity is assumed for the far infrared field.

3.5.1. Kinetic temperature estimates

Rotational temperatures derived from ammonia observations lead in general to underestimates of the kinetic temperature (e.g. Walmsley & Ungerechts 1983). In the case of hot core sources however, it has in general been assumed that the density, radiation field and optical depth are sufficiently high that level populations are close to being thermalized. We examine in this section the extent to which the estimates for the $^{15}\text{NH}_3$ rotational temperature in G10.47+0.03 are underestimates of the kinetic temperature.

Figure 3.3 shows a plot of the model predictions of T_{rot} between metastable levels as a function of T_{kin} for assumed densities of 10^6 and 10^7 cm^{-3} . In order to take account of optical

depth effects, we need to make an assumption about the $^{15}\text{NH}_3$ concentration in G10.47 and we do this combining the column density estimate from Sect. 3.4 with the $\text{NH}_3(4,4)$ source size from Cesaroni et al. (1994) (Table 6); we have also made a 30 percent correction for population in non-metastable levels. We find in this way $n(^{15}\text{NH}_3)/(dv/dr) = 9.3 \cdot 10^{-4} \text{ cm}^{-3}/\text{km s}^{-1}\text{pc}^{-1}$ or $n(\text{NH}_3)/(dv/dr) = 0.28 \text{ cm}^{-3}/(\text{km s}^{-1}\text{pc}^{-1})$ for an isotope ratio of 300 and an average linewidth of 6.9 km s^{-1} . This corresponds to an ammonia column density averaged over the VLA source of $5 \cdot 10^{18} \text{ cm}^{-2}$ as compared to the Cesaroni et al. estimate of $1.4 \cdot 10^{19} \text{ cm}^{-2}$. T_{rot} has been computed by fitting the intensities output by the program for the $^{15}\text{NH}_3$ metastable transitions with $J=2-6$ in the same fashion as for the observational data. The fits are in general “reasonable” but Fig. 3.3 shows that at a density of 10^7 cm^{-3} , T_{rot} underestimates T_{kin} by 40 K at a temperature of 200 K and by 80 K at a temperature of 300 K. When we fit the corresponding G10.47 data in this fashion, we obtain $T_{\text{rot}}=185\pm 20 \text{ K}$ which corresponds to $T_{\text{kin}}=240 \text{ K}$ for $n(\text{H}_2)=10^7 \text{ cm}^{-3}$. At lower densities, the discrepancy is larger but given the large ammonia concentration (of order 30 cm^{-3}), we find molecular hydrogen density estimates below $3 \cdot 10^6 \text{ cm}^{-3}$ most unlikely.

3.5.2. The excitation of non-metastable levels of $^{15}\text{NH}_3$

In this section, we consider what one can learn about the hot core from our upper limit on $^{15}\text{NH}_3(4,3)$ in G10.47. For G10.47, we assume the values derived above for the temperature (200–300 K) and the ammonia concentration. Using these parameters and neglecting the influence of the FIR radiation field, we compute the intensity ratio $T_L(4,3)/T_L(3,3)$ which one would expect for $^{15}\text{NH}_3$ in G10.47 as a function of molecular hydrogen density (Fig. 3.4, upper panel). With our observed upper limit on $T_L(^{15}\text{NH}_3(4,3))$ in G10.47 (3σ) we can set an upper limit of $5 \cdot 10^7 \text{ cm}^{-3}$ to the density. This indicates that the gas in the G10.47 hot core cannot be very highly clumped. The *mean* density in G10.47 derived by Cesaroni et al. (1994) on the basis of their VLA measurement and the virial theorem is 10^7 cm^{-3} and it seems probable that the density is between these limits.

The total NH_3 and $^{15}\text{NH}_3$ column densities depend crucially on the assumed partition function and the extent to which non-metastable levels are populated. We have therefore used the results of the statistical equilibrium calculations to directly calculate the partition function. The results are shown in the lower panel of Fig. 3.4. Here, we plot the partition function Z for either ammonia isotopomer

$$Z = 2 \cdot \sum_{ortho} \frac{n(J, K)}{n(0, 0)} + 3 \cdot \exp(-E(1, 1)/kT) \sum_{para} \frac{n(J, K)}{n(1, 1)} \quad (3.2)$$

where $n(J, K)$ are the populations of the (J, K) levels (sum of both inversion states where present) and the ground level is $(1, 1)$ for para and $(0, 0)$ for ortho. We assume thermalization

between (1,1) and (0,0) which may in practice be incorrect. From Fig. 3.4, one sees that at high densities, Z reaches the LTE value (80 at 200 K). At densities below 10^7 cm^{-3} the non-metastable levels of NH_3 become depopulated. For the case of $^{15}\text{NH}_3$ towards G10.47, we can put an upper limit on $Z(200 \text{ K})$ of 40 due to the non-detection of the (4,3) line. A Boltzmann population of only metastable levels leads to $Z(T) = 26.5(T[\text{K}]/200)$. Hence, at most 30% of $^{15}\text{NH}_3$ can be in non-metastable levels in G10.47 which justifies the assumption made in Sect. 3.5.1.

3.6. Discussion

The temperature from $^{15}\text{NH}_3$ should represent a mean temperature taken through the entire region in contrast to the temperature found with the VLA, which is only indicative for the surface layer of the molecular clump. This may imply a temperature gradient with higher T inside the clumps confirming the interpretation as centrally heated cores. Another possibility could be that the (4,4) excitation temperature at the surface of hot cores is smaller than the kinetic temperature. This would be surprising since one expects metastable ammonia transitions to be thermalized at hot core densities. Hence, we consider our results to be evidence for the presence of an embedded star in the hot core associated with the UC HII region G10.47+0.03.

After adopting the source size measured with the VLA towards G10.47, we were able to correct the $^{15}\text{NH}_3$ results for the beam filling factor so that direct comparisons with the NH_3 VLA results were possible (Section 3.4). Although our optically thin $^{15}\text{NH}_3$ observations should trace *all* the molecular gas, we see column densities smaller by a factor of 3 than estimated from the interferometer data. Possible explanations for this discrepancy are:

1. The VLA source size could be misleading given that we know little about the internal structure of these objects. We have used a source sizes of $2.4''$ observed by Cesaroni et al. (1994) to correct our beam averaged $^{15}\text{NH}_3$ column density and to derive a source averaged column density. One possibility is that this source size overestimate the angular dimension as seen in $^{15}\text{NH}_3$. It is reasonable to expect the effective source size seen in the optically thick NH_3 lines to be larger than that seen in $^{15}\text{NH}_3$. Direct interferometric $^{15}\text{NH}_3$ observations are needed to test this.
2. We have assumed that the $[\text{NH}_3]/[^{15}\text{NH}_3]$ ratio is equal to the normal interstellar value of 300. If fractionation or other processes cause this assumption to be incorrect, our derived ammonia column densities will be correspondingly in error. If for example we use a value of 390 as suggested by Dahmen et al. (1995) for sources 5 kpc from the galactic center, our column density estimates will increase by a factor 1.3.
3. A temperature gradient within the hot core may cause the column density derived

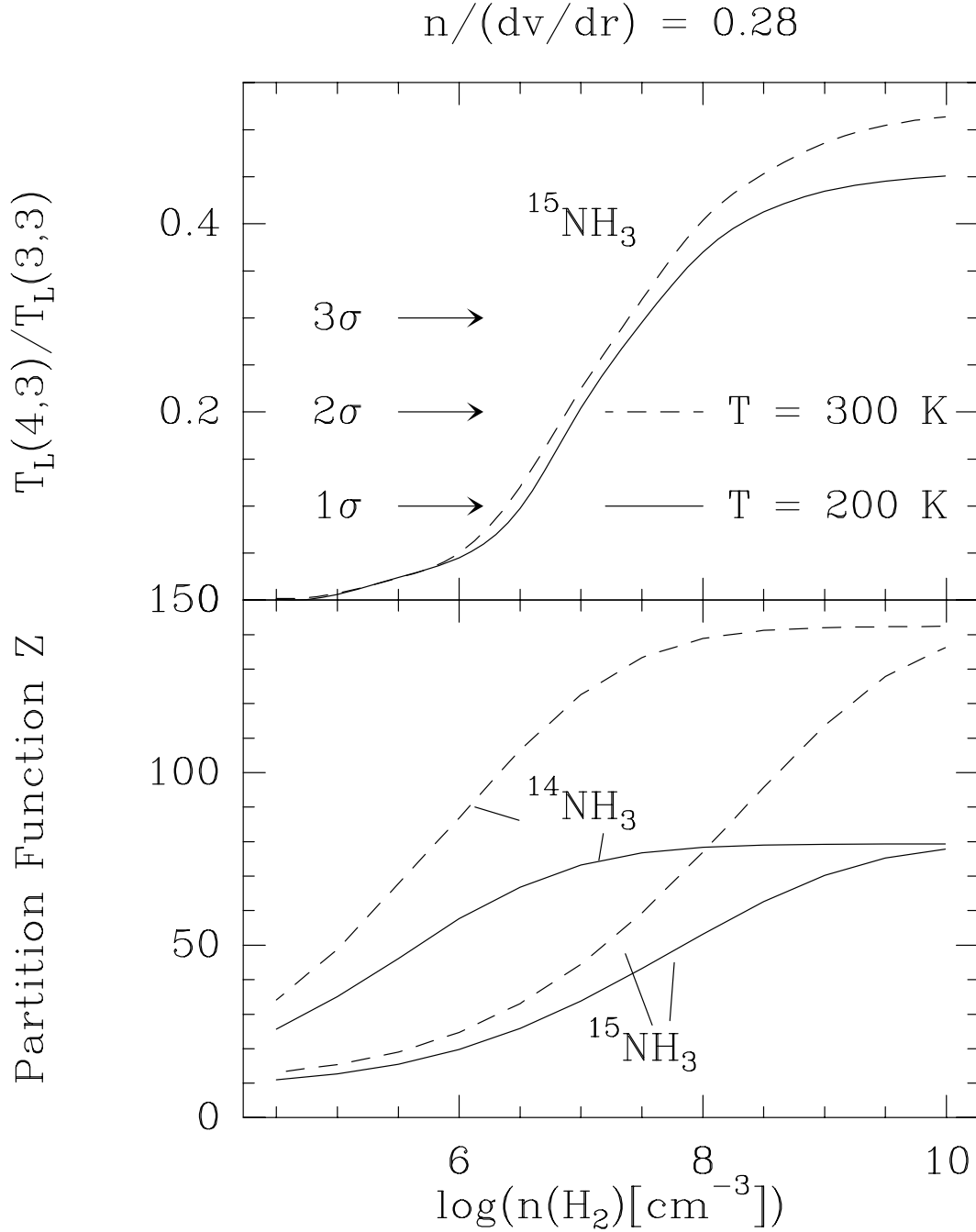


Fig. 3.4.— Predictions of statistical equilibrium calculations for a ratio $n(\text{NH}_3)/(dv/dr) = 0.28 \text{ cm}^{-3}/(\text{km s}^{-1}\text{pc}^{-1})$. Results are shown as a function of density at temperatures of 300 K (dashed) and 200 K (full lines). The top panel shows predictions for the intensity ratio $T_L(4,3)/T_L(3,3)$ for $^{15}\text{NH}_3$. The observed 1σ , 2σ and 3σ limits for G10.47 are shown by the arrows on the left. The lower panel shows the results of the partition function for both NH_3 and $^{15}\text{NH}_3$ as computed using Eq. (5).

on the basis of the hyperfine satellite intensities, as has been done by Cesaroni et al. (1994), to be overestimated. This can occur because the main line and the satellites penetrate to different depths. An increase of temperature from outside to inside favors the satellites and simulates high optical depth. Some VLA-spectra (see Fig. 6 a,b of Cesaroni et al. 1994) suggest such an effect towards G10.47. There are even pixels where the satellites appear stronger than the main line.

4. The uncertainties in the partition function discussed in the previous section (see Fig. 3.4) may partially explain differences in derived column densities.

Probably, a combination of the possibilities listed above explains the lower column density from $^{15}\text{NH}_3$. What is perhaps more important to note is that the discrepancy is *only* a factor 3. Thus, the high ammonia column densities — and by inference high hydrogen column densities — in hot cores are real.

3.7. Conclusions

We find that for certain “extreme” sources, e.g. G10.47+0.03, it is possible to derive the parameters of the high density gas on the basis of $^{15}\text{NH}_3$ observations. For this object, we were able to measure several metastable $^{15}\text{NH}_3$ transitions and derive a kinetic temperature of 240 ± 40 K. This is larger than the brightness temperature of the $\text{NH}_3(4,4)$ line observed with the VLA (Cesaroni et al. 1994) indicating a higher temperature averaged over the core than the surface temperature sampled by optically thick transitions. This suggests that the core in G10.47+0.03 is heated by an embedded object.

We did not detect the $^{15}\text{NH}_3(4,3)$ line towards this source. This allowed us to set an upper limit of $5 \cdot 10^7 \text{cm}^{-3}$ to the molecular hydrogen density in the core. There are not many reliable ways of estimating hydrogen densities in such regions and so further efforts to detect this line would be useful.

We have derived the ammonia column density from our observations for the purpose of comparing them with the value obtained by other means. Ammonia column density determinations in the past have usually relied on measurement of the hyperfine satellites of one or more transitions and thus on the determination of the line optical depth. Then on the basis of some estimate of the partition function, one derives the “total” ammonia column density. There are various assumptions involved in this procedure which are debatable (for example equal excitation temperatures for the hyperfine components). The column density which we have derived from our $^{15}\text{NH}_3$ measurements has its own set of uncertainties but involve a different and independent approach. The result is that we find a column density lower by a factor of three than found by the usual method. While the reasons for this discrepancy are interesting, it is more important that our results show that

the *extremely large* column density found previous is not enormously in error. Both large ammonia abundances and large hydrogen densities are needed to explain the observations.

REFERENCES

- Cesaroni R., Walmsley C.M., Churchwell E. 1992, A&A 256, 618
Cesaroni R., Churchwell E., Hofner P., Walmsley C.M., Kurtz S. 1994, A&A 288, 903
Churchwell E., Walmsley C.M., Cesaroni R. 1990, A&AS, 83, 119
Dahmen G., Wilson T., Matteucci F. 1995, A&A 295, 194
Danby G., Flower D.R., Valiron P., Schilke P., Walmsley C.M. 1988, MNRAS 235, 229
Deguchi S. 1981, ApJ 249, 145
De Jong T., Chu S.-I, Dalgarno A. 1975, ApJ 199, 69
Hermsen W., Wilson T.L., Walmsley C.M., Batrla W. 1985, A&A 146, 134
Hermsen W., Wilson T.L., Walmsley C.M., Henkel C. 1988, A&A 201, 285
Mauersberger R., Wilson T.L., Henkel C. 1986, A&A 160, L13
Olm L., Cesaroni R., Walmsley C.M. 1993, A&A 276, 489
Schilke P., Walmsley C.M., Mauersberger R. 1992, A&A 247, 516
Walmsley C.M., Ungerechts H. 1983, A&A 122, 164
Wyrowski F. 1994 , Diplomarbeit, University of Bonn
Wyrowski F., Walmsley C.M. 1996, A&A 314, 265

Chapter 4

Probing the IR-field of hot cores

4.1. Introduction

Massive O-B stars form in dense condensations within molecular clouds. The high dust extinction within such condensations obscures their innermost parts in the near and mid-IR making it difficult to study the internal structure in these wavelength regions. Recently it has been recognized that one tracer for O-B stars in the earliest phases of their evolution is the presence of emission from high excitation molecular lines. Such molecular hot cores are usually found in the neighborhood of compact HII regions and have masses in the range 10-3000 M_{\odot} and temperatures of order 200 K (Churchwell 1991). One of the important characteristics of these objects is their internal radiation field or (equivalently) the distribution of dust temperature. Since the infrared radiation in the interior is not directly observable, due to the extinction mentioned above, one has to resort to indirect methods. One such method is observing rotational transitions at radio wavelengths excited due to radiative pumping by IR dust photons (see Table 4.1).

Most of the work done so far has been concerned with the Orion hot core and Sgr B2. Churchwell et al. (1986) analyzed HNCO as a probe of FIR radiation. Vibrationally excited HC₃N has been studied by Goldsmith et al. (1982, 1985). A recent interferometer molecular line survey of Orion KL by Blake et al. (1996) gives insight into the spatial distribution of HNCO and vibrationally excited HC₃N. Other examples of vibrationally excited molecules studied in star formation regions are HCN (Ziurys & Turner 1986), NH₃ (Mauersberger et al. 1988), and CH₃CN (Clark et al. 1976; Olmi et al. 1996a).

Two particularly interesting young embedded objects are the hot cores associated with the UC HII regions G10.47 and G31.41. They have been studied using the VLA in high excitation ammonia lines (Cesaroni et al. 1994) and with both the 30-m telescope and Plateau de Bure interferometer in methyl cyanide (Olmi et al. 1996a, 1996b). Both sources have also been observed in our ¹⁵NH₃ and C¹⁷O studies (see Chapter 2 and 3). The sources

Table 4.1: Wavelengths of the pumping IR radiation of different molecules, their Einstein coefficients and critical densities.

Molecule	Transition	λ_{EXC} (μm)	A_{ul} (s^{-1})	n_{cr} cm^{-3}	vibration
NH ₃	$v_2 = 1 - 0$	10	5	10^{13}	umbrella
HCN	$v_2 = 1 - 0$	14	3.7		bend
HC ₃ N	$v_4 = 1 - 0$	11	0.003	$6 \cdot 10^{10}$	C-C stretch
	$v_5 = 1 - 0$	15	2.2	$2 \cdot 10^{13}$	HCC bend
	$v_6 = 1 - 0$	20	0.15	$8 \cdot 10^{11}$	CCN bend
	$v_7 = 1 - 0$	45	$6 \cdot 10^{-4}$	10^9	CCC bend
CH ₂ CHCN	$v_{15} = 1 - 0$	29			out of plane
	$v_{11} = 1 - 0$	42			in plane CCN bend
HNCO	$v_4 = 1 - 0$	13			in plane bend
	$v_6 = 1 - 0$	15			out of plane
	$v_5 = 1 - 0$	17			in plane
	$K_a = 2 - 1$	110			rot. <i>b</i> -type
	$K_a = 1 - 0$	330			rot. <i>b</i> -type

are associated with hot high column density molecular gas with characteristics similar to those of the hot core seen towards the Orion KL region but much more massive. From the dust emission the mass of the compact cores are found to be of the order of $2000 M_{\odot}$ within a region of about 0.05 pc. Complementary, we decided to observe also W3(OH), a clump with a more moderate mass.

Here we present single dish observations of radiatively excited transitions of HCN, HC₃N, HNCO, NH₃ and CH₂CHCN towards these hot cores.

4.2. Observations

The observations were carried out in July 1996 using the IRAM 30-m telescope on Pico Veleta. We observed simultaneously at 3, 2, and 1.3 mm with half power beam widths of 22'', 16'', and 12''. Lists of the observed sources and frequencies are given in Tables 4.2 and 4.3. The main targets have been the sources G10.47, G31.41, and W3(H₂O), but some other sources were observed in some frequency bands as well. This is accounted for by giving a code in the tables for the sources observed in each band.

We used the facility 3 mm, 2 mm, and 1.3 mm (G1 and G2) SIS receivers with system temperatures of 300–450 K, 650–900 K, and 800–3000 K, respectively, depending on weather and elevations. The alignment between the different receivers was checked through continuum cross scans on planets and found to be accurate to within 2'' for the 3 mm,

Table 4.2: Observed sources

Source	α_{1950}	δ_{1950}	v_{LSR} in km/s	code
G10.47	18:05:40.36	-19:52:21.3	+67.0	1
G10.62	18:07:30.67	-19:56:29.4	+67.0	2
G29.96	18:43:26.92	-02:42:36.4	+98.7	3
G31.41	18:44:59.11	-01:16:06.8	+97.0	4
G34.26	18:50:46.21	+01:11:11.7	+59.1	5
W3(H ₂ O)	02:23:17.25	+61:38:57.3	-49.0	6

Table 4.3: Frequency setup

Bandname	ν_{center} in GHz	observed sources
BAND3-HCN	86.25	1,4,6
BAND3-HNCO	87.8	1,3,4,6
BAND3-109	109.41	1,4
BAND3-110	110.095	1-6
BAND2-NH3	140.3	1,4
BAND2-154	154.23	1,3,4,6
BAND2-155	154.85	1-6
BAND1-215	215.25	1-6
BAND1-218	218.97	1,4,6
BAND1-HNCO	219.58	1,3,4,6
BAND1-228	228.1	1,4
BAND1-HCN	258.28	1,4,6

2 mm, and first 1.3 mm receiver. A misalignment of up to 5'' was observed for the second 1.3 mm millimeter receiver.

Our spectrometers were an autocorrelator with 1633 channels and 0.32 MHz resolution and two filter-banks with 1 MHz resolution and 512 channels. This led to typical velocity resolutions between 1 and 2 km/s. All lines have been observed in the lower sideband with typical sideband rejections of 30, 10, 20 dB at 3, 2, and 1.3 mm, respectively.

The wobbling secondary mirror was used with a beam throw of 120'' and a frequency of 0.25 Hz resulting in linear baselines of the spectra. To obtain main beam brightness temperature as intensity scale, the antenna temperature has been multiplied by the ratio of the forward and the main beam efficiency which were taken from Table A.1 of the 30-m manual (Wild 1995).

The focus was checked at the beginning of each night on Jupiter or Saturn. Since the two 1.3 mm receivers have somewhat different foci, we select in these cases a focus position giving a compromise between the different receivers more weighted to the 1.3 mm G1 which

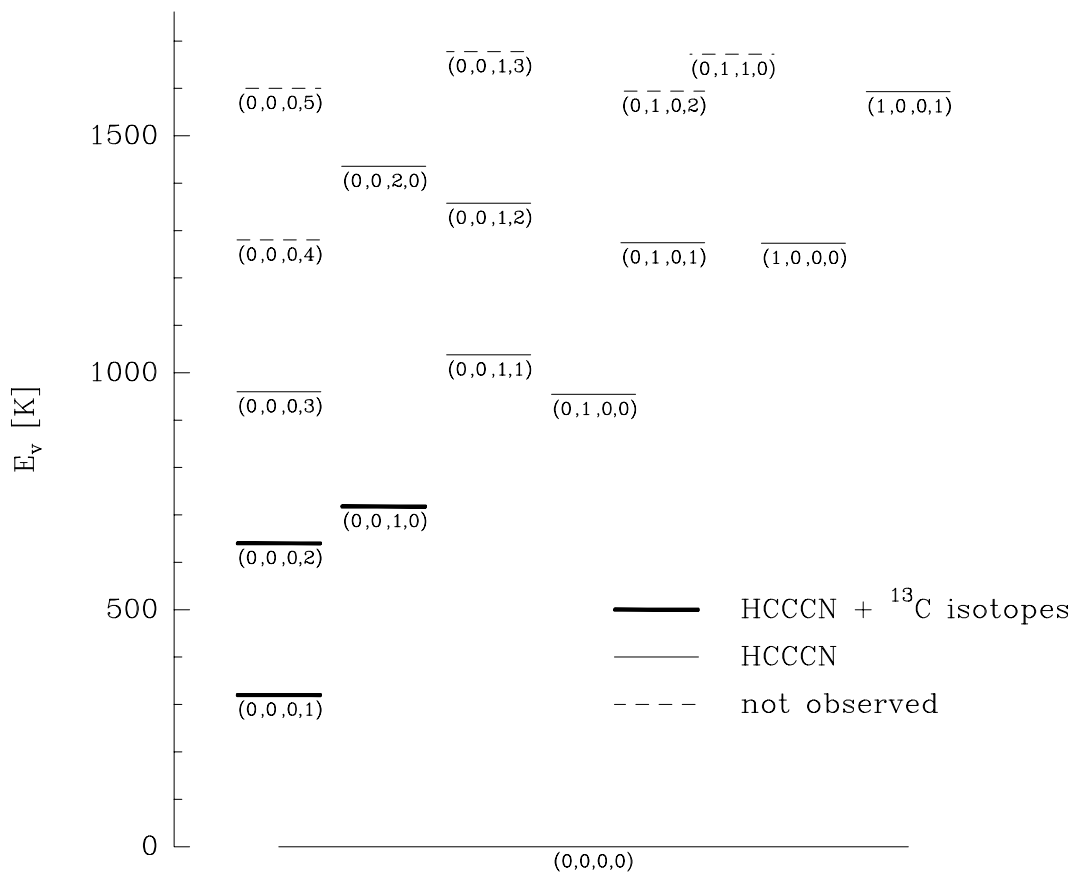
Vibrational energy levels (v_4, v_5, v_6, v_7) of HCCCN

Fig. 4.1.— Vibrational energy levels of HCCCN. v_4 is the quantum number of the lowest stretching vibration, and v_5, v_6, v_7 are bending vibrations. All detected lines are marked and the remaining were not covered by our observing bands.

has the same focus as the 3 and 2 mm receivers. The resulting gain loss is smaller than 10%. Pointing was checked hourly by cross scans on planets, G10.62, and W3(OH) and was found to be good within $4''$.

4.3. Vibrationally excited cyanoacetylene

4.3.1. Frequencies of vibrationally excited states

The linear pentatomic molecule cyanoacetylene has seven modes of vibration, four stretching modes and three bending modes which are doubly degenerate (Mallinson & Fayt 1976). An overview of the various fundamental vibrations is given in Table 4.1. The stretching modes ν_1, ν_2, ν_3 , which lie more than 3000 K above ground, are omitted. Besides the fundamental modes of vibration also overtones and combinations modes

can be observed. A level diagram of all modes lower than 1700 K is shown in Fig. 4.1. Several of these modes are coupled by anharmonic resonances (Yamada & Creswell 1986). Laboratory studies of the infrared spectrum have been made firstly by Turrel et al. (1957) and more accurately by Mallinson & Fayt (1976) who determined band centers for all seven fundamentals with high precision. The first interstellar detection of vibrationally excited states of this molecule was done by Clark et al. (1976) towards the Orion hot core.

Since most of the vibrationally excited rotational lines observed by us are first detections in interstellar space, we would like to discuss briefly how the frequencies are obtained with the help of the molecular constants derived from laboratory measurements. Besides the identification of observed lines which lie outside the frequency ranges analyzed in the laboratory, this was necessary to predict the frequencies in other wavelength ranges for future studies.

Vibrations slightly change the average bond lengths of the molecule, leading to a decrease of the rotational constant B in case of stretching and an increase in case of bending modes. Thus the rotational constant is changed from its equilibrium value B_e to

$$B = B_e - \sum_i \alpha_i (v_i + d_i/2) - J(J+1)D \quad (4.1)$$

(Townes & Schawlow 1955) where the α_i give the first order correction to the rotational constant for the vibrational modes i with quantum number v_i and degeneracy d_i and the second term represents the usual correction due to the centrifugal stretching of the molecule during rotation.

A linear combination of two orthogonal bending modes with a 90 degrees phase difference is equivalent to a rotation about the figure axis which can be described by an additional angular momentum l about this axis. The degeneracy of the bending modes is lifted due to the Coriolis force which is different for bending of the molecule perpendicular and parallel to the rotational axis. This interaction of rotation and vibration results in a splitting of

$$\Delta\nu = \frac{q_i}{2}(v_i + 1)J(J+1) \quad (4.2)$$

for $|l| = 1$. The q_i are the coupling constants for the interaction. l can take the values $v, v-2, \dots, -v$ and the selection rule for J changing transitions is $\Delta l = 0$. For higher l the splitting is usually too small to be observed. Values of the constants α_i and q_i for some vibrations are given in Table 4.4.

The theoretical description of the vibration of polyatomic molecules is further complicated by perturbations between states of nearly the same energy. This leads to a repulsion of the perturbed energy levels and to a change in the effective rotational parameters. The coupling of the different vibrational modes is due to anharmonic terms in the molecular potential and the perturbations are therefore called anharmonic resonances.

Table 4.4: Molecular constants of HC₃N for the observed isotopomer taken from Mallinson & Zafra (1978).

Constant	HCCCN	HC ¹³ CCN	HCC ¹³ CN
B_0/MHz	4549.058	4529.755	4530.195
α_5/MHz	-1.813	-1.558	-1.552
α_6/MHz	-9.262	-9.075	-8.983
α_7/MHz	-14.605	-14.020	-14.184
q_5/MHz	2.570	2.519	2.516
q_6/MHz	3.582	3.593	3.635
q_7/MHz	6.538	6.579	6.529
D_0/kHz	0.5444		

Resonances of modes of interest for our study are discussed in detail by Yamada & Creswell (1986).

To actually reproduce measured frequencies from theory to an accuracy of less than 1 MHz, which is needed for the interpretation of our spectra, it is necessary to take also the effect of perturbation between vibrational states into account. Therefore we used alternatively the effective rotational constants B_{eff} and D_{eff} , which were fitted by Yamada & Creswell (1986) to their measurements with sufficient accuracy for all the different levels shown in Fig. 4.1, to compute the line frequencies despite of l -type doubling and resonance interaction:

$$\nu = 2B_{\text{eff}}(J + 1) - 4D_{\text{eff}}(J + 1)^3 \quad (4.3)$$

These effective constants were only given for the main isotopomer. We calculated the frequencies of the weaker isotopomeric species with the help of the parameters B_0 , D_0 , α_i , and q_i determined from the analysis of transition in the region 26.5–40.0 GHz by Mallinson & Zafra (1978) which are given in Table 4.4:

$$B_v = B_0 - \alpha_i \quad (4.4)$$

$$\nu_0 = 2B_v(J + 1) - 4D_0(J + 1)((J + 1)^2 - 1) \quad (4.5)$$

$$\nu = \nu_0 \pm q_i(J + 1) \quad (4.6)$$

The accuracy of extrapolating this fit of the low frequency transitions to high frequency transitions in the range from 3 to 1.3 mm is a priori unknown, but we will see in the next section that this procedure works surprisingly well and lead to the identification of ¹³C substituted HC₃N in vibrationally excited states without ambiguity.

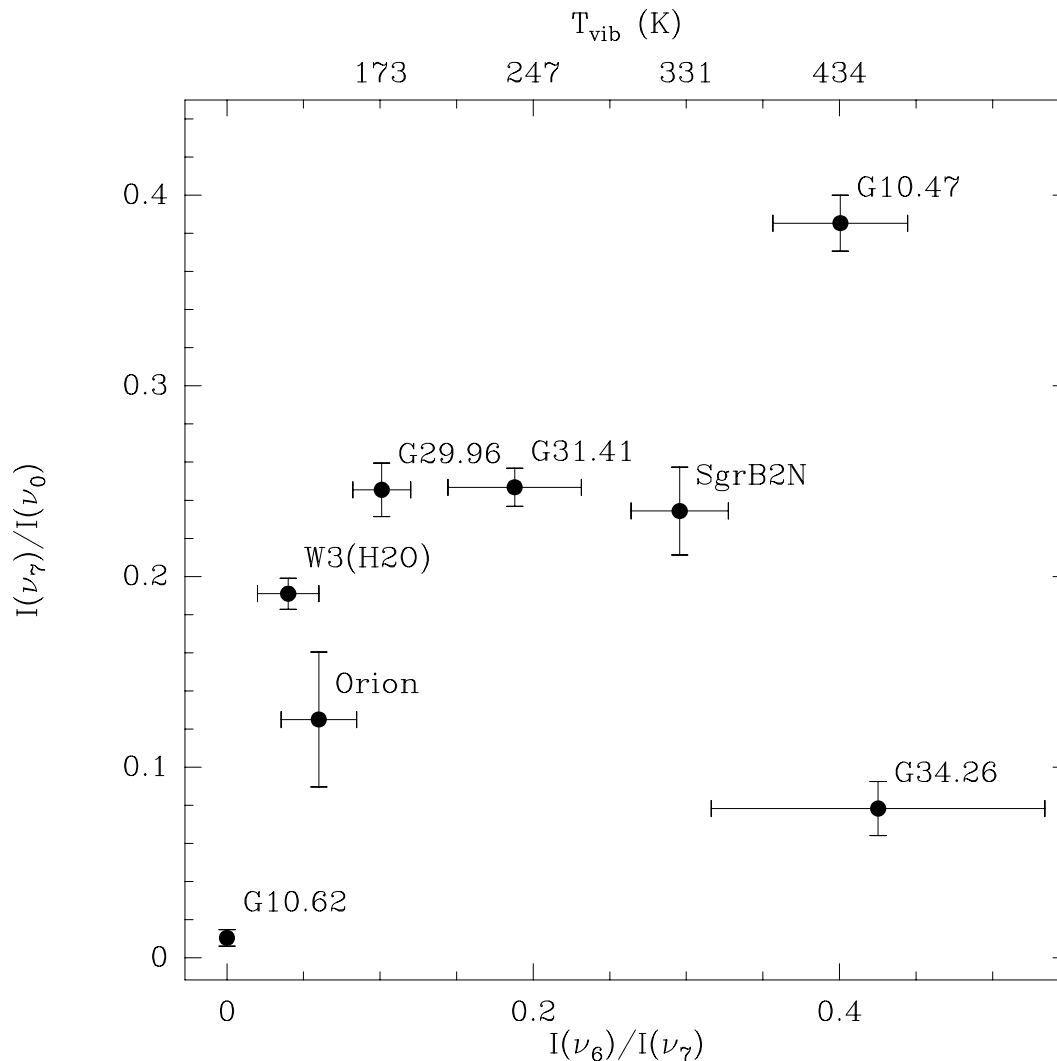


Fig. 4.2.— Ratios of line intensities in the vibrational states ν_0 , ν_7 and ν_6 towards the observed hot cores and, additionally, for the hot cores Orion KL and Sgr B2N where the values of the (12–11) intensities are taken from Goldsmith et al. (1985) and de Vicente (1994).

4.3.2. The whole sample

At 155 GHz, we detected $\text{HC}_3\text{N}(17-16)$ in its ground and lowest (ν_7) vibrationally excited states towards all six sources and the ν_6 state in all sources except G10.62. To analyze the different excitation conditions in the sources, we plotted the ratios of the integrated line intensities against each other in Fig. 4.2. For comparison purposes, the well-known hot core sources Orion KL and Sgr B2N were added with their line intensities taken from the literature (Goldsmith et al. 1985 and de Vicente 1994). Since the vibrational ground state line of HC_3N is expected to be dominated by more extended emission, the ratio between the ν_7 and the ground state is not a measure of the vibrational temperature

but rather a rough measure of the relative amount of molecules in vibrationally excited states in the whole region, whereas the ratio of the intensities in the excited states v_6 and v_7 can be converted to a vibrational temperature of the hot core assuming optically thin conditions:

$$\frac{I_6}{I_7} = \exp\left(-\frac{\Delta E_{67}}{kT_{\text{vib}}}\right) \quad (4.7)$$

Ratios of 0.1, 0.2, and 0.4 then correspond to 170, 250, and 430 K, respectively. There is a trend for higher vibrational temperatures with a larger amount of vibration relative to the extended ground state emission. The only exception is G34.26. In this complex, UC HII regions of different morphologies are found (e.g. Gaume et al. 1994). Hence, star formation in different evolutionary states is present within our 30-m beam. The high vibrational temperature could belong to the dense cores associated with the water masers and the high ground state emission to the bulk of a halo forming surrounding gas (see the discussion of Garay & Rodriguez 1990 on different ammonia structures in this source). In G10.62 there is nearly no vibrational excitation present. The trend to higher excitation is then also a trend of higher mass with the mediate massive cores W3(H₂O) and Orion KL at the lower end, and the very massive cores Sgr B2N and G10.47 at the higher end. The position of G10.47 is exceptional in comparison to the other sources. In this source, also many other vibrationally excited states were detected which is discussed in detail in the next section.

4.4. HC₃N in G10.47+0.03

4.4.1. The identifications

We detected rotational transitions in eleven vibrationally excited states of HC₃N (six of these are detected for the first time in interstellar space) towards the hot core associated with the UC HII region G10.47+0.03. This allows the most detailed study of vibrational (as opposed to rotational) excitation in a molecular cloud so far. Since the line blending problem becomes severe at 1.3 mm, the HC₃N lines are best identified at 3 and 2 mm. We show the spectra obtained at these wavelengths together with identifications and a formal fit with $T=500$ K in Figs. 4.3 and 4.4 (for details about the fit see the Chapter 5). We have detected transitions in the $(v_4, v_5, v_6, v_7) = (0,0,0,1), (0,0,0,2), (0,0,0,3), (0,0,1,0), (0,0,2,0), (0,0,1,2), (0,1,0,0), (0,1,0,1)$ bending vibrational states and also the $(1,0,0,1)$ and $(1,0,0,0)$ stretching vibrational levels. One may compare with Orion where despite deep searches only the $(0,0,0,1), (0,0,0,2)$ and $(0,0,1,0)$ states have been found (Clark et al. 1976; Goldsmith et al. 1982, 1985; Blake et al. 1996). An overview of the detected states is shown in Fig. 4.1 where one sees they range up to more than 1500 K above ground. Lines of all the levels which are marked as “not observed” lay outside our observing bands. The observed parameters of the lines are given in Appendix A.

An example of modes with two quanta of vibration excited is shown in the upper

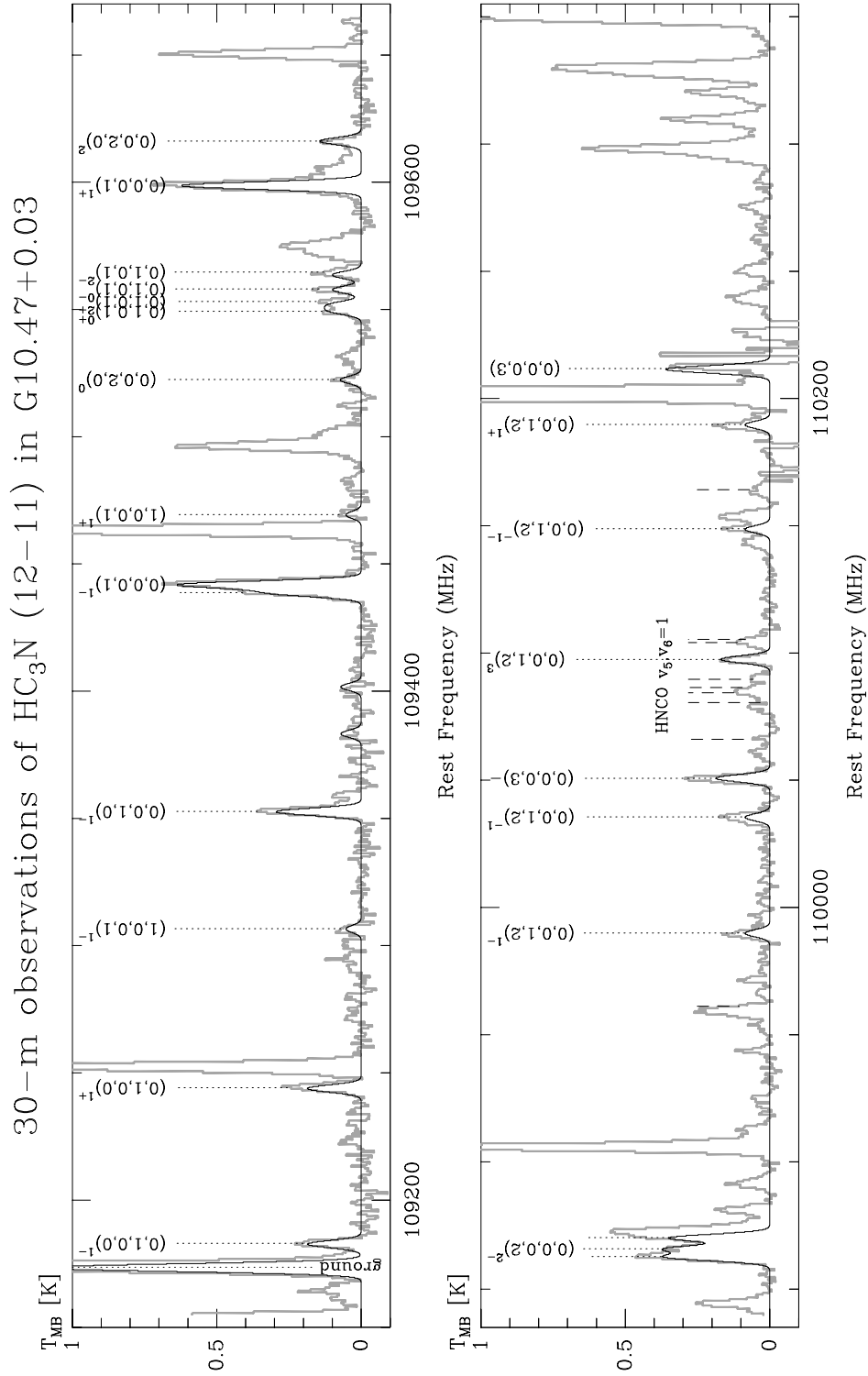


Fig. 4.3.— 30-m spectra of $\text{HC}_3\text{N}(12-11)$ towards G10.47. The identified vibrational excited states are marked with dots and their vibrational quantum numbers (v_4, v_5, v_6, v_7) . The applied fit to HC_3N assumes one single temperature for all lines of 500 K. Vibrationally excited HNC0 is marked with dashes. The strong line at 110.2 GHz is the ^{13}CO line which shows several absorption features caused by the small wobbler throw of $2'$.

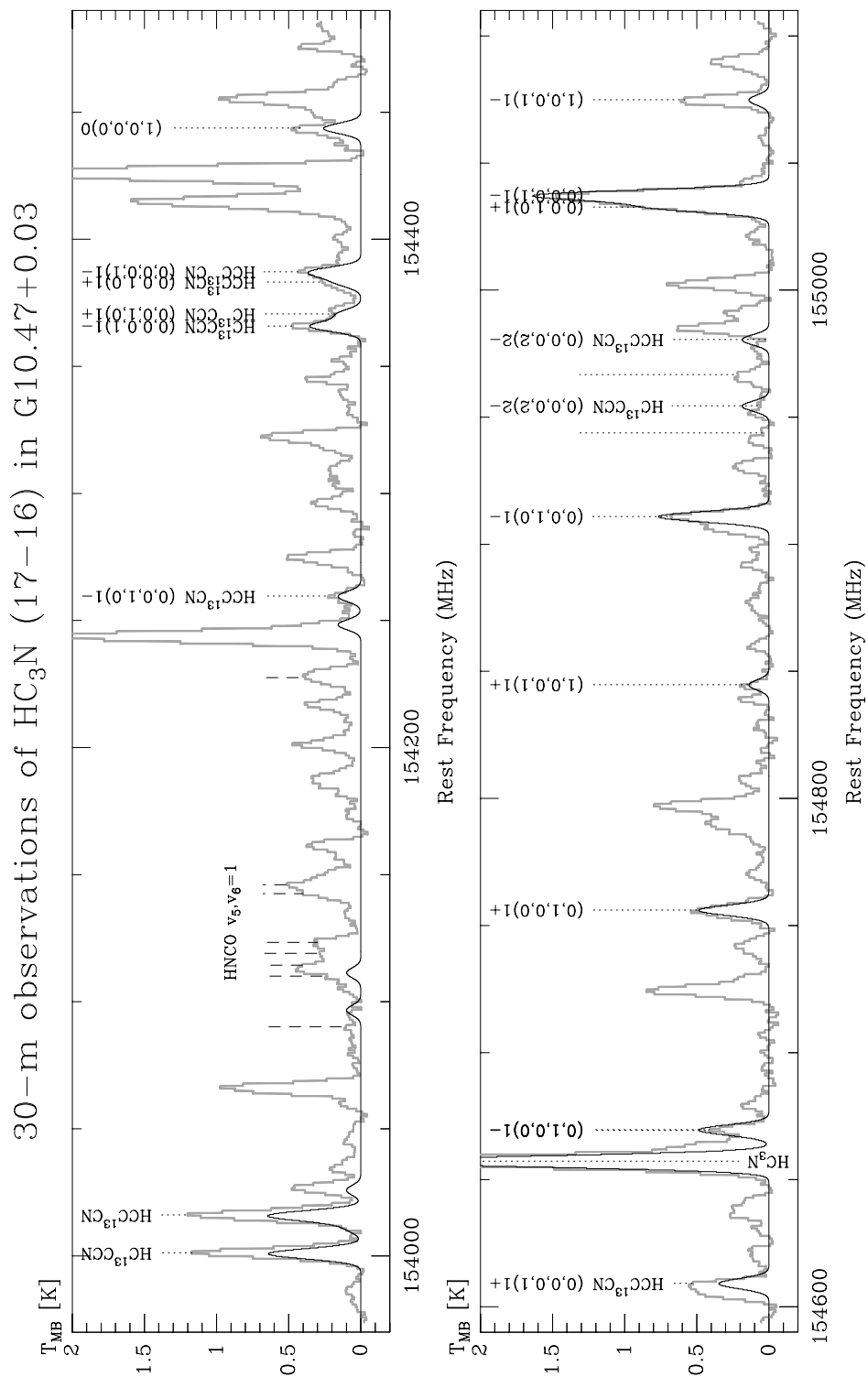


Fig. 4.4.— Same as Fig. 4.3 but HC₃N(17-16)

Table 4.5: Observed and calculated frequencies of vibrationally excited HC₃N isotopomers at 154 GHz.

Transition	ν_{obs} (MHz)	$\Delta\nu_{\text{obs}}$ (MHz)	ν_{cal} (MHz)	O-C (MHz)
HCC ¹³ CN $v_6 = 1^-$	154259.1	1.6	154259.6	-0.5
HC ¹³ CCN $v_7 = 1^-$	154365.7	0.6	154365.8	-0.1
HC ¹³ CCN $v_6 = 1^+$	154371.8	1.5	154370.6	1.2
HCC ¹³ CN $v_6 = 1^+$	154382.5	1.6	154383.2	-0.7
HCC ¹³ CN $v_7 = 1^-$	154387.6	1.0	154387.2	0.4
HC ¹³ CCN $v_7 = 2^0$	154941.0	0.4	154943.8	-2.8
HC ¹³ CCN $v_7 = 2^{2-}$	154952.0	0.5	154954.5	-2.5
HC ¹³ CCN $v_7 = 2^{2+}$	154964.5	0.9	154966.8	-2.3
HCC ¹³ CN $v_7 = 2^0$	154967.5	1.3	154969.9	-2.4

panel of Fig. 4.5. The combination mode (0,1,0,1), which lies about 1300 K above ground, is split into four components with $|l|=0, 2$. This splitting is due to l -type doubling and, additionally, due to anharmonic resonances in the (1,0,0,0)-(0,1,0,1)-(0,0,2,0)-(0,0,0,4) system (Yamada & Creswell 1986). Out of this four state resonance also two $v_6 = 2$ lines, about 1450 K above ground, are seen. Here the splitting of the $|l|=2$ lines is too small to be observed and both lines overlap resulting in a relatively high intensity. One should note the excellent coincidence of line frequencies measured in the laboratory and towards the hot core source G10.47 which gives strong confidence into the identification of these lines. Evidence for (0,0,1,1) lines is found in a 1.3 mm spectrum near the C¹⁸O(2-1) line. Fig. 4.6 shows close to the predicted frequencies three spectral features. Small errors in the prediction are possible because of large perturbations (Yamada & Creswell 1986). Also all lines in our observed bands with three quanta of vibration excited are clearly identified ((0,0,1,2) and (0,0,0,3)) in the lower panel of Fig. 4.3. The highest lying detected lines are three lines in the (1,0,0,1) mode 1600 K above ground. Although the signal-to-noise of these detections is rather low (3-5 σ), all three lines are very well reproduced by our LTE fit (Figs. 4.3 and 4.4, 109306.7, 109469.4, 154844.8 MHz) with $T=500$ K. The line at 155074.9 GHz seems to be blended with a U-line. A line in the pure stretching mode v_4 is detected at 154443.8 MHz. A possible blend with the ethanol $7_{16} - 6_{24}$ line at 154442.7 MHz is believed to be weak considering the results of Section 5.3.5 but there is still a blend with an unknown, extended spectral feature.

Moreover, we have also detected for the first time the $v_7 = 1, 2$ and the $v_6 = 1$ states of ¹³C substituted HC₃N. No DCCCN was found and HCCC¹⁵N lines have not been in our observed bands but are expected to be too weak to be observed anyway. The identifications of these lines is shown in more detail in the middle and lower panels of Fig. 4.5. The assignments were done according to the frequencies discussed in the last section. The l -type

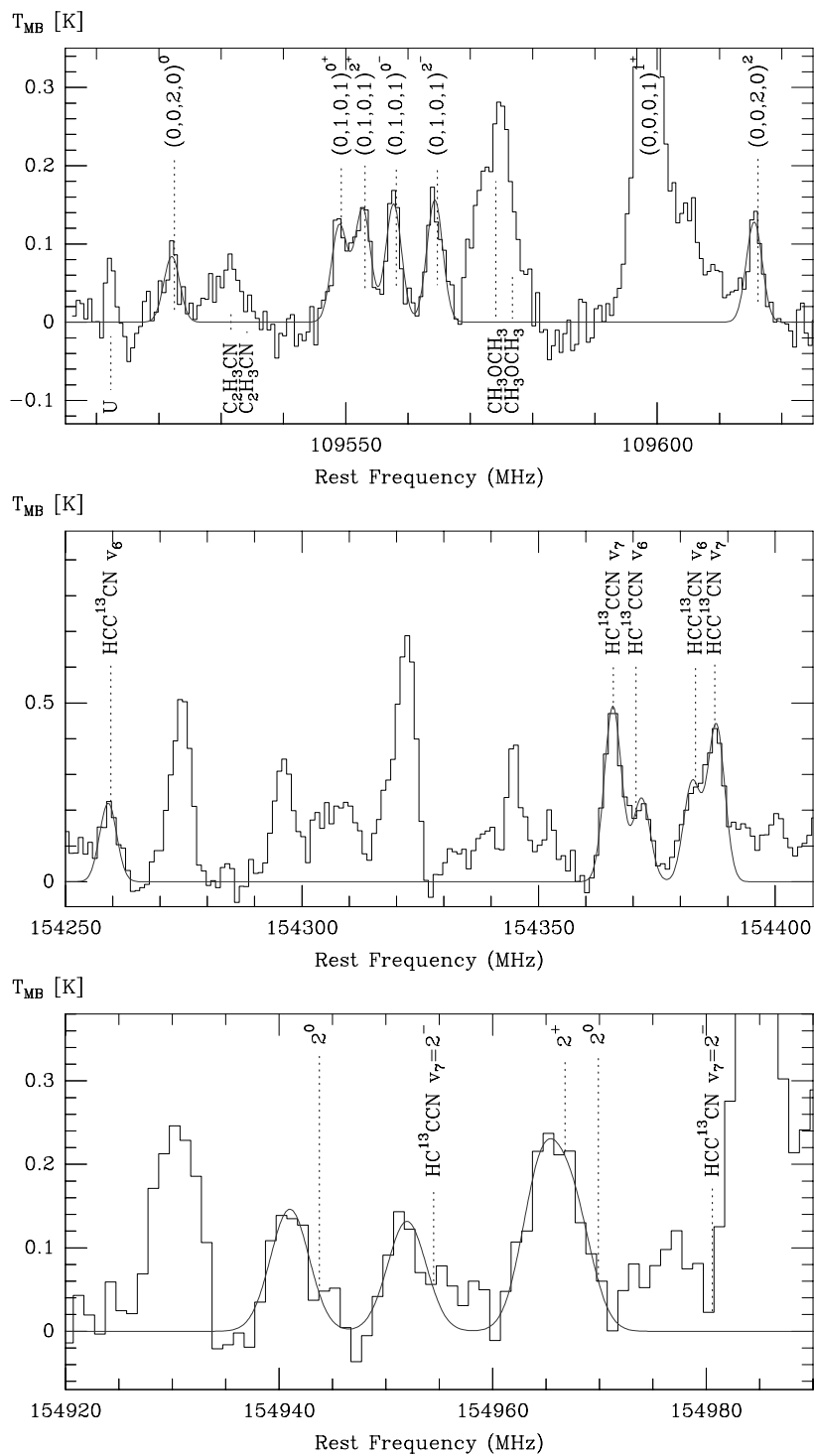


Fig. 4.5.— HC_3N spectra towards G10.47 showing in the upper panel the combination mode v_5v_7 and the overtone $2v_6$, in the middle panel the fundamental modes v_7 and v_6 of two ^{13}C substituted HC_3N species, and in the lower panel their $2v_7$ overtones. The fitted line is a Gaussian fit with the line widths fixed to 8.25 km s^{-1} (the width measured for the v_5 lines) and the frequency and intensity as free parameters.

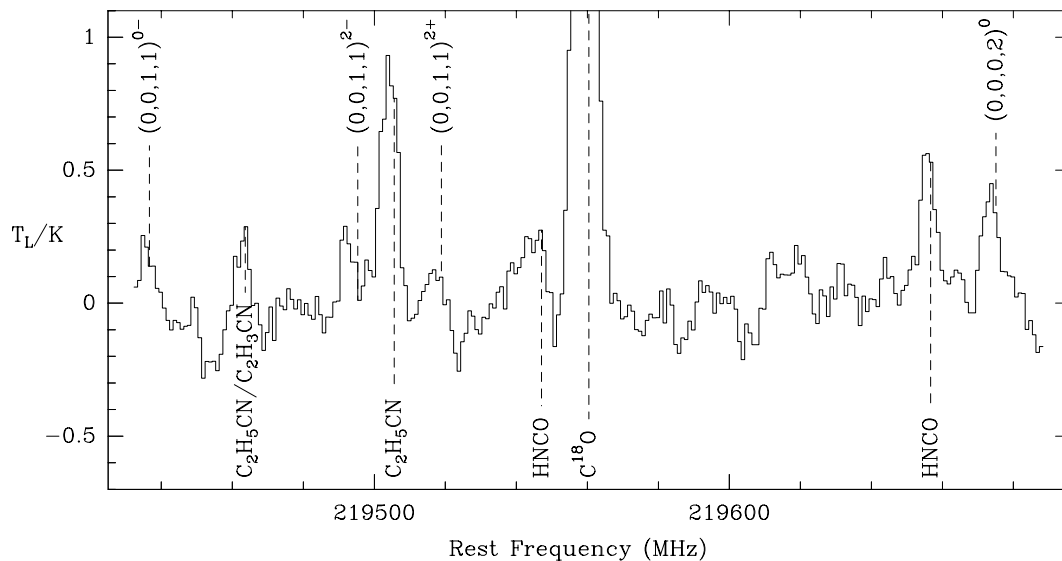


Fig. 4.6.— HC_3N (0,0,1,1) lines detected close to $\text{C}^{18}\text{O}(2-1)$ in G10.47+0.03.

doubling of the $|l|=2$ state was unknown and estimated to be equal to the splitting of the main isotopomer. Predicted and measured frequencies, given in Table 4.5, agree within a few MHz, which is remarkable since the frequencies are extrapolated from centimeter laboratory measurements. The relatively strong line at 154965 MHz in the lower panel of the figure is presumably due to the blending of two lines of different isotopomers (HC^{13}CCN $v = 2^+$ and HCC^{13}CN $v = 2^0$) and was fitted with two Gaussian lines. In contrast to the lines with only one quantum of vibration excited, the $v_7 = 2$ lines observed show a systematic offset from the predictions. The l -type doubling prediction itself is better than 0.5 MHz.

4.4.2. The level population

A first estimate of the vibrational temperature in G10.47+0.03 can be obtained by assuming optically thin conditions and plotting the observed intensities in a Boltzmann plot against excitation for all detected lines in the observed BAND3-109 band. Since the lines are observed simultaneously with the same front- and backends, the relative calibration is excellent. The resulting plot is shown in Fig. 4.7 where one sees that one obtains a reasonable fit with a formal excitation temperature of 485 K (as compared to only 150 K in Orion). We omitted the ground state which forms in a more extended cooler region and is deviant by a factor 4. The analysis of the ^{13}C substituted HC_3N , detected at 155 GHz, leads to a similar temperature estimate, but the accuracy of the Boltzmann fit is considerably lower due to the lower signal-to-noise ratio of the detections (see also Fig. 4.7).

The ratios of intensities of the main isotopomer and of ^{13}C substitutes can be used to

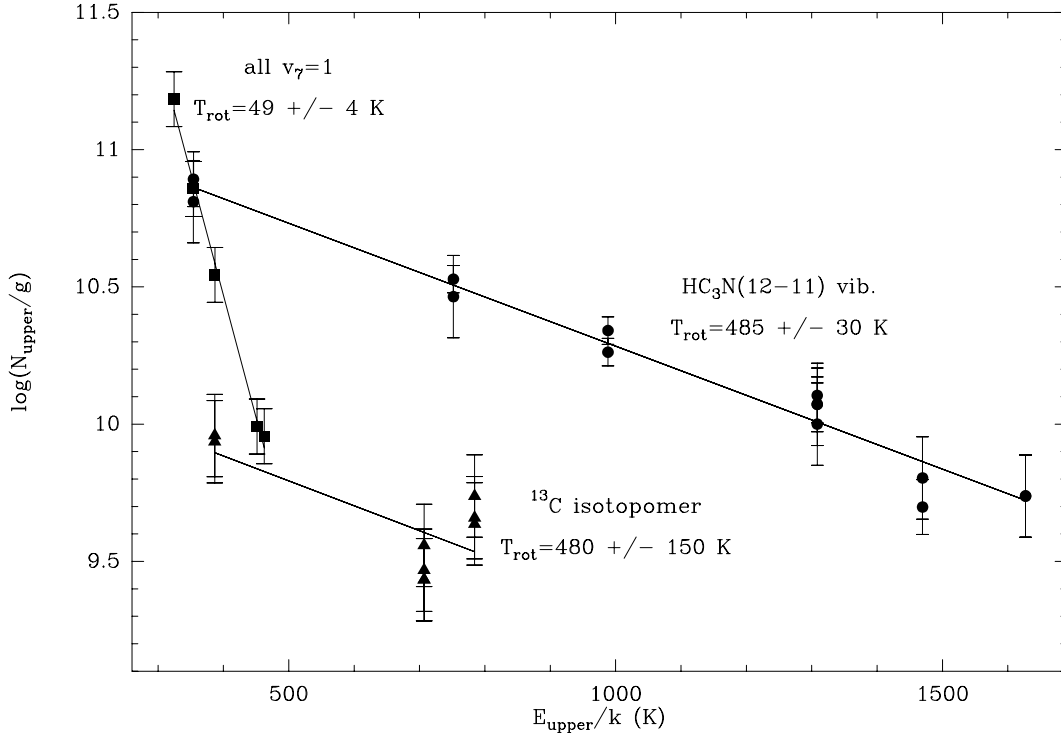


Fig. 4.7.— Boltzmann plot of all detected lines of vibrationally excited $\text{HC}_3\text{N}(12-11)$ in the observed band BAND3-109 (dots), all v_7 lines (squares) with different J , and all lines of ^{13}C isotopomer (triangles). All intensities were corrected to match the 109 GHz beam by assuming a source size much smaller than the beams.

estimate the optical depths of the corresponding transitions. This is done, assuming an $^{12}\text{C}/^{13}\text{C}$ abundance ratio X and equal excitation and filling factors for the lines, with the following formula:

$$\frac{I_{12}}{I_{13}} = \frac{1 - \exp(-\tau)}{1 - \exp(-\tau/X)} \quad (4.8)$$

The ratio X is a function of galactocentric distance (Dahmen et al. 1995) and is, for a distance of 5.8 kpc from the sun, 40. The resulting optical depths for the v_7 lines of $\text{HC}_3\text{N}(17-16)$ is then 19 ± 5 and for the v_6 lines 20 ± 10 . Since the optical depth is estimated for the 155 GHz range (or $J=17$) and the vibrational temperature is determined at 110 GHz (or $J=12$), we have to calculate the expected optical depth at the latter frequency. One can show that for a linear molecule with $T_{\text{ex}} \gg h\nu/k$ the ratio of τ at different J is about J_i^2/J_j^2 (see for example Genzel 1992) in LTE and therefore, the optical depth at 110 GHz is still about 10. Hence, the assumption of optically thin lines, which we made to derive a vibrational temperature, is clearly violated.

Besides the population of levels of different vibrational excitation but constant J , we can also study the level population for a constant state of vibration. We detected the v_7 vibrational state at 3, 2, and 1.3 mm and can therefore cover a wide range of rotational

excitation within this vibrational mode. As a preliminary result, we report also the detection of the ν_7 at 36 GHz with the Effelsberg 100-m telescope. The resulting rotational Boltzmann plot for all observed ν_7 lines is shown in Fig. 4.7. In contrast to the very high temperature found for the different vibrationally excited states, the temperature which fit the rotational population of the ν_7 mode is only 50 K. This is of course again misleading, since we already saw that the optical depth of the lines is considerable and, due to the above mentioned dependence of optical depth on J , high J lines are depressed and a small rotational temperature is simulated.

Therefore we have to interpret the observed intensities in terms of these high optical depths and this can be done by including the optical depth into a LTE analysis of the intensities (e.g. Olmi et al. 1996a):

$$\int T dv = \frac{8\pi^3 \nu \mu^2 S}{3k} \frac{N_{\text{tot}}}{ZX} \exp\left(-\frac{E}{kT}\right) G(\tau) R(\nu) \eta \quad (4.9)$$

Every transition is characterized by its frequency ν , line strength S and μ , the relevant component of the dipole moment of the molecule. The population of the upper level with energy E of the transition is described by the total column density N_{tot} of the molecule, its partition function Z , the isotopomeric ratio X , and the temperature T . The function $G(\tau)$ corrects for the optical depth of the line (Stutzki et al. 1989):

$$G(\tau) = \int \frac{1 - \exp(-\tau g(v))}{\tau \Delta v} dv \quad (4.10)$$

$$\approx \frac{1 - \exp(-\tau l)}{\tau l}, \quad \tau l = 0.679 \tau^{0.911} \quad (4.11)$$

The approximation of the integral with the given expression is valid for a Gaussian line profile and leads to errors of 15% (4%) for τ in the range of 0.01 to 100 (0.01 to 10). In contrast to the simpler optical depth correction for only the line center (given by setting $\tau l = \tau$) suggested by e.g. Turner (1991) and Olmi et al. (1996a), the correction also accounts for the line broadening as function of optical depth. However, this one component approach would produce rectangular line shapes, which are not observed. Instead, even the high optical depth lines are still Gaussian suggesting a more complicated line forming process at work, e.g. macroturbulence or large velocity gradients. Having optically thin and thick lines available, the filling factor η can be estimated as well. The optical depth itself, which enters into $G(\tau)$, is given by

$$\tau = \frac{8\pi^3 \nu \mu^2 S}{3k} \frac{N_{\text{tot}}}{ZX} \exp\left(-\frac{E}{kT}\right) \frac{1}{T \Delta v} \quad (4.12)$$

The function $R(\nu)$ corrects for the weakening of the spectral line emission by dust absorption due to very high total column densities of about 10^{25} cm^{-2} involved and could already play a role at 1.3 mm in case of $\tau_{1.3}$ of order unity:

$$R(\nu) = \exp\left[-\tau_{1.3} \left(\frac{\nu}{\nu_{1.3}}\right)^2\right] \quad (4.13)$$

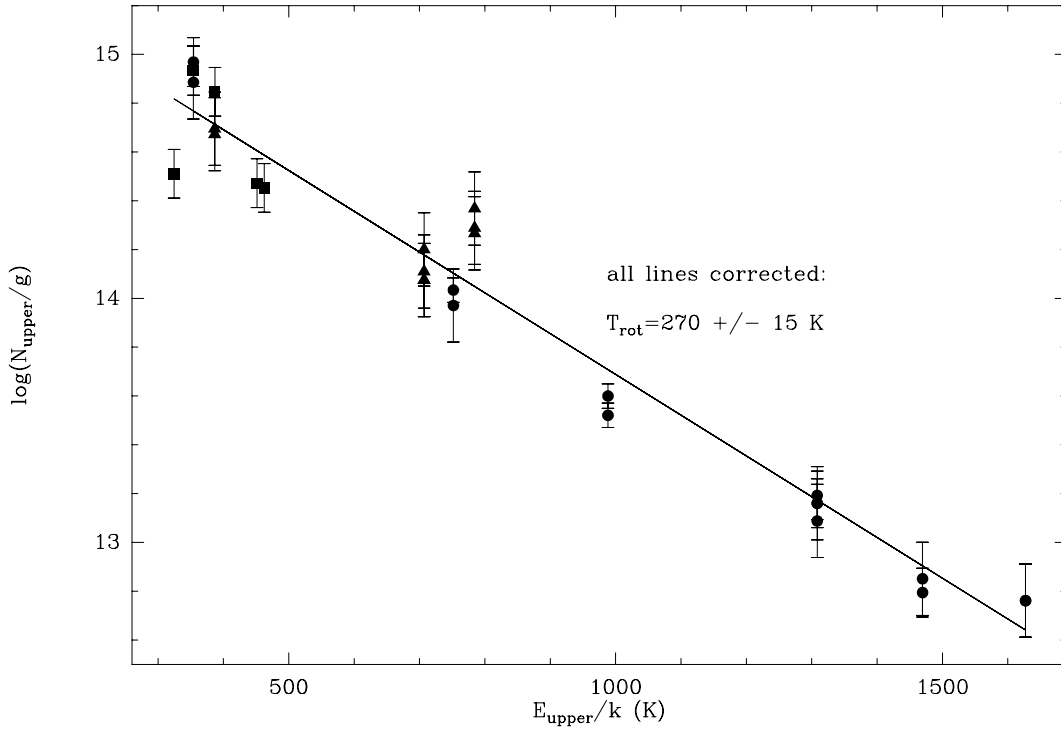


Fig. 4.8.— Boltzmann plot of the same lines seen in Fig. 4.7 but now corrected for optical depth (also for line broadening) with a source size of $0.65''$, an isotopomeric ratio of 40, and a line width of 8 km s^{-1} .

Table 4.6: Results of LTE model fits including optical depth to the HC_3N data. The $\tau_{\text{cor}}?$ flag indicates, whether we corrected for line broadening or not.

$\tau_{\text{cor}}?$	X	Δv (km s^{-1})	χ_{min}^2	T (K)	θ_S (arcsec)
no	20	8	33	330	1.0
	30		60	300	0.95
	40	85	260	0.9	
yes	30	7	60	310	1.0
	20	8	36	330	0.7
	30		56	290	0.7
	40		71	270	0.65
30	7	56	280	0.75	

Here, the frequency dependence of the dust opacity is assumed to be 2 in the millimeter wavelength range (see Chapter 6 for an observational estimate of the dust opacity index). We include this effect here, since it could also cause the low rotational temperature of v_7 lines with different J (Fig. 4.7).

Using these formulae, one can search for the minimum of the corresponding least square sum of this LTE fit to the observations. The free parameters which enter the game are T , N_{tot} , θ_S , $\tau_{1.3}$, dv , and, because of the relatively large errors in the assumed isotopomeric

ratio, also X . The best fit values of several parameter combinations are given in Table 4.6. Only for unusual low values of X the optical depth of the dust at 1.3 mm $\tau_{1.3}$ plays a crucial role. In the other cases also solutions without this effect are possible. A Boltzmann plot in which the intensities are corrected for optical depth, beam filling, and different X , is shown in Fig. 4.8 and an example of the dependence of the χ^2 -sum on the model parameters is given in Fig. 4.9: with fixed Δv and X , we varied the source size and dust opacity and determined for these parameter the temperature and column density which minimize the χ^2 -sum. Within the size-opacity space the contours give the confidence levels of 1, 2, and 3σ for four degrees of freedom which confine the source size to a range of $0.55''$ to $0.8''$ and the dust opacity to values lower than 0.6. The temperature within these limits is about 270 K and the HC_3N column density about $4 \times 10^{18} \text{ cm}^{-2}$. Smaller values of X lower the optical depths and accordingly the resulting column density, but increase the temperature. Without correcting for the line broadening due to optical depth effects, larger source sizes are needed to account for the intensity of the optical thick lines.

4.4.3. The excitation of the lines

All of these estimates rely on the assumption of LTE which is probably quite good in the light of the LTE fit which yielded to Fig. 4.8. But for a full understanding of the optical depth effects, a detailed modeling of the level population by statistical equilibrium calculation together with radiative transfer through a model cloud, is needed but would go beyond the objectives of the present analysis. Here, we just want to estimate whether the lines are populated mainly by collision or radiation. At the so-called critical density $n_{crit} = \beta A_{ul} / \gamma_{lu}$, where A_{ul} is the transition probability of spontaneous radiation, γ_{lu} the collisional rate coefficient and β the escape probability, collisional excitation can compensate for the radiative decay. Therefore, if the density is considerably lower than the critical density, only excitation by the radiation field can lead to population of the levels.

The radiative transition probability between vibrational states can be obtained by far-infrared absorption measurements. In the case of HC_3N this has been done by Uyemura & Maeda (1974) and Uyemura et al. (1982) for all the fundamental stretching and bending modes, respectively. The obtained infrared intensities of the modes can then be converted to Einstein coefficients (see appendix of Deguchi et al. 1979) which is done in Table 4.1.

Since no measurements or calculations of the collisional cross sections which change the vibrationally state of HC_3N are available, approximations have to be found. We will follow the suggestion of Goldsmith et al. (1982), who used the semi-empirical formula for vibrational relaxation times as a function of temperature, reduced mass, and energy of vibration in diatomic molecules which is given by Millikan & White (1963). With this relation we calculated deexcitation cross sections and converted them to collisional excitation rates using detailed balance. This is done for a temperature of 300 K and the

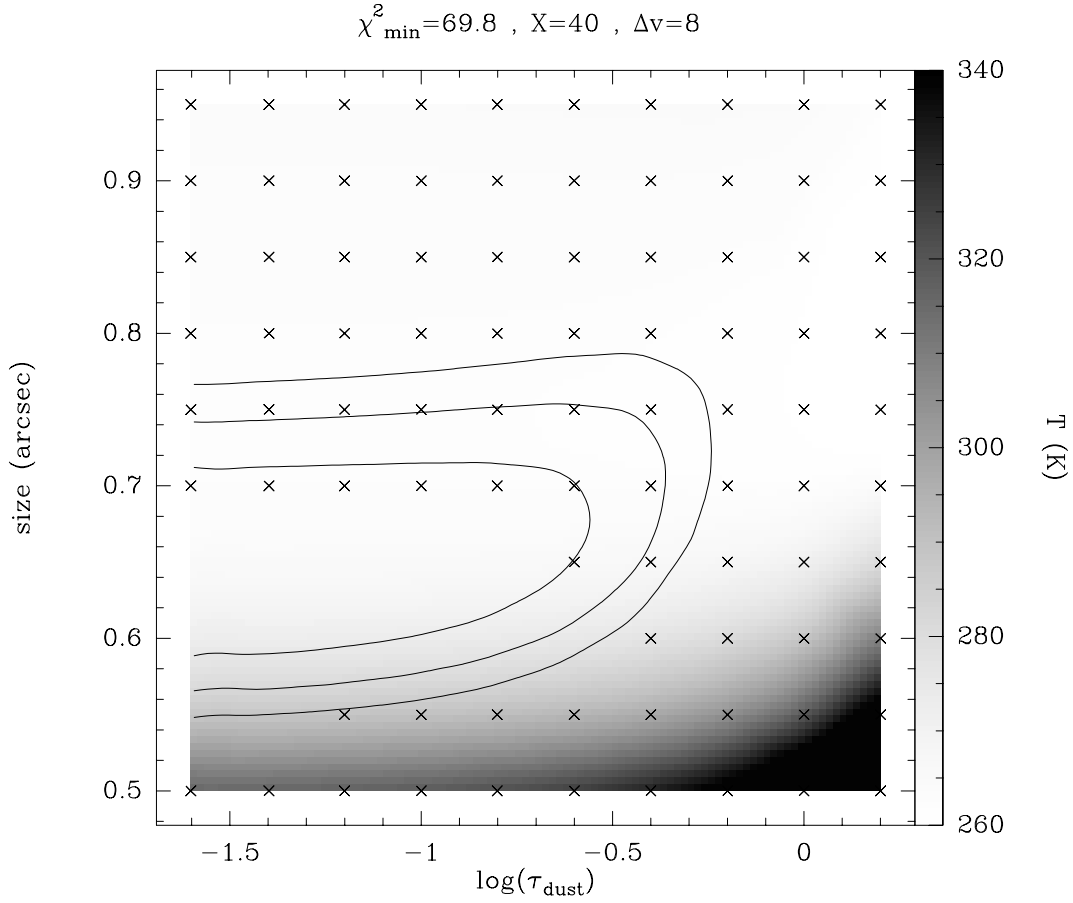


Fig. 4.9.— Results of LTE analysis of the observed vibrationally excited HC_3N lines assuming a $^{12}\text{C}/^{13}\text{C}$ ratio of 40 and a linewidth of 8 km s^{-1} . The contours give the confidence levels of 1, 2, and 3σ for four degrees of freedom. The greyscale is the fitted temperature and the crosses mark positions of violation of the luminosity criterion (see Sect. 4.6).

resulting critical densities are shown in the last column of Table 4.1. The density in the hot core associated with G10.47 is of the order 10^7 cm^{-3} (Cesaroni et al. 1994 and also Chapter 3) and therefore the vibrationally excited states cannot be populated collisionally, but require excitation by a strong IR radiation field unless strong radiative trapping in the infrared reduces the radiation probability to an effective value of A_{ul}/τ_{IR} where the optical depth in the IR could exceed the radio optical depth by a factor 10 to 100 (Genzel 1992). This might be possible for the $\text{HC}_3\text{N } \nu_7$ state in extreme cases. We will discuss the radiation field in more detail after a short presentation of other tracers of IR radiation.

Table 4.7: Line parameters of HCN and NH₃ in G10.47+0.03.

Line	$\int T_{\text{MB}} dv$ (K km s ⁻¹)	T_{MB} (K)	v_{LSR} (km s ⁻¹)	FWHM
HC ¹⁵ N(3-2) v_0	9.2	0.81	67.0	10.7
HCN(3-2) v_2^a	3.6	0.35	67.7	9.4
NH ₃ (2,1)-(1,1) v_2	3.8	0.41	69.8	8.7

^a observed with the CSO by P. Schilke & R. Cesaroni

4.5. Other radiatively excited molecules

Supplementary to the observations of HC₃N, we used HCN, NH₃, HNCO, and CH₂CHCN as a probe of the radiation field in the selected sources. An overview of their pumping wavelengths is given in Table 4.1.

4.5.1. Vibrationally excited hydrogen cyanide

The linear, triatomic molecule HCN has three fundamental modes of vibration (v_1, v_2, v_3): the CH group oscillation against the N atom v_1 about 3000 K above ground, the bending of the molecular axis v_2 , and the C-H stretch v_3 about 5000 K above ground. The vibrationally excited bending state $v_2 = 1$ of HCN was first detected by Ziurys & Turner (1986) towards IRC+10216 and Orion KL, and $v_2 = 2$ by Schilke et al. (1997) in Orion KL.

Here we report the detection of the vibrationally excited (3-2) transition of HCN in the (0,1,0) bending mode towards G10.47 with the CSO. This mode lies 1025 K above ground state and is radiatively excited by 14 μm photons. To estimate the ground state population in order to measure the degree of vibrational excitation from the relative population of the levels, we observed HC¹⁵N (3-2) with the 30-m telescope. Both lines are shown in the upper panel of Fig. 4.10 and their line parameters are given in Table 4.7. The velocities and line profiles are very similar which argues for a common origin of the lines. Assuming the emitting source to be small compared to the beam sizes and adopting a ¹⁴N/¹⁵N ratio of 300 (Wilson & Matzeucci 1992), we derive a vibrational temperature of 270 K for this source. If the vibrationally excited line is not optically thin (Ziurys & Turner estimated $\tau = 2$ in Orion KL), this temperature is only a lower limit. In G31.41 the line is only tentatively detected.

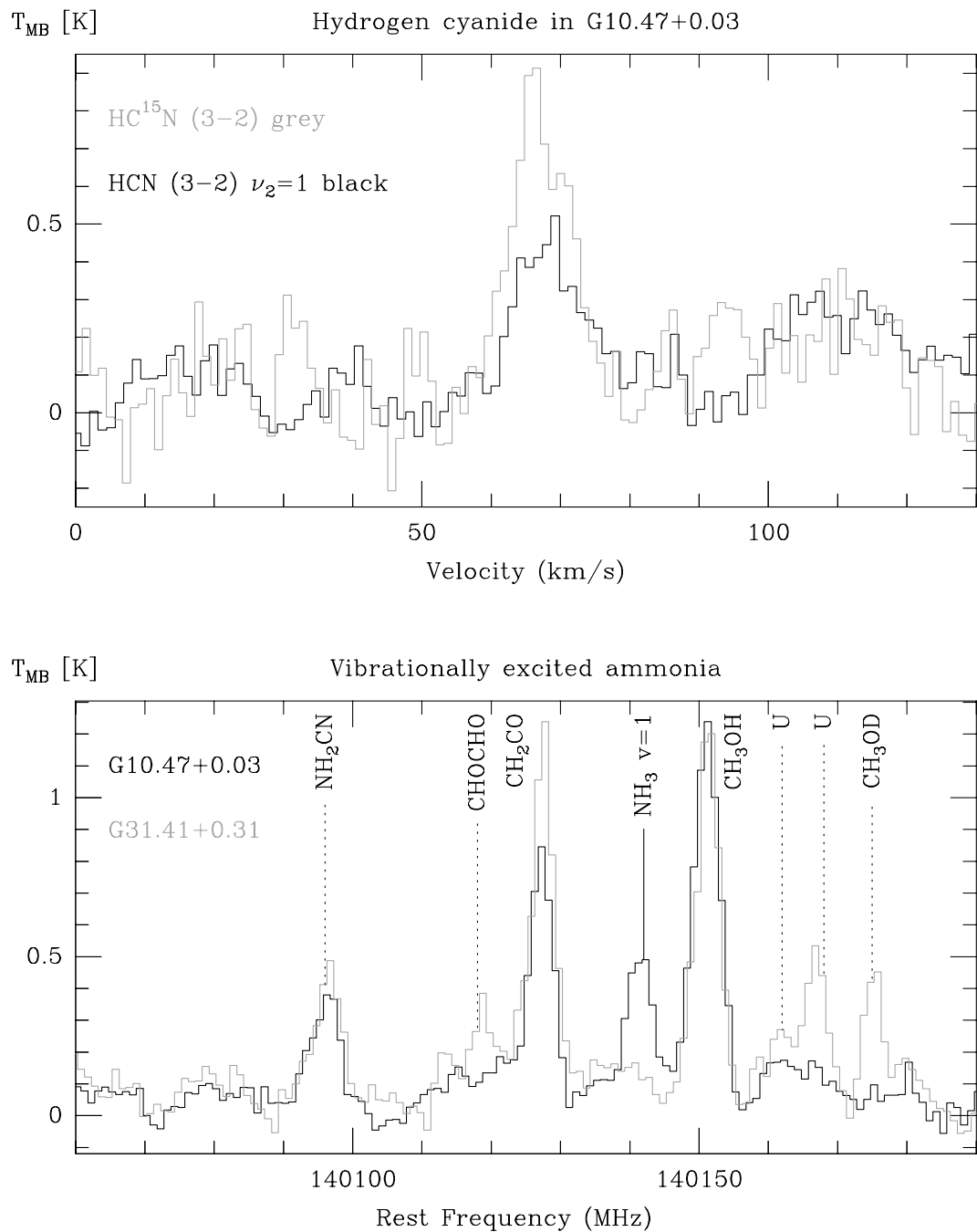


Fig. 4.10.— Further vibrationally excited molecules in G10.47+0.03: vibrationally excited HCN (upper panel) observed with the CSO is compared to optically thin ground state emission from a rare isotopomer and vibrationally excited NH_3 (lower panel) is shown in comparison with a spectrum towards G31.41+0.31 (not on the same scale).

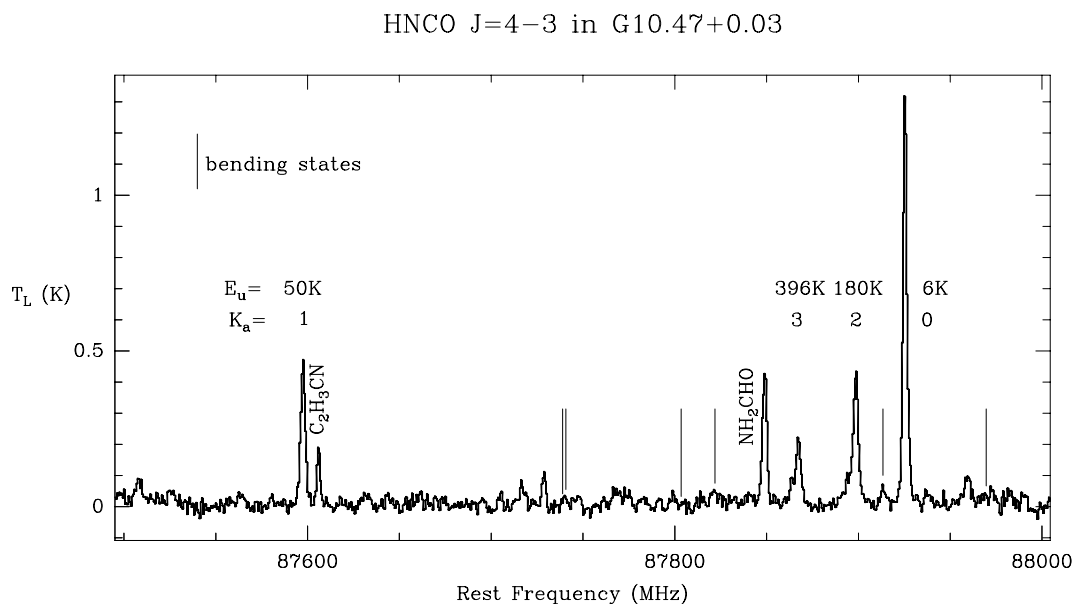


Fig. 4.11.— The $J=4-3$ transition of the slightly asymmetric rotor HNCO in G10.47+0.03. Lines for all possible K_a are detected and labeled together with their upper energies. Frequencies of lines in excited bending states are marked.

4.5.2. Vibrationally excited ammonia

The ν_2 ammonia state is 1400 K above ground and was first observed in Orion KL by Mauersberger et al. (1988) and subsequently also detected in several other sources by Schilke et al. (1990). Here we extended the search of this transition to the sources G10.47+0.03 and G31.41+0.31. We only detected the line in G10.47+0.03 where the line is the strongest ever observed (Table 4.7). In the lower panel of Fig. 4.10 the spectra towards G10.47+0.03 and G31.41+0.31 are compared to each other. Since both sources have about the same column density of ammonia in its vibrational ground state, the non-detection of $\text{NH}_3 \nu_2$ in G31.41+0.31 clearly demonstrates again the uniqueness of G10.47+0.03. Comparison with observations of ammonia in the ground vibrational state (Cesaroni et al. 1992) leads to a vibrational temperature of 300 K. Again this is only a lower limit on the vibrational temperature due to unknown optical depth of the ν_2 transition.

4.5.3. Isocyanic acid

HNCO in different K_a ladders

The slightly asymmetric rotor HNCO was shown to be useful as a probe of the Far IR radiation field because its different K_a ladders are connected with each other via b -type transitions in the Far IR which force the excitation temperatures between levels in a K_a

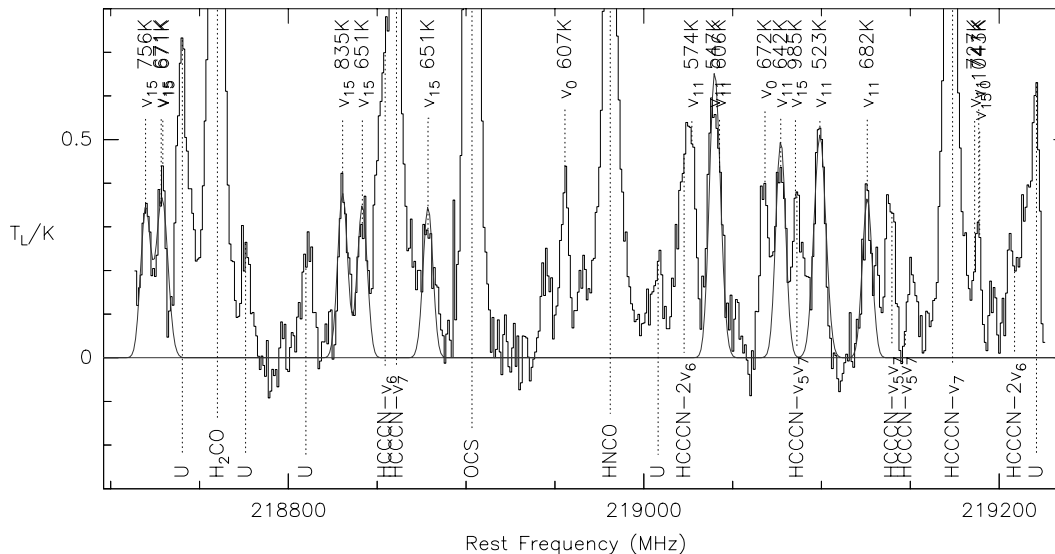


Fig. 4.12.— Vibrationally excited vinyl cyanide in G10.47+0.03 at 218 GHz. The lines are marked with their vibrational mode and upper energies given. Unblended lines are fitted with Gaussians with one fixed linewidth and fixed separations between the lines.

ladder into equilibrium with the apparent radiation temperature (Churchwell et al. 1986). A sample spectrum of HNCO in G10.47+0.03 is shown in Fig. 4.11. Transitions from all K_a ladders (i.e. $K_a=0,1,2,3$) at this frequency are clearly detected. Fitting rotational temperatures to all observed lines, lead to $T_{\text{rot}}=40$ K for $K_a=0$ which is populated by $330 \mu\text{m}$ photons and to $T_{\text{rot}}=480$ K for the other ladders which are connected by radiation from 50 to $110 \mu\text{m}$. Here again G10.47 is exceptional and is the only source in which the highest lying $K_a=3$ line could be detected.

Vibrationally excited HNCO

Towards G10.47+0.03, we report the first detection of vibrationally excited HNCO. Using the frequencies from laboratory measurements of Yamada (1977), a group of spectral line features in our 3 and 2 mm measurements can be attributed to HNCO in its v_4, v_5 and v_6 vibrational states which lie between 800 and 1100 K above ground (see Figs. 4.3, 4.4, and 4.11). No excitation analysis can be performed since the line strengths in the vibrationally excited states are not known.

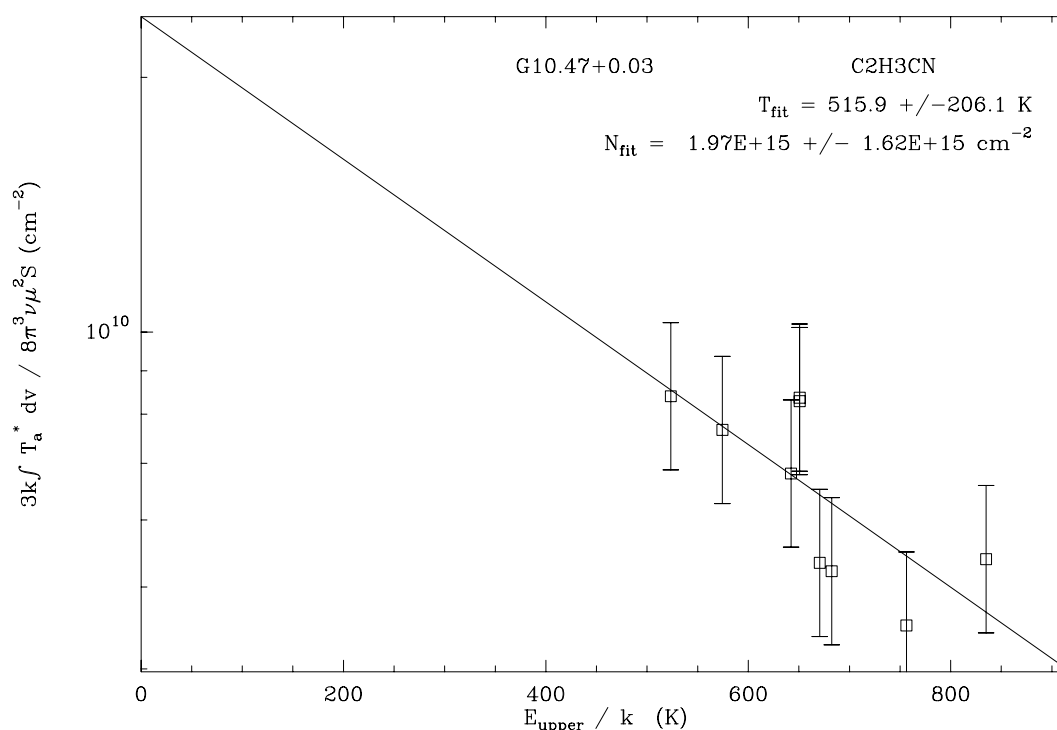


Fig. 4.13.— Boltzmann plot of all vibrationally excited CH_2CHCN lines fitted in Fig. 4.12.

4.5.4. Vibrationally excited vinyl cyanide

Several lines of vibrationally excited CH_2CHCN could be identified (Fig. 4.12) in G10.47+0.03 at 218 GHz. The frequencies for the in plane CCN bend ν_{11} at 342 K, and the CCN out of plane bend ν_{15} at 486 K, are taken from the JPL catalog (Poynter & Pickett 1985; Pickett et al. 1996). In Fig. 4.13 we show a Boltzmann plot of the observed lines which yield a temperature of 520 ± 200 K which seems to be artificially increased by optical depth effects as in the case of HC_3N . But in this case, we have no lines of weaker isotopomers available. Applying the same corrections as for HC_3N to the fitting procedures leads only to a reduction of the temperature to 450 K which is mainly due to the high intensity of the line at 825 K. Without this line, which could be a blend with an unknown line, a temperature of 300 ± 100 K can be fitted.

Vibrations of such a large molecule lie energetically low and are easily excited, so that one can expect also for other complex molecules (e.g. $\text{CH}_3\text{CH}_2\text{CN}$, see Chapter 5) observable vibrational excitation. But most of the frequencies are still unknown and may contribute to many of the unknown lines.

4.6. Characteristics of the IR source

Most of the critical densities of the IR transitions are much too high for them to be populated by collisions (cf. 4.4.3). Hence, they must be radiatively excited and therefore probe the IR radiation field of the observed sources at the pumping frequencies of the rotational lines. The total column densities involved ($10^{24} - 10^{25} \text{ cm}^{-2}$) lead to high optical depths in the infrared and the obtained vibrational temperatures of the IR levels are expected to measure the dust temperature.

One important property of an IR source is its total bolometric luminosity which can be derived from the IRAS fluxes. This luminosity gives us a constraint on the possible temperature and size of the source by applying the Stefan–Boltzmann law. With the IRAS luminosity $L_{\text{IRAS}} = 5 \times 10^5 L_{\odot}$ for G10.47 (Cesaroni et al. 1994) we have:

$$L_{\text{IRAS}} \geq \pi \theta_S^2 d^2 \sigma T^4 \quad (4.14)$$

θ_S is the source size, d the distance of the source, T the temperature and σ the Stefan–Boltzmann constant. This constrains the temperature for assumed source sizes of $2''$ and $0''.5$ to 140 and 390 K, respectively.

Since the detection of ^{13}C species of HC_3N revealed that the lines of the main isotopomer are optically thick, we can use their brightness temperature to relate source size and temperature in another way:

$$T = T_L \frac{\theta_B^2}{\theta_S^2} \quad (4.15)$$

Here θ_B denotes the beam size. Putting both formulas together, we can calculate for each observed v_7 line a unique source size and temperature (assuming equality in Eq. 4.14). The 3 and 2 mm lines lead to a size of $1''.25$ and 175 K whereas the 1.3 mm lines result in a size of $0''.7$ and 230 K.

In addition, we used this luminosity constraint for our LTE fit. In Fig. 4.9 the range of forbidden source sizes and temperatures is marked with crosses, allowing for a 50% error in the IRAS luminosity. The source size is then constrained to values between $0''.55$ and $0''.7$.

However, we do not expect this combination of IR-source size and temperature to explain *all* observed vibrationally excited lines. For the excitation of the very high lying modes certainly higher temperatures are necessary which then in turn extend over smaller source regions. The most likely scenario is an increase of temperature to the inside of the source (see also Chapter 3) seen in the high lying states of HC_3N which then probe the innermost parts of the hot cores. This can only be revealed by subarcsecond interferometer studies of these lines in the future.

4.7. Conclusions

G10.47+0.03 has shown to be a unique source in terms of high excitation molecular lines. Using different molecular tracers to probe the IR radiation field of the hot core, we derive excitation temperatures of 175-300 K for the radiatively pumped lines but still higher temperatures may excite the highest lying modes of vibration. The size of the IR source is found to be about 1".

In this study many vibrationally excited states of HC₃N have been detected for the first time in interstellar space showing the valuable interrelation between laboratory spectroscopy and astrophysics and the particular usefulness of this molecule to trace a wide range of rotational *and* vibrational excitation.

REFERENCES

- Blake G.A., Mundy L.G., Carlstrom J.E., Padin S., Scott S.L., Scoville N.Z., Woody D.P. 1996, ApJ 472, L49
- Cesaroni R., Walmsley C.M, Churchwell E. 1992, A&A 256, 618
- Cesaroni R., Churchwell E., Hofner P., Walmsley C.M., Kurtz S. 1994, A&A 288, 903
- Churchwell E., Wood D., Myers P.C., Myers R.V. 1986, ApJ 305, 405
- Churchwell E. 1991, in *the Physics of Star Formation and early Stellar Evolution*, NATO Asi, eds. C.J. Lada and N. Kylafis
- Clark F.O., Brown R.D., Godfrey P.D., Storey J.W.V., Johnson D. 1976, ApJ 210, L139
- Dahmen G., Wilson T., Matteucci F. 1995, A&A 295, 194
- Deguchi S., Nakada Y., Onaka T. 1979, Publ. Astron. Soc. Japan 31, 105
- Garay G., Rodriguez L.F. 1990, ApJ 362, 191
- Gaume R.A, Fey A.L, Claussen M.J 1994, ApJ 432, 648
- Genzel R. 1992 , in "The galactic Interstellar Medium", p275, (Burton W.B., Elmegreen B.G., Genzel R.), Springer
- Goldsmith P.F, Krotkov R., Snell R.L. 1982, ApJ 260, 147
- Goldsmith P.F, Krotkov R., Snell R.L. 1985, ApJ 299, 405
- Mallinson P.D., Fayt A. 1976, Molec. Phys. 32, 473
- Mallinson P.D., de Zafra R.L 1978, Molec. Phys. 36, 827
- Mauersberger R., Henkel C., Wilson T.L. 1988, A&A 205, 235
- Millikan R.C., White D.R. 1963, J. Chem. Phys. 39, 3209
- Olmi L., Cesaroni R., Walmsley C.M. 1996a, A&A 307, 599
- Olmi L., Cesaroni R., Neri R., Walmsley C.M. 1996b, A&A 315, 565
- Pickett H.M., Poynter R.L., Cohen E.A., Delitsky M.L., Pearson J.C., Müller H.S.P., "Submillimeter, millimeter, and microwave line catalog", JPL Publication 80-23, Revision 4, Pasadena CA, 1996
- Poynter R.L., Pickett H.M. 1985, Appl. Opt. 24, 2235

- Schilke P., Mauersberger R., Walmsley C.M., Wilson T.L. 1990, A&A 227, 220
- Schilke P., Groesbeck T.D., Blake G.A., Phillips T.G. 1997, ApJS 108, 301
- Stutzki J., Genzel R., Graf U.U., Harris A.I. 1989, ApJ 340, L37
- Townes C.H., Schawlow A.L. 1955, "Microwave spectroscopy", Dover, New York
- Turner B.E. 1991, ApJS 76, 617
- Turrel G.C., Jones W.D., Maki A. 1957, J. Chem. Phys. 26, 1544
- de Vicente, P. 1994, PhD thesis, Universidad Complutense de Madrid
- Uyemura M., Maeda S. 1974, Bull. Chem. Soc. Japan 47, 2930
- Uyemura M., Deguchi S., Nakada Y., Onaka T. 1982, Bull. Chem. Soc. Japan 55, 384
- Wild 1995: The 30m Manual, IRAM Tech. Report 377/95
- Wilson T.L., Matteucci F. 1992, A&A Rev. 4, 1
- Yamada K.M.T. 1977, J. Mol. Spectr. 68, 423
- Yamada K.M.T., Creswell R.A. 1986, J. Mol. Spectr. 116, 384
- Ziurys L.M., Turner B.E. 1986, ApJ 300, L19

Chapter 5

The chemical state of hot cores

5.1. Introduction

The gas in the vicinity of newly forming high mass (proto) stars is heated to temperatures high enough to evaporate the ices on interstellar dust grains and hence, a chemistry quite different to that known in cold dark clouds is expected. The main question addressed in this chapter is the chemical state of hot molecular gas probed by the abundances of several complex organic molecules.

Most studies of the chemistry of hot molecular gas has been made towards the high mass star forming regions Sgr B2 and Orion KL, whose chemical compositions have been determined by means of systematic line surveys (see Schilke et al. 1997 and references therein in case of Orion and Sutton et al. 1991 in case of Sgr B2). Recently also two other hot core sources have been the target of line surveys in the 345 GHz range: G34.26+0.15, studied by Macdonald et al. (1996), and W3(OH), observed by Helmich et al. (1997). The picture emerging from these observations is that, due to the evaporation of molecules from the grain surfaces, these sources contain very large abundances of saturated molecular species compared to the absence or rather low abundances of these species in cold molecular gas.

Besides these single dish observations, there recently have been performed also interferometer studies of complex molecules in regions of high mass star formations: Orion KL has been observed at 3 mm using BIMA by Wright et al. (1996) and at 1.3 mm using OVRO by Blake et al. (1996), Mehringer & Snyder (1996) determined the locations of various complex molecules in G34.26, Miao et al. (1995) in Sgr B2(N), and for a discussion of IRAM Plateau de Bure interferometer observations of W3(OH) see Chapter 6.

Much efforts have been made in the last few years to model the chemistry of hot cores, i.e. to include the effects of grains on the chemistry during a cold collapse phase and to model the subsequent gas-phase chemistry of the evaporated molecules in an hot

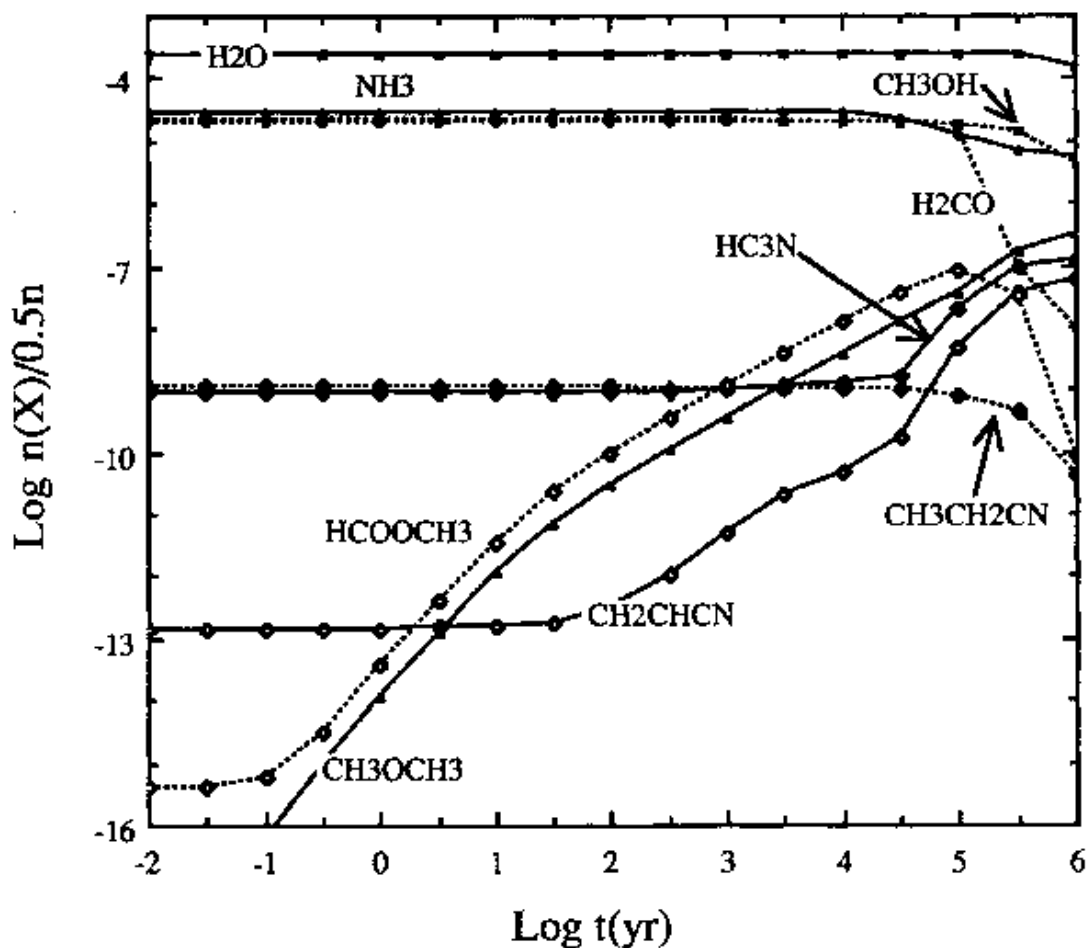


Fig. 5.1.— Predictions of the time evolution of the fractional abundances of important N- and O-bearing molecules after the evaporation from the grain mantles (taken from Caselli et al. 1993).

environment after the onset of the heating due to the process of high mass star formation (Brown et al. 1988; Charnley et al. 1992; Caselli et al. 1993; Millar et al. 1997). These models are capable of explaining the high observed abundances of hydrogenated and deuterated species, but there is still a need for further restrictions of theoretical formation routes by observations of the abundances of complex molecules in a larger sample of hot cores. Those will provide different physical conditions helping to constrain the chemical models and their dependence on physical parameter such as luminosity and age of the sources. An example for theoretical predictions of the time evolution of complex molecules by Caselli et al. (1993) is shown in Fig. 5.1 for the physical conditions in the Orion Compact Ridge.

Here we want to extend the study of the chemical composition of hot cores to the sources which have been the targets of our search for vibrationally excited molecules in the previous chapter. For this purpose we covered selected frequency ranges at 3, 2 and 1.3 mm,

which enables us now to analyze a multitude of transitions of several complex molecules detected serendipitously and to determine their abundances in the hot core sources. For the details of the observations, the observed sources and frequency bands, refer to Chapter 4.

5.2. Determination of molecular abundances

In this section we want to describe briefly how estimates of the molecular abundances in hot core gas can be obtained (see the discussions in Blake et al. 1987; Turner 1991; Sutton et al. 1994).

The identification of the lines has been made on basis of the molecular line data in the JPL catalog (Poynter & Pickett 1985; Pickett et al. 1996 and online at <http://spec.jpl.nasa.gov>) which has been included into an extension of the Grenoble molecular line reduction software CLASS by P. Schilke.

The integrated intensity of an observed transition is related to the column density N_u in its upper level:

$$\frac{N_u}{g_u} = \frac{3k \int T_l dv}{8\pi^3 \nu \mu^2 S} \quad (5.1)$$

Here g_u denotes the statistical weight of the level, ν the frequency of the transition, μ the relevant component of the dipole moment of the molecule, and S the line strength of the transition. This relation is only valid in case of small optical depth and as long as $T_{ex} \gg h\nu/k, T_{bg}$ holds. While the latter is true for most of the cases in hot molecular gas, many lines towards hot cores have considerable optical depths and special care has to be taken in interpreting these lines (see the discussion of the HC₃N results towards G10.47 in Chapter 4).

If several transitions of a molecular species are observed, a rotational temperature can be fitted to them by means of the following equation

$$\frac{N_u}{g_u} = \frac{N_T}{Q(T_{rot})} \exp\left(-\frac{E_u}{kT_{rot}}\right) \quad (5.2)$$

where N_T is the total molecular column density, Q the partition function, and E_u the energy of the upper level. The rotational temperature gives a crude estimate of the level of excitation and allows lower limits to be set to T_{kin} if population is via collision. For a discussion of solving the statistical equilibrium equations to estimate the kinetic temperature see Chapter 2 and 3.

If lines are blended, which often is the case in hot cores in the millimeter and sub-millimeter wavelength ranges, it is a problem to determine the integrated intensity $\int T dv$ of a line reliably. To overcome this problem, P. Schilke (1996) has developed a technique to fit the complete spectrum of a multitude of molecular species at once using

a molecular line catalog based on the JPL catalog data. The fit solves properly for the optical depths in the lines and leads to estimates of the free parameters T_{ex} , N_{tot} , Δv , v_{LSR} , and source size for each species by trying to minimize the χ^2 -sum between data and model spectrum. We used this technique to estimate the column density of methyl formate (see Section 5.3.3) in a spectral range where this species is blended with itself and with vibrationally excited CH_3CN .

Molecular abundances are normally given relative to the most abundant interstellar molecule H_2 . Since this molecule is difficult to observe due to its lack of a permanent dipole moment, its column density has to be estimated indirectly from observations of optically thin lines of CO isotopomers. This has been done for the molecular environment of hot cores in Chapter 2. Here we are interested only in the hot core component itself, and therefore we use the observed C^{17}O peak intensity to derive total H_2 column densities (see Eq. 6.3 in Chapter 6) and, in the following sections, the molecular abundances are given relative to this column density. A problem which might arise for single dish observations are the sharp temperature gradients that one expects in hot core sources since they are presumably heated by embedded stars. That being the case, low excitation transitions will in general have higher beam filling factors than high excitation transitions. In particular, this may cause a problem when comparing with C^{17}O for which only low excitation transitions are available.

5.3. Discussion of the observed molecular species

In models of hot core chemistry (Charnley et al. 1992) three kinds of molecules are distinguished: those passively trapped in grain mantles originating from gas phase reaction before freezing onto the grains, those synthesized actively on the grain mantles after freezing, and those which are created in the warm gas after release of the grain mantles. In what follows observations of several molecules belonging to different groups are discussed. Parameter derived for the molecules can be found in Table 5.1. The given abundances are all beam averaged values referred to the $\text{C}^{17}\text{O}(2-1)$ beam, assuming sizes of the emitting regions much smaller than the beam.

5.3.1. $\text{CH}_3\text{CH}_2\text{CN}$ —Ethyl cyanide

The organic asymmetric rotor $\text{CH}_3\text{CH}_2\text{CN}$ with permanent dipole moments of $\mu_a=3.84$ Debye and $\mu_b=1.23$ Debye was observed in several transitions in all six sources. One of our observing bands covers a-type lines from a wide range of energy levels and therefore will be used to determine rotational temperatures and column densities. A sample spectrum of this band towards the source W3(OH) is shown in Fig. 5.2 and the line

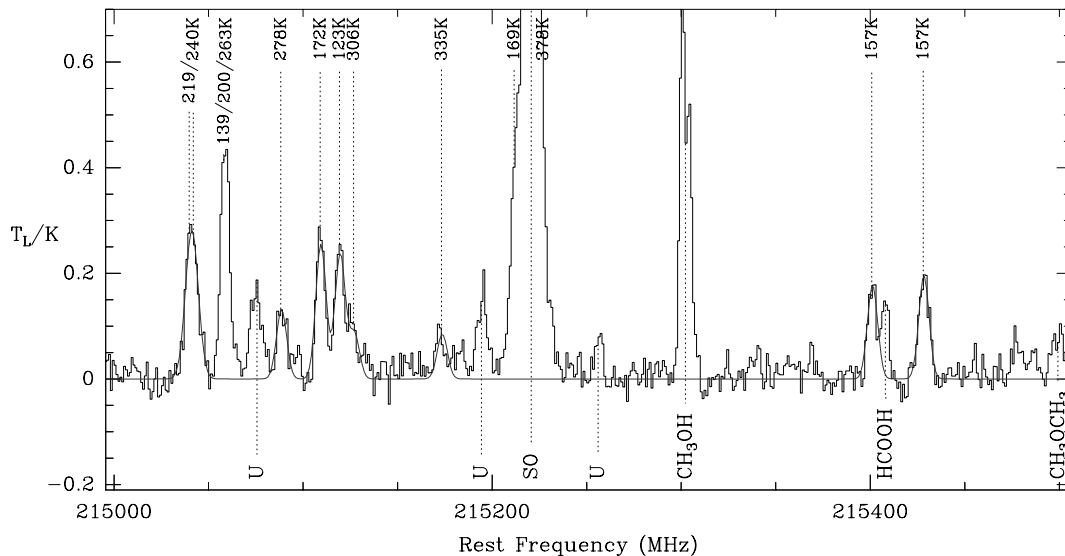


Fig. 5.2.— Sample spectrum of $\text{CH}_3\text{CH}_2\text{CN}$ in BAND1-215 towards the source W3(OH). The lines of this molecule are marked with their upper energies from above and fitted with multiple Gaussians with fixed line width and separation. Other species are marked from below.

parameters are given in Table A.4. Since some of the lines overlap partially, all lines were fitted using fixed separations between the lines using the laboratory frequencies. Also the line widths were held fixed to a value estimated from unblended lines. As can be seen in the spectrum, eight lines can be fit quite well simultaneously. The upper energies and line strengths of the lines at 215039.7 and 215041.9 GHz were averaged and added, respectively, and a correction to the line width of this feature according to the separation of both lines was applied. We omitted the blend of the three lines at 215059 GHz. The LSR velocity of the whole multiplet in W3(OH) is -48 km s^{-1} and therefore the lines originate from the hot core associated with the water masers (see also the Chapter 6) whereas the methanol line in the band is double peaked and has a contribution also from the ultracompact HII region.

The Boltzmann plots of these lines from all observed sources are shown in Fig. 5.3. In G10.62 only the strongest lines were observed and the fit is quite uncertain. The biggest departures from a Boltzmannian level population are seen in G10.47, the source with the highest fitted $\text{CH}_3\text{CH}_2\text{CN}$ column density. A reason for this could be that the lines become optically thick, and hence the lines with the biggest values of $S\mu^2$ (215109 and 215041 MHz) are deviant. A hint for this behavior is also seen in G31.41 and G34.26. But since no lines of ^{13}C isotopomers are observed, it is not possible to correct for optical depth effects and one has to be aware that in what follows, the derived abundances are only lower limits in these cases. Also the derived rotational temperature should be seen as an upper limit. In other observing bands also b-type lines are observed, but these lie systematically above the fit for the a-type lines. This effect was also observed by Turner (1991) in Orion who discussed several explanation for such a behavior of asymmetric rotors, namely pumping

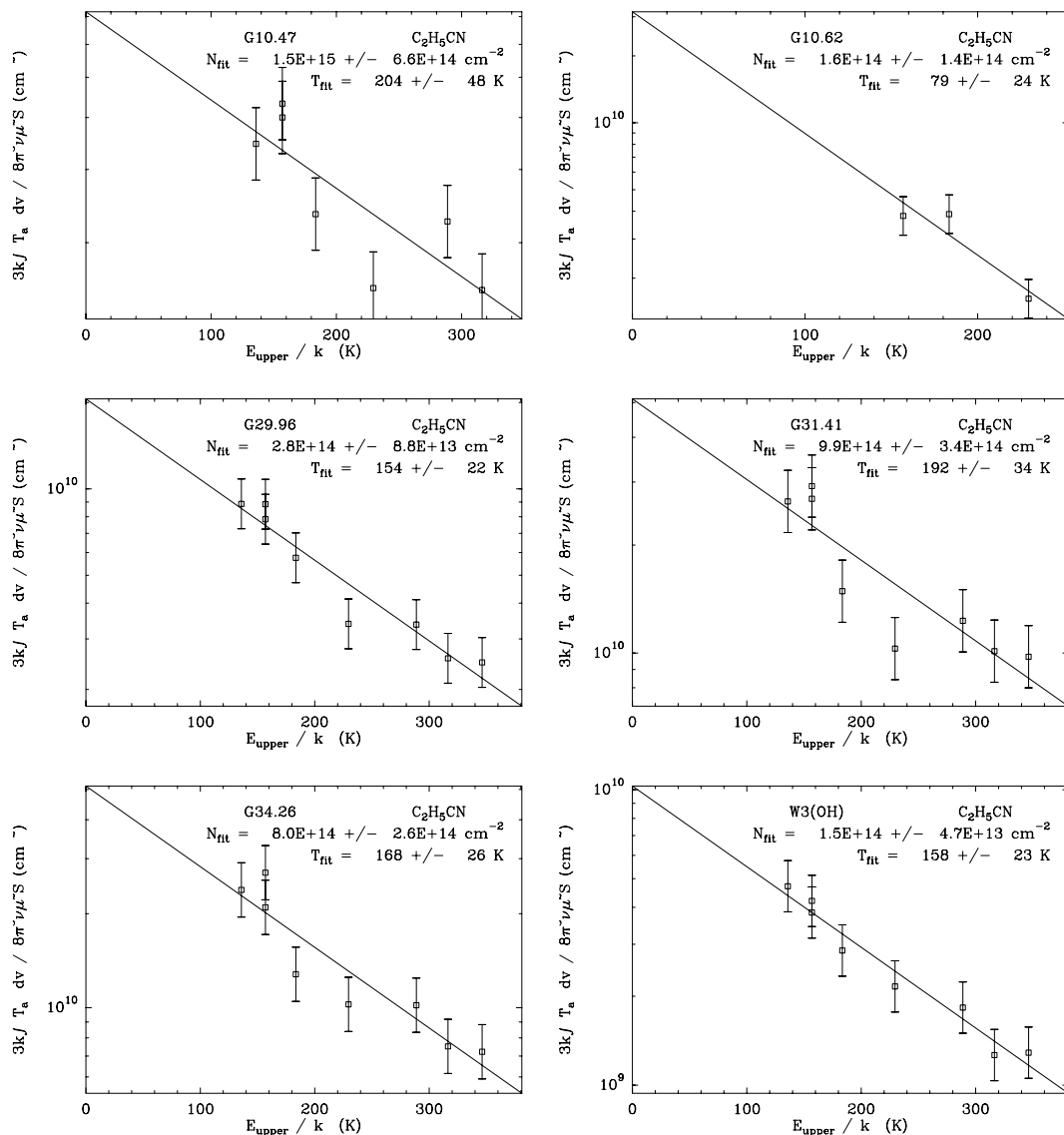


Fig. 5.3.— Boltzmann plots of CH₃CH₂CN lines in BAND1-215.

mechanisms for these lines and the effects of optical depth. His conclusion is that opacity effects are likely in all of the molecules but in the cases of CH₃CH₂CN and CH₂CHCN also pumping mechanisms are possible.

Here, and in what follows, we have not included the contribution of vibrationally excited lines into the partition function since there is still a lack of data for these lines in many complex molecules.

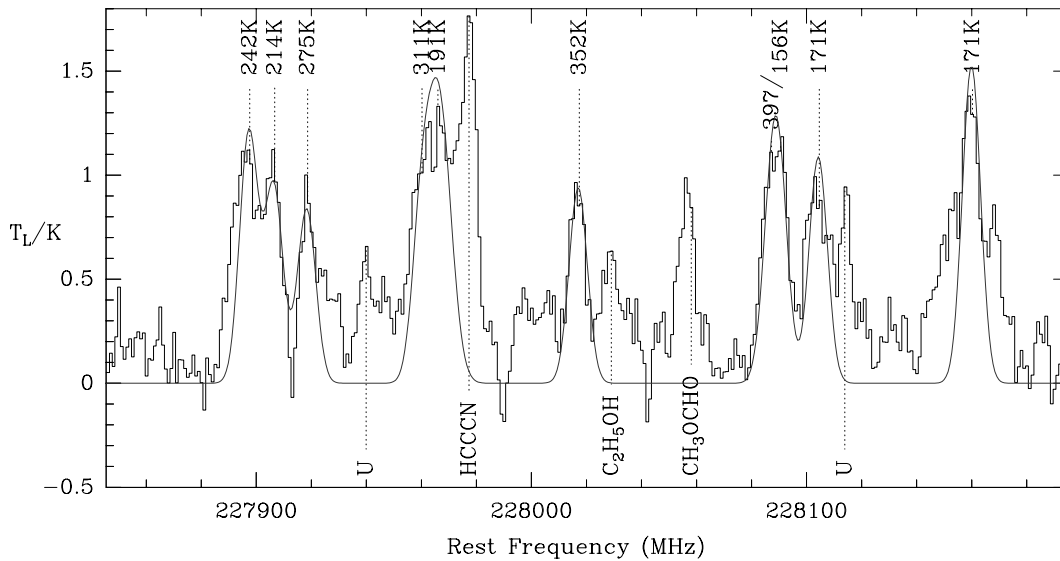


Fig. 5.4.— Sample spectrum of CH_2CHCN in BAND1-228 towards the source G10.47+0.03.

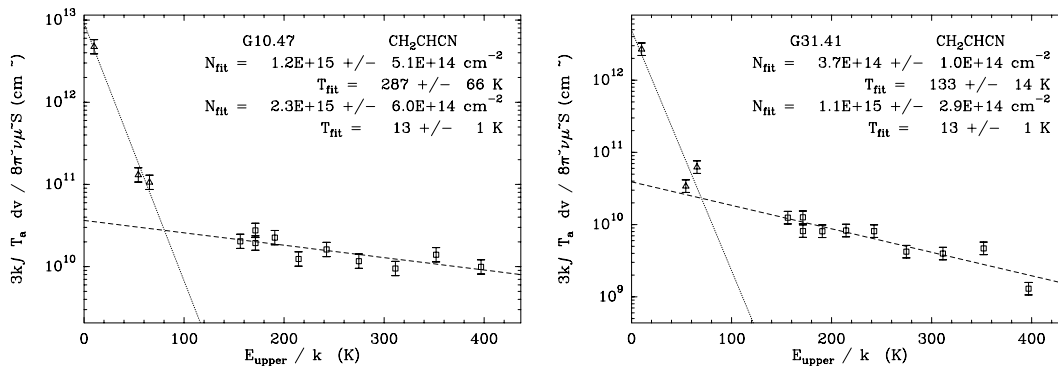


Fig. 5.5.— Boltzmann plots of CH_2CHCN lines in BAND1-228. The lines with $E_{\text{upper}} < 100$ K are observed at 140 and 154 GHz and give evidence for a colder more extended component. Except the 10 K transition, all lines are a-type transition.

5.3.2. CH_2CHCN —Vinyl cyanide

The asymmetric rotor CH_2CHCN has dipole moments quite similar to $\text{CH}_3\text{CH}_2\text{CN}$ ($\mu_a=3.82$ Debye, $\mu_b=0.89$ Debye). Many a-type transitions are found in the band at 228 GHz and a sample spectrum of the lines detected in this band is shown in Fig. 5.4 and the line parameters are given in Table A.5. The same procedure as in the case of $\text{CH}_3\text{CH}_2\text{CN}$ has been used to estimate the line intensities, since the lines are not only blended by each other but also a “noise” of unidentified lines is visible in the spectra which would lead to errors in the derived intensities if they would be simply derived by integration over a certain frequency interval. For the fixed line widths we used the $\text{CH}_3\text{CH}_2\text{CN}$ values. Because of the loss of observing time due to strong wind, only G10.47 and G31.41 are

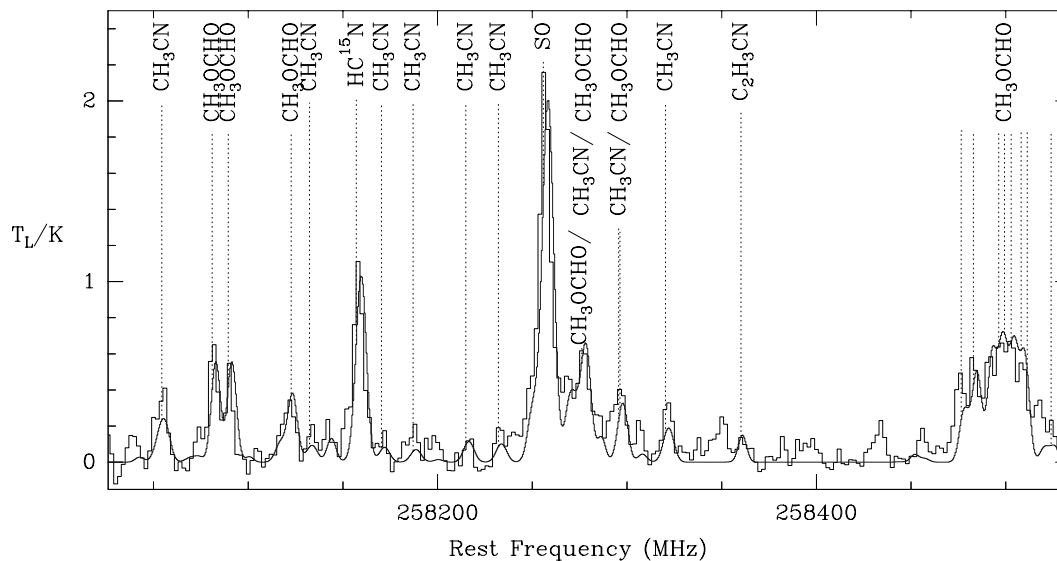


Fig. 5.6.— Sample spectrum of HCOOCH_3 in BAND1-HCN towards the source G31.41. To overcome the blending problem in this frequency band, we used the XCLASS software, which is capable of fitting many species at once, with $T=155$ K and $N(\text{HCOOCH}_3)=1.5 \cdot 10^{15} \text{ cm}^{-2}$.

observed in this frequency band. The resulting Boltzmann plots are shown in Fig. 5.5 where also some lower energy transitions are include which could be due to a more extended halo (see discussion of Olmi et al. 1996). Although several transitions of vibrationally excited CH_2CHCN have been observed in G10.47 (see Chapter 4) we do not include these levels in the partition function for sake of consistency with the other molecules. This underestimates the column density for a temperature of e.g. 225 K by 30%.

5.3.3. HCOOCH_3 —Methyl formate

Methyl formate lines are found nearly everywhere in our observed bands. But most of the time lines appear in multiplets with nearly the same upper energies which makes it difficult to derive rotational temperatures. The values of the dipole moments are $\mu_a=1.63$ Debye and $\mu_b=0.68$ Debye. The only band with an acceptable upper energy range of the lines from about 150 to 300 K is BAND1-HCN which has been observed towards G10.47, G31.41, and W3(OH). Unfortunately many of the lines in this band are blended, either with themselves or with lines of vibrationally excited CH_3CN . Therefore we used the fitting software XCLASS (P. Schilke) to solve the blending problem. A typical fit is shown in Fig. 5.6 where one can see that the software can also account for the highly blended feature at 258500 MHz. Although the temperature is not very well determined by the fit, the total column density is quite accurate since it must account mainly for the total intensity of the blended feature.

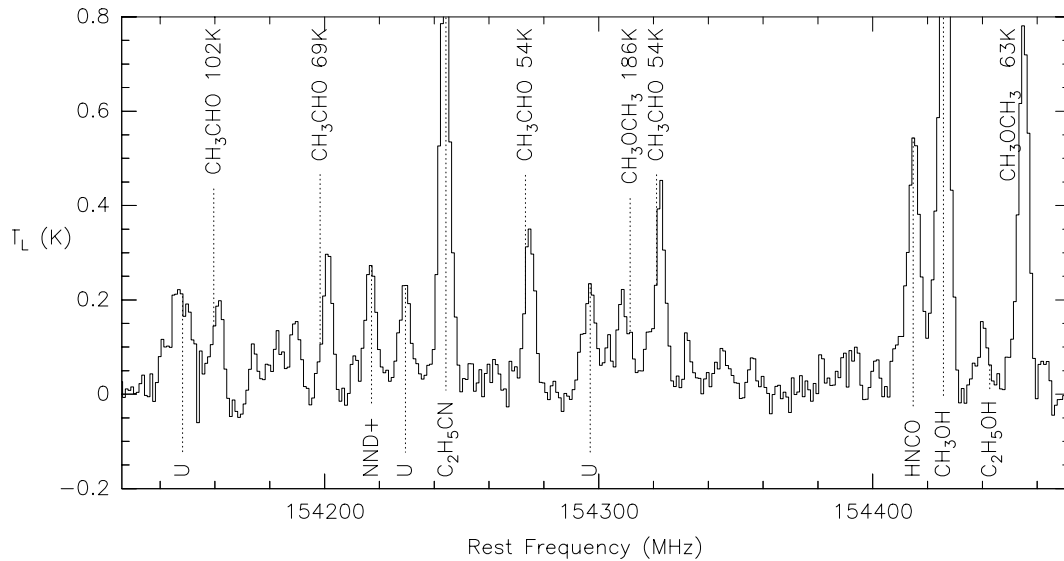


Fig. 5.7.— Sample spectrum lines of CH_3OCH_3 and CH_3CHO in BAND2-154 towards the source G31.41. Note that there is also a line feature at the frequency of NND^+ .

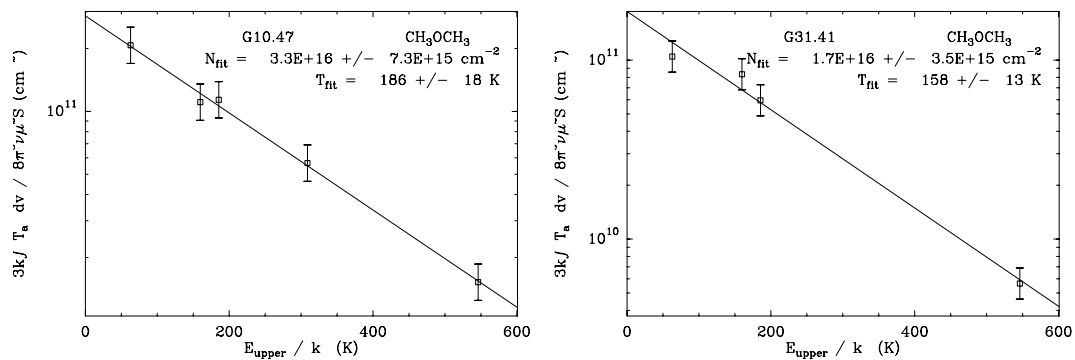


Fig. 5.8.— Boltzmann plots of CH_3OCH_3 lines at 140 and 154 GHz.

5.3.4. CH_3OCH_3 —Dimethylether

The molecule CH_3OCH_3 with a permanent dipole moment $\mu_b=1.3$ Debye was detected with several transitions at 140 and 154 GHz. A sample spectrum towards G31.41 is shown in Fig. 5.7, the line parameters are given in Table A.6 and Boltzmann plots of the lines are shown in Fig. 5.8. For G29.96 and W3(OH) only the $14_{8,6} - 15_{7,8}$ and $11_{1,10} - 10_{2,9}$ transitions at 154 GHz were observed and have been used to derive rotational temperature and column density. The observed lines are well separated from other spectral features and therefore simply the integral over the whole line was used to determine the intensities.

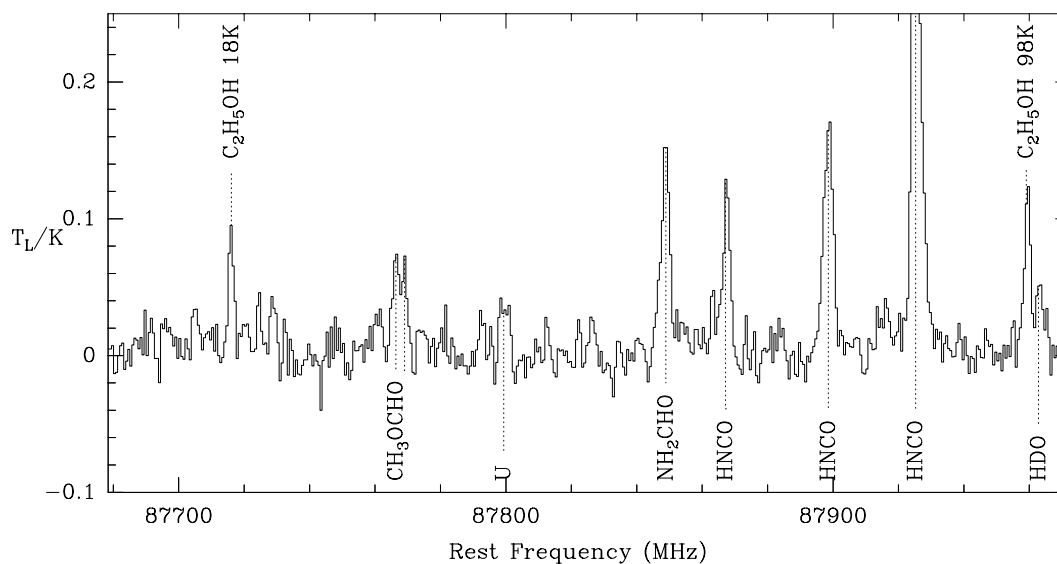


Fig. 5.9.— Sample spectrum of $\text{CH}_3\text{CH}_2\text{OH}$ in BAND3-HNCO towards the source G31.41. Note that there is also a hint for a high lying transition of HDO.

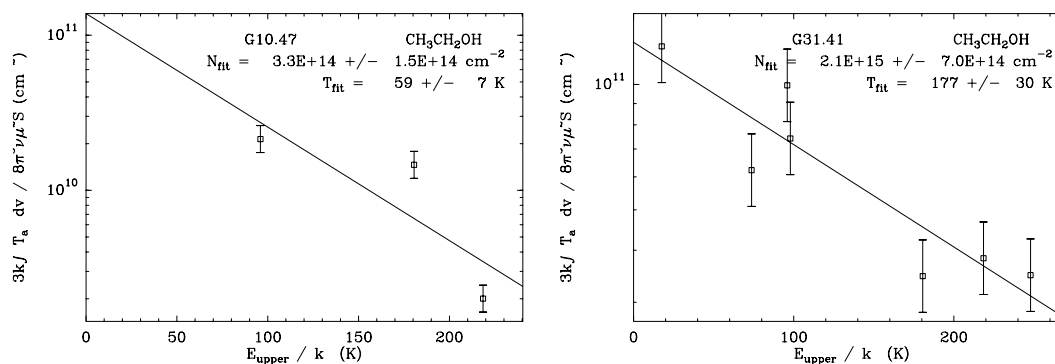


Fig. 5.10.— Boltzmann plots of $\text{CH}_3\text{CH}_2\text{OH}$ lines in 3 mm bands.

5.3.5. $\text{CH}_3\text{CH}_2\text{OH}$ —Ethanol

The number of sources where ethanol was detected has been increased rapidly in the last few years (Millar et al. 1995; Ohishi 1996). Here we report detections of several detections of ethanol lines towards G10.47 and G31.41. A sample spectrum at 87 GHz is given in Fig. 5.9, the line parameters in Table A.7, and Boltzmann plots of the detected lines are shown in Fig. 5.10. The number of lines detected towards G31.41 and the resulting rotational temperature, which is consistent with temperatures derived for other molecular species in this sources, give confidence in the column density estimate. The lines in G10.47 are rather weak, and the determined column density should be used only as a coarse estimate. Since two lines of ethanol have been covered in the 30m C^{17}O survey at 112 GHz, we can give for the other sources (see Table 2.1 in Chapter 2) an upper limit for the beam averaged ethanol column density of $6 \times 10^{14} \text{ cm}^{-2}$ assuming a temperature of 150 K and a

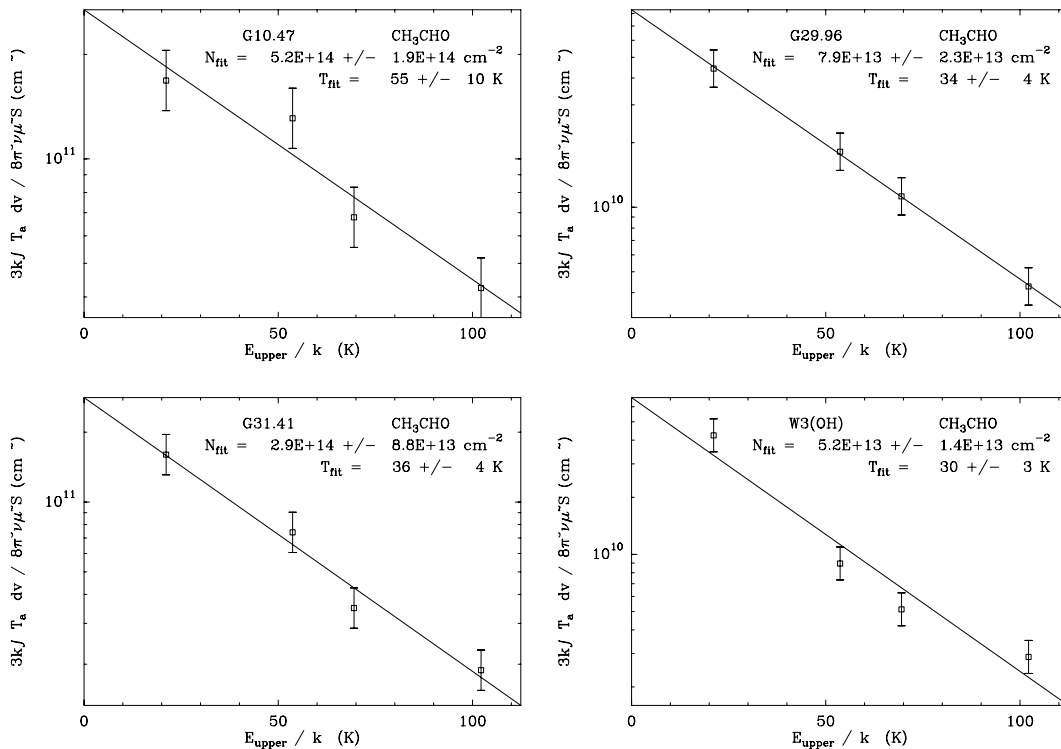


Fig. 5.11.— Boltzmann plots of CH₃CHO lines at 112 and 154 GHz.

typical line width of 8 km s^{-1} . This upper limit (1σ) is about consistent with the detection of ethanol in G34.26 by Millar et al. (1995).

5.3.6. CH₃CHO—Acetaldehyde

To our knowledge acetaldehyde has only been detected towards high mass star forming regions in Sgr B2 and Orion KL (Turner 1991). At 154 GHz, we were able to observe four lines of CH₃CHO simultaneously (see a sample spectrum in Fig. 5.7) towards four sources and the corresponding Boltzmann plots are shown in Fig. 5.11. Additionally, one line falls into the C¹⁷O(1–0) band: we have detected a feature at 112248.7 MHz towards G9.62, G11.94, G12.21, G19.61, and G45.47 which may be the $6_{1,6} - 5_{1,5}$ line of CH₃CHO at an excitation of 21 K. This line is included into the Boltzmann plots after correction for the different beam sizes assuming a point source, and compares very well in terms of excitation with the lines found at 154 GHz. The line parameters are given in Table A.8.

In contrast to the other complex molecules discussed so far, the CH₃CHO lines are fitted with a rather low rotational temperature, suggesting an origin of the line in the colder surroundings of the hot cores.

Table 5.1: Results of RD-analysis of several molecules. The column densities are beam averaged but all abundances are referred to the 224 GHz beam for better comparison. The H₂ column density is derived from C¹⁷O(2–1) observations.

Molecule	Source	ν_{obs} (GHz)	N_{T} (cm ⁻²)	T_{rot} (K)	X
H ₂	G10.47+0.03	224	2.26(23)		1
	G10.62-0.38		7.77(23)		
	G29.96-0.02		1.95(23)		
	G31.41+0.31		1.76(23)		
	G34.26+0.15		5.14(23)		
	W3(OH)		1.33(23)		
CH ₃ CH ₂ CN	G10.47+0.03	215	1.5±0.7 (15)	205±50	7(-9)
	G10.62-0.38		1.6±1.4 (14)	80±35	2(-10)
	G29.96-0.02		2.8±0.9 (14)	155±20	2(-9)
	G31.41+0.31		9.9±3.5 (14)	195±35	6(-9)
	G34.26+0.15		8.0±2.6 (14)	170±25	2(-9)
	W3(OH)		1.5±0.5 (14)	160±25	1(-9)
CH ₂ CHCN	G10.47+0.03	228	1.2±0.5 (15)	290±65	5(-9)
	G31.41+0.31		3.7±1.0 (14)	135±15	2(-9)
HCOOCH ₃	G10.47+0.03	258	1.5±0.2 (15)	130±40	5(-9)
	G31.41+0.31		1.5±0.4 (15)	175±40	6(-9)
	W3(OH)		1.2±0.2 (15)	185±50	7(-9)
CH ₃ OCH ₃	G10.47+0.03	140/154	3.3±0.7 (16)	190±20	3(-7)
	G29.96-0.02		7.2±6.0 (15)	250±140	8(-8)
	G31.41+0.31		1.7±0.4 (16)	160±15	2(-7)
	W3(OH)		2.5±1.0 (15)	80±15	4(-8)
CH ₃ CH ₂ OH	G10.47+0.03	87	3.3±1.5 (14)	60±10	7(-9)
	G31.41+0.31		2.1±0.7 (15)	180±30	8(-8)
CH ₃ CHO	G10.47+0.03	154	5.2±1.9 (14)	55±10	5(-9)
	G29.96-0.02		7.7±2.3 (13)	35±5	8(-10)
	G31.41+0.31		2.9±0.9 (14)	40±5	3(-9)
	W3(OH)		5.2±1.4 (13)	30±5	8(-10)

Table 5.2: Intensities of lines from deuterated molecules

Species	ν (MHz)	transition	$I(\text{G10.47})$ (Kkm s $^{-1}$)	$I(\text{G31.41})$ (Kkm s $^{-1}$)
HDO	87962.810	$7_{3,5} - 6_{4,2}$	—	0.6
NH $_2$ D	110153.017	$1_{1,1} - 1_{0,1}$	1.8	2.3
CH $_3$ OD	110188.859	$1_{1,0} - 1_{1,1}$	blend	1.0
	110262.641	$2_{2,1} - 2_{1,1}$	0.6	1.0
	140175.203	$4_{3,2} - 4_{2,2}$	—	2.0
NND $^+$	154217.096	$2 - 1$	3.9	2.9

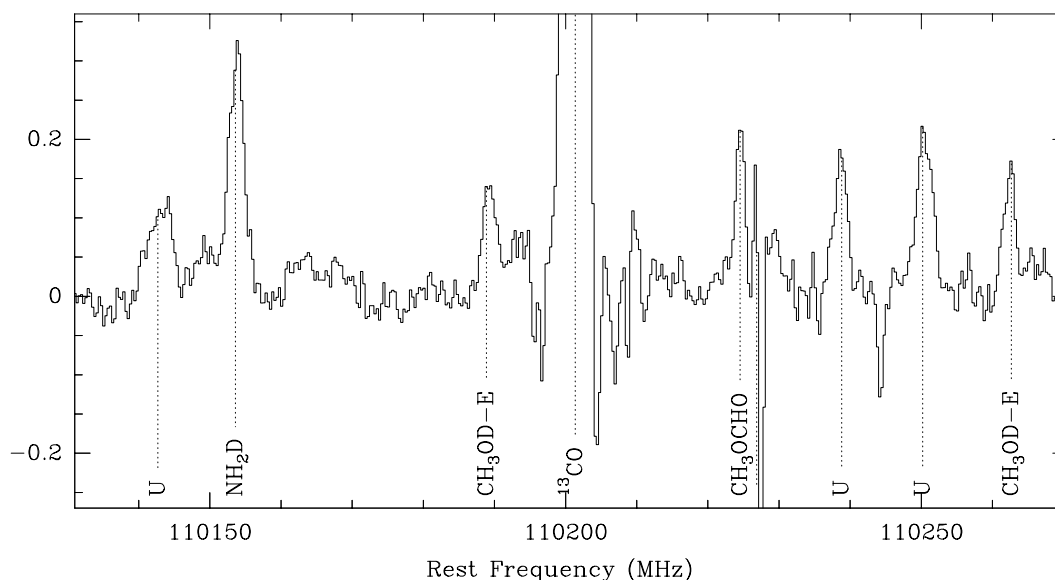


Fig. 5.12.— Sample spectrum of NH $_2$ D and CH $_3$ OD in BAND3-110 towards the source G31.41. The absorption features might be due to foreground ^{13}CO .

5.3.7. Deuterated molecules

Also several deuterated molecules can be identified in the observed frequency bands. The detections are summarized in Table 5.2.

The three deuterated methanol lines (CH $_3$ OD) detected in G31.41 cover only a small range in upper energies from 10–28 K which makes estimates of the rotational temperature quite uncertain. Therefore we cannot use the lines to estimate the temperature. Close to the 140 GHz CH $_3$ OD line with an upper energy of 28 K, also a CH $_3$ OH line is found ($18_{9,9} - 18_{9,10}$) but with upper energy of 407 K. For a realistic kinetic temperature between 100–200 K the abundance ratio between CH $_3$ OD and CH $_3$ OH is between 0.005 and 0.03 which is consistent with the results of Mauersberger et al. (1988) for Orion. The same analysis for G10.47, assuming T=200 K, leads to an upper limit of 0.01.

There is a weak line feature at the frequency of an HDO line at 87 GHz in G31.41. There is no overlap with other known lines. But the column density which can be calculated from the intensity of the feature assuming a temperature of 200 K is more than a factor 10 higher than the column density of HDO found in the analysis of Gensheimer et al. (1996). Therefore it seems likely that the line is blended with an unknown line or anomalously excitation effects are the cause of the high line intensity.

The $\text{NH}_2\text{D}/\text{NH}_3$ ratio can be estimated with the detected deuterated ammonia line at 110 GHz. We compare this low excitation line with its $^{15}\text{NH}_3(1,1)$ counterpart (see Chapter 3 in case of G10.47 and Wyrowski & Walmsley 1996 in case of G31.41) to get rid of any temperature dependence. With a $^{14}\text{N}/^{15}\text{N}$ ratio of 300, this leads to $\text{NH}_2\text{D}/\text{NH}_3$ ratios of 0.003 and 0.007 for G10.47 and G31.41, respectively. Jacq et al. (1990) determined this ratio for G34.26 and W51e and found values of 0.01 to 0.03, whereas the Orion value measured by Walmsley et al. (1987) is 0.003. It has to be noted that the low lying transition very likely samples also a component of colder gas in the environment of hot cores as is evident from the $^{15}\text{NH}_3$ Boltzmann plot discussed in Chapter 3.

To our knowledge, there are no detections of NND^+ towards high mass star forming regions till now. In view of the large amount of unidentified lines at 2 mm towards our observed hot core sources, the detections of the NND^+ (2–1) lines towards G10.47 and G31.41 should be considered as very tentative. But the feature detected is coincident with the NND^+ frequency and assuming LTE and temperatures between 50 and 150 K, a column density for the sources of $5 - 15 \times 10^{12} \text{ cm}^{-2}$ is derived. Observations of other transitions are needed to confirm the detections. Observations of the main isotopomer are not available towards the sources.

5.4. The chemical age of hot cores

We are now in a position to actually compare the results of the previous section with predictions of models for the hot core chemistry.

The $[\text{D}]/[\text{H}]$ ratio in the local interstellar medium is 1.6×10^{-5} (Wilson & Rood 1994). Therefore the high abundance of deuterated molecules mean enhancements towards hot cores by factors of 100–1000. But a large fractionation is expected only for cold clouds and therefore the general explanation of this finding is that fractionation must have occurred in an early cold dense core phase followed by the freezing of the then D-rich molecules onto the grains (Plambeck & Wright 1987). The observations of the large abundances of CH_3OD and NH_2D towards hot cores is then a direct hint for the dust grain origin of the enhanced NH_3 and CH_3OH abundances in the hot core gas phase. These “parent” mantle species lead then in the warm gas to the formation of so-called “daughter” molecules such as CH_3CN , CH_3OCH_3 , and HCOOCH_3 (Charnley et al. 1992). The abundances of the latter two has

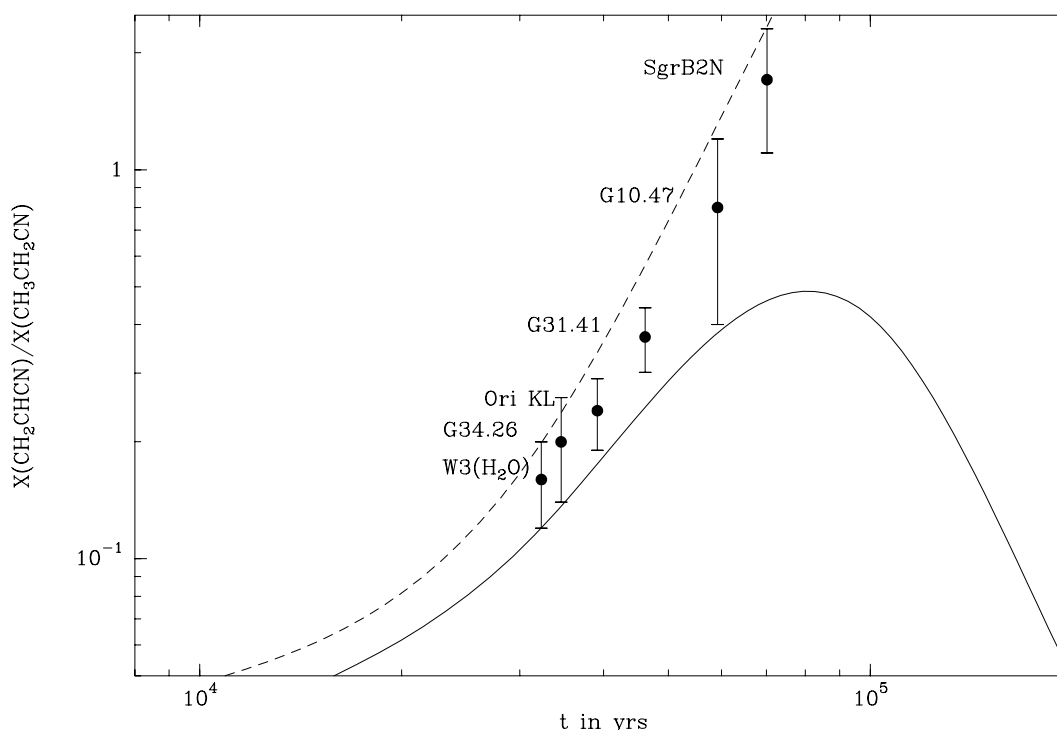


Fig. 5.13.— Comparison of predictions for the abundance ratio of the parent/daughter pair $\text{CH}_3\text{CH}_2\text{CN}/\text{CH}_2\text{CHCN}$ with observational results (see text for references). The predictions are taken from Caselli et al. (1993) for their Hot Core ($T \sim 200$ K, $n \sim 10^7$ cm^{-3} , solid line) and their Compact Ridge model ($T \sim 100$ K, $n \sim 10^6$ cm^{-3} , dashed line).

been determined by us in the last section and require a time of about 10^4 years for their formation after the onset of a heating source. In principle, the chemical processing of these molecules might be used as chemical clocks for the hot gas to determine the time passed away since the onset of a heating source. But this would require good estimates of the abundances of the parent molecule CH_3OH which could not be determined on basis of our data. The high observed deuterated ratios are believed to stay for about 10^5 yrs (Rodgers & Millar 1996).

The observed high abundances of $\text{CH}_3\text{CH}_2\text{CN}$ and $\text{CH}_3\text{CH}_2\text{OH}$ cannot be explained by gas phase reactions (Charnley et al. 1992, 1997; Caselli et al. 1993) and therefore it is likely that these species are formed on the grain surfaces. After evaporation gas phase reactions with $\text{CH}_3\text{CH}_2\text{CN}$ leads then to the formation of CH_2CHCN (Caselli et al. 1993) and therefore this parent/daughter pair can be used as a chemical clock. This is shown in Fig. 5.13 with a comparison of Caselli et al. model predictions and observational results for the CH_2CHCN -to- $\text{CH}_3\text{CH}_2\text{CN}$ ratio. The G10.47 and G31.41 data are taken from the present analysis, the W3(OH) result will be discussed in Chapter 6, the Orion value is estimated from the interferometer observations of Blake et al. (1996) for a temperature range

of 100-200 K, and the results for SgrB2N and G34.26 have been discussed in Mehringer & Snyder (1996). Caselli et al. ran models for the physical parameters of the Orion Hot Core ($T \sim 200$ K, $n \sim 10^7$ cm $^{-3}$) and Compact Ridge ($T \sim 100$ K, $n \sim 10^6$ cm $^{-3}$). Using these two models as the extrema for the physical conditions in the other hot cores, their ages are confined to the range from 25000 to 70000 yrs with W3(H₂O) as youngest and SgrB2N as oldest source. A sharp decrease of the abundances of many complex molecules after 10^5 years is predicted, and therefore solutions with $t > 10^5$ yrs are unlikely.

5.5. Conclusions

Column densities of the complex molecules CH₃CH₂CN, CH₂CHCN, CH₃OCH₃, HCOOCH₃, CH₃CH₂OH, and CH₃CHO were determined towards several hot cores in this chapter which provide a valuable data base for further theoretical studies of hot core chemistry. Comparison with chemical models lead to a chemical time scale of 5×10^4 years after onset of the heating sources.

REFERENCES

- Blake G.A., Sutton E.C., Masson C.R., Phillips T.G. 1987, ApJ 315, 621
 Blake G.A., Mundy L.G., Carlstrom J.E., Padin S., Scott S.L., Scoville N.Z., Woody D.P. 1996, ApJ 472, L49
 Brown P.D., Charnley S.B., Millar T.J. 1988, MNRAS 231, 409
 Caselli P., Hasegawa T.I., Herbst E. 1993, ApJ 408, 548
 Charnley S.B., Tielens A.G.G.M., Millar T.J. 1992, ApJ 399, L71
 Gensheimer P.D., Mauersberger R., Wilson T. 1996, A&A 314, 281
 Helmich F.P., van Dishoeck E.F. 1997, ApJS in press
 Jacq T., Walmsley C.M., Henkel C., Baudry A., Mauersberger R., Jewell P.R. 1990, A&A 228, 447
 Macdonald G.H., Gibb A.G., Habing R.J., Millar T.J. 1996, A&AS 119, 333
 Mauersberger R., Henkel C., Jacq T., Walmsley C.M. 1988, A&A 194, L1
 Mehringer D.M., Snyder L.E. 1996, ApJ 471, 897
 Miao Y., Mehringer D.M., Kuan Y., Snyder L.E. 1995, ApJ 445, L59
 Millar T.J., Macdonald G.H., Habing R.J. 1995, MNRAS 273, 25
 Millar T.J., Macdonald G.H., Gibb A.G. 1997, A&A 325, 1163
 Ohishi M. 1996, in "Molecules in astrophysics: probes and processes", ed. by E.F. van Dishoeck, Kluwer
 Olmi L., Cesaroni R., Walmsley C.M. 1996, A&A, 307, 599
 Plambeck R.L., Wright M.C.H. 1987, ApJ 317, L101

- Pickett H.M., Poynter R.L., Cohen E.A., Delitsky M.L., Pearson J.C., Müller H.S.P.,
“Submillimeter, millimeter, and microwave line catalog”, JPL Publication 80-23,
Revision 4, Pasadena CA, 1996
- Poynter R.L., Pickett H.M. 1985, *Appl. Opt.* 24, 2235
- Rodgers S.D., Millar T.J. 1996, *MNRAS* 280, 1046
- Schilke P., Groesbeck T.D., Blake G.A., Phillips T.G. 1997, *ApJS* 108, 301
- Sutton E.C., Jaminet P.A., Danchi W.C., Blake G.A. 1991, *ApJS* 77, 255
- Sutton E.C., Peng R., Danchi W.C., Jaminet P.A., Sandell G., Russel A.P.G. 1994, *ApJS*
97, 455
- Turner B.E. 1991, *ApJS* 76, 617
- Walmsley C.M., Hermsen W., Henkel C., Mauersberger R., Wilson T.L. 1987, *A&A* 172,
311
- Wilson T.L., Rood R.T. 1994, *ARA&A* 32, 191
- Wright M.C.H., Plambeck R.L., Wilner D.J. 1996, *ApJ* 469, 216
- Wyrowski F., Walmsley C.M. 1996, *A&A* 314, 265

Chapter 6

An interferometer study of gas and dust in W3(OH)

6.1. Introduction

Millimeter interferometers allow us to obtain reliable determinations of the cloud structure in star forming regions and hence the mass distribution. Both millimeter wavelength dust emission and the emission in optically thin isotopomers of CO are thought to trace the H₂ distribution and therefore the mass. One approach is to observe both tracers in a given object and to compare the results. This is best done at a wavelength of 1.3 mm where dust emission is optically thin but readily observable and where one can observe the (2–1) transitions of e.g. C¹⁷O at similar frequencies.

One of the nearest high mass star forming regions is the molecular clump associated with the prototypical ultracompact HII region and maser source W3(OH). Figure 6.1 shows a CO map from Lada et al. (1978) superposed on the corresponding red Palomar Sky Survey print towards the W3/W4 region. The giant molecular cloud complex W3 is sited in the Perseus arm of the Galaxy at the edge of the HII region W4 which is ionized by a young open OB cluster. This cluster seems to be responsible for the first identified galactic chimney (Normandeau et al. 1996) from which hot gas is transported out of the galactic disk into the halo. But it is also interacting with the adjacent molecular clouds. The ionization front advances into the molecular gas given rise to a thin layer of fragmented, compressed warm molecular clouds. One of the cloud cores harbors the ultracompact HII region W3(OH), so named because it coincides with strong OH maser emission.

The W3(H₂O) source at a distance of 2.2 kpc (Humphreys 1978) is a warm, high

Parts of this chapter are published in Astronomy and Astrophysics 320, L17 (1997) in collaboration with P.Hofner, P.Schilke, C.M.Walmsley, D.J.Wilner, and J.E.Wink.

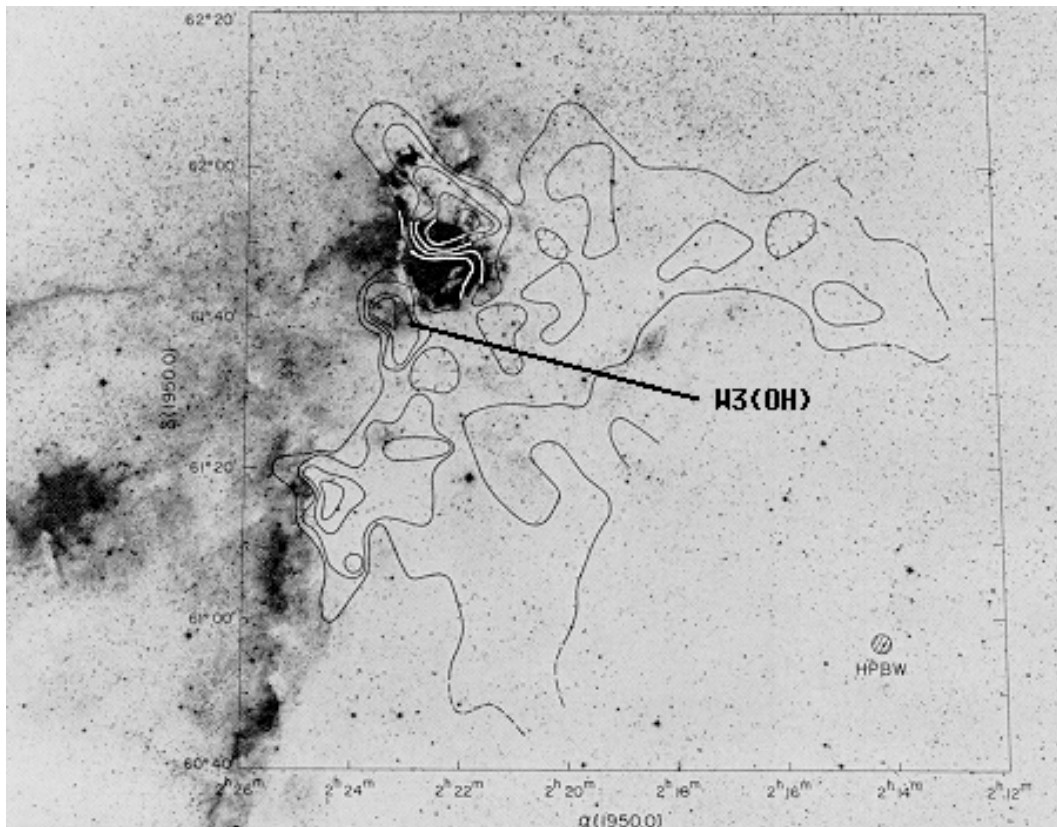


Fig. 6.1.— CO(1-0) map from Lada et al. (1978) superposed on the corresponding red Palomar Sky Survey print towards the W3/W4 region showing the interaction of ionized and molecular gas which led to the formation of a narrow, clumpy, high density molecular layer.

density molecular clump (Turner & Welch 1984) or hot core associated with water masers $6''$ (0.06 pc) east of W3(OH). The strong methanol and OH masers in this direction (Menten et al. 1988) are associated with the ionized gas whereas the H₂O masers appear to be embedded in W3(H₂O) to the east. The water masers seem to be part of a bipolar flow which is driven by a jet seen in synchrotron radiation at centimeter wavelengths (Reid et al. 1995). Wink et al. (1994) used the IRAM Interferometer to study the W3(H₂O) hot core at 3 mm and detected a continuum source at the molecular line peak which they attributed to emission from hot dust. They estimated a temperature of 100 K for the gas from their methyl cyanide observations and used this to determine a gas mass of 30 M_⊙. Observations by Wilner et al. (1995) with the BIMA array at 88 GHz confirmed the interpretation of the continuum emission as being due to dust and allowed an improved mass estimate of 10–20 M_⊙. A single dish molecular line study by Helmich et al. (1994) concluded that the temperature of the molecular gas was likely to be 220 K. Those characteristics taken together suggest that the W3(H₂O) hot core is rather similar in character to the well known hot core in Orion (Churchwell 1991 and Walmsley & Schilke 1992).

We performed new interferometer observations towards this source in order to confirm that the 3 mm continuum is indeed due to dust emission and to determine the frequency dependence of the dust opacity with new 1.3 mm observations. From this we hoped to get an improved estimate of the mass of the hot core. Another aim was to observe simultaneously a rare isotopomer of CO to get an independent mass estimate. Besides emission from the CO isotopomer, several other lines were observed, which are used to study the chemistry of the sources and the relation between thermal and masering gas.

6.2. Observations and data reduction

The observations were carried out in winter 1995/1996 with the IRAM 4-element Array on the Plateau de Bure (Guilloteau et al. 1992). The primary beam of the 15-m antennas is $45''$ at 112 GHz and $22''$ at 225 GHz. The synthesized beam was $3''.4 \times 2''.8$ at 112 GHz and $1''.6 \times 1''.4$ at 225 GHz. We were insensitive to structures larger than $17''$ at 112 GHz and $6''.5$ at 225 GHz. The phase center used for the observations was (α (J2000) = $02^h 27^m 04^s 28$, δ (J2000) = $61^\circ 52' 24''.6$) and offsets in this chapter are given relative to this position. Our observations of W3(OH) were interspersed at 20 minute intervals with observations of the calibrator 0224+671 for which we used fluxes of 1.1 Jy at 112 GHz and 0.52 Jy at 225 GHz. These fluxes were derived from comparison with NRAO 530 (10.9 Jy at 112 GHz and 7.0 Jy at 225 GHz on Mar 30 1996) and 3C454.3 (4.5 Jy at 112 GHz on Dec 21 1995).

We observed simultaneously at 2.6 and 1.3 mm using SIS receivers with noise temperatures of 40 and 60 K, respectively. The correlator was split so that two units with bandwidths of 40 and 80 MHz were centered at the frequencies of $C^{17}O(1-0)$ and $(2-1)$ (112358.988 MHz and 224714.368 MHz respectively) with 256 and 128 channels. The remaining units of 160 MHz bandwidths and 64 channels were blue- and red-shifted by 100 MHz to sample the 3 mm and 1.3 mm continuum. The latter frequencies were chosen to be “line free” but some lines were nevertheless detected in these frequency ranges (see below). Velocity resolutions were 0.4 km s^{-1} for $C^{17}O(1-0)$, 0.8 km s^{-1} for $C^{17}O(2-1)$, 6.7 km s^{-1} in the units used for 3 mm continuum, and 3.3 km s^{-1} in the units used for 1.3 mm continuum.

Continuum maps were constructed using “line free” frequency ranges. At both observing frequencies, the strong ultra-compact HII region W3(OH) is clearly visible and this fact allowed us to apply a process of iterative phase-only “self-calibration” to the continuum maps with only positive clean components as a model (GILDAS task `uv_selfcft`, Guilloteau & Wink, priv. comm.). This greatly increases the dynamical range which was initially too poor to detect the H_2O maser source at 3 mm. In order to produce line maps in $C^{17}O(1-0)$ and $(2-1)$ and in the other transitions detected, the continuum was subtracted from the line data in the uv-plane.

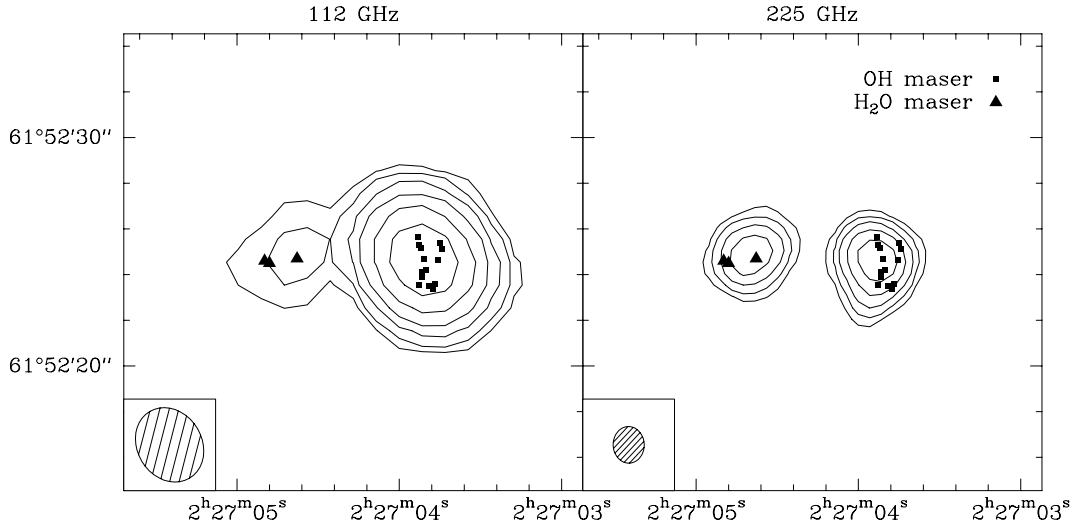


Fig. 6.2.— IRAM PdB continuum maps towards W3(OH) at 112 and 225 GHz. Contour steps in both panels are 0.05, 0.1, 0.2, 0.4, 0.8, 1.6 Jy/beam and positions of OH and H₂O maser emission are indicated.

6.3. The millimeter continuum emission

6.3.1. Results

Figure 6.2 shows our continuum maps at 112 and 225 GHz which we did by summation of the uv data of line-free channels. The r.m.s. noise in the maps is 10 mJy/beam at both frequencies after the self-calibration. The 112.5 GHz map is dominated by the UC HII region but we also detect the continuum source close to the center of expansion of the water masers at an offset of ($6''.0$, $0''.2$) from W3(OH) with a flux of 100 mJy after subtracting a weak positive halo introduced by contamination from W3(OH) due to residual phase errors. This is consistent with the results of Wink et al. (1994). At 225 GHz this source is detected with angular size $2''.2 \times 1''.8$. It is apparently marginally resolved with a deconvolved size of $1''.3$, in contrast to the 88 GHz observation of Wilner et al. (1995) which yielded an upper limit of $0''.5$. The integrated flux is 1.3 Jy at an offset of ($5''.5$, $0''.2$) from W3(OH). This is about $0''.5$ offset from the position reported by Wilner et al. (1995) and one possible interpretation is that we see in addition to the 88 GHz point source more extended emission with a slightly steeper spectral index which is not visible at 3 mm. Another interpretation for the observed size of the emission would be that the emission at 1.3 mm becomes optically thick, but this is unlikely in view of the relatively low brightness temperature of 16 K, much smaller than the expected dust temperatures. One should note that on scales smaller than our beam, W3(OH) is resolved into a clumpy shell-like structure (Dreher & Welch 1981). Therefore, a centroid is not well defined and this can result in discrepancies of several tenths of an arc second in determining positions relative to W3(OH).

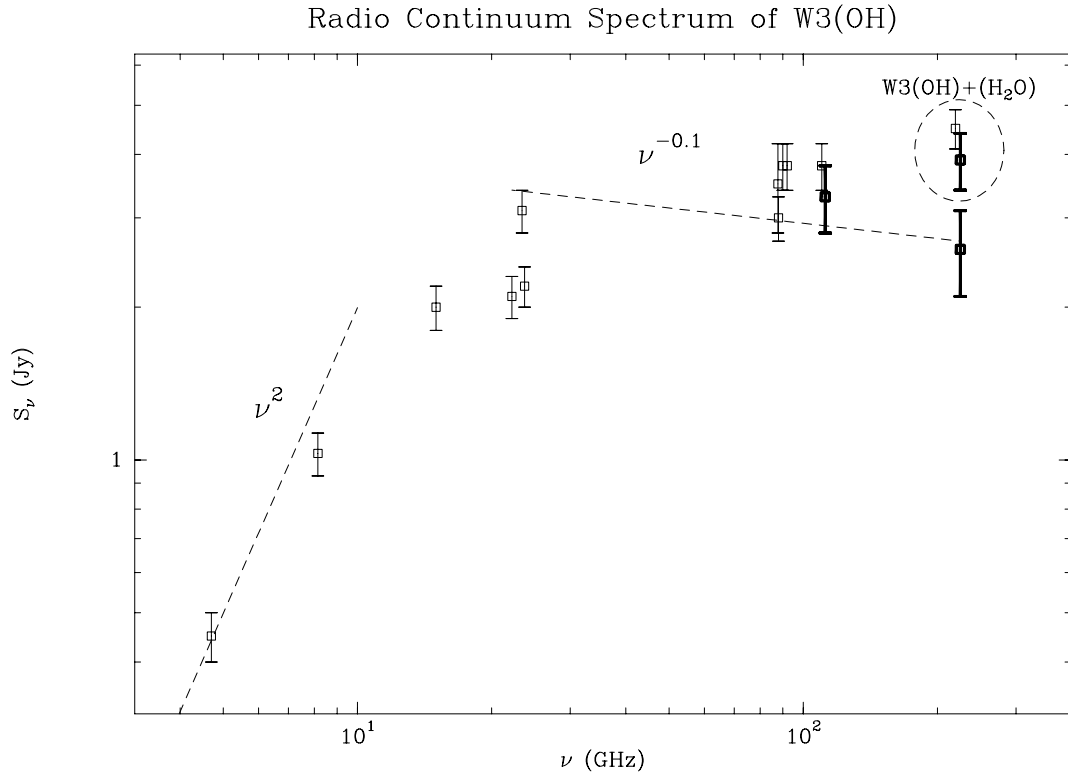


Fig. 6.3.— Radio continuum spectrum of W3(OH) showing our new 3 mm and 1.3 mm flux measurements (thick bars) in comparison with previous results. The thermal radiation of an homogeneous HII region is shown in the optically thick and thin limits (dashed lines). In the upper right, the observed total flux is compared to the result of Woody et al. (1989). The other fluxes are taken from Guilloteau et al. (1985: 4.7 GHz), Baudry et al. (1993: 8.15 GHz), Dreher & Welch (1981: 15, 22.2, 88 GHz), Wilson et al. (1991: 23.4 GHz), Guilloteau et al. (1983: 23.7 GHz), Wilner et al. (1995: 87.7 GHz), and Wink et al. (1994).

6.3.2. The radio continuum spectrum

Figure 6.3 shows the radio continuum spectrum of the ultracompact HII region with flux values from the literature and our observations. The turnover from optically thick to thin emission is seen at about 10 GHz. Our 3 mm measurement, for which we derive an integrated flux of 3.3 Jy, compares very well with previous observations (Wink et al. 1994; Wilner et al. 1995) and also the 1 mm integrated flux of 2.6 Jy is consistent within the errors with extrapolated optically thin emission from the HII region. In the upper left is the flux measured by Woody et al. (1989), who did not resolve both sources, compared to our total flux. Reuter (priv. comm.) measured a continuum flux of 6.3 Jy/beam with the IRAM 30-m telescope at 225 GHz in excess of our combined flux of both sources, W3(OH) and W3(H₂O), indicating a missing flux of 2.4 Jy by the interferometer due to extended emission in the 11'' 30-m beam.

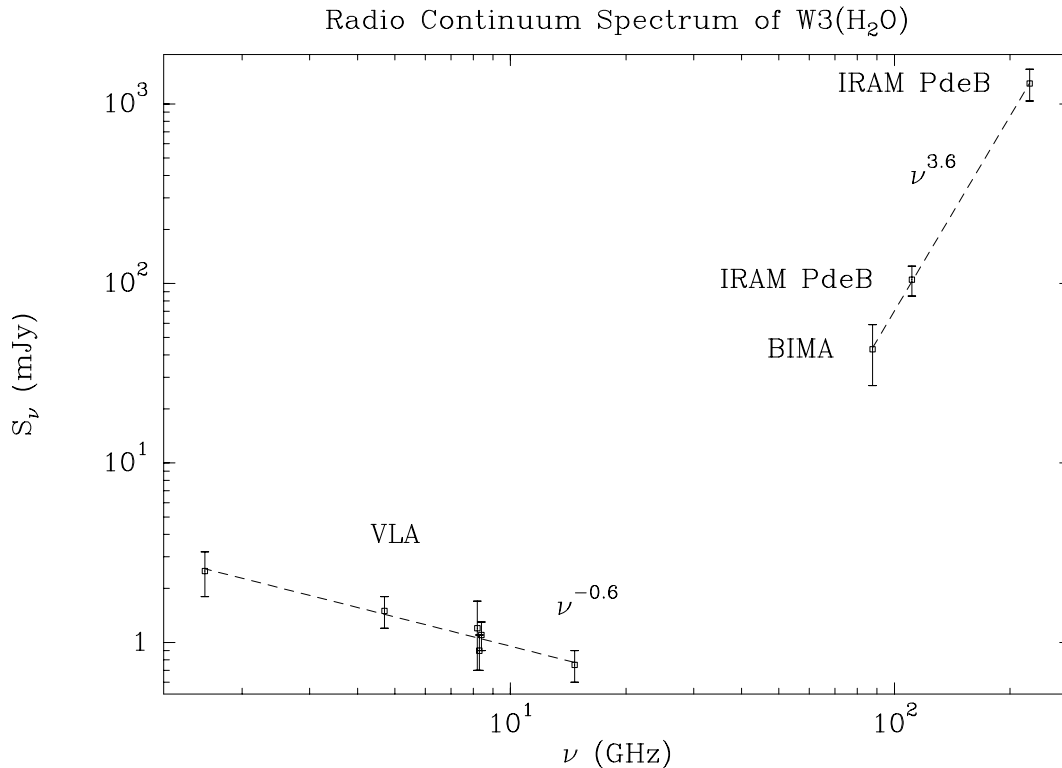


Fig. 6.4.— The radio continuum spectrum of W3(H₂O). At low frequencies, one observes synchrotron emission associated with the outflow (Reid et al. 1995) and at high frequencies dust emission from the hot core.

The important point here is that our flux calibration is reliable within about 20 %. This is important to mention because in mm interferometry calibration is not an easy task. One has to deal mainly with time-varying quasars as calibration sources and has to merge observations from different dates.

After discussing the uncertainties in the fluxes, we can now go on to the spectrum towards W3(H₂O). Our measurement of the continuum emission at 3 and 1.3 mm allows for the first time a reliable estimate of the dust opacity spectral index at millimeter wavelengths. In Fig. 6.4, we show the radio continuum spectrum of W3(H₂O) including our new high frequency measurement. In contrast to the continuum spectrum of W3(OH), the source towards the water masers shows a completely different behavior. At wavelengths longward of 1 cm, synchrotron emission from the jet associated with the bipolar molecular outflow is dominant (Reid et al. 1995). Between 85 and 225 GHz in contrast, the spectral index is approximately 3.6 and dust emission dominates. The simplest interpretation is that the dust is optically thin with opacity varying as $\nu^{1.6}$. This seems to be slightly flatter than the dust opacity index in Orion which was estimated by Wright et al. (1992) to be 2. Most effects such as optical depth or temperature gradients tend to make the spectral index flatter and then 1.6 is only a lower limit.

6.3.3. Mass estimates from the dust emission

Knowledge of the opacity index allows us to refine our estimate of the hot core mass. Here we will use the same approach as Wilner et al. (1995): the assumptions are radial power laws for the density and temperature structure and the following expression for the dust opacity:

$$\rho \propto r^{-\alpha}, \quad T \propto r^{-0.4}, \quad \kappa \propto \lambda^{-\beta}. \quad (6.1)$$

An exponent of e.g. 1.5 for the density resembles a freely collapsing cloud. But the estimate of the mass is quite independent of the assumed power law. The exponent of the radial thermal structure of 0.4 is that of an optically thin cloud after solving for the energy balance between heating by a central source and reradiation by the grains. The dust opacity at 1.3mm is the one given by Hildebrand (1983). Then the resulting mass is a function of the dust temperature at the outer radius:

$$M = \frac{0.01 \text{ cm}^2 \text{ g}^{-1} 2500}{\kappa_{1.3}} \frac{1}{T} M_{\odot}. \quad (6.2)$$

Here we used the observed opacity index β of 1.6. If one assumes equality of dust and gas temperatures and uses the temperature of 220 K estimated by Helmich et al. (1994) and the dust opacity from Hildebrand (1983), one derives a value of 10 M_{\odot} for the core seen in continuum emission.

6.4. C¹⁷O emission

Another approach to estimate masses is to use an optically thin line. We decided to use the rare CO isotopomer C¹⁷O since even C¹⁸O seems to become optically thick in hot core sources. Results of a small single dish survey of C¹⁷O towards hot cores to refine the column density and mass estimates of the sources, has already been shown in Chapter 2. W3(OH) has been also one of the observed sources. The abundance ratio C¹⁷O over H₂ is 5×10^{-8} (with [C¹⁸O]/[H₂]= 1.7×10^{-7} , Frerking et al. 1982, and [C¹⁸O]/[C¹⁷O]=3.5, Matteucci 1991) and one has to take the hyperfine structure into account. Although we can't resolve the hyperfine structure in our sources, we have to account for the widening of the line. To estimate the column density, we use the formula given by Genzel (1992) which is valid over a wide range of temperatures and densities:

$$N(\text{H}_2) = 10^{22} I(\text{C}^{17}\text{O}(2-1)) \quad (\text{cm}^{-2}/(\text{Kkm/s})) \quad (6.3)$$

The mass of a Gaussian emission distribution is then given by the integral over the clump:

$$M(\text{H}_2) = \frac{\pi ab}{4 \ln 2} N(\text{H}_2) m(\text{H}_2) \quad (6.4)$$

where a and b are major and minor half-power widths of the emission and $m(\text{H}_2)$ the mass of the hydrogen molecule.

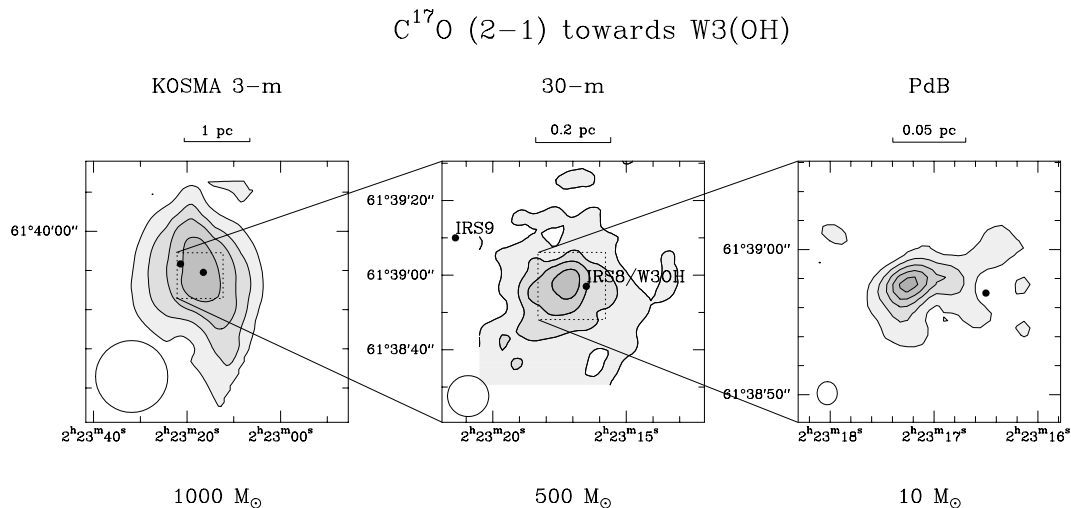


Fig. 6.5.— Mass distribution traced by $C^{17}O$ towards W3(OH) on three different length scales. The contours are 30, 50, 70, 90% of peak emission in all panels. The dots are the positions of the IR sources found by Wynn-Williams et al. (1972). The different beam sizes are indicated in each case in the lower left.

6.4.1. Gas mass distribution

Figure 6.5 shows the mass distribution traced by $C^{17}O$ towards W3(OH) on three different length scales. The GMC core of W3(OH), which was already shown in Fig. 6.1, is easily recognized also in $C^{17}O$ seen with the KOSMA 3-m telescope (see Chapter 2 for a description of the observations) although it is only marginally resolved in the $110''$ beam. On this scale we see a total of $1000 M_{\odot}$.

On the next scale seen with the 30-m at an angular resolution of $11''$ (Hofner et al. 1997), the cloud core out of which the stars powering the ultracompact HII region W3(OH) were born, becomes clearly visible embedded in a halo of lower column density gas. There are still $500 M_{\odot}$ seen in this map. The infrared sources found by Wynn-Williams et al. (1972) are marked. One of them coincide with the UC HII whereas the other is not associated with the core.

With the interferometer the more extended, lower column density component is now completely resolved out and the molecular cloud fragment which shelters the water maser source becomes distinct from the ultracompact HII region. The total gas mass which we derive for that hot core is $10 M_{\odot}$.

In Fig. 6.6, we show our integrated intensity maps in $C^{17}O$ superimposed on the continuum maps. As in the case of $C^{18}O$ (Wink et al. 1994), the $C^{17}O$ emission seen with the interferometer is concentrated on the water maser complex. The continuum emission coincides with the maximum in $C^{17}O$. The $J=2-1$ emission has a compact core with a half-power size of $4''.7 \times 2''.7$ at p.a. 70° , which is more extended than the continuum. There

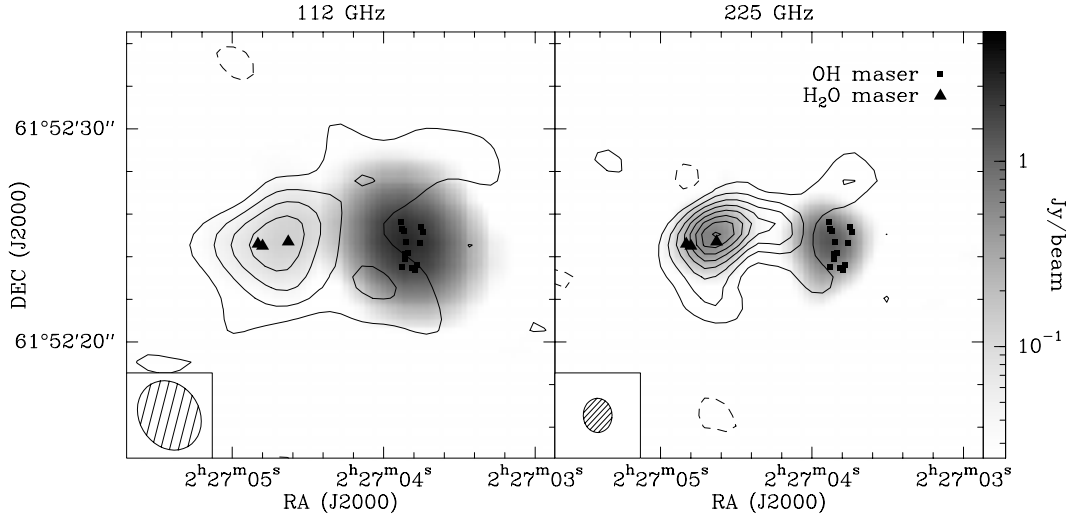


Fig. 6.6.— $\text{C}^{17}\text{O}(1-0)$ integrated emission (left panel, contours) and $\text{C}^{17}\text{O}(2-1)$ (right panel, contours) from the W3(OH) region compared with continuum emission (grey logarithmic scale). Contour steps are 3 and 5.6 Kkm s^{-1} for (1-0) and (2-1), respectively. The positions of the OH masers are from Reid et al. (1980) and the positions of the H_2O masers from Dreher & Welch (1981).

is also in both the (1-0) and (2-1) transitions a weak tongue of emission in C^{17}O which wraps around the UC HII region suggesting that the cloud is being disrupted by the HII region.

6.4.2. Hot core mass

We can also use our C^{17}O results to determine the mass and column density of the molecular gas. The integrated $\text{C}^{17}\text{O}(2-1)$ intensity in a $1''.5$ beam towards W3(H_2O) is 40 Kkm s^{-1} and the ratio of the (2-1) and (1-0) intensities is 1.8 (smoothed to the resolution at 3 mm). This is consistent with emission by hot optically thin gas and one can thus apply canonical formulae (see Genzel 1992) to derive an H_2 column density of $4 \times 10^{23} \text{ cm}^{-2}$. If we integrate this over the region of observed line emission, we derive a mass of $11 M_\odot$ or, integrated over the size of the continuum source, of $4 M_\odot$.

Both of these are considerably less than the upper limit to the virial mass (roughly $60 M_\odot$) which one derives from the observed line widths and the angular size of the gas indicating that the virial assumption is not valid due to the dynamics of the outflow. Using the mm-continuum and C^{17}O to trace the mass also misses non-gas matter in form of stars which could be responsible for the discrepancy. It is interesting to note that the masses we derive for the hot core gas are comparable to the mass of the star which is presumably responsible for the observed high temperatures. Model calculations we have carried out

suggest that one requires a central star of luminosity at least 10^4 solar luminosities to account for temperatures of 100 K at radii of 1000 AU. Such a star if on the ZAMS (spectral type B0, see Panagia 1973) should have a mass of roughly $15 M_{\odot}$ which is comparable to our estimate for the hot core mass based on the millimeter emission.

6.5. Complex molecules in W3(OH)

In addition to $C^{17}O$ we detected several other lines in the image side bands and in the spectral units which we used to probe the continuum. This adds up to a total spectral coverage of 1.5 GHz. In Fig. 6.7 the whole spectral range is shown towards the hot core. The advantage of getting also the spectral information from the continuum units is obvious: in this way it is possible to avoid strong line emission in the continuum maps. But weak line emission which is seen nearly everywhere makes it difficult to define a continuum level. Additionally, the information obtained from the lines themselves provide valuable insights into the chemistry of the region.

6.5.1. Identification and morphology

The identifications of the observed lines are shown in the composite spectra of Fig. 6.7: there are complex organics like methanol, dimethyl ether, methyl formate, ethyl and vinyl cyanide, there are transitions from ground and vibrationally excited cyanoacetylene and also sulphur bearing molecules like SO and OCS. Some lines are still unidentified. There is even evidence for weak emission from ethanol at 112434.2 GHz ($14_{9,5}g^+ - 14_{9,5}g^-$), 224823.1 GHz ($13_{1,12} - 12_{1,11}$), and 227891.9 GHz ($13_{1,12} - 12_{1,11}$). At 112490.8 GHz, there might be a C_3H_2 line ($7_{4,3} - 7_{3,4}$) detected.

One can divide the molecules observed at 1.3 mm into two groups: molecules which show strong emission towards the hot core and the ultracompact HII region, and molecules which are strong only towards the hot core, these are the nitrogen bearing molecules, as can be seen in Fig. 6.8. Surprisingly, there seems to be a small positional and also spectral offset between nitrogen and oxygen bearing molecules towards the hot core indicating chemical diversity on sub-arcsecond scale. This is more evident in looking at position-velocity plots of different molecules (Fig. 6.9) where CH_3OH and CH_3CH_2CN emission are clearly separated by about $0''.5$ with the $C^{17}O$ emission more or less in-between. Whether this is due to chemical gradients or a double source remains open for the present. The emission from oxygen bearing molecules coincides with the dust continuum peak. It might be that the peak of the nitrogen bearing molecules is physically related to the second cm-continuum source observed by Reid et al. (1995) but we need higher angular resolution observations to verify this. One should note that this offset between oxygen and nitrogen bearing species

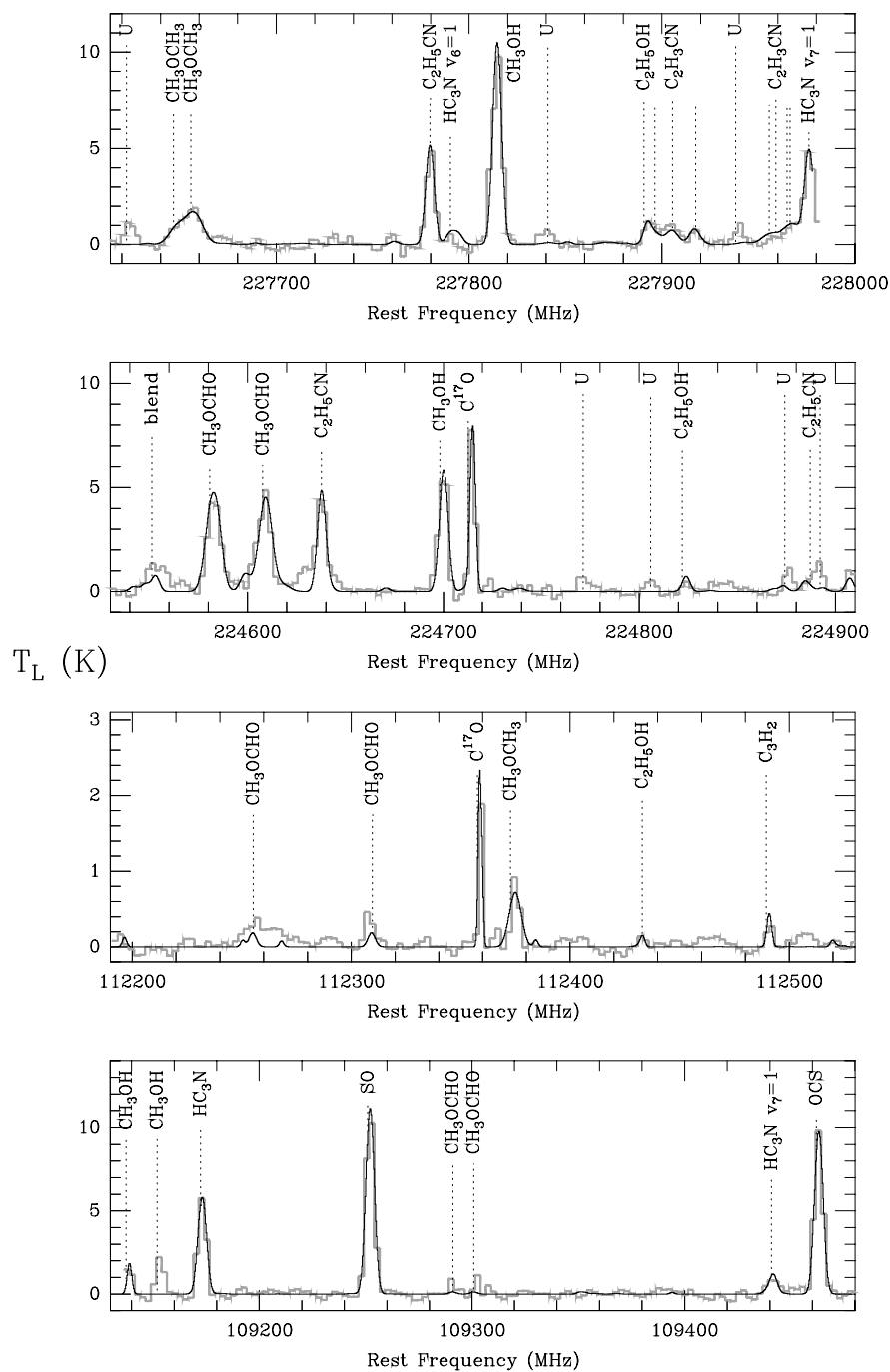
W3(H₂O) observations with PdB

Fig. 6.7.— Total observed spectral range towards W3(H₂O, N-peak) with different correlator units merged into one spectrum. The panels show the results at 3 and 1.3 mm in the lower and upper sidebands, respectively. The identified molecules are fitted using a single temperature, column density and source size for each (see Table 6.2).

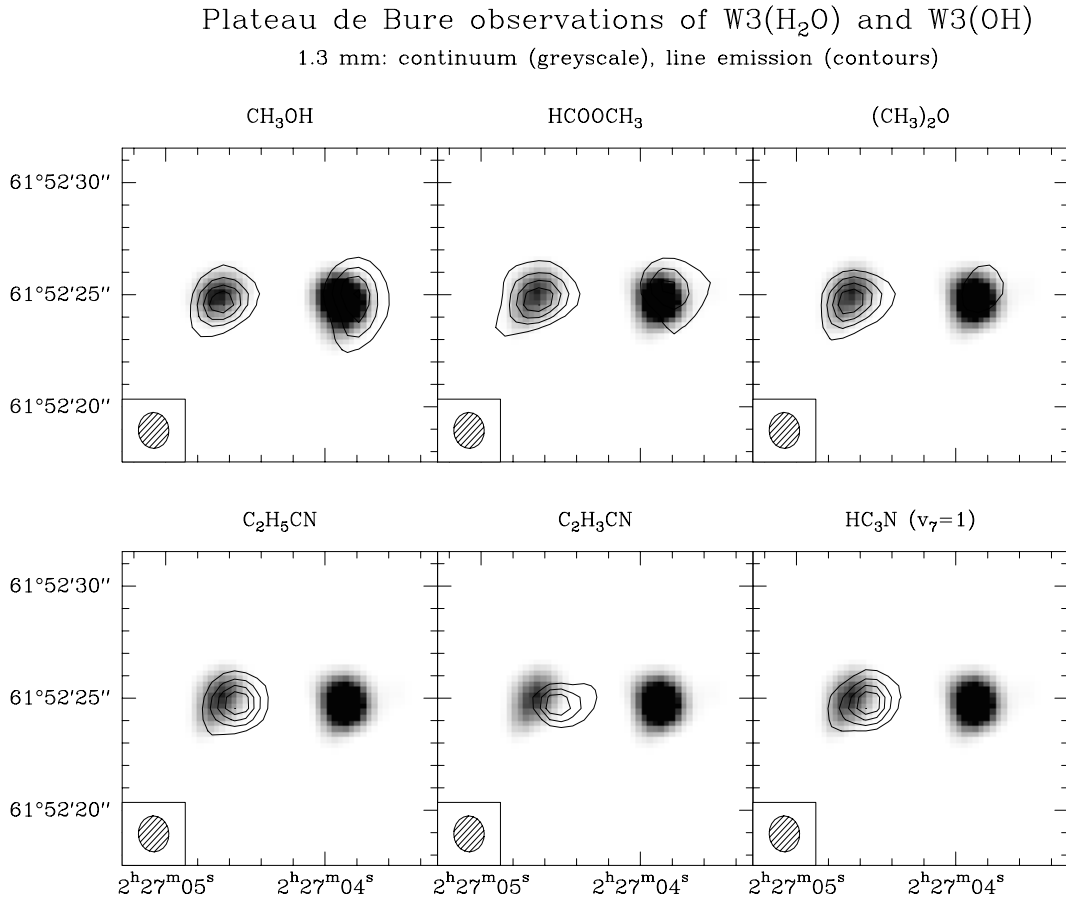


Fig. 6.8.— 1.3 mm maps of several complex molecules towards W3(OH) illustrating the chemical differences between the hot core and the ultracompact HII region. In each panel, the grey-scale presents the 1.3 mm continuum and the contours the molecular line emission.

is just what is seen in the offset between Compact Ridge and Hot Core in Orion. The difference is however that in W3(OH) the dust continuum coincides with the oxygen bearing molecules and not, as in the case of Orion, with the nitrogen species.

Because of these chemical differences, we give the measured line parameters of the observed molecules in Table 6.1 for three characteristic locations: the nitrogen and oxygen peaks towards the hot core, ($2''$, $0''$) and ($2''.5$, $0''$) offset from the phase center, and the oxygen peak of the ultracompact HII region traced by methanol at an offset of ($-3''.5$, $0''.5$). Note that lines from different correlator units can have very different line widths due to the different channel spacings (see the section on the observations). We did not fit single Gaussians to the weak lines from CH_2CHCN and $\text{CH}_3\text{CH}_2\text{OH}$ but used the XCLASS software to fit them all together to resolve blending problems. That this works very well can be seen in particular in the upper panel of Fig. 6.7 where the blended spectral features of CH_3OCH_3 , $\text{CH}_3\text{CH}_2\text{OH}$, CH_2CHCN , and HC_3N are fitted.

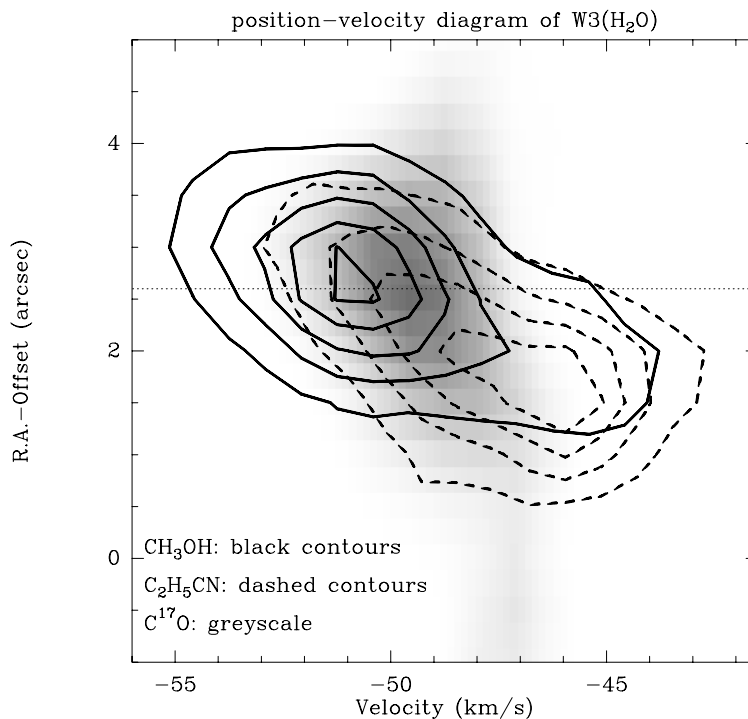


Fig. 6.9.— Position-velocity diagram of CH₃OH, CH₃CH₂CN, and C¹⁷O towards the hot core W3(H₂O). The position of the 1.3 mm continuum peak is marked with a dotted line.

6.5.2. Analysis

The observed lines can be used to estimate molecular abundances. We already discussed in Chapter 5 how estimates for molecular abundances can be derived. In the optical thin limit, the column density in the upper level of a transition is proportional to its observed integrated line intensity. But to derive the total column density of a species one has to know the temperature. We can only determine for HC₃N, CH₃OH, and CH₃OCH₃ temperatures from the interferometric observations since for these species two or more lines with different excitations have been observed. In the other cases, we use the temperatures of our 30-m results (CH₃CH₂CN, HCOOCH₃) and of the results of the 345 GHz line survey of Helmich & van Dishoeck (1997). The advantage of the interferometer observations is that one can get reliable estimates of the source sizes: the angular sizes of the emitting regions seen in Fig. 6.8 are 1".2 towards the hot core and 1".7 towards the HII region (deconvolved). C¹⁷O, SO, OCS, and vibrationally excited ground state HC₃N are found to be more extended with an average size of 3".3. The determination of the column densities has been done using the XCLASS software (see Chapter 5 for a description of the fit routine by P. Schilke).

In the following, we will discuss the results for some molecules in more detail:

At 3 mm, we detected rotational HC₃N(12–11) transitions from both the vibrationally

Table 6.1: Line parameters of observed (strong) lines towards the nitrogen and oxygen peak of the hot core, and towards the methanol peak of W3(OH). For non-detection the 1σ RMS is given.

Molecule	Transition	ν (MHz)	W3(H ₂ O) O-peak			W3(H ₂ O) N-peak			W3(OH) O-peak		
			T_{MB} (K)	v_{LSR} (km s ⁻¹)	Δv	T_{MB} (K)	v_{LSR} (km s ⁻¹)	Δv	T_{MB} (K)	v_{LSR} (km s ⁻¹)	Δv
HC ₃ N v_7	25–24	227977.3	4.1	-48.4	6.5 ^a	5.5	-47.1	6.5 ^a	0.6		
CH ₃ OH	16 _{9,8} – 15 _{9,7}	227814.5	15.6	-50.6	5.8	9.6	-48.8	8.3	24.0	-45.7	3.3
CH ₃ CH ₂ CN	25 _{3,22} – 24 _{3,21}	227781.0	4.0	-48.8	6.8	5.4	-47.2	6.6	0.6		
CH ₃ OCH ₃	24 _{3,22} – 24 _{2,23}	227657.0	3.2	-49.8	6.5 ^a	^b			1.3	-45.0	3.5 ^a
CH ₃ OCH ₃	26 _{5,21} – 26 _{4,22}	227648.0	2.2	-51.2	6.5 ^a	^b			0.9	-46.7	3.5 ^a
C ¹⁷ O	2–1	224714.4	10.7	-49.5	4.2	9.2	-48.9	4.0	0.4		
CH ₃ OH	20 _{9,11} – 19 _{8,11}	224699.4	10.5	-50.3	5.3	6.5	-49.4	6.5	11.2	-45.4	3.0
CH ₃ CH ₂ CN	25 _{4,22} – 24 _{4,21}	224638.7	4.5	-47.9	6.7 ^a	5.1	-46.9	6.7 ^a	0.3		
HCOOCH ₃ -E	18 _{6,12} – 17 _{6,11}	224609.3	5.9	-49.5	8.1	4.5	-47.2	11.2	4.8	-44.4	6.4
HCOOCH ₃ -A	18 _{6,12} – 17 _{6,11}	224582.5	6.0	-50.1	8.7	4.5	-49.1	10.7	5.0	-45.2	4.7
CH ₃ OCH ₃	15 _{2,14} – 14 _{3,11}	112374.3	1.2	-51.2	8.6	1.0	-50.9	9.0	1.0	-48.4	4.0
C ¹⁷ O	1–0	112359.0	2.6	-49.4	5.4	2.5	-49.2	5.5	0.3		
OCS	9–8	109463.1	8.5	-48.4	10.5	8.4	-47.9	10.7	4.1	-44.7	11.7
HC ₃ N v_7	12–11	109441.9	1.1	-47.1	11 ^a	1.1	-47.2	11 ^a	0.3		
SO	3 ₂ – 2 ₁	109252.2	10.1	-47.6	9.0	10.3	-47.3	8.8	4.0	-44.9	11.8
HC ₃ N	12–11	109173.6	5.5	-47.2	12.8	5.9	-46.8	12.4	2.1	-44.8	13.2
CH ₃ OH	16 ₋₂ – 16 _{1E}	109153.2	2.5	-49.2	11 ^a	2.3	-48.9	11 ^a	1.1	-42.3	11 ^a

^a fixed linewidth

^b lines not separable

ground and the lowest bending mode $v_7 = 1$. In Fig. 6.10, HC₃N in the ground state is seen as extended emission towards both the hot core and the UC HII, but the excited bending mode, which lies about 300 K above ground, is seen only towards the hot core. This mode can be excited in the infrared through radiation from dust (45 μm) and the vibration temperature can be used to estimate the temperature of the dust radiation field (see Chapter 4). The ratio of the peak temperatures of ground and vibrational excited lines determines a vibrational temperature:

$$\frac{I_{\text{vib}}}{I_{\text{grd}}} = \exp\left(\frac{-320 \text{ K}}{T_{\text{vib}}}\right) \quad (6.5)$$

It is $T_{\text{vib}} = 180 \pm 50$ K, consistent within the errors with the single dish data from Helmich et al. (1994) for the gas. A contribution of more extended cooler gas would lower this result and high optical depth in the ground state line would lead to a higher estimate. It indicates that gas and dust temperature are about the same and justifies this assumption for deriving the dust mass. At 227 GHz, another $v_7 = 1$ line is detected. But the XCLASS fit with $T_{\text{vib}} = 180$ K overestimates the intensity of a $v_6 = 1$ line at 227791.6 GHz. To pump this line 20 μm photons are required and the radiation field at this wavelength might therefore

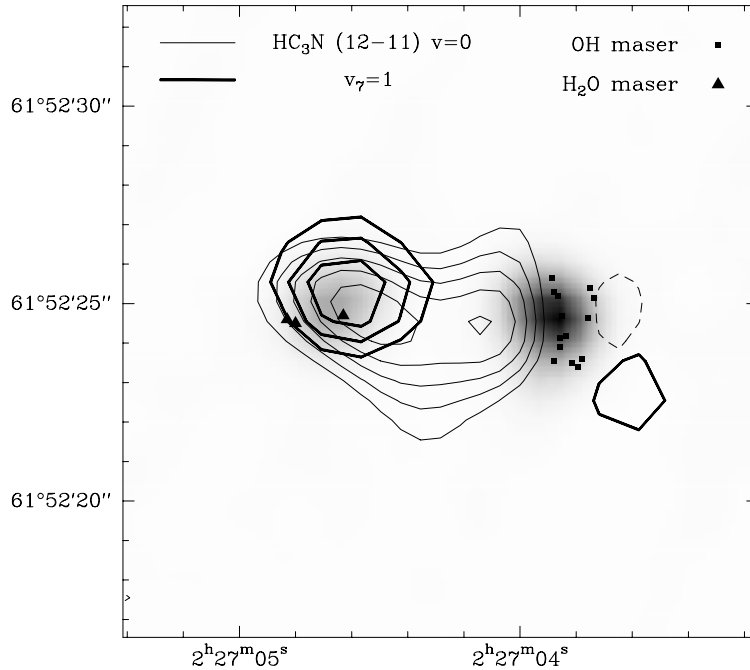


Fig. 6.10.— HC_3N (12–11) in W3(OH) in ground (thin contours) and lowest lying vibrationally excited state (thick) superposed on the 1.3 mm continuum.

be too weak to pump the $v_6 = 1$ line.

At 1.3 mm, two methanol lines were detected with lower level energies of about 300 and 500 K (Fig. 6.11). Hence, they can be used to estimate the rotational temperature of methanol. Here we show the observations towards the hot core peaks and the UC HII. Fitting all lines together, the temperature is consistent with the estimate by Helmich et al. (1994). But with the interferometer we can fit the hot core and the UC HII separately and it turns out that the temperature towards the hot core is significantly higher (hot core: $T_{\text{rot}} = 290 \pm 65$ K, UC HII: $T_{\text{rot}} = 185 \pm 25$ K). The location of the methanol emission towards the north-west of the HII region coincides with the location of the methanol absorption observed with the VLA by Wilson et al. (1991). Hence, we can compare our T_{rot} estimate with previous results: Wilson et al. (1991) found $T \sim 100\text{--}160$ K and the OH observations of Wilson et al. (1990) and Baudry et al. (1981) results in 160 ± 30 K. This also suggests that the absorption and emission originates from the same gas.

The C^{17}O observations are used to determine the H_2 column density with which we can now derive methanol abundances: in the hot core it is 1×10^{-6} , about twice the abundance reported in the Orion Compact Ridge (Sutton et al. 1994), but towards the UC HII we could only derive a lower limit of 3×10^{-6} which is as high as in some outflow sources (Bachiller et al. 1995).

Table 6.2, gives an overview of the observed column densities and abundances towards the hot core positions and the HII region. The column densities might be compared with

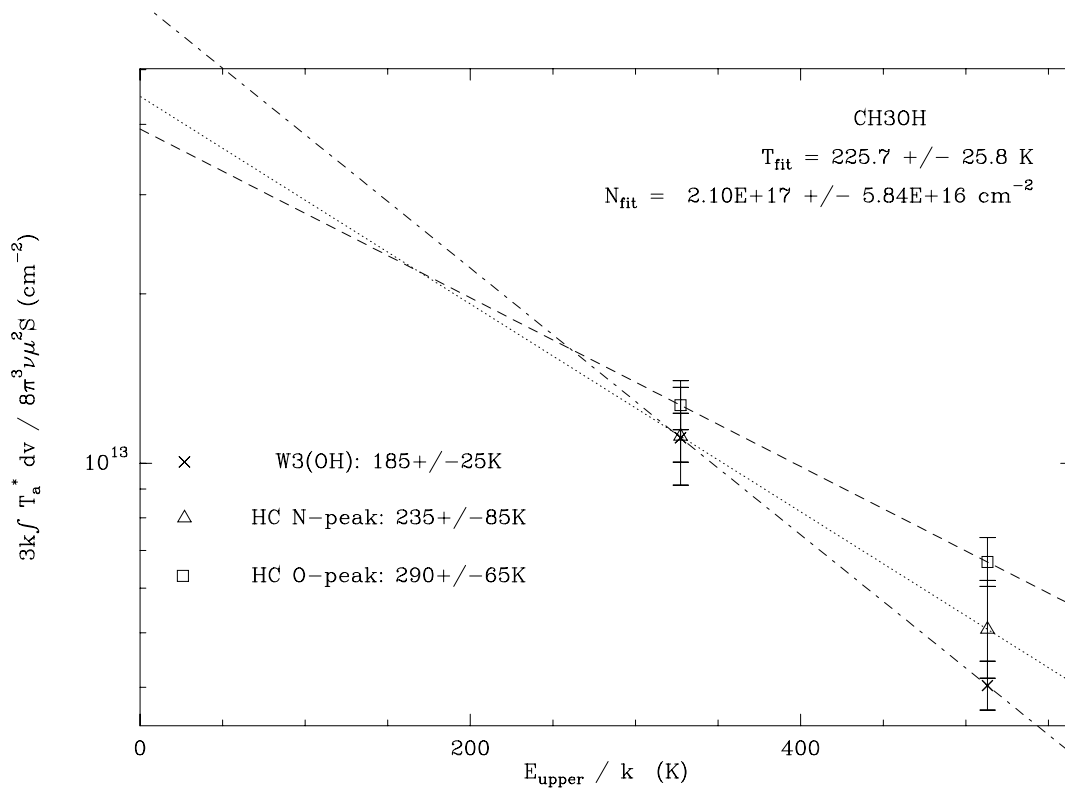


Fig. 6.11.— Boltzmann plot for CH₃OH in W3(OH) showing different excitations in hot core and UC HII.

the results from Helmich & van Dishoeck (1997) using the CSO with a beamsize of 15'': we convert their beam average column densities to source average column densities using our observed source sizes. In the larger CSO beam, there is clearly more C¹⁷O emission compared to our observations which were insensitive to structure larger than 6''.5. The interferometer acts like a filter for the small scale structure towards the hot core and the HII region and is therefore more appropriate to estimate their physical parameters. The results for OCS, CH₃OH, and CH₃OCH₃ compare very well with the CSO results. We found a much lower SO column density but our observations are probably affected by high optical depth in the SO line in contrast to Helmich & van Dishoeck who used optically thin isotopomers to estimate $N(\text{SO})$. HCOOCH₃ is also deviant, in temperature and column density. Assuming the temperature estimate from Helmich & van Dishoeck of 140 K, our column density result is only lowered by 20%. The cause of the discrepancy is unclear.

The derived abundances are compared with the results of the 345 GHz line survey of Sutton et al. (1994): we compared our oxygen peaks with the Compact Ridge results and the nitrogen peak with the Orion Hot Core results. The correspondence of the chemistry in the W3(H₂O) hot core with the Orion Hot Core is very good (using for SO the more reliable result of Helmich & van Dishoeck) and suggest very similar chemical histories for both objects. The W3(H₂O) oxygen peak, however, shows in comparison with the Orion

Table 6.2: Obtained W3(OH) physical parameters in comparison with Orion Hot Core (HC) and Compact Ridge (CR) abundances ($X(\text{Ori})$ taken from Sutton et al. 1994) and column densities estimated by Helmich & van Dishoeck (1997: $N(\text{CSO})$, source averaged). The positions are the nitrogen and oxygen peaks towards the hot core (hc-N/O), and the methanol peak towards the ultracompact HII region (HII-O).

Molecule	Position	Size ($''$)	T (K)	N (cm^{-2})	$N(\text{CSO})$ (cm^{-2})	X	$X(\text{Ori})$
C^{17}O	hc-N/O	3.3	100^a	1.7(16)	2.0(17)	5(-8)	
	HII-O			<3(15)			
SO	hc-N	3.3	100^a	4.9(15)	2.6(16)	1.5(-8)	2(-7) ^{HC}
OCS	hc-N	3.3	100^a	4.8(15)	4.6(15)	1.5(-8)	1(-8) ^{HC}
HC_3N	hc-N	1.2	180^b	1.0(15)	2(15)	3(-9)	2(-9) ^{HC}
$\text{CH}_3\text{CH}_2\text{CN}$	hc-N	1.2	160^c	1.8(15)		5(-9)	3(-9) ^{HC}
CH_2CHCN	hc-N	1.2	160^e	2.8(14)		8(-10)	1.5(-9) ^{HC}
	hc-O	1.2	290^d	3.3(17)	4.6(17)	1.0(-6)	4(-7) ^{CR}
CH_3OH	HII-O	1.7	185^d	2.0(17)		>3(-6)	
	hc-O	1.2	80^d	7.0(16)	1.0(17)	2(-7)	2(-8) ^{CR}
CH_3OCH_3	HII-O	1.7	100^d	9.3(15)		>1.5(-7)	
	hc-O	1.2	185^c	6.9(16)	3.5(16)	2(-7)	3(-8) ^{CR}
HCOOCH_3	HII-O	1.7	185^c	2.6(16)		>4(-7)	
	hc-O	1.2	200^e	5(15)		1.5(-8)	1.5(-9)

^a estimated by Helmich & van Dishoeck (1997) for C^{17}O .

^b comparison of peak values ground and vib.

^c 30-m result from Chapter 5

^d rotational temperature

^e best guess

Compact Ridge, much higher abundances of the oxygen bearing molecules. This might be due to the different physical conditions of the objects: in contrast to the compact ridge, the W3(H_2O) oxygen peak is associated with strong millimeter emission from hot dust and a much higher temperature is likely (~ 200 K in comparison to about 100 K in the Compact Ridge).

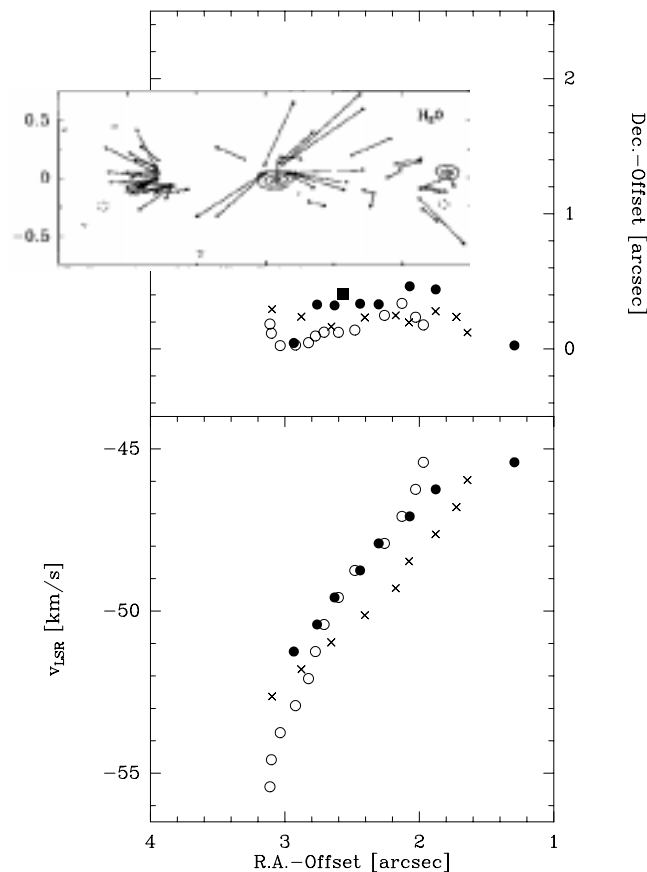


Fig. 6.12.— Peak positions measured in different channels for $\text{C}^{17}\text{O}(2-1)$ (filled circles), $\text{A-CH}_3\text{OH } 16_{9,8} - 15_{9,7}$ (empty circles), and $\text{CH}_3\text{CH}_2\text{CN } 25_{3,22} - 24_{3,21}$ (crosses) towards $\text{W3(H}_2\text{O)}$ with a synthesized beam size of $1''.6 \times 1''.4$. The 225 GHz continuum position is denoted by a filled square. The inset on the left panel shows the water maser proper motion vectors from Alcolea et al. (1992) together with the 15 GHz map of Reid et al. (1995).

6.6. The relation between thermal and masering gas

We detected in the upper sideband the $16_{9,8} - 15_{9,7}$ transition of methanol at 227814.50 MHz (Anderson et al. 1992) and the $25_{3,22} - 24_{3,21}$ transition of ethyl cyanide at 227780.968 MHz. These two transitions have lower level excitation energies of 316 and 140 K respectively and are thus expected to be emitted in dense hot environments. It is thus not surprising that regions emitting in these lines are compact ($\sim 1''$ deconvolved) and coincide with the water maser source. In Fig. 6.12, we show the positions of maximum emission in C^{17}O , $\text{CH}_3\text{CH}_2\text{CN}$, and in CH_3OH derived from channel maps in all three lines.

The interesting point which emerges from Fig. 6.12 is that the peak positions from channel maps towards the water maser source are distributed in a structure which is elongated E–W. Similar behavior was seen in methyl cyanide by Wink et al. (1994, their

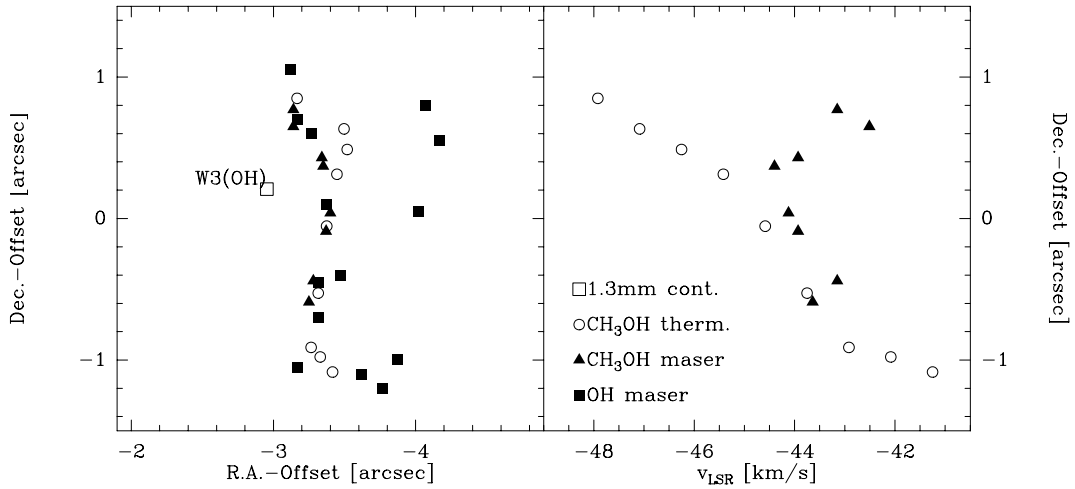


Fig. 6.13.— Peak positions measured in different channels for $\text{CH}_3\text{OH-A } 16_{9,8} - 15_{9,7}$ (empty circles) towards the ultracompact HII region W3(OH) in comparison with the positions of OH and CH_3OH masers.

Fig. 9). The shape and size of this structure are similar to the orientation and spatial extent of the water masers mapped by Alcolea et al. (1992) in a VLBI proper motions study. The latter are thought to be in a bipolar flow with an expansion velocity of 20 km s^{-1} . The fact that all of these different tracers have the same orientation suggests that the high excitation molecules trace the sides of the cavity carved out by the outflow. Moreover, the fact that $\text{C}^{17}\text{O}(2-1)$ (a low excitation transition) has a similar spatial distribution suggests that on arc second size scales the bulk of the mass is in the high temperature gas traced by $\text{CH}_3\text{CH}_2\text{CN}$ and CH_3OH . Towards this structure, red-shifted velocities are to the west and blue-shifted to the east. However, the water maser data show no very clear blue-red E-W asymmetry. Another scenario is that the hot core gas seen in CH_3OH and $\text{CH}_3\text{CH}_2\text{CN}$ is in a disk seen edge-on and that the wind is interacting with the surface of this disk and thus giving rise to the water masers. Also a double source cannot be excluded, where the components are associated with the two cm continuum sources seen by Reid et al. (1995) and have different velocities. In case of an outflow as the cause of the velocity gradient, the flow lifetime would be 1000 y. Using the Virial theorem, a dynamical mass of $30 M_\odot$ can be assigned to the observed velocity structure:

$$\frac{M_{dym}}{M_\odot} = 230 \frac{R}{\text{pc}} \left[\frac{v}{\text{km/s}} \right]^2 \quad (6.6)$$

Hence, also a disk with a central mass of about $20 M_\odot$ cannot be ruled out.

Towards the UC HII we can only analyze methanol (Fig. 6.13). But here a comparison with methanol masers is very interesting. The triangles show the positions of the methanol masers observed by Menten et al. 1988) and the crosses mark the positions of OH masers as observed by Reid et al. There is an excellent positional agreement between the methanol

thermal and maser emission at the eastern edge of OH emission within $0''.2$. But in the velocity domain both split up at about $v = -45$ km/s. The masers originate in the foreground gas and amplify the continuum from the HII region. At velocities greater -45 km/s we see then thermal methanol emission from behind the HII region. The good correspondence between thermal and maser emission allows to characterize the physical conditions for the maser emission with the results for the thermal emission, namely a temperature of 185 K and a lower limit for the methanol abundance of $3 \cdot 10^{-6}$.

6.7. Conclusions

This study has allowed us to determine that dust with an opacity index of 1.6 is responsible for the continuum at mm wavelength towards W3(H₂O) and to compare mass estimates of different types for the molecular hot core W3(H₂O). Using estimates both from the millimeter dust emission and from optically thin C¹⁷O, we conclude that the mass of the hot (100-200 K) gas within 1000 AU of the young star responsible for the observed activity is in the order of $10 M_{\odot}$. This is comparable to the probable mass of the young embedded star.

Between the hot core and the ultracompact HII region chemical differences are found, and there is even evidence for chemical gradients on subarcsec scale towards the water maser source leading to an offset of $\sim 0''.5$ between the peaks of nitrogen and oxygen bearing molecules. The analysis of the molecular abundances suggest a chemical state of the nitrogen peak comparable to the Orion Hot Core. In comparison to the Orion Compact Ridge, the oxygen bearing molecules are enhanced by an order of magnitude.

Our data show that the E–W orientation of the channel map peaks and the velocity gradient seen by Wink et al. is a general characteristic of the hot core gas which is either related to the bipolar outflow inferred by water maser proper motions, with a rotating disk or a double source. Only higher resolution can resolve this issue. In general, towards both sources the orientation and spatial extend of masers coincide with the thermal emission.

REFERENCES

- Alcolea J., Menten K.M., Moran J.M., Reid M.J. 1992, in *Astrophysical Masers*, ed. A.W.Clegg and G.E.Nedoluha, publ. Springer (Heidelberg)
- Anderson T., Herbst E., De Lucia F. 1992, ApJS, 82, 405
- Bachiller R., Liechti R., Walmsley C.M., Colomer F. 1995, A&A 295, L51
- Baudry A., Walmsley C.M., Winnberg A., Wilson T.L. 1981, A&A 102, 287
- Baudry A., Menten K.M., Walmsley C.M., Wilson T.L. 1993, A&A 271, 552
- Churchwell E. 1991, in *the Physics of Star Formation and early Stellar Evolution*, NATO

- Asi, eds. C.J. Lada and N. Kylafis
Dreher J.W., Welch W.J. 1981 ApJ 245, 857
Frerking M.A., Langer W.D., Wilson R.W. 1982, ApJ 262, 590
Genzel R. 1992, in "The galactic Interstellar Medium", p275, (Burton W.B., Elmegreen B.G., Genzel R.), Springer
Guilloteau S., Stier M.T., Downes D. 1983, A&A 126, 10
Guilloteau S., Baudry A., Walmsley C.M. 1985, A&A 153, 179
Guilloteau S. et al. 1992 A&A 262, 624
Helmich F.P., Jansen D.J., de Graauw T., Groesbeck T.D., van Dishoeck E.F. 1994 A&A, 283, 626
Helmich F.P., van Dishoeck E.F. 1997, A&AS 124, 205
Hildebrand R.H. 1983, Nature 83, 24436
Hofner P., Wyrowski F., Walmsley C.M., Churchwell E., in prep.
Humphreys R.H. 1978, ApJS 38, 309
Lada C.J., Elmegreen B.G., Cong H.-I., Thaddeus P. 1978, ApJ 226, L39
Matteucci F. 1991, in *Chemistry in Space*, eds. Greenberg J.M. & Pirronello V., Kluwer
Menten K.M., Reid M.J., Moran J.M., Wilson T.L., Johnston K.J., Batrla W. 1988, ApJ 333, L83
Normandeau M., Taylor A.R., Dewdney P.E. 1996, Nature 380, 687
Panagia N. 1973, AJ 78, 929
Reid M.J., et al. 1980, ApJ 239, 89
Reid M.J., Argon A.L., Masson C.R., Menten K.M., Moran J.M. 1995, ApJ 443, 238
Sutton E., Peng R., Danchi W.C., Jaminet P.A., Sandell G., Russel A. 1994, ApJS 97, 455
Turner J.L., Welch W.J. 1984, ApJ 287, L81
Walmsley C.M., Schilke P. 1992, in *Dust and Chemistry in Astronomy*, eds. Millar T.J., Williams D.A., IOP Publ.
Wilner D.J., Welch W.J., Forster J.R. 1995, ApJ 449, L73
Wilson T.L., Walmsley C.M., Baudry A. 1990, A&A 231, 159
Wilson T.L., Johnston K.L., Mauersberger R. 1991, A&A 251, 220
Wink J.E., Duvert G., Guilloteau S., Güsten R., Walmsley C.M., Wilson T.L. 1994, A&A 281, 505
Woody et al. 1989, ApJ 337, L41
Wright M.; Sandell G.; Wilner D.J.; Plambeck R. L. 1992, ApJ 393, 225
Wynn-Williams C.G., Becklin E.E., Neugebauer G. 1972, MNRAS 160, 1

Part II

Photon dominated regions

Chapter 7

The carbon recombination line in selected star forming regions

7.1. Introduction

There are many recent studies of photon dominated regions (PDRs) in a variety of far infrared fine structure lines and in particular in the [C II] 158 μm transition (e.g. Jaffe et al. 1994; Hermann et al. 1997). Rather less information is available about the carbon radio recombination lines, which historically were one of the first indications of the presence of partially ionized gas in transition regions between ionized and molecular material. This prompted Natta et al. (1994) to investigate the combination of ionized carbon 158 μm and radio recombination lines in the framework of existing theoretical models of PDRs (Tielens & Hollenbach 1985). However, the observational side of their study was restricted to selected positions towards the Orion HII region/molecular cloud.

Here we describe observations of the carbon recombination line in several nearby nebulae recently studied in FIR fine structure lines, where radiation from massive stars is interacting with molecular material, and apply the techniques of Natta et al. to infer informations about the physical conditions in the PDRs. More detailed theoretical and observational studies of the star forming regions NGC 2023 and Orion A are presented in Chapter 8 and 9.

7.2. History and theory

The discovery of radio recombination lines, predicted by Kardashev (1959) to be observable towards HII regions, has played an important role in the development of our knowledge of high mass star formation in the Galaxy. Firstly observed by Dravskikh & Dravskikh (1964) and Höglund & Mezger (1965), they offer as spectral lines the

possibility to trace galactic structure, and as radio lines, unaffected by dust extinction, the opportunity to probe also the ionized parts of regions of recent star formation which are still deeply embedded in their parental molecular clouds. Comprehensive discussions of radio recombination lines are given in Dupree & Goldberg (1970) and Rohlfs & Wilson (1996).

In ionized gas, the recombination of ions with electrons leads to a cascade of the electron through many excited states down to the ground state, emitting a series of observable recombination lines. Transitions between highly excited states lead to recombination lines in the radio range, where the orbits of the recombining electrons are large compared to the size of the ions, and the frequencies are given by the usual Rydberg formula:

$$\nu_{mn} = cZ_{\text{eff}}^2 R_M \left(\frac{1}{n^2} - \frac{1}{m^2} \right) \quad (7.1)$$

$$R_M = \frac{R_\infty}{1 + m_e/M} \quad (7.2)$$

Here Z_{eff} denotes the effective charge of the nucleus which is for our purposes in the radio range equal to one. A transition is characterized by its upper and lower levels m and n , respectively, and transitions are denoted according to $m - n = 1, 2, \dots$ as $n\alpha, n\beta, \dots$ transitions. m_e is the mass of the electron and R_M is the Rydberg constant, corrected for the reduced mass of the system, so that different nuclear masses M lead to slight shifts of the line frequencies with respect to the hydrogen line. This led first to the discovery of the helium line by Lilley et al. (1966) and shortly thereafter to the discovery of the so-called ‘‘anomalous’’ line by Palmer et al. (1967) which turned out to be due to carbon (see discussion in the next paragraph).

An instructive example of a radio recombination line spectrum is given in Fig. 7.1 (for details about the observations see Chapter 9). The spectrum is dominated by the strong hydrogen recombination line and the velocity scale is referred to this line. Below the spectrum, we marked the computed recombination line frequencies according to different nuclear masses so that the hydrogen and helium lines can be readily identified. Both are broad lines with the same velocity and therefore likely originate from the same regions. Considering atomic abundances, the next lines showing up in the spectrum should be lines from carbon, nitrogen or oxygen, but only a narrow line situated between $m_\Lambda=4$ and 12 is visible with relatively strong intensity. Originating from an HII region, one would expect an intensity at best proportional to the abundance of these species or less than 10^{-3} of the hydrogen intensity. In order to identify this anomalous line, we first have to discuss the intensities of recombination lines: an expression for the integral line intensity is given by Natta et al. (1994), which is for lines with different n

$$T_L \Delta v = 1.95 T^{-1.5} b_n (1 - \beta_n T_C/T) \text{EM} \exp(X_n) \frac{c}{\nu_n}. \quad (7.3)$$

The line intensity $T_L \Delta v$ is given in K km s^{-1} , T in Kelvin, c in km s^{-1} , and ν in MHz. b_n and β_n denote the deviation of the level population from a Boltzmann distribution and

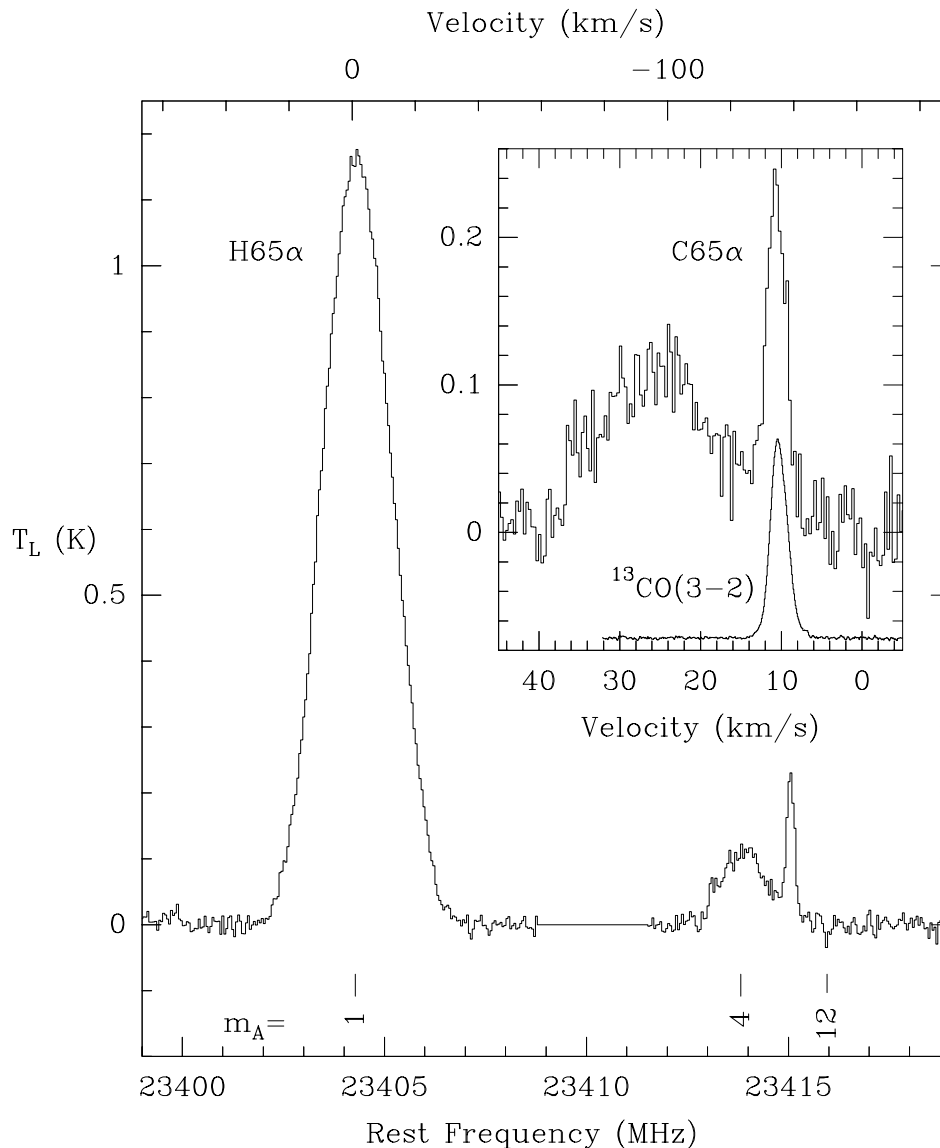


Fig. 7.1.— A spectrum of radio recombination lines at 23 GHz towards the Orion Bar showing the hydrogen, helium and carbon line. Predictions of the line frequencies according to Eq. 7.1 are marked with the masses of the nuclei. The velocity scale is referred to the hydrogen line. The insert in the upper right shows a blow-up of the helium/carbon feature, with velocity reference to the carbon line. For comparison, the $^{13}CO(3-2)$ line, observed by Lis et al. (1997), averaged over the same region, is inserted (peak intensity 24 K). For details about the recombination line observations refer to Chapter 9.

we will use in the following the departure coefficients calculated by Salem & Brocklehurst (1979) for hydrogenic ions. The factor β_n accounts for stimulated emission proportional to a background continuum source T_C . The emission measure EM is $\int ds n_e n_i$ in units of pc cm^{-6} , and $\exp(X_n)$ comes from the Saha equation with $X_n = 157800/n^2/T$. Due to the dependence of the line intensity on a negative power of the temperature, one expects strong lines from ions in cool media with still high emission measures. This is true for carbon in the interface zones between HII regions and molecular clouds, since its ionization potential of 11.3 eV is lower than the 13.6 eV needed to ionize hydrogen and therefore FUV radiation can penetrate into the clouds and ionize carbon but not oxygen (13.62 eV) or nitrogen (14.53 eV). The discrepancy between calculated frequency of the carbon line and its actual position is simply explained by different velocities of the gas in the HII region ($\approx 0 \text{ km s}^{-1}$) and the ionized carbon. And indeed, the comparison of velocities and line widths of molecular gas and ionized carbon in the insert in Fig. 7.1 shows convincingly the association of carbon with the molecular cloud ($\approx 10 \text{ km s}^{-1}$).

7.3. Ionized carbon in models of PDRs

In this chapter and as well in Chapter 8 we are going to use the technique set forth by Natta et al. (1994) to derive physical parameters of the observed PDRs from a combination of carbon recombination and fine structure lines. Therefore we will briefly review their procedure.

We have already discussed a formula for the line intensity of recombination lines in the last section and concentrate now on the far infrared carbon line. Their intensity can be calculated with

$$I(158\mu\text{m}) = \frac{h\nu A_{ul}}{4\pi} \int ds \beta(s) f_u(s) n_{\text{CII}}(s) \quad (7.4)$$

where the integral is taken over the line-of-sight s , β is the escape probability out of a semi-infinite plane-parallel cloud (Tielens & Hollenbach 1985), f_u is the fraction of carbon ions in the upper level of the fine structure doublet (see for example Genzel 1992), and n_{CII} is the ionized carbon density. The escape probability approach is necessary since the optical depth of the fine structure line is typically of order unity.

Natta et al. (1994) used for their analysis two input models, both homogeneous: isothermal models with the parameter n and T , and the one-dimensional, semi-infinite PDR models of Tielens & Hollenbach (1985) with n and incident FUV flux G_0 as independent parameters. In the latter, the temperature and C^+ concentration structure is determined by solving the equation of energy balance and chemical equilibrium in the model cloud. The carbon abundance used is the value measured towards the Orion Nebula ($3 \cdot 10^{-4}$). The recombination and fine structure line intensities are then obtained by integration along the line-of-sight assuming a face-on view of the PDR. Edge-on models and clumpy models will be discussed in Chapter 8 for the case of the NGC 2023 PDR.

Table 7.1: Sources observed in the C91 α carbon recombination line.

Source	$\alpha(1950)$ h m s	$\delta(1950)$ ° ' "
IC 63	00 55 58.0	60 37 07
RMC (IR6306)	06 30 37.0	04 37 16
S 106	20 25 33.7	37 12 50
NGC 7023	21 01 00.0	67 57 54
DR 21	20 37 14.0	42 08 52
DR 21 (OH)	20 37 13.8	42 11 55
S 140	22 17 41.1	63 03 42

7.4. Observations

The observations were made with the 100-m telescope at Effelsberg in July and August 1996, except S 140 which was observed together with NGC 2023 in 1994 (see Chapter 8). A list of the observed sources is given in Table 7.1. The frequency of the observed C91 α lines is 8589.104 MHz resulting in a beamsize of 82". Pointing was checked through observation on NGC 7027, W3(OH), and 3C161. The observations on NGC 7027 were used to establish the absolute temperature scale assuming a continuum flux of 6.25 Jy and a telescope sensitivity of 2.7 K/Jy. The scatter in different calibration observations of NGC 7027 is smaller than 20%. DR 21 was observed in position switching mode and all other sources in frequency switching mode. The spectrometer was an autocorrelator yielding a spectral resolution of 0.2 km s⁻¹ in case of NGC 7023 and 0.4 km s⁻¹ for the other sources. The average integration time on a source has been 7 hours.

7.5. Results and discussion

We give in Table 7.2 the results of Gaussian fits to the observed spectra shown in Fig. 7.2. In case of non-detections we give the 1 σ level of the noise in the observed spectra. In the following, we are going to discuss the results source by source together with their interpretation in comparison to model results (Section 7.3).

7.5.1. S 140

S 140 is a small, bright HII region on the south–west border of the molecular cloud L 1204. It is excited by the B0 star HD 211880 located to the south–west of the ionized rim. To the north–east (about 1' or 0.3 pc offset at a distance of 900 pc) is a small group of embedded infrared sources which form a strong FIR source with a luminosity of $2 \cdot 10^4 L_{\odot}$ (Harvey et al. 1978). S 140 has also been the subject of intensive study in molecular lines

Table 7.2: C91 α line parameters. For non-detection the 1σ noise level in the spectrum is given.

Source	Offsets (arcsec)	$\int T_{\text{MB}} dv$ (K km s $^{-1}$)	T_{MB} (K)	v_{LSR} (km s $^{-1}$)	FWHM (km s $^{-1}$)	$I([\text{C II}] 158 \mu\text{m})$ 10^{-4} erg/cm 2 /sec/sr
IC 63			0.01			1.3 ^a
RMC (IR6309)			0.01			4 ^b
S 106	(0, 0)	0.69	0.07	-4.0	8.9	8 ^c
S 106	(30, -30)	0.40	0.04	-3.5	9.8	
NGC 7023	(-20, 30)	0.11	0.12	2.3	0.88	8.5 ^d
NGC 7023	(0, 0)	0.05	0.07	2.6	0.8	
DR 21		0.76	0.07	-5.1	10	22.4 ^e
DR 21 (OH)			0.01			
S 140	(0, 0)	0.17	0.05	-7.4	3.2	3.2 ^b
S 140	(-60, -60)	0.14	0.03	-7.2	5	

^a Jansen et al. (1996)

^b Schneider et al. (1995)

^c Schneider priv. comm.

^d Chokshi et al. (1988)

^e Lane et al. (1990)

(Blair et al. 1978; Ungerechts et al. 1986; Zhou et al. 1993; Zhou et al. 1994) and atomic fine structure transitions (Keene et al. 1985; Boreiko et al. 1990; Hernichel et al. 1992). C166 α and C141 α emission was found by Knapp et al. (1976) towards the infrared source with angular resolutions of 22.5' and 21' respectively. Recently, Smirnov et al. (1995) have measured C166 α at three positions with 9' resolution but to our knowledge there has not been work done at higher frequencies. Schneider et al. (1995) have recently mapped the [C II] 158 μm line towards S 140 at 55'' angular resolution and this prompted us to observe C91 α towards this source.

Towards S 140, our observations were confined to two positions. The two positions measured in S 140 were towards the embedded IR sources (offset (0, 0)) and towards the ionization front (offset (-60'', -60'')). We have clearly detected C91 α emission both towards the infrared stars as well as towards the ionization front. This is of interest as previous carbon line detections in these regions were made with relatively large beams (e.g. Smirnov et al. 1995). Using the [C II] 158 μm intensity towards S 140 observed by Schneider et al. (1995) together with our radio measurements, we derive from the models in Fig. 7.3 a density of about $5 \cdot 10^4$ cm $^{-3}$ and an incident FUV field of $G_0 \approx 100 - 200$. The FUV field towards IRS 1 is slightly higher than towards the ionization front. If the B0 star HD 211880 were to be the only source of FUV flux, G_0 would decrease from 150 at the ionization front

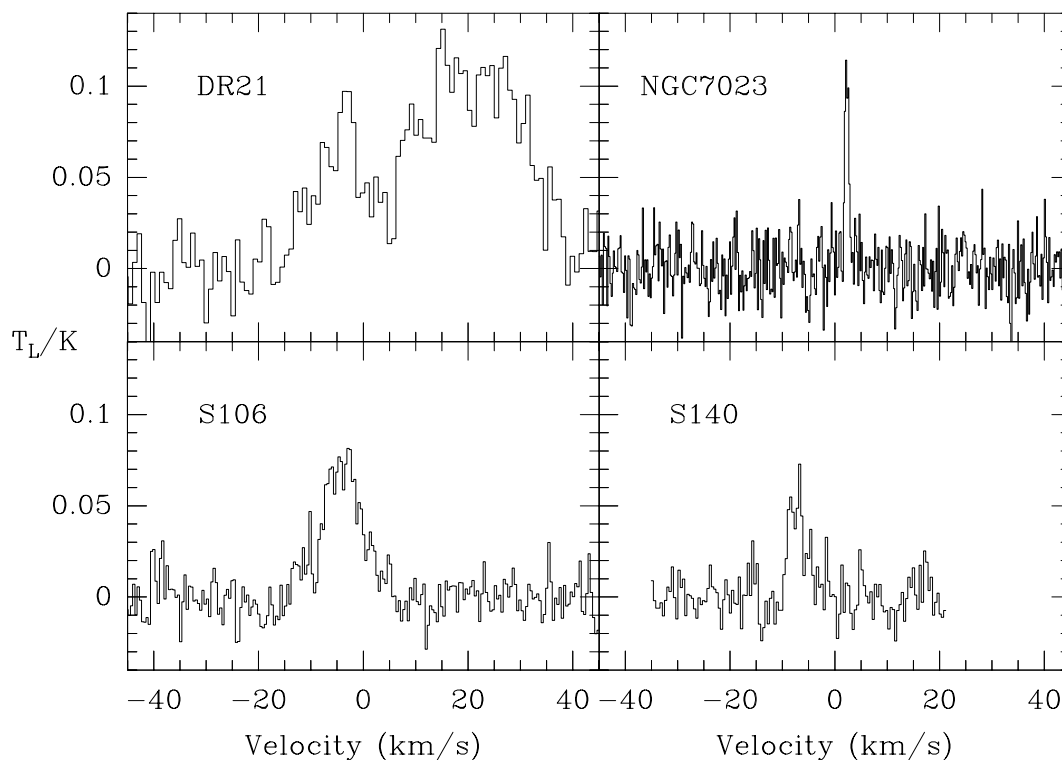


Fig. 7.2.— Carbon C91 α recombination lines towards several PDRs. The broad feature in the DR21 spectrum at 20 km s⁻¹ is the helium line from the HII region.

(Keene et al. 1985) to 100 at the position of the embedded infrared sources. It is possible however that one of the embedded stars contributes to the FUV flux.

7.5.2. S 106

The bipolar HII region S 106 is embedded in a large molecular cloud which is excited by a luminous O star, S 106 IR, giving rise to an extended PDR. Carbon monoxide and neutral carbon were studied by Little et al. (1995). Very recently, Schneider (priv.comm.) obtained a map of the CII and OI fine structure lines towards this source which we decided to supplement with C91 α observations.

We detected a broad (≈ 10 km s⁻¹) carbon recombination line towards the position of S 106 IR. This might be due to a contribution from an element heavier than carbon, e.g. sulphur which has been already detected towards a number of sources but the signal-to-noise is too bad to be definite. Emission at another peak of atomic carbon at an offset of (30,-30) is consistent with a source which is small compared to the beam centered at the S 106 IR position. Comparison with the models in Fig. 7.3 suggests a density in the PDR upward of 10⁵ cm⁻³.

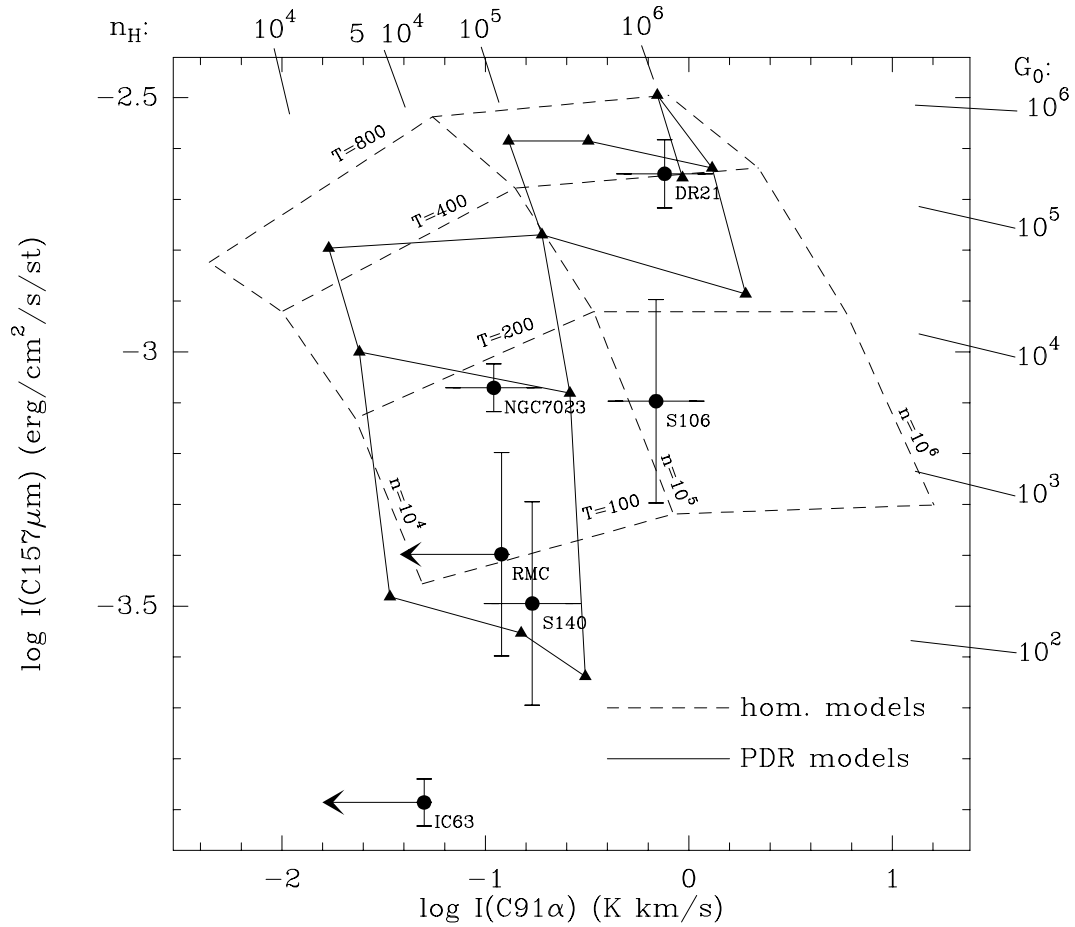


Fig. 7.3.— Plot of our observed C91 α observations versus the corresponding [C II] 158 μm intensities (filled circles with error bars). The predictions of homogeneous models are shown as dashed grid for temperatures of 100, 200, 400 and 800 K, and densities of 10^4 , 10^5 , 10^6 cm^{-3} . Filled triangles give the results of PDR model predictions and their parameters are given on the outside of the box.

7.5.3. NGC 7023

The bright reflection nebula NGC 7023 is a cloud with physical parameters close to those of IC 63. It is illuminated by a B3 star with a radiation field of 2600 times the interstellar UV flux (Chokshi et al. 1988) and the detailed chemical study of Fuente et al. (1993) results in densities between 10^4 and 10^5 cm^{-3} from model calculations which also showed that shocks are not dominant in this cloud. Pankonin and Walmsley (1978) detected already the C158 α recombination line but found only an upper limit of 0.15 K for the C110 α line. Far infrared [CII] 158 μm emission was observed by Chokshi et al. (1988) and was found to peak at the position of the illuminating star.

The carbon recombination line width, which we detected towards the FIR emission peak, is the smallest ever observed and leads therefore to a very stringent upper limit on

the temperature in the PDR: corrected for the instrumental spectral resolution, the line width is 0.85 km s^{-1} corresponding via

$$(\Delta v_{\text{th}}[\text{km/s}])^2 = 0.0458 \frac{T[\text{K}]}{M[\text{amu}]} \quad (7.5)$$

to a temperature of 190 K assuming only thermal broadening. Since there might be also contributions to the line width by turbulence or a systematic velocity field, this linewidth gives only an upper limit on the temperature. This is consistent with the temperature which the isothermal models suggest in this source. From the PDR models (Fig. 7.3) we infer a FUV field of $10^3 G_0$, consistent within the errors with the value given by Chokshi et al. (1988), and a density of $5 \cdot 10^4 \text{ cm}^{-3}$. Emission observed at the position of the illuminating star is consistent with a source small compared to the beam centered on the FIR peak.

7.5.4. DR 21

DR 21 is known to be an active site of star formation at a distance of about 3 kpc. Carbon recombination lines in DR 21 has been studied before by Pankonin et al. (1977) for several n . The highest n line reported is the C91 α line from (Pankonin, unpublished) with low S/N and no line parameters given. Therefore we decided to reobserve this line. The region was studied in far-infrared fine structure lines by Lane et al. (1990). Preliminary results of a new [C II] 158 μm study by Köster (priv. comm.) revealed a second site of intense [C II] 158 μm emission at the position of the OH maser 3' to the north of DR 21 (DR 21(OH)). This detection prompted us to search also at this position for the C91 α line but no emission was found. The detection at central position is well explained by models with densities as high as 10^6 cm^{-3} and a radiation field of several 10^4 up to $10^5 G_0$.

7.5.5. IC 63 and RMC

IC 63 is a prime example of the interaction of a bright early type star with interstellar matter. As such, it provides a good laboratory to test theories on this interaction. Compared to other PDRs that have been well studied in the past (e.g. the Orion Bar, M 17, S 140), IC 63 is relatively simple. There are no shocks present. Also, there are no luminous protostars embedded in this cloud. This makes analysis of the results much easier and provides for a better test of the theories. Recently, the comet-like reflection nebula IC 63 has been observed in many lines of molecular species and in the far infrared line of ionized carbon (Jansen et al. 1994, 1996) The cloud at a distance of 230 pc from the sun, is exposed to several hundred times the mean Galactic UV field by the B0.5p star γ Cas which is at a projected distance of 1.3 pc. The FUV flux is slightly higher than in S 140.

We could only derive an upper limit for the C91 α emission which support the very

low gas-phase carbon abundance of 4×10^{-4} estimated by Jansen et al. (1996). For a discussion of the influence of the assumed values for the carbon abundance on the models see Chapter 8.

The Rosette molecular cloud complex extends south-east of the illuminating OB association NGC 2244. [CII] $158\mu\text{m}$ has been observed by Schneider (1995) who found the strongest emission at the boundary between HII region and molecular cloud where the radiation field is 125 times the interstellar UV flux. A lower limit for the hydrogen density is estimated on basis of $^{13}\text{CO}(2-1)$ observations to be $4 \cdot 10^3 \text{ cm}^{-3}$. Similar to IC 63 the PDR in RMC is seen almost edge-on.

The non-detection of C91 α in this sources can be used to give an upper limit of $5 \cdot 10^4 \text{ cm}^{-3}$ in this source.

7.6. Conclusions

Several PDRs of star forming regions have been observed in the carbon recombination line C91 α , most of them for the first time at least with a beam of $80''$, which is comparable to the beam of FIR observations. The densities found by comparison with PDR models are about $5 \cdot 10^4 \text{ cm}^{-3}$ in case of S 140 and NGC 7023, and clearly upwards of 10^5 cm^{-3} in case of DR 21 and S 106. The exceptional small linewidth of the C91 α line towards NGC 7023 allows us to place an upper limit of 190 K for the temperature in the CII region.

REFERENCES

- Blair G.N., Evans N.J. II, Vanden Bout P.A., Peters W.L. 1978, ApJ 219, 896
 Boreiko R.T., Betz A.L., Zmuidzinas J. 1990, ApJ 353, 181
 Chokshi A., Tielens A.G.G.M., Werner M.W., Castelaz M.W. 1988, ApJ 334, 803
 Dravskikh Z.V., Dravskikh A.F. 1964, Astron. Tsirk., 282, 2
 Dupree A., Goldberg L. 1970, ARAA 8, 231
 Fuente A., Martin-Pintado J., Cernicharo J., Bachiller R. 1993, A&A 276, 473
 Genzel R. 1992, in "The galactic Interstellar Medium", p275, (Burton W.B., Elmegreen B.G., Genzel R.), Springer
 Harvey P. M., Campbell M. F., Hoffmann W. F 1978, ApJ 219, 891
 Herrmann, F., Madden, S. C., Nikola, T., Poglitsch, A., Timmermann, R., Geis, N., Townes, C. H., & Stacey, G. J. 1997, ApJ 481, 343
 Hernichel J., Krause D., Röhrig R., Stutzki J., Winnewisser G. 1992, A&A 259, L77
 Höglund B., Mezger P.G. 1965, Science 150, 339
 Jaffe D.T., Zhou S., Howe J.E., Stacey G.J. 1994 ApJ 436, 203
 Jansen D.J., van Dishoeck E.F., Black J.H 1994, A&A 282, 605

- Jansen D.J., van Dishoeck E.F., Keene J., Boreiko R.T., Betz A.L. 1996, *A&A* 309, 899
- Kardashev N.S. 1959, *Soviet Astr.* 3, 813
- Keene J., Blake G.A., Phillips T.G., Huggins P.J., Beichman C.A. 1985 *ApJ* 299, 967
- Knapp G.R., Brown R.L., Kuiper T.B.H., Kakar R.K. 1976, *ApJ* 204, 781
- Lane A.P., Haas M.R., Hollenbach D.J., Erickson E.F. 1990, *ApJ* 361, 132
- Lilley A.E., Palmer P., Penfield H., Zuckerman B. 1966, *Nature* 211, 174
- Lis, D. C., Keene, J., & Schilke, P. 1997, in prep.
- Little L.T., Kelly M.L., Habing R.J., Millar T.J. 1995, *MNRAS* 277, 307
- Natta A., Walmsley C.M., Tielens A. 1994, *ApJ* 428, 209
- Palmer P., Zuckerman B., Penfield H., Lilley A.E., Mezger P.G. 1967, *Nature* 215, 40
- Pankonin V., Thomasson P., Barsuhn J. 1977, *A&A* 54, 335
- Pankonin V., Walmsley C.M. 1978, *A&A* 67, 129
- Rohlfs K., Wilson T.L. 1996, "Tools of Radio Astronomy", Springer
- Salem M., Brocklehurst M. 1979, *ApJS* 39, 633
- Schneider N. 1995, PhD thesis, University of Cologne
- Schneider N. et al. 1995, "Large Scale Submm-CO and FIR [CII] observations of the Rosette Molecular Complex and S140/L1204", Proceedings of the 2nd Cologne-Zermatt Symposium, Winnewisser G., Pelz G.(Ed.)
- Smirnov G.T., Sorochenko R.L., Walmsley C.M. 1995, *A&A* 300, 923
- Tielens A. , Hollenbach D. 1985, *ApJ* 291, 722
- Ungerechts H., Walmsley C.M., Winnewisser G. 1986, *A&A* 157, 207
- Zhou S., Evans N.J., Mundy L.G., Kutner M.L. 1993, *ApJ* 417, 613
- Zhou S., Butner H.M., Evans N.J. II, Güsten R., Kutner M.L., Mundy L.G. 1995, *ApJ* 428, 219

Chapter 8

A detailed study of the PDR associated with NGC 2023

8.1. Introduction

One of the interesting developments of the past few years has been the increase in our understanding of the structure of the interface regions between HII regions and molecular clouds. Such interfaces are commonly called “Photon Dominated Regions” or PDRs. The increase in understanding is partly due to the relative ease to observe the FIR fine structure lines which are mainly responsible for cooling PDRs. The [C II] fine structure transition at $158 \mu\text{m}$ is perhaps the best tracer of PDRs. A discussion of the characteristics of this transition is given in the review article of Genzel (1992). Detailed 1-dim. models of PDR structure have been computed by Tielens & Hollenbach (1985).

In this paper we consider the intensity ratio of the carbon radio recombination lines and the FIR carbon fine structure line. This ratio turns out to be density sensitive as discussed by Natta et al. (1994) who used the Effelsberg 100-m to make observations of C91 α at 3 cm towards Orion and compared the measured intensity with measurements of the [C II] $158 \mu\text{m}$ line by Stacey et al. (1993). The basic point made by Natta et al. was that at the densities of importance in Orion, the [C II] $158 \mu\text{m}$ intensity is roughly proportional to the C^+ column density as long as the [C II] $158 \mu\text{m}$ optical depth is low, whereas the radio recombination line intensity is proportional to the carbon emission measure ($\int N_e N(\text{C}^+) ds$). The consequence is that the ratio of their intensities is approximately proportional to density. The detailed calculations of Natta et al. show that this statement only holds up to densities of about 10^6 cm^{-3} . At higher densities, heating by collisional deexcitation of

This chapter is published in slightly modified form in Wyrowski, Walmsley, Natta, Tielens 1997, A&A 324, 1135

vibrational states of H_2 becomes increasingly effective and causes a temperature rise which reduces the intensity of the radio line. But at lower densities, the ratio of the radio and FIR line intensities is a reasonable density estimator.

One of the interesting results from the Natta et al. study was the detection of the carbon radio line at relatively large distances from the source of UV radiation. The $\text{C91}\alpha$ line was found 1 pc in projected distance to the east of the Trapezium stars at a position where the radiation field was roughly a factor of 500 lower than, for example, towards the star $\Theta^1\text{C}$ responsible for most of the ionization. This suggested it would be useful to observe $\text{C91}\alpha$ towards other sources where measurements of the $[\text{C II}]$ 158 μm line are available and where the UV radiation field is expected to be moderate. We therefore carried out $\text{C91}\alpha$ measurements towards the source NGC 2023 using the Effelsberg 100-m telescope.

The reflection nebula NGC 2023 is a site where a cluster of young pre main–sequence stars has been detected in the L 1630 cloud (E. Lada et al. 1991). The main source of ultraviolet photons is thought to be the B1.5 star HD 37903 (Harvey et al. 1980) although a more highly reddened object, “star C” (Sellgren et al. 1992 and references therein) may be important in the southern part of the region. HD 37903 has a visual extinction of only 1.4 magnitudes and is thought to be situated near the front side of L 1630. The visual scattered light distribution is well fit by a spherical model centered on HD 37903 with a dust free cavity of size 25" (Witt et al. 1984). This corresponds to 0.05 pc at a distance of 415 pc (Anthony-Twarog 1982).

Carbon recombination lines were detected from the region by Knapp et al. (1975) and studied at higher angular resolution by Pankonin & Walmsley (1976, 1978). They were interpreted as being due to the combination of a core of dimensions roughly 0.15 pc and a halo whose size is thought to be an order of magnitude larger. The $[\text{C II}]$ 158 μm line emission has been mapped with an angular resolution of approximately 1' (Jaffe et al. 1990; Howe et al. 1991; Jaffe et al. 1994). Their maps show a structure centered just to the south of HD 37903 with a dimension of roughly 0.3 pc. Higher angular resolution views of the PDR have been obtained in the molecular hydrogen $v=1-0$ S(1) line by Gatley et al. (1987) and Field et al. (1994). Burton et al. (1992) showed that the H_2 emission is in large parts due to fluorescence and that it is spatially correlated with 8727 Å $[\text{C I}]$ emission which (see Natta et al. and references therein) is thought to be produced in the same region as the radio lines. Burton et al. estimated densities above 10^5 cm^{-3} in this C^+ layer and Fuente et al. (1995) derived similar values for the adjacent molecular region from their CN data.

In this paper, we present a $\text{C91}\alpha$ map of NGC 2023. We supplement the radio recombination line data with a map of C^{18}O (2–1) and (3–2) towards NGC 2023 using the 3-m KOSMA telescope. We have estimated physical parameters in both the molecular and photon–dominated regions and compare the two. Section 8.2 outlines our observational techniques and Sect. 8.3 summarizes the main observational results. In Sect. 8.4, we consider a variety of models aimed at allowing estimates of the physical parameters in

Table 8.1: Line parameters derived from Gaussian fits of C91 α .

Source	Offsets ($''$)	T_{MB} (K)	V_{LSR} (km s^{-1})	$\Delta v_{1/2}$ (km s^{-1})
NGC2023	(60, 0)	0.05 ± 0.02	10.3 ± 0.4	3.7 ± 0.6
	(60, -60)	0.09 ± 0.02	9.9 ± 0.2	2.4 ± 0.5
	(60,-120)	< 0.02		
	(0, 0)	0.06 ± 0.03	10.3 ± 0.3	2.1 ± 0.8
	(0, -60)	0.21 ± 0.03	10.1 ± 0.8	1.2 ± 0.2
	(0,-120)	0.16 ± 0.03	10.3 ± 0.8	1.2 ± 0.2
	(0,-180)	< 0.04		
	(-60, -60)	0.09 ± 0.02	10.5 ± 0.1	2.1 ± 0.3
	(-60,-120)	0.14 ± 0.02	10.1 ± 0.1	1.2 ± 0.2
	(-60,-180)	0.07 ± 0.02	10.1 ± 0.1	1.1 ± 0.4
	(-120, -60)	< 0.04		
	(-60, 0)	0.08 ± 0.03	10.5 ± 0.2	1.8 ± 0.6

the NGC 2023 PDR. Section 8.5 is devoted to the characteristics of the molecular gas in NGC 2023 and Sect. 8.6 summarizes our conclusions.

8.2. Observations

8.2.1. C91 α 100-m observations

The observations were carried out using the Effelsberg 100-m telescope on November 7 and 8, 1994. The half-power beamwidth at this frequency is $82''$. Pointing was checked through observations on NGC 7027 and 3C 161 at roughly hourly intervals and has an accuracy of $5''$. The receiver was the facility dual-channel HEMT with a receiver temperature of 70–80 K. The observing mode was frequency switching with a throw of 1.5 MHz symmetrically with respect to the line frequency. The spectrometer was an autocorrelator which was split into two sections of 512 channels and centered on the C91 α (8589.104 MHz) and the H91 α line (8584.821 MHz). A bandwidth of 2.5 MHz was used yielding a spectral resolution of 0.2 km s^{-1} .

8.2.2. C¹⁸O KOSMA observations

We mapped C¹⁸O (2–1) and (3–2) towards NGC 2023 using the 3-m KOSMA telescope (see Winnewisser et al. 1990) on Gornegrat in conjunction with the Cologne dual channel SIS receiver system. The half-power beamwidths of the telescope at the frequencies of C¹⁸O

(2–1) (219560.333 MHz) and C^{18}O (3–2) (329330.505 MHz) are $115''$ and $75''$, respectively. Pointing was checked on Venus and was found to be accurate within $30''$. We observed in position switching mode with a reference position at $(-15', 0')$ offset from HD 37903.

The receivers were operated in double sideband mode and calibration was carried out using the normal chopper calibration technique. In the case of C^{18}O (3–2) this is somewhat inaccurate due to the presence of the strong nearby atmospheric water absorption which causes the image band opacity to be considerably different from that in the signal band (the intermediate frequency is 1.5 GHz). We have corrected for this using the model atmosphere of Grossman (1989) and estimate our error to be 15% in both lines by comparing the line intensities at the offset $(0, -1')$ from day to day. We used the facility acousto-optic spectrometers with spectral resolutions of 0.2 and 0.6 km s^{-1} and bandwidths of 287 and 1388 MHz at 220 and 330 GHz respectively.

In order to check for high optical depth in the C^{18}O emission, we also measured C^{17}O (2–1) (224714.371 MHz) and (3–2) (337061.096 MHz) at 12 positions around the offset $(0, -1')$. For this transition, the calibration of the (3–2) data is less sensitive to the atmospheric water line.

8.3. Observational results

In NGC 2023, the line intensities were sufficiently strong that we were able to make a small map. The central position of our NGC 2023 map was the position of the star HD 37903 ($\alpha(1950) = 05^{\text{h}}39^{\text{m}}07.3$, $\delta(1950) = -02^{\circ}16'58''$) and offsets given later in this paper are relative to this position. We give in Table 8.1 the line parameters determined from Gaussian fits and in Fig. 8.1 we show the corresponding spectra.

8.3.1. $\text{C}91\alpha$

Figure 8.2 shows a contour map of the integrated $\text{C}91\alpha$ intensity towards NGC 2023 (solid lines). The emission peaks at the position $(1'', -81'')$ relative to HD 37903 and in declination the angular half-power width which we measure is $136''$ or $108''$ (0.22 pc) if we correct for a beamsize of $82''$ assuming a Gaussian source distribution. One can compare this with the $[\text{C II}]$ $158 \mu\text{m}$ map of Jaffe et al. (1994) which is also shown in Fig. 8.2 (dashed lines). The $[\text{C II}]$ $158 \mu\text{m}$ emission peaks slightly north of the radio emission peak. This is more easily seen in Fig. 8.3 where we show a north–south cut through the illuminating star HD 37903. From Gaussian fits, we find an offset of $50''$ (0.1 pc) between the peaks of the radio and infrared line emission. The pointing uncertainty of the far-infrared measurements is $15''$ and so we consider this offset significant.

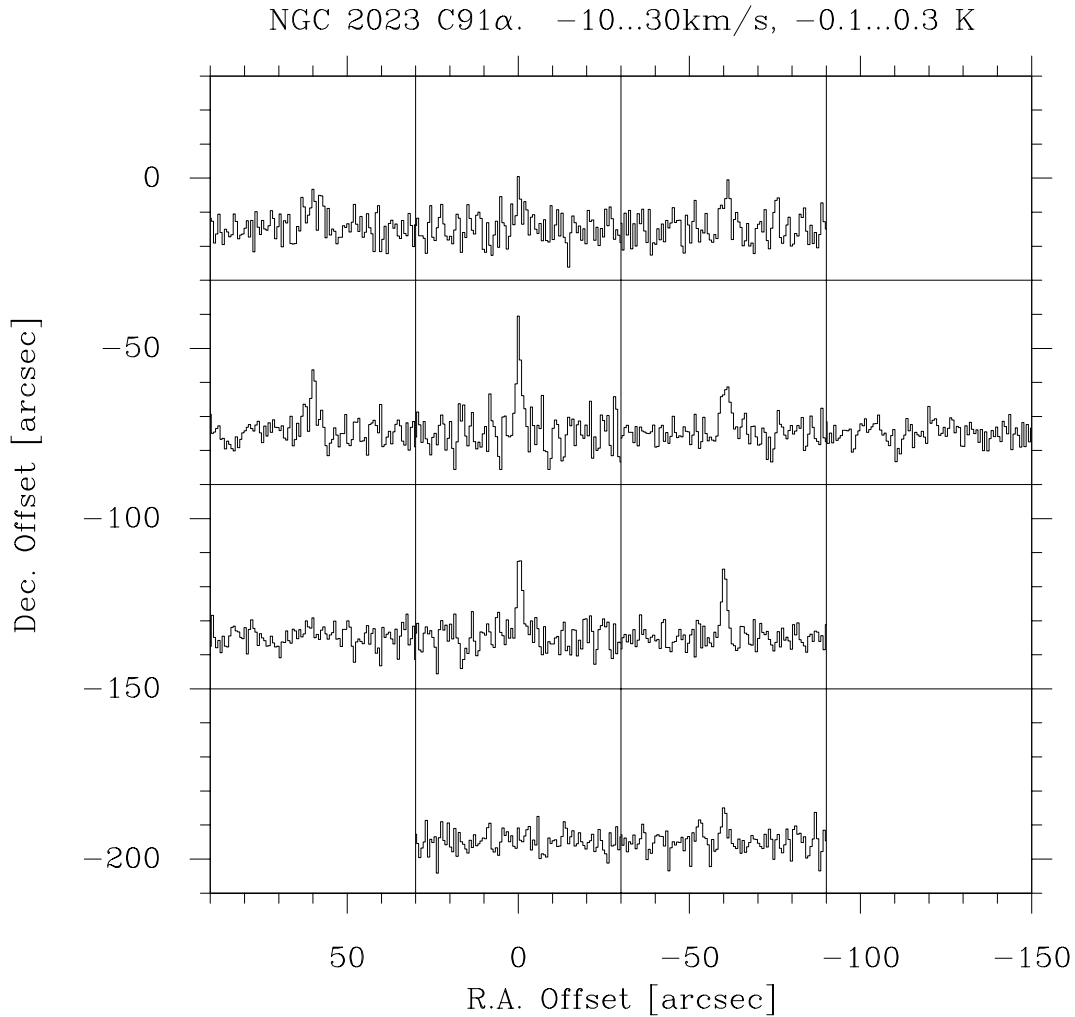


Fig. 8.1.— C91 α lines detected in NGC 2023. Abscissa is LSR velocity from -10 to 30 km s⁻¹ and ordinate is line temperature from -0.1 to 0.3 K.

8.3.2. C¹⁸O

In Fig. 8.4, we show a comparison of our integrated C¹⁸O (2–1) and (3–2) maps towards NGC 2023 with the contours of C91 α emission. There is a general agreement between the two which is somewhat surprising at first glance because C91 α is thought to form in the hot PDR layer closest to the exciting star whereas C¹⁸O is presumably abundant in the cooler molecular region. From our data, the C¹⁸O (3–2) maximum is at (6'', -66'') which is within pointing errors coincident with the C91 α peak. The angular half-power width in declination which we derive from our C¹⁸O (3–2) map is 172'' which becomes 155'' after deconvolving with an 75'' beam. The corresponding linear size is 0.31 pc.

It is interesting also that the line profiles observed in C¹⁸O and C91 α are similar which also argues for very close links between the two. We have examined our C¹⁸O data for velocity shifts or gradients across the region mapped and find that the C¹⁸O (3–2) velocity

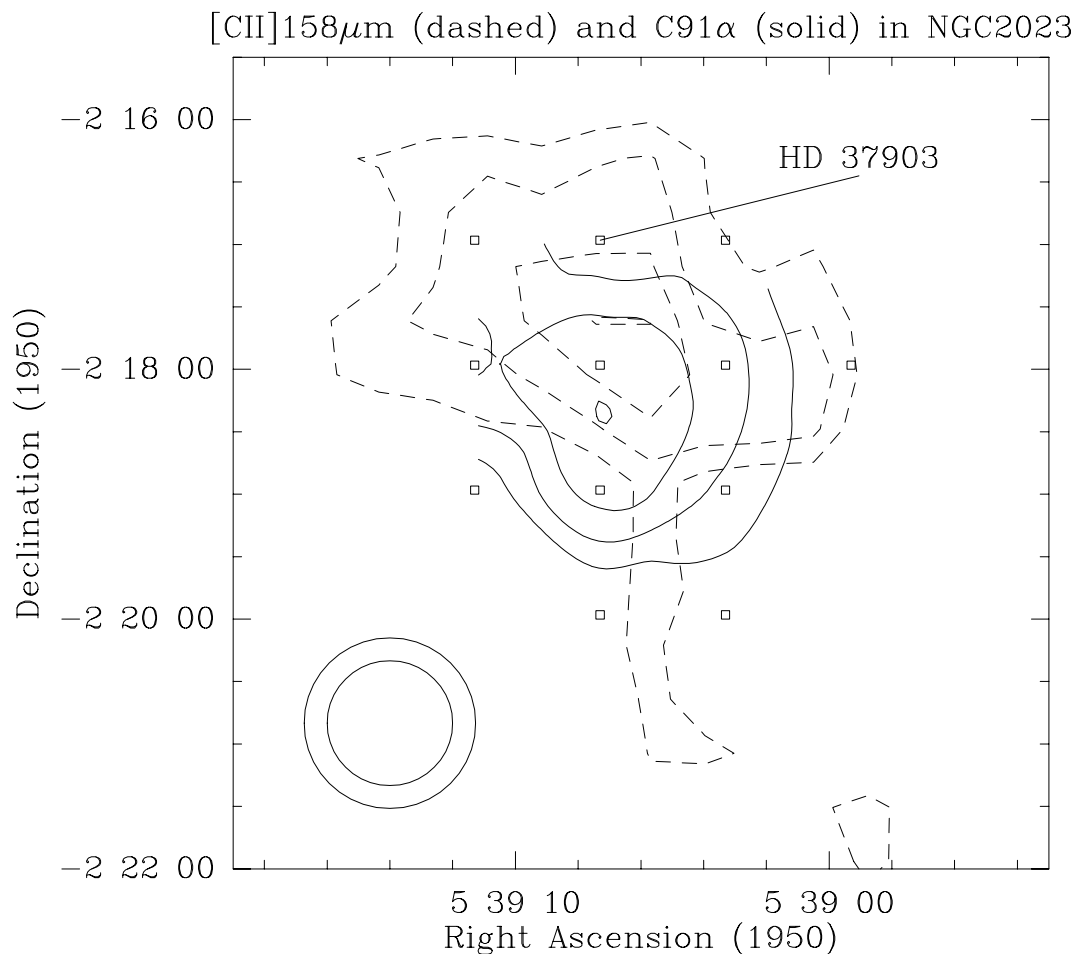


Fig. 8.2.— Integrated intensity maps of the radio recombination line C91 α (solid) and of the [C II] 158 μ m far infrared line (dashed, taken from Jaffe et al. 1994). Contours are 40, 60, 80, 100 % of peak intensity for both lines ($I(\text{C91}\alpha)=0.28 \text{ K km s}^{-1}$, $I(\text{C158})=7.6 \cdot 10^{-4} \text{ erg/cm}^2/\text{sec/sr}$). The beamsizes of 60 and 82'' for the FIR and radio observations are indicated. The small squares show the positions observed in C91 α .

varies by at most 0.3 km s^{-1} . This puts a limit on any core rotation of $1.7 \text{ km s}^{-1}/\text{pc}$.

Our C¹⁷O (2–1) and (3–2) observations have poor signal-to-noise ratio and we have therefore averaged the twelve positions measured (1.–1',–3..0') in both C¹⁸O and C¹⁷O. In this way, we determine the integrated intensity ratio C¹⁸O(3–2)/C¹⁷O(3–2) to be 4.8 ± 0.5 and the ratio C¹⁸O(2–1)/C¹⁷O(2–1) to be 3.1 ± 0.4 .

In order to compare our C¹⁸O (2–1) and (3–2) data, we have smoothed the (3–2) observations to a beam of 115 '' and taken the ratio of the two maps. The integrated intensity ratio $I(3-2)/I(2-1)$ along a north–south strip through HD 37903 is shown in Fig. 8.5 and a maximum in excitation is visible about 1' south of HD 37903.

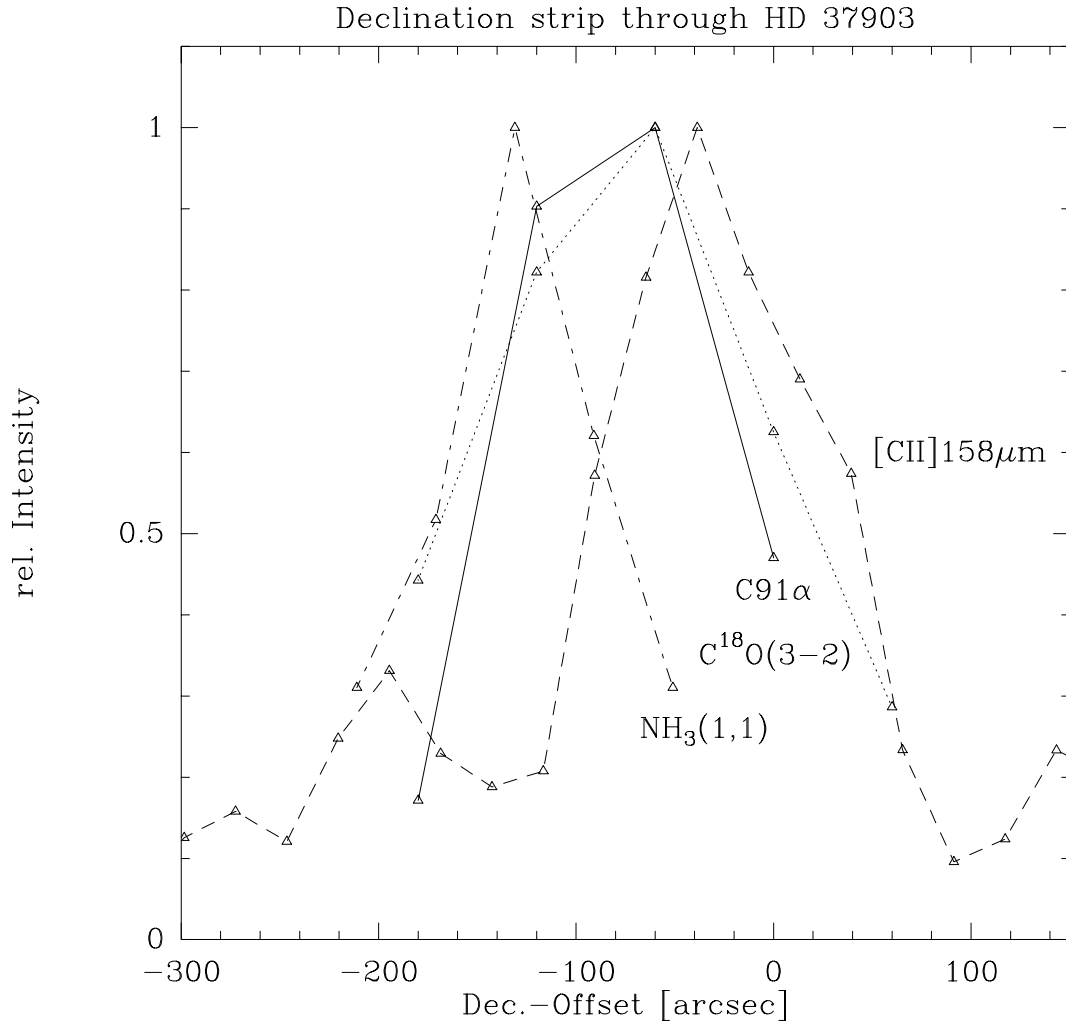


Fig. 8.3.— Cross scans along $\alpha(1950) = 5^h39^m07^s.3$ through HD 37903. The ammonia data are taken from Miller (1984). The maximum intensities are 9.2 K km s^{-1} , 0.7 K km s^{-1} and $7.6 \cdot 10^{-4} \text{ erg/cm}^2/\text{s/sr}$ for the C^{18}O , radio and FIR observations, respectively.

8.3.3. Comparison of $\text{C}91\alpha$ with molecular tracers in NGC 2023

In Fig. 8.3, we compare cuts in the FIR and radio carbon lines with observations in $\text{NH}_3(1,1)$ (Miller 1984) and $\text{C}^{18}\text{O}(3-2)$. With our spatial resolution, the peak in $\text{C}91\alpha$ and C^{18}O coincides roughly with the arc of $\text{H}_2 1-0 \text{ S}(1)$ emission mapped by Gatley et al. (1987). This structure, which is also seen in $\text{CO}(1-0)$ (Gatley et al.), probably represents the limb-brightened edge of a bubble blown by HD 37903. The C^{18}O emission may partly form in this region but clearly also originates in cooler material further from the star as evidenced by the ammonia emission (Fig. 8.3) which peaks $130''$ to the south of HD 37903 and $50''$ to the south of the peak in $\text{C}91\alpha$. This suggests a picture in which ammonia, which is more sensitive to photodissociation than C^{18}O , is confined to dense clumps relatively far from the exciting star.

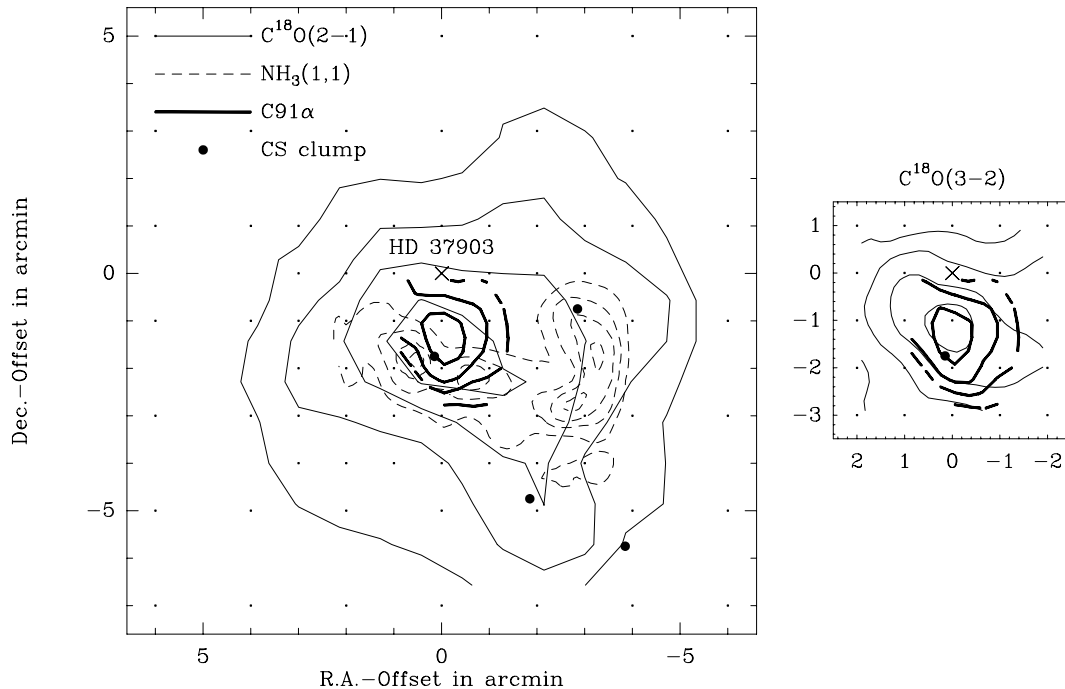


Fig. 8.4.— C^{18}O (2–1) (left panel) and (3–2) (right panel) in NGC 2023 (solid lines) in comparison with $\text{C}91\alpha$ (thick), NH_3 (1,1) (dashed, Miller 1984) and positions of CS clumps identified by Lada et al. (1991) shown as filled circles. Contours are 30, 50, 70, 90% of the peak values: $I(\text{C}^{18}\text{O} (2-1))=10.0 \text{ Kkm s}^{-1}$, $I(\text{C}^{18}\text{O} (3-2))=9.2 \text{ Kkm s}^{-1}$, $I(\text{C}91\alpha)=0.28 \text{ Kkm s}^{-1}$, $I(\text{NH}_3 (1,1))=4.2 \text{ K}$.

8.4. Physical parameters of the NGC 2023 PDR

The characteristics of the NGC 2023 PDR depend on physical parameters such as the density and UV field emitted by the star as well as on the geometry. They also depend on the gas phase abundances of critical elements such as oxygen and carbon. In this article, we have in general used solar abundances (i.e. $\text{C}/\text{H}=3.0 \cdot 10^{-4}$ and $\text{O}/\text{H}=5.0 \cdot 10^{-4}$ as in the Natta et al. study) but have also carried out some calculations using recent estimates for the “interstellar” abundances (see e.g. Mathis (1996), $\text{C}/\text{H} = 1.4 \cdot 10^{-4}$ and $\text{O}/\text{H} = 3.8 \cdot 10^{-4}$, the “Orion” value). The “interstellar” abundances may in fact be more relevant to NGC 2023 but for purposes of comparison with other models, the computations with solar values are useful. The PDR geometry relative to the observer and the exciting star can also play an important role. We discuss in this section face-on models where the star is assumed to be in the foreground relative to the PDR and edge-on models where star and gas are at the same distance from the sun.

We consider two main hypotheses while doing this. The first of these is that the carbon far infrared and radio lines are produced in the same region. With this assumption, we use the techniques discussed by Natta et al. (1994) to derive physical parameters for the region

Excitation in NGC 2023

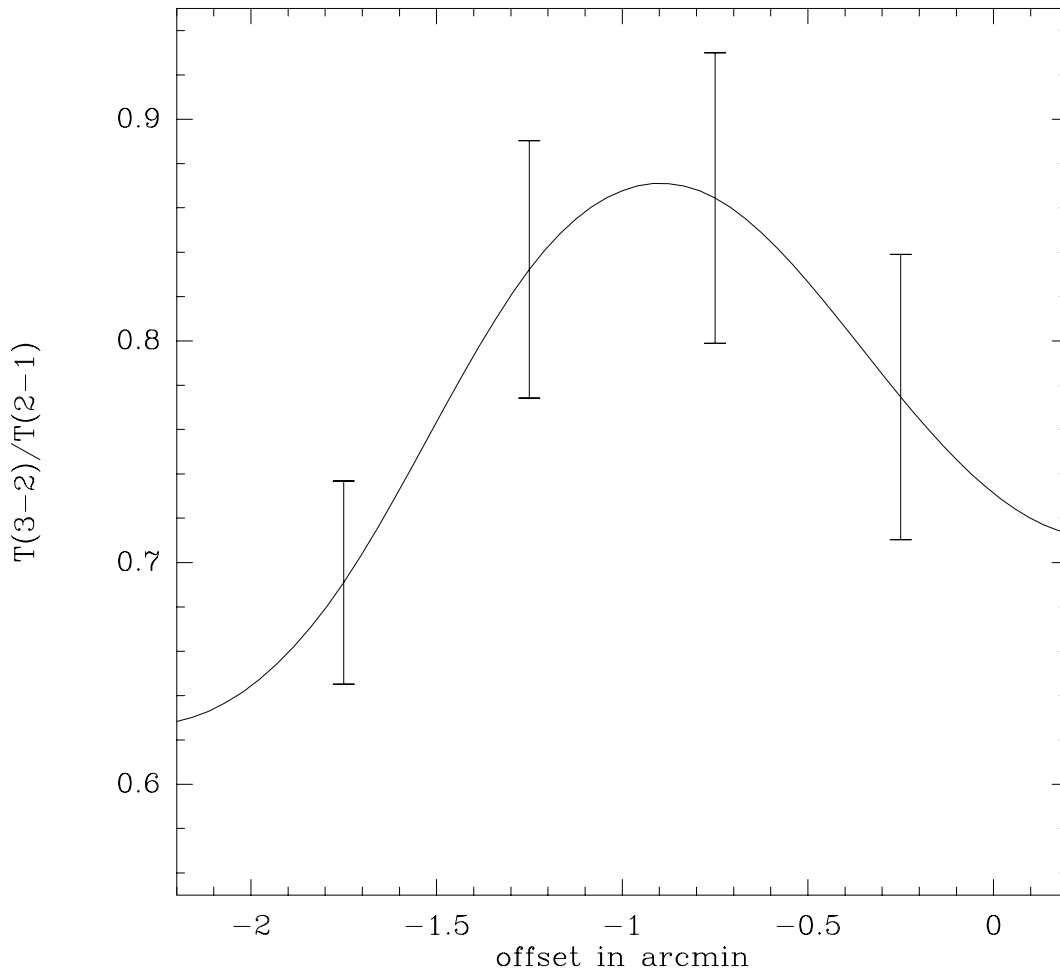


Fig. 8.5.— C^{18}O (3-2) and (2-1) integrated intensity ratio along a north-south strip through HD 37903.

where carbon is singly ionized. This technique can be used as long as the PDR material is relatively homogeneous. However, there is evidence (e.g. Field et al. 1994) that the NGC 2023 PDR is highly clumped. Moreover, in such a clumpy medium, it seems probable that a situation will occur where the radio lines are emitted by the surfaces of the dense clumps whereas the $[\text{C II}]$ 158 μm line (which has a critical density of $\sim 3000 \text{ cm}^{-3}$) comes at least in part from lower density inter-clump gas. In this case, a direct comparison of $[\text{C II}]$ 158 μm and $\text{C91}\alpha$ may be misleading and the question arises of whether combining our radio data with observations of other PDR tracers is indeed useful. The $[\text{O I}]$ 63 μm line with a critical density of $5 \cdot 10^5 \text{ cm}^{-3}$ (Tielens & Hollenbach 1985) seems a better candidate in this respect and thus we consider what constraints on the density and temperature of the NGC 2023 PDR clumps can be derived on the assumption that $[\text{O I}]$ 63 μm and $\text{C91}\alpha$ form in the same layer. We discuss also the extent to which the recent models of Steiman-Cameron et al. (1996), who interpret their observations of a number of far infrared

lines towards NGC 2023 in terms of a two-component model, need modification in the light of the radio recombination line data.

First however, we consider the homogeneous models and in particular the face-on case.

8.4.1. Face-on homogeneous PDR models

We use the technique devised by Natta et al. (1994) to derive the density and radiation field in the PDR region seen towards NGC 2023. In order to do this, we need to account for the differences in angular resolutions between the far IR ($60''$) and radio observations ($82''$) and we have therefore convolved the [C II] $158 \mu\text{m}$ map with a Gaussian of $\sqrt{82^2 - 60^2}''$ HPBW in order to reach the resolution of the radio observations.

The comparison of the observations with model results is shown in Fig. 8.6 (cf. Fig. 5 of Natta et al. 1994). We show (asterisks and open squares) the observed [C II] $158 \mu\text{m}$ and C91 α intensities NGC 2023 compared with a grid of homogeneous isothermal models (dashed lines). We also have computed a small grid of homogeneous PDR models (filled triangles, Tielens & Hollenbach 1985) where density and incident FUV field G_0 are used as input parameters. G_0 is the FUV field measured in units of the equivalent Habing (1968) flux of $1.6 \cdot 10^{-3} \text{ ergs/cm}^2/\text{sec}$ appropriate to the average interstellar medium.

Comparison of PDR model predictions with observations shows that the hydrogen number density varies from $5 \cdot 10^4 \text{ cm}^{-3}$ towards HD 37903 to 10^5 cm^{-3} at offset (0,-60) with the incident radiation field in both cases being of order 500 times the interstellar value. The temperature of an isothermal model consistent with the carbon line data is of order 100 K.

As a check on our results, we have selected the position (0,0), for which we determine from the two C lines a density of $3 \cdot 10^4 \text{ cm}^{-3}$ and a temperature of 125 K and calculated the [O I] $63 \mu\text{m}$ intensity for a simple isothermal model (see Sect. 4.3) with these parameters. We predict in this manner a [O I] $63 \mu\text{m}$ intensity of $3.5 \cdot 10^{-3} \text{ erg/cm}^2/\text{sec/sr}$ roughly in agreement with the observed value (Steiman-Cameron et al. 1996) of $2 \cdot 10^{-3} \text{ erg/cm}^2/\text{sec/sr}$.

We note also that the FUV radiation field derived above ($G_0 \sim 500$) is an order of magnitude lower than that estimated by Steiman-Cameron et al. on the basis of the FIR dust continuum. In this case however (see Fig. 8.6), G_0 is mainly sensitive to [C II] $158 \mu\text{m}$ rather than to the radio line and the FIR continuum approach seems more direct. Moreover, as discussed below, use of interstellar rather than solar abundance for C causes the inferred G_0 to increase to values compatible with the FIR continuum estimate ($G_0 \sim 8000$). For comparison, the radiation field expected at a distance of 0.16 pc ($80''$ at the distance of NGC 2023 which is the observed offset of C91 α from HD 37903) from a B1.5V star (see Draine & Bertoldi 1996) is about 2000 times the mean interstellar radiation field if one neglects dust extinction.

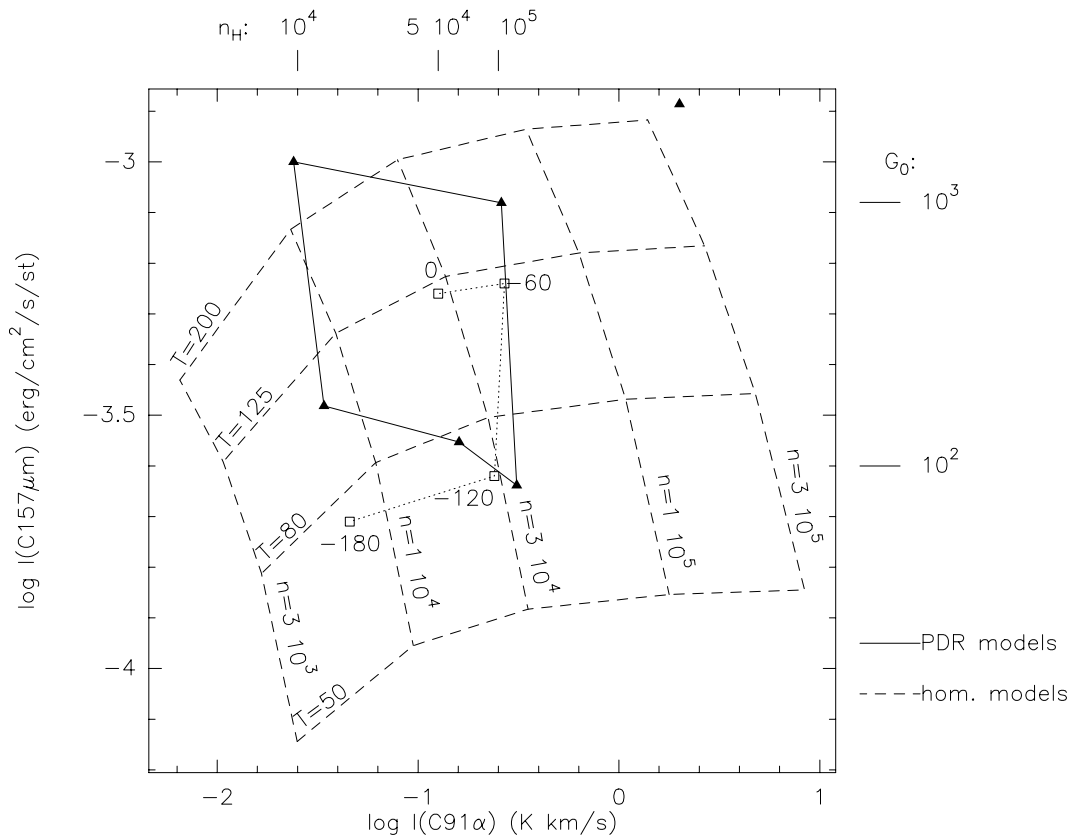


Fig. 8.6.— Results of model calculations showing the Log of the FIR line intensity plotted against the Log of the integrated intensity of the [C II] 158 μm line. The dashed grid shows results for $T=50, 80, 125,$ and 200 K and for hydrogen density between $3 \cdot 10^3$ and $3 \cdot 10^5$ cm^{-3} . The open squares are data points for NGC 2023 (the numbers denote the offsets from HD 37903) and the filled triangles are PDR model predictions based upon the results of Tielens & Hollenbach. Models are given for parameter pairs (G_0, n) where G_0 is the incident radiation field in units of the local value and n is the hydrogen density. No correction has been made for stimulated amplification of the radio lines.

On the other hand, at the $(0, -120'')$ offset, we estimate a density of 10^5 cm^{-3} but a radiation field of only 100 times the mean interstellar value. Thus, the density remains high at considerable distances from HD 37903. It seems likely that this reflects the properties of high density clumps within the molecular cloud.

8.4.2. Edge-on homogeneous models

The fluorescent molecular hydrogen emission observations of NGC 2023 by Gatley et al. (1987, see also Field et al. 1994) suggest an edge-on geometry for the PDR. This is

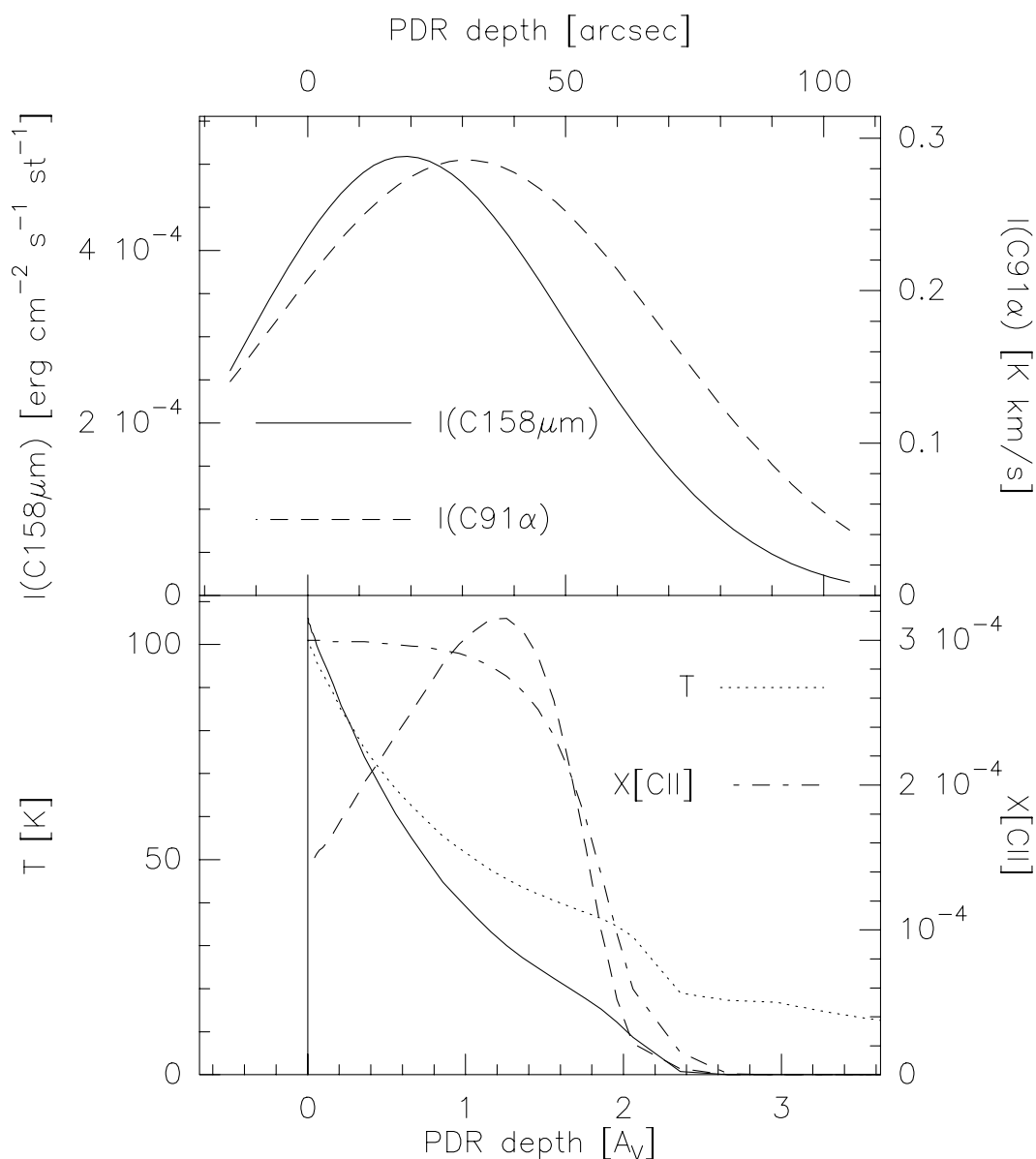


Fig. 8.7.— The figures show a cut through a PDR in an edge-on model with $G_0 = 100$, $n_H = 10^4 \text{ cm}^{-3}$ and depth along the line of sight $d = 5 \cdot 10^{18} \text{ cm}$. The lower panel shows the intensities of radio and the FIR line as a function of PDR depth and the physical parameters T and $X[\text{C}^+]$ from which the intensities are calculated. In the upper panel these intensities are folded with an 82 and 60'' beam, respectively.

further supported by the observed offset between radio and ammonia emission which can be qualitatively understood in an edge-on model in terms of the high photodissociation rate of NH_3 (see the models of Sternberg & Dalgarno 1995) which causes ammonia to be most abundant in heavily extinguished regions far from the star. With this in mind, we have calculated models with edge-on geometry and a finite thickness d for the PDR.

In an edge-on scenario, the offset between FIR and radio lines could arise because of the different depths in the PDR from which the lines originate. The intensity of the C91 α line, which is proportional to $T^{-1.5}$, increases with depth into the PDR and reaches a peak just in front of the transition zone C⁺/CI/CO (Fig. 8.7). The [C II] 158 μm line on the other hand, has its maximum intensity closer to the surface of the PDR. PDR models show that this difference is of the order $\Delta A_v = 1$ largely independent of G_0 or n_H or equivalently a hydrogen column density of $2 \cdot 10^{21} \text{ cm}^{-2}$. The observed offset between FIR and radio lines (0.1 pc) then corresponds to a hydrogen density of $\simeq 7000 \text{ cm}^{-3}$ which is comparable to the density estimates (10^4 cm^{-3}) derived on the basis of similar arguments from the observed size of the structure seen in vibrationally excited H₂ emission (Field et al. 1994).

There are however difficulties with this interpretation. The model shown in Fig. 8.7 ($n_H = 10^4 \text{ cm}^{-3}$, $G_0 = 100$) would lead to an offset between FIR and radio line of about 15'' but would need a PDR depth along the line of sight of 1.6 pc in order to explain the observed intensity of the radio line. Such an elongation along the line of sight seems highly unlikely (see discussion in Sect. 8.5) and we therefore reject this possibility. We conclude that a density gradient perpendicular to the line of sight is needed to explain the observations in the framework of an edge-on model. An alternative is a clumpy model as discussed in the next section.

8.4.3. Clumpy models

There are good reasons to expect PDRs to be clumped on size scales considerably lower than our effective linear resolution (see e.g. Tielens et al. 1993, Field et al. 1994). In the case of NGC 2023, Steiman-Cameron et al. (1996) have presented a two component model which accounts for their observations of the fine structure lines of [O I], [C II], and [Si II] as well as the available data for the mm-submm lines of CO. They conclude that the data are best fit by a model with warm (750 K) dense (10^5 cm^{-3}) clumps with a beam filling factor of 0.11 immersed in a cooler (250 K) halo of relatively low density (750 cm^{-3}). In this model, the [C II] 158 μm emission comes mainly from the low density extended medium, while the [O I], [Si II], and high level CO emission originates in the dense clumps. The observed offset between [C II] 158 μm and C91 α then is caused by the fact that [C II] 158 μm is dominated by the low density gas in the central cavity around HD 37903 whereas C91 α peaks up in the surrounding high density shell.

As shown by our homogeneous models discussed above, the low density extended component of Steiman-Cameron et al. contributes negligible to the observed C91 α emission. Moreover, the high density component also fails (due to its low beam filling factor and high temperature) to account for the observed C91 α flux (see Fig. 8.6). Finally, we note that these models have trouble accounting for the observed C91 α linewidth (1.2 km s^{-1} , see Table 8.1) which corresponds to an upper limit of 400 K on the kinetic temperature.

We now consider whether one can find two component models which account approximately for both the radio and FIR data. In such a clumpy model, it is clear that the carbon radio lines will form preferentially in the dense clumps (see discussion of Natta et al. 1994). The clumps will not make important contributions to the [C II] 158 μm emission unless their beam-filling factor is large but this is not necessarily the case for the [O I] 63 μm line with its much higher critical density. We therefore now discuss models where [O I] 63 μm and C91 α form in the same region.

In particular, we have selected the observations at offset (30'',-30'') and analyzed a ‘‘clumpy model’’ for the emission of C91 α and [O I] 63 μm (see Meixner & Tielens 1993 for a more general discussion of clumpy PDR models). We consider the emission in these two tracers from spherical clumps of radius r_c and volume filling factor f_v immersed in a cloud of size L . The beam-filling factor of the clumps is then $0.75L f_v/r_c$. We suppose that the clumps are homogeneous with density n_{H} and temperature T and that carbon is singly ionized in a layer in which the hydrogen column density is $8 \cdot 10^{21} \text{ cm}^{-2}$ (Tielens & Hollenbach 1985). With these assumptions, we compute the volume filling factor f_v required to account for the observed intensity in C91 α (0.2 K km/s) and [O I] 63 μm towards NGC 2023 (see Steiman-Cameron et al. for a compilation of the OI data). In the case of C91 α , $f_v(\text{C91}\alpha)$ is determined by an equation of the type,

$$I_\nu(\text{C91}\alpha) = f_v(\text{C91}\alpha) f_{em} j_\nu(\text{C91}\alpha) \cdot L \quad (8.1)$$

where $f_{em} = 1$ for $N_c = n_{\text{H}} r_c < N_{cr} = 8 \cdot 10^{21} \text{ cm}^{-2}$ and $f_{em} = 1 - (1 - r_{cr}/r_c)^3$ for $N_c > N_{cr}$ ($r_{cr} = N_{cr}/n_{\text{H}}$). $j_\nu(\text{C91}\alpha)$ is the C91 α emissivity as given e.g. by Dupree & Goldberg (1970).

Figure 8.8 shows contours of $f_v(\text{C91}\alpha)$ computed using Eq. 8.1 as a function of density and temperature. The calculations have been carried out for $L=0.2$ pc and $r_c=0.02$ pc. Since the C91 α emissivity scales inversely with the gas temperature, warmer gas has to be denser (ie., higher emission measure) in order to explain the same observed intensity. Likewise, for the same gas temperature, a smaller volume/beam filling factor requires emission by denser gas. If one supposes the clumps to have beam-filling factors ($f_b = 7.5 f_v$) below unity, one requires densities above $2 \cdot 10^4 \text{ cm}^{-3}$ at 10 K and above $6 \cdot 10^4$ at 100 K in order to explain the observed C91 α intensity.

One can carry out an analogous calculation for [O I] 63 μm where however there is the extra complication that in general the [O I] lines are optically thick and hence that the [O I] emissivity must be modified accordingly. Thus, one has :

$$I([\text{O I}] 63 \mu\text{m}) = f_v(\text{OI}) f_{em} j([\text{O I}] 63 \mu\text{m}) \beta(\tau_l) \cdot L \quad (8.2)$$

where the escape probability (Hollenbach & McKee 1979, Eq. 5.10) $\beta(\tau_l)$ behaves roughly

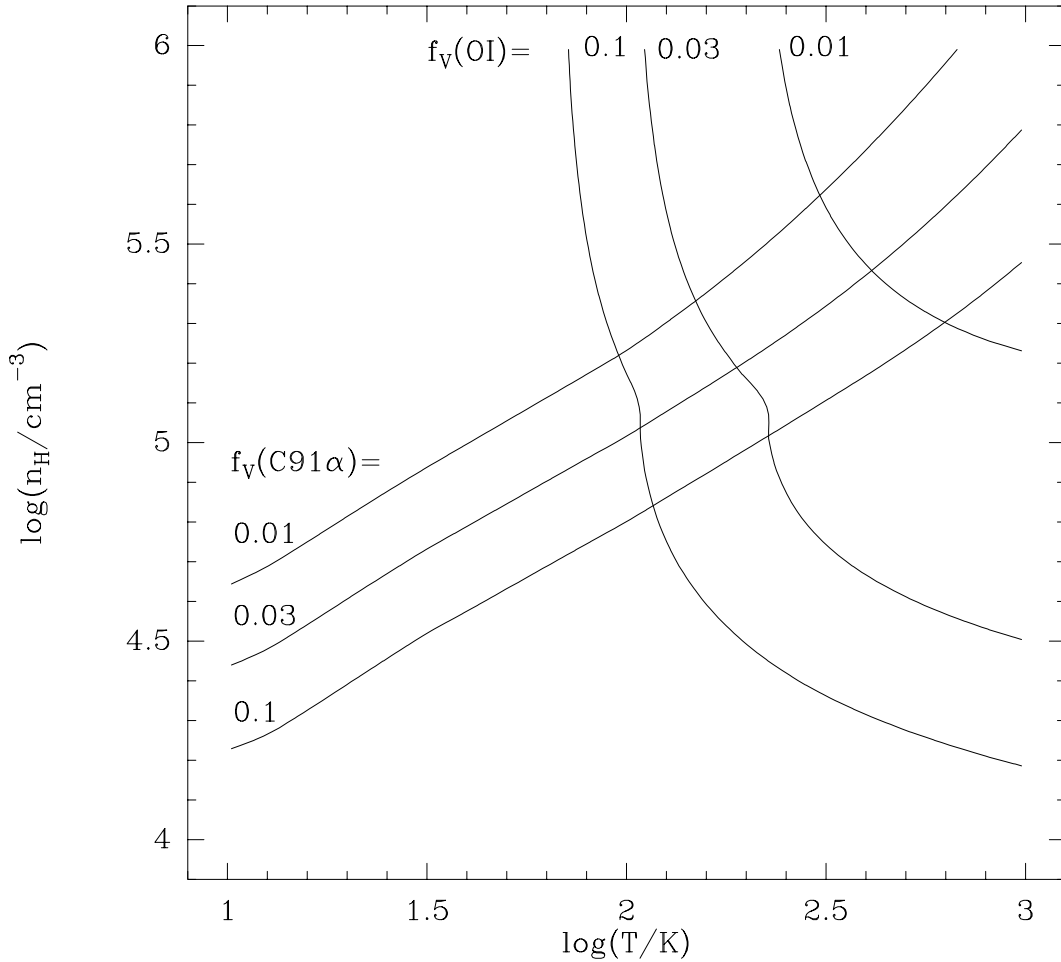


Fig. 8.8.— Volume filling factor f_v required to account for the observed NGC 2023 C91 α and [O I] 63 μm line intensities as a function of density and temperature in a clumpy model with depth along line of sight $L=0.2$ pc and clump radius $r_c=0.02$ pc. The observed C91 α intensity is taken to be 0.2 Kkm s^{-1} and the observed [O I] 63 μm intensity to be $3.6 \cdot 10^{-3} \text{ erg/cm}^2/\text{sec/sr}$. Contours are shown in the density–temperature plane for $f_v = 0.1, 0.03,$ and 0.01 . Intersections of these curves for the same value of f_v allow one to deduce density–temperature combinations which explain both C91 α and [O I] 63 μm .

as $1/\tau_l$ for large line optical depth τ_l . The [O I] emissivity $j([\text{O I}] 63 \mu\text{m})$ can be computed using the expressions given, for example, by Hollenbach et al. (1991, Appendix B) and one thus can compute the filling factor $f_v(OI)$ required to explain the observed [O I] 63 μm intensity ($I([\text{O I}] 63 \mu\text{m})=3.6 \cdot 10^{-3} \text{ erg/cm}^2/\text{sec/sr}$, Steiman–Cameron et al. 1996). In this way, we have derived the loci of constant f_v given in Fig. 8.8.

The [O I] 63 μm emission from a clump in these models is usually optically thick. At high densities where the level populations are approximately thermalised, the line intensity thus depends only on temperature and beam (or volume) filling factor. This accounts for

the rough density independence above 10^5 cm^{-3} shown by the [O I] $63 \mu\text{m}$ contours in Fig. 8.8.

Models which simultaneously fit both the [O I] $63 \mu\text{m}$ and C91 α data require densities and temperatures in the range $7 \cdot 10^4$ – $4 \cdot 10^5 \text{ cm}^{-3}$ and 100–300 K (consistent with the C91 α line width), respectively. The volume filling factor varies correspondingly between 0.1 and 0.01. Thus, two component models with high density warm clumps (where C91 α and [O I] $63 \mu\text{m}$ form) immersed in a low density medium ($n \sim 1000 \text{ cm}^{-3}$ which gives rise to [C II] $158 \mu\text{m}$), can account for the observations. This model is in qualitative agreement with the results of Steiman-Cameron et al. There is however an important difference: namely, we find that the clumps must be significantly cooler (~ 100 – 300 K vs. $\sim 750 \text{ K}$).

Our models of course are somewhat arbitrary (e.g. in the choice of r_c) but we think they provide a useful estimate of the physical conditions in the clump. They do not however attempt to fit other data such as the high-J CO lines which need to be understood in a more complete treatment of this problem. Understanding this will require treating the radiative transport in a manner analogous to that used for the homogeneous models of Sect. 8.4.1.

8.4.4. Effect of “interstellar abundances” on inferred densities

As mentioned above, our results are sensitive to the assumed O and C abundances. We here briefly consider the nature of this dependence. The main effect is on the intensity of the C91 α line which is proportional to the square of the gas phase carbon abundance (since $n(\text{C}^+)$ is essentially equal to n_e). Thus overestimating the carbon abundance by a factor of 2 causes us to underestimate the hydrogen density required to account for the observations by a factor of 4. The analogous effect for the [C II] $158 \mu\text{m}$ line is merely linear and causes us to underestimate G_0 .

We have attempted to assess the effect of changed abundances upon the models shown in Fig. 8.6. This suggests for example that one can fit our data at (0,-60) with a face-on model having $n_H = 7 \cdot 10^5 \text{ cm}^{-3}$ and $G_0 = 8000$. The FUV field is in better agreement with that obtained by Steiman-Cameron et al. using the FIR continuum data. The conclusion we draw from this is that the density estimates given in this section should probably be revised upwards roughly by a factor of 4.

8.5. Characteristics of the molecular core in NGC 2023

We consider in this section the characteristics of the molecular core in NGC 2023 which we can derive from our C^{18}O observations.

Our measurements of $C^{18}O$ (2–1) and $C^{18}O$ (3–2) allow us to place important constraints on the molecular gas associated with the NGC 2023 PDR. When analyzing these data, we will make two assumptions which we now discuss briefly. The first is that the basic density structure (i.e. density and volume filling factor) of the molecular gas and of the PDR is the same. Thus in a homogeneous model, the density in the region responsible for $C^{18}O$ emission and that in the layer responsible for $C91\alpha$ emission are identical. They differ in the degree of penetration of the UV field and consequently in the temperature. This assumption is justified by the general agreement in spatial and velocity distributions of $C^{18}O$ and $C91\alpha$ (see Fig. 8.4) but it is certainly debatable.

A second assumption is that the molecular/PDR region seen towards NGC 2023 is not greatly elongated along the line of sight. Molecular cores are often elongated but an aspect ratio of more than 2 is unusual (Myers et al. 1991) and we thus conclude that the depth of the $C^{18}O$ emitting region in the line of sight direction is less than 0.6 pc (or twice the value estimated as the half-power diameter in Sect. 8.3.2). Again the assumption is questionable but it seems a reasonable starting hypothesis. It would incidentally invalidate some of the more extreme edge-on models discussed in Sect. 8.4.2.

With these two assumptions in mind, we now consider the significance of our observed $C^{18}O(3-2)/C^{18}O(2-1)$ ratio (see Fig. 8.5). Our $C^{17}O$ results (see Sect. 8.2.2) show that $C^{18}O$ is close to being optically thin in NGC 2023 and from the observed $C^{18}O(3-2)/C^{17}O(3-2)$ integrated intensity ratio, we estimate the $C^{18}O(3-2)$ optical depth is at most 0.5 (the interstellar $C^{18}O/C^{17}O$ abundance ratio is estimated to be 3.2 ± 0.2 in the local ISM (Wilson & Rood 1994). Alternatively, we used the ^{13}CO intensities measured by Kramer et al. (1996, see also Kramer 1992) together with an interstellar $^{13}CO/C^{18}O$ ratio of 7.3 (estimated from the local ISM $^{16}O/^{18}O$ and $^{12}C/^{13}C$ ratios given by Wilson & Rood) to estimate the optical depth in the $C^{18}O$ lines and found $\tau(2-1)=0.45 \pm 0.05$ and $\tau(3-2)=0.4 \pm 0.05$.

In view of this, it seems reasonable as a first estimate to use the usual (low optical depth LTE) formula to calculate the $C^{18}O$ column densities and the molecular rotation temperature. We find $T_{\text{rot}}=13 \pm 3$ K and $N(C^{18}O) = (4 \pm 1) \cdot 10^{15} \text{ cm}^{-2}$ which for $C^{18}O/H_2 = 2.3 \cdot 10^{-7}$ (Lada et al. 1994) corresponds to $N(H_2) = 1.7 \cdot 10^{22} \text{ cm}^{-2}$. This corresponds to a visual extinction of approximately 18 magnitudes and (using the assumption about the depth of the molecular core along the line of sight mentioned earlier), the H_2 density must be at least 10^4 cm^{-3} .

With this in mind, we have carried out statistical equilibrium calculations aimed at predicting the $C^{18}O(3-2)/C^{18}O(2-1)$ intensity ratio as a function of density and temperature. We have used here an LVG approach to estimate the line escape probability for a $C^{18}O$ column density to line width ratio of $10^{15.5} \text{ cm}^{-2}/(\text{km s}^{-1})$ which corresponds roughly to the LTE estimate given above. However, given that the $C^{18}O$ lines are optically thin, this assumption does not greatly influence the results. More critical are the collisional rates for which we have used the results of Flower & Launay (1985). The results, displayed

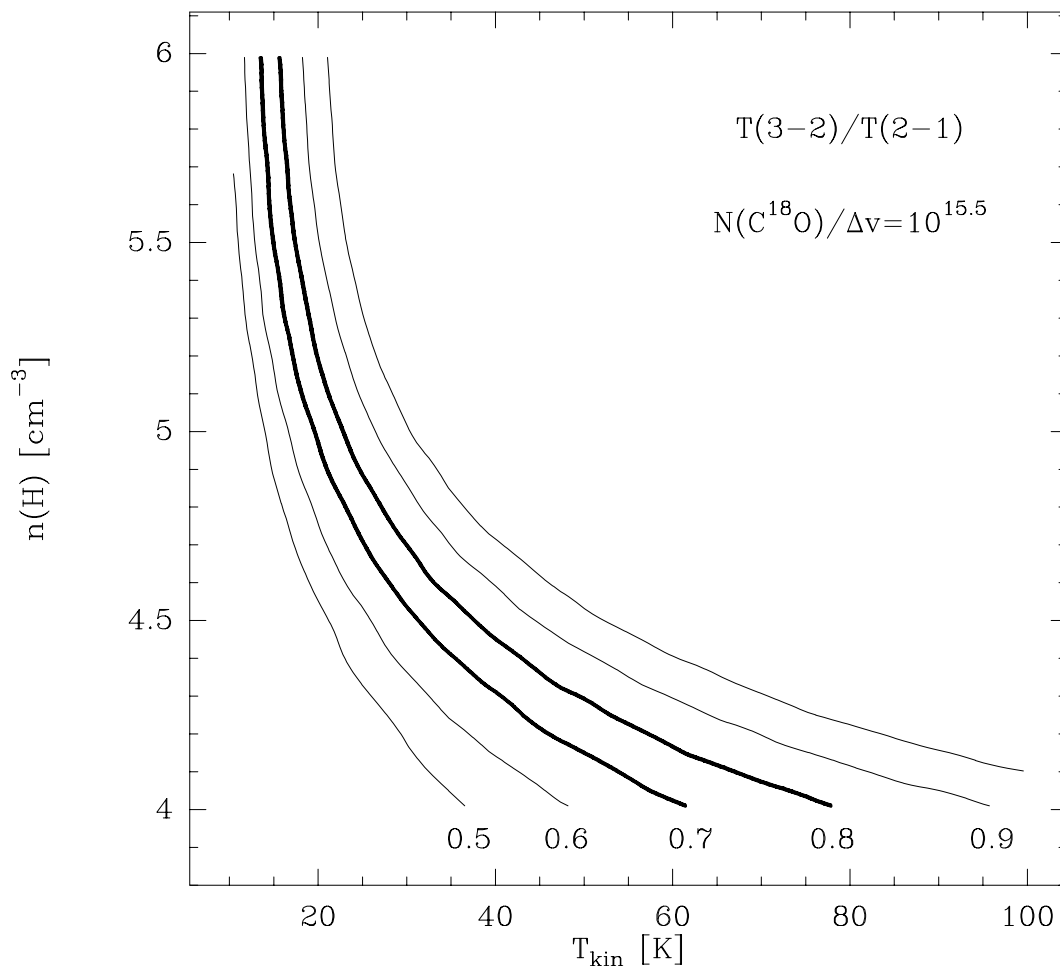


Fig. 8.9.— Predictions of the $\text{C}^{18}\text{O}(3-2)/(2-1)$ line ratio for $N(\text{C}^{18}\text{O})/\Delta v = 10^{15.5} \text{ cm}^{-2}/\text{km s}^{-1}$ using a statistical equilibrium model. The range of observed values are indicated by thick contours.

in Fig. 8.9, show the predicted ratio of $\text{C}^{18}\text{O}(3-2)/(2-1)$ as a function of density and temperature. One sees that the kinematic temperature is constrained to the range 13–80 K. This is consistent with the results of Jaffe et al. (1990) who observed $\text{C}^{18}\text{O}(2-1)$ with a $32''$ beam and found a main-beam brightness temperature of 11.8 K $100''$ SE of HD 37903. Below 20 K, densities of above 10^5 cm^{-3} are implied by the observations and under these conditions, the lower levels of C^{18}O are close to being thermalised. At higher temperatures, lower densities are possible and at 80 K (Jaffe et al. 1990, Jansen et al. 1994 based upon CO data), the density may be as low as 10^4 cm^{-3} . There is probably a great range of temperatures in the molecular core seen in C^{18}O . Walmsley & Ungerechts (1983) estimated temperatures of order 15–20 K at three positions in NGC 2023 on the basis of their ammonia data and it is likely that the ^{12}CO observations may sample a surface layer similar to that observed in CN (Fuente et al. 1995).

On this basis, we conclude that the total hydrogen density in the molecular core is at

least 10^4 cm^{-3} and most probably above 10^5 cm^{-3} . This is consistent with estimates made by Fuente et al. (1995). It should be compared with the values estimated in Sect. ?? for the hydrogen density in the region responsible for C91 α and [C II] 158 μm emission. Our estimates for the density in the molecular core are consistent with those derived for the homogeneous face-on model of Sect. 8.4.1.

The above results allow us to determine the mass and overall properties of the molecular core observed in C¹⁸O. We determine a mass of $30 M_{\odot}$ by integrating our observed C¹⁸O column density over the molecular core. The turbulent kinetic energy in the cloud (see Harju et al. 1993) is $4 \cdot 10^{44}$ ergs and the gravitational energy (for spherical geometry) $3 \cdot 10^{44}$ ergs. Thus to within geometrical uncertainties, the molecular cloud is virialised.

8.6. Discussion and conclusions

The main conclusion from this work is that a large fraction of the gas seen towards NGC 2023 is at densities above 10^5 cm^{-3} . Put in other terms, the beam filling factor of such high density gas cannot be much less than unity. This is true both for the ionized atomic gas which emits carbon radio recombination lines and the molecular component seen in C¹⁸O emission. We estimate that there are $30 M_{\odot}$ of molecular gas in the molecular core associated with NGC 2023 corresponding to about 20 magnitudes of visual extinction. The amount of partially ionized gas is probably a factor of 2 lower. It seems likely that the densities in the molecular and partially ionized layers are similar although the temperatures differ by 1–2 orders of magnitude. Verification of this using other density tracers would be useful.

It is worth noting that various other tracers besides the CI radio recombination lines and OI fine structure lines indicate the presence of high densities in the NGC 2023 PDR. First, the observed H₂ S(1)1-0/2-1 line ratio 80'' south of HD 37903 indicates partial thermalisation of the $v=1$ level. The inferred densities are somewhat controversial due to uncertainty in the collision rates and range from 10^4 to 10^5 cm^{-3} with the most reliable estimates at the high end of the range (Black and van Dishoeck 1987, Sternberg and Dalgarno 1989, Burton et al. 1990, Draine and Bertoldi 1996). The spatial structure of the H₂ emission (Gatley et al. 1987, Field et al. 1994) indicates the presence of a dense shell with a filling factor which is probably too small to account for the C91 α observations. On the other hand, the intense CO(7-6) emission observed by Jaffe et al. (1990) also indicates the presence of a warm dense component (10^5 cm^{-3}) with beam filling factor of order unity.

Our data do not have sufficient angular resolution to make definitive statements concerning the geometry or structure of the PDRs seen towards NGC 2023. Nevertheless, they show that combining the radio lines with other PDR tracers can allow useful limits to be placed on the physical parameters of the high density clumps. In particular, using

[O I] 63 μm in combination with the radio lines has allowed us to estimate densities upward of 10^5 cm^{-3} and temperatures of order 200 K in the region where carbon is ionized.

REFERENCES

- Anthony-Twarog B.J. 1982, AJ 87, 1213
 Black J.H., van Dishoeck E.F. 1987, ApJ 322, 412
 Burton M.M., Hollenbach D.J., Tielens A.G.G.M. 1990, ApJ 365, 620
 Burton M.G., Bulmer M., Moorhouse A., Geballe T.R., Brand P.W.J.L. 1992, MNRAS 257, 1
 Draine B.T., Bertoldi F. 1996, ApJ 468, 269
 Dupree A., Goldberg L. 1970, ARAA 8, 231
 Field D., et al. 1994, A&A 286, 909
 Flower D.R., Launay J.M. 1985, MNRAS 214, 271
 Fuente A., Martin-Pintado J., Gaume R. 1995, ApJ 442, L33
 Gatley I. et al. 1987, ApJ 318, L73
 Genzel R. 1992, in "The galactic Interstellar Medium", p275, (Burton W.B., Elmegreen B.G., Genzel R.), Springer
 Grossman E. 1989, "AT - Atmospheric Transmission Software, User's Manual", Univ. of Texas, Austin
 Habing H.J. 1968, Bull. Astr. Inst. Netherlands, 19, 421
 Harju J., Walmsley C.M., Wouterloot J.G.A. 1993, A&AS 98, 51
 Harvey P.M., Thronson H.A., Gatley I. 1980, ApJ 235, 894
 Hollenbach D., McKee C.F. 1979, ApJS 41, 555
 Hollenbach D., Tielens A., Takahashi T. 1991, ApJ 377, 192
 Howe J.E., Jaffe D.T., Genzel R., Stacey G.J. 1991, ApJ 373, 158
 Jaffe D.T., Genzel R., Harris A.I., Howe J.E., Stacey G.J., Stutzki J., 1990, ApJ 353, 193
 Jaffe D.T., Zhou S., Howe J.E., Stacey G.J. 1994, ApJ 436, 203
 Jansen D.J., van Dishoeck E.F., Black J.H. 1994, A&A 282, 605
 Knapp G.R., Brown R.L., Kuiper T.B.H. 1975, ApJ 196, 167
 Kramer C. 1992, PhD. thesis, Univ. of Cologne
 Kramer C., Stutzki J., Winnewisser G. 1996, A&A 307, 915
 Lada C.J., Lada E.A., Clemens D.P., Bally J. 1994, ApJ 429, 694
 Lada E.A., De Poy D.L., Evans N.J. II, Gatley I. 1991, ApJ 371, 171
 Mathis J.S. 1996, ApJ 472, 643
 Meixner M., Tielens A. 1993, ApJ 405, 216
 Miller M. 1984, Doktorarbeit, University of Cologne
 Myers P.C., Fuller G.A., Goodman A.A., Benson P.J. 1991, ApJ 376, 561
 Natta A., Walmsley C.M., Tielens A. 1994, ApJ 428, 209
 Pankonin V., Walmsley M. 1976, A&A 48, 341

- Pankonin V., Walmsley C.M. 1978, A&A 67, 129
Sellgren K., Werner M.W., Dinerstein H.L. 1992, ApJ 400, 238
Stacey G.J. et al. 1993 , ApJ 404, 219
Steiman-Cameron T.Y., Haas M.R., Tielens A., Burton M. 1996, ApJ, in press
Sternberg A., Dalgarno A. 1989, ApJ 347, 863
Sternberg A., Dalgarno A. 1995 , ApJS 99, 565
Tielens A. , Hollenbach D. 1985 , ApJ 291, 722
Tielens, A.A.G.M., Meixner, M.M., van der Werf, P.P., Bregman, J., Tauber, J.A.,
Stutzki,J., Rank, D. 1993, Sci 262, 86
Walmsley C.M., Ungerechts H. 1983, A&A 122, 164
Wilson T.L., Rood R.T. 1994, ARAA 32, 191
Winnewisser G., Zimmermann P., Hernalshel J., Miller M., Schieder R. 1990, A&A 230, 248
Witt A.N., Schild R.E., Kraiman J.E. 1984, ApJ 281, 708

Chapter 9

Carbon radio recombination lines towards the Orion Nebula

9.1. Introduction

The neutral gas surrounding H II regions is an excellent laboratory for the purpose of understanding the interactions between the UV radiation of young newly formed stars and the surrounding molecular clouds. Such photon dominated regions (PDRs) have been the subject of both theoretical (e.g. Tielens & Hollenbach 1985; Sternberg & Dalgarno 1995) and observational attention (e.g. Herrmann et al. 1996). The most easily observable example of a PDR is perhaps that provided by the Orion Nebula and the surrounding hot neutral gas. Of particular interest is the elongated bar-like feature to the south-east of the Orion Trapezium stars known as the Orion Bar (see Tielens et al. 1993; Hogerheijde et al. 1995; van der Werf et al. 1996 for recent discussions). The Bar is elongated in a direction on the plane of the sky almost perpendicular to the line of sight to the O6 star $\Theta^1\text{C Ori}$ in the trapezium, which is responsible for ionizing the H II region and heating the neutral gas. This fact makes it possible for us to observe stratification within the Bar along the line of sight to $\Theta^1\text{C Ori}$. Thus, the Bar seen in free-free emission from the ionized gas is clearly offset with respect to the Bar seen in rovibrational lines of H_2 and fine structure lines of C II and O I from the neutral gas. These in turn are offset relative to the Bar as seen in various molecular species (see Tielens et al. 1993; Herrmann et al. 1996 for examples). It has been concluded that the observed stratification is consistent with a mean hydrogen density of $5 \times 10^4 \text{ cm}^{-3}$. On the other hand, high angular resolution maps of the Bar in various molecular transitions (Tauber et al. 1994) have shown that the neutral gas is structured and quite inhomogeneous with clump densities as high as 10^6 cm^{-3} .

This chapter is published in Wyrowski, Schilke, Hofner, Walmsley 1997, ApJ 487, L171.

The carbon radio recombination lines offer an alternative approach to studying PDRs. Their emission is invariably optically thin and proportional to the *square* of the electron density (or equivalently of the carbon abundance in the neutral regions where carbon is singly ionized). Natta et al. (1994) demonstrate moreover that one can use the ratio of the radio line intensity to that of the far infrared [C II] 158 μm line to infer the density in the layer where carbon is singly ionized. They observed C91 α with the Effelsberg 100-m telescope at several positions in Orion and derived densities of 10^6 cm^{-3} . These observations however were made with a relatively poor angular resolution ($80''$) which rendered difficult the comparison with other PDR tracers in Orion. We have therefore undertaken new carbon radio line observations with the objective of allowing a comparison both with far infrared and molecular line data. In the first place, we have mapped the C65 α line using the Effelsberg 100-m telescope at an angular resolution of $40''$. This allows a reasonable comparison with the far infrared fine structure line maps of Stacey et al. (1993). Secondly, we have used the VLA to map C91 α towards the Bar with $10''$ resolution. This can usefully be compared with the H $_2^*$ maps of van der Werf et al. (1996) as well as with recent studies of $^{13}\text{CO}(3-2)$ made with the CSO telescope (Lis et al. 1997). In this paper, we present the results of the carbon radio line mapping and show that the stratification seen in other species is also clearly present in the VLA C91 α maps.

9.2. Observations

9.2.1. C65 α observations of Orion with the Effelsberg 100-m telescope

The observations were carried out using the Effelsberg 100-m telescope on 4 sessions in September 1993, March 1994, January and December 1996. Pointing was tested on 3C120 and 3C161 at hourly intervals and has an accuracy of $5''$. The facility K-band maser was used with system temperatures of 150 to 200 K. We observed a $5'$ square region centered between the Bar and the Trapezium in a total power mode with reference positions $75'$ to the east. The spectrometer was a autocorrelator which was split into two sections of 512 channels and centered on C65 α (23415.9609 MHz) and H65 α (23404.2793 MHz). Each section had a bandwidth of 12.5 MHz yielding a spectral resolution of 0.3 km s^{-1} . The telescope half-power beamwidth at 23.416 GHz is $40''$.

9.2.2. C91 α observations of the Orion Bar with the VLA

We observed the Orion Bar in July 1996 using the VLA in its D configuration. The basic observing parameters were as given in Table 9.1. The phase center of our map was chosen to be slightly offset from the Bar in order to map also the total continuum radiation of the Orion A H II region. We observed a bandpass calibrator at intervals of 3 hours

Table 9.1: VLA Observing Parameters

Rest Frequency (C91 α)	8.589104 GHz
Total Bandwidth	3.125 MHz
Number of Channels	256
Channel Separation	12 KHz (0.43 km s ⁻¹)
Synthesized Beam FWHM	11.7 x 9.0 arcsec
Primary Beam FWHM	5.2 arcmin
Phase Center of Map	$\alpha_{1950}=05:32:51.30, \delta_{1950}=-05:26:21.0$
Time On Source	7 hours

and made phase calibrations every 25 minutes. The data were processed using AIPS and resulted in synthesized beams of $11.7'' \times 9.0''$ with natural weighting and a final RMS noise of 2 mJy per beam (0.3 K) in a channel map. Our main difficulty is separating the blend of He91 α and C91 α which is done by subtraction of a linear spectral baseline from every data point in the uv plane using small windows in the immediate neighborhood of the carbon line. This works well for the Bar but could lead to overestimation of the line emission where the helium line dominates the spectra. A 3.5 cm continuum image was produced by summing over the line free channels. Comparing C91 α VLA observations smoothed to the corresponding 100-m beam ($80''$) with C91 α 100-m observations carried out in August 1996 of the Bar, we found that we underestimate the C91 α intensity due to the missing short spacing information by less than 30%.

9.3. Observational results

9.3.1. Morphology of carbon radio line emission

In Fig. 9.1, our C91 α (VLA) and C65 α (100-m) recombination line maps are shown compared with each other. Despite the difference in angular resolutions, one notes that the same basic features are seen on both maps. One sees the Bar to the south-east, a compact (1 arc minute in size) region $30''$ to the south-west of Θ_1 C Ori in the central portion of the map, and another feature close to the BN-KL region on the northern edge of the map.

It is interesting to compare our C65 α (100-m) integrated intensity map with the [C II] 158 μ m contours from Stacey et al. (1993). In this case, both lines are probing ionized carbon and with similar angular resolution. It is striking to note again the similarity of the general characteristics of these maps in spite of different excitation characteristics (see Natta et al. 1994). Thus, we conclude that the FIR and radio lines come from essentially the same regions in space although the recombination line shows a higher contrast and there are likely to be differences on scales of a few arc seconds.

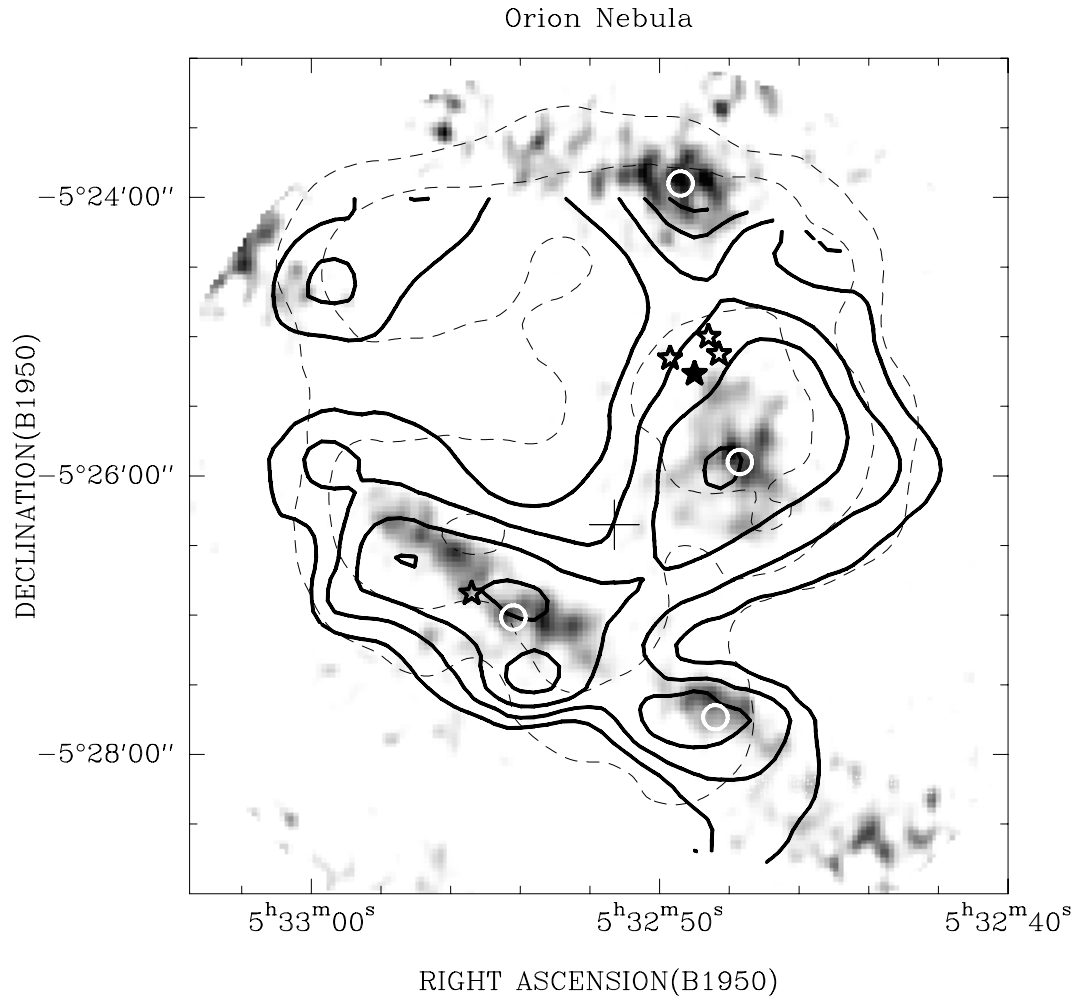


Fig. 9.1.— Comparison of C91 α (VLA) integrated intensity (HPBW 10'', greyscale) and C65 α (100-m) integrated intensity (40'' HPBW, bold contours, contours are 30, 50, 70, 90 % of peak intensity 0.9 K km s^{-1}). The dashed contours are [C II] 158 μm of Stacey et al. (1993, contours 50, 70, 90 % of peak intensity $3.9 \cdot 10^{-3} \text{ erg cm}^{-2}\text{s}^{-1}\text{sr}^{-1}$). The star symbols mark the positions of the Trapezium stars ($\Theta_1\text{C Ori}$ filled) and $\Theta_2\text{A Ori}$. Position used in Table 9.2 are marked as white circles and the phase center is marked by a cross.

That the regions seen in the carbon radio lines represent PDRs in the vicinity of ionization fronts is demonstrated by Fig. 9.2. It shows our VLA C91 α map compared with our 3.5 cm continuum map representing the distribution of free-free emission from the ionized gas. The Bar as seen in C91 α is parallel to but offset by about 20'' (0.05 pc) from the Bar of ionized gas. This is in the direction away from $\Theta_1\text{C Ori}$ and is thus consistent with ionization and heating from that source. The distribution of $^{13}\text{CO}(3-2)$ observed by Lis et al. (1997) using the CSO with a 20'' HPBW is offset a further 20'' to the SE relative to C91 α and thus, the carbon radio line emission is neatly sandwiched between the ionized and molecular media.

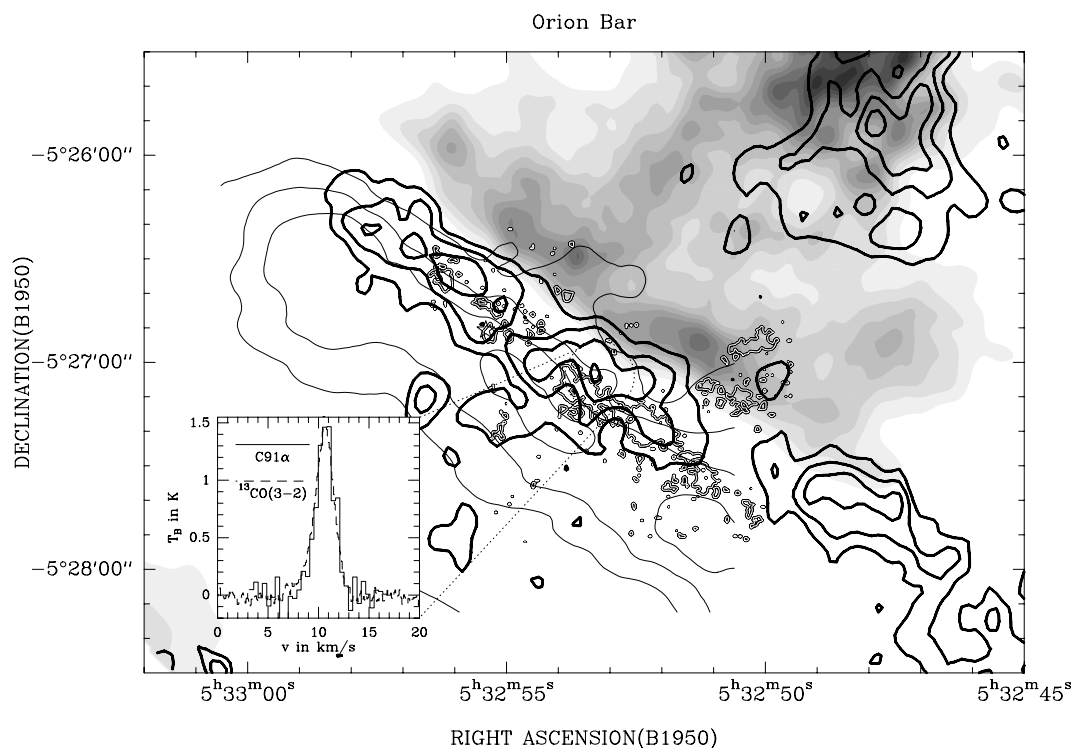


Fig. 9.2.— VLA 3.5 cm continuum (grey-scale) compared to C91 α (VLA) integrated intensity (thick full contours: 30, 50, 70, 90 % of peak intensity 5.5 K km s^{-1}) and $^{13}\text{CO}(3-2)$ integrated intensity from Lis et al. (1997, thin contours, only the region around the Bar was mapped). The black and white contours are $\text{H}_2(1-0 \text{ S}(1))$ image of van der Werf et al. (1996). The insert in the lower left shows a comparison of C91 α (smoothed to $20''$) and ^{13}CO (peak 29 K) spectra towards the indicated position in the Bar.

A sample spectrum of the C91 α line towards the Bar is shown as an insert in Fig. 9.2 compared with the corresponding ^{13}CO spectrum. One sees from this that the line profiles are very similar indicating a close link between the two. This kinematical agreement between molecular gas and carbon emission is found nearly everywhere showing the C II region to be very quiescent with only small velocity shifts. At most positions, the line emission is narrow with line widths between 2 and 2.5 km s^{-1} . The VLA linewidths can be converted into upper limits on the kinetic temperature between 1000 and 1600 K in the region responsible for the C91 α emission in the Bar (assuming thermal broadening to be solely responsible for the observed line width). The carbon lines are broader towards the clump of C91 α emission to the SW of the Trapezium where we find an upper limit to the temperature of 3000 K .

Table 9.2: Integrated Intensities of C91 α , C65 α , and [C II] 158 μm at selected positions. The C91 α data was smoothed to a 40'' beam in order to match the different beam sizes.

Object	Offset arcsec	I(C91 α) K km s $^{-1}$	I(C65 α) K km s $^{-1}$	I([C II] 158 μm) 10^{-4} erg cm $^{-2}$ s $^{-1}$ sr $^{-1}$
Bar SW	(-45, -85)	1.7	0.75	22
Bar center	(45, -40)	2.1	0.79	28
Orion South	(-55, 25)	2.6	0.83	36
North of KL	(-30, 145)	2.9	0.89	29

9.3.2. Level populations in the C91 α emitting region

By smoothing our VLA C91 α data to 40'' resolution, we can make a direct estimate of the ratio of the intensities of the two recombination lines at several positions and Table 9.2 gives the results. We also give the [C II] 158 μm intensities at the same positions derived from the maps of Stacey et al. (1993).

Table 9.2 shows that we observe typical line intensity ratios $T_l \Delta v(\text{C91}\alpha) / T_l \Delta v(\text{C65}\alpha)$ between 2.3 and 3.3 and ratios $T_l \Delta v(\text{C91}\alpha) / I([\text{C II}] 158 \mu\text{m})$ of 800 K km s $^{-1}$ erg $^{-1}$ cm 2 s sr. One can compare the former with the ratios expected for hydrogenic departure coefficients (b_n 's) which, for example, are 5 for $T=800$ K and an electron density n_e of 10 cm $^{-3}$ (see Natta et al. Fig. 7). Given our limits on the electron temperature and for reasonable electron densities, it is not possible to get agreement between observations and the line ratios predicted by hydrogenic recombination theory. We believe that the explanation of this is that dielectronic recombination of the type discussed by Walmsley & Watson (1982) causes the populations to be closer to being thermalised than hydrogenic theory predicts. If one goes to the extreme of thermalised level populations ($b_n = 1$), the predicted $T_l \Delta v(\text{C91}\alpha) / T_l \Delta v(\text{C65}\alpha)$ is 2.7. A more reasonable assumption might be that atoms with a $^2P_{3/2}$ core have thermalised populations whereas atoms with $^2P_{1/2}$ cores are hydrogenic. Then, applying Eq. 8 from Walmsley & Watson (1982), we find $T_l \Delta v(\text{C91}\alpha) / T_l \Delta v(\text{C65}\alpha)$ is 3.1 for $T=200$ K and $n = 10^5$ cm $^{-3}$. Given the errors, both of these are consistent with the observations and we conclude that the dielectronic process drives the level populations close to the values expected in LTE. In the following discussion, we have for simplicity set the b_n 's equal to unity.

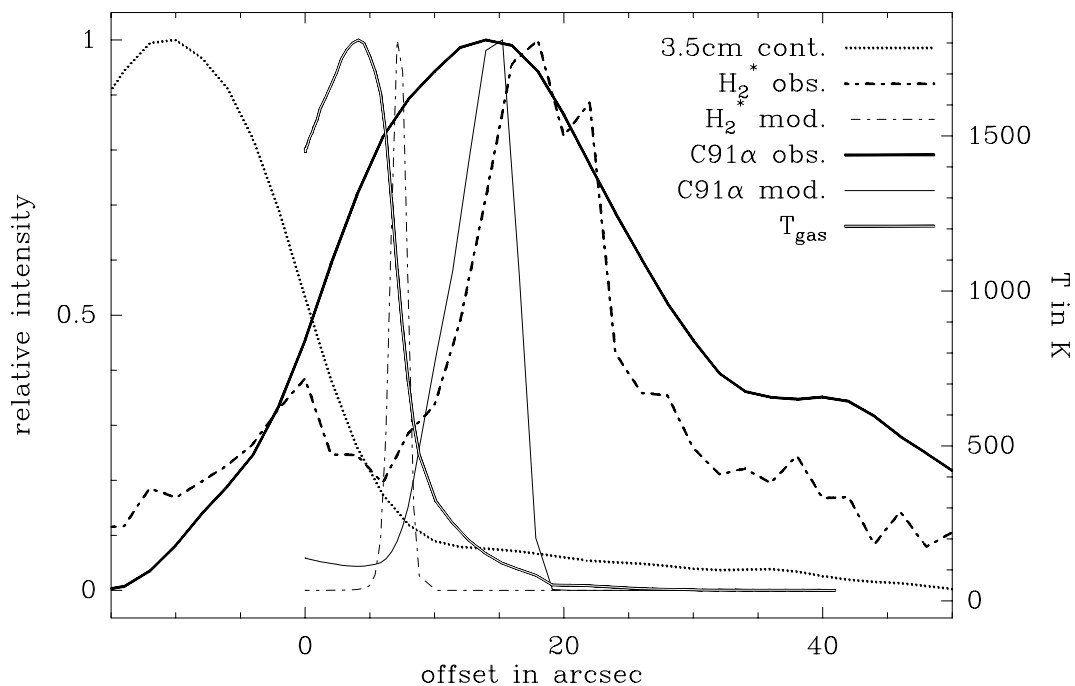


Fig. 9.3.— Averaged intensity distribution of 3.5 cm continuum, H_2 (1-0 S(1)), and C91 α across the Bar. The thin lines show for comparison results of PDR model calculations scaled to $n(\text{H})=7 \times 10^4 \text{ cm}^{-3}$ and $G_0 = 10^5$. The double line shows the model temperature distribution (right hand scale).

9.3.3. Comparison with molecular hydrogen emission

Hot neutral gas in the neighborhood of ionization fronts is also traced by emission in the NIR $2\mu\text{m}$ lines of H_2 which are collisionally excited at temperatures upwards of 1500 K although one may observe fluorescence at low temperatures. It is thus of interest to compare our VLA map of C91 α with the emission in the 1-0 S(1) line of H_2 which was imaged by van der Werf et al. (1996). The qualitative result of this is that the Bar as seen in H_2 corresponds generally with the carbon radio lines when one takes into account the difference in angular resolutions.

A closer view reveals that the carbon radio line emission appears to peak slightly closer to $\Theta_1\text{C Ori}$ than does the emission from vibrationally excited molecular hydrogen. One obtains some insight into the situation from Fig. 9.3 which shows the results of an homogeneous edge-on model derived using the PDR models of Tielens & Hollenbach (1985) with $n(\text{H})=10^5 \text{ cm}^{-3}$ and $G_0 = 10^5$ extrapolated to a density of $7 \times 10^4 \text{ cm}^{-3}$. We assume a perfectly edge-on model without a tilt. The intensity of the C91 α line, which is proportional to $T^{-1.5}$, increases with depth into the PDR and reaches a peak just in front of the transition zone $\text{C}^+/\text{C I}/\text{CO}$. The observed cross cuts of C91 α and H_2 v=1-0 S(1) shown in Fig. 9.3 are averaged over the Bar and the half-power point of the 3.5 cm continuum is used to define the ionization front. In contrast to the prediction of the homogeneous model,

the observed C91 α emission is broader and extends farther into the Bar. But while the predictions for C91 α are in qualitative agreement with observation, the same is not true for molecular hydrogen which is expected by theory to lie between ionization front and C91 α .

The explanation of this is unclear but one possibility is that the heat input to the observed H₂ emission is due to a shock. One difficulty with this interpretation (see Hill and Hollenbach 1978; Tielens et al. 1993) is the general quiescence of the gas in the Bar discussed in Sect. 3.1. However, explaining our result seems to require either considerable heat input or fluorescence in a layer at a depth in the Bar corresponding to roughly 5 magnitudes of visual extinction.

9.3.4. Physical parameters in the C91 α emitting region

We now summarize briefly the constraints on density and temperature in the layer of the Bar emitting C91 α . As noted in Sect. 9.3.1, we can place a limit of 1600 K on the kinetic temperature. In order to explain the observed C91 α line intensity (5 K km s⁻¹ peak value), we find (taking $b_n = 1$, see last section) that the carbon line emission measure $E_l = \int n_e n(C^+) ds$ (in pc cm⁻⁶) is equal to $2250 T_3^{1.5}$ where $T_3 = T/1000$. For an Orion carbon abundance $[C]/[H] = 3.4 \times 10^{-4}$ (Peimbert 1993) and assuming $n_e = n(C^+)$, we estimate the hydrogen density in the layer responsible for the observed C91 α emission to be $n_H = 4 \cdot 10^5 T_3^{0.75} L_B^{-0.5}$ where L_B (pc) is the depth of the Bar along the line of sight (of order 0.6 pc according to Hogerheijde et al. 1995). Thus for temperatures between 200 and 1600 K and $L_B = 0.6$, we find n_H between 5×10^4 and 2.5×10^5 cm⁻³ assuming a beam filling factor of 1. This is consistent with recent estimates of the density on basis of CN and CS observations with comparable resolution (Simon et al. 1997) and also consistent with our results of the previous section for a typical temperature in the C91 α emission region of 300 K.

9.4. Conclusions

Our data show convincingly that carbon is ionized in a layer intermediate between molecular gas and ionization front. We put an upper limit on the temperature of the C II layer of 1600 K and find that the hydrogen density must be between 5×10^4 and 2.5×10^5 cm⁻³. We also have found evidence that the dielectronic recombination process discussed by Walmsley & Watson (1982) plays an important role in populating high n levels under the conditions of the Orion Bar PDR. Finally, we show that current models have difficulty in explaining the morphology of the vibrationally excited molecular hydrogen emission relative to ionized carbon in the Orion Bar.

REFERENCES

- Herrmann, F., Madden, S. C., Nikola, T., Poglitsch, A., Timmermann, R., Geis, N., Townes, C. H., & Stacey, G. J. 1997, ApJ 481, 343
- Hill, J. K., & Hollenbach, D. J. 1978, ApJ 225, 390
- Hogerheijde, M. R., Jansen, D., & Van Dishoeck, E. F. 1995, A&A 294, 792
- Lis, D. C., Keene, J., & Schilke, P. 1997, in prep.
- Natta, A., Walmsley, C. M., & Tielens, A. G. G. M. 1994, ApJ 428, 209
- Peimbert, M. 1993, Rev. Mex. Astron. Astrofis. 27, 9
- Simon, R., Stutzki, J., Sternberg, A., & Winnewisser, G. 1997, A&A 327, L9
- Stacey, G. J. et al. 1993, ApJ 404, 219
- Sternberg, A., & Dalgarno, A. 1995, ApJS 99, 565
- Tauber, J. A., Tielens, A. G. G. M., Meixner, M., & Goldsmith, P. F. 1994, ApJ 422, 136
- Tielens, A. G. G. M., & Hollenbach, D. 1985, ApJ 291, 722
- Tielens, A. G. G. M., Meixner, M. M., van der Werf, P. P., Bregman, J., Tauber, J. A., Stutzki, J., & Rank, D. 1993, *Science* 262, 86
- Walmsley, C. M., & Watson, W. D. 1982, ApJ 260, 317
- van der Werf, P. P., Stutzki, J., Sternberg, A., Krabbe, A. 1996, A&A 313, 633

Part III

Conclusions and prospects

Conclusions and prospects

In this thesis, physical and chemical conditions in hot cores and photon dominated regions towards high mass star forming regions have been investigated.

The first two chapters were dedicated to the measurements of densities and temperatures in the hot molecular gas surrounding young massive stars. In particular, we studied in detail the hot core associated with the UC HII region G10.47+0.03. The parsec-scale warm lower density gas ($\sim 10^5 \text{ cm}^{-3}$, $\sim 25 \text{ K}$) was traced with C^{17}O whereas the high density hot core gas ($\sim 10^7 \text{ cm}^{-3}$, $\sim 200 \text{ K}$) was traced with $^{15}\text{NH}_3$. For both of these optically thin tracers, deviations from LTE conditions were analyzed using large velocity gradient models.

The most detailed study of vibrational (as opposed to rotational) excitation in a molecular cloud so far, has been presented in Chapter 4 using the molecules HCN, HC_3N , NH_3 , HNC, and CH_2CHCN . In particular, the hot core source G10.47+0.03 revealed a panoply of new detections of vibrational excitation in interstellar space leading to dust temperature estimates of 175–300 K in the inner 0.03 pc of the source. HC_3N has shown to be extremely useful in covering a wide range of rotational and vibrational excitation with millimeter observations. Besides the excitation analysis, which is presented in this thesis on the basis of single dish observations, a valuable extension of this study will be high resolution interferometer observations. These profit from the small angular size of the sources and should reveal the position of the vibrationally excited emission relative to the ultracompact HII region, hot core, and water masers. We have in this thesis presented the first astronomical measurements of vibrationally excited emission from the ^{13}C isotopomers of HC_3N . Our results have made clear that laboratory measurements are now needed to determine exact frequencies for these lines.

For several hot core sources, estimates of the abundances of complex organic molecules have been presented which can be used in conjunction with chemical models to determine their chemical age ($\sim 5 \cdot 10^4$ yrs; i.e the time after the evaporation of parent molecules from grain mantles due to the onset of high mass star formation and the consequent heating). It has been shown that the high anomalous (in terms of gas phase chemistry) abundances of $\text{CH}_3\text{CH}_2\text{CN}$, CH_3OCH_3 and HCOOCH_3 are a general characteristic of the observed hot core sources. We did not in this study obtain reliable estimates of methanol abundances. This would be a useful future goal since methanol is believed to be together with H_2CO the main driver for the formation of complex oxygen bearing molecules. Thus a large survey for methanol abundances in hot core sources is needed, which could be carried out in conjunction with a search for further strong emitters of vibrationally excited lines using $\text{HC}_3\text{N } \nu_5$ lines as a tracer.

The high resolution (0.016 pc) observations of the high mass star forming region W3(OH) presented in Chapter 6 offered a detailed view of two different stages of high

mass star formation simultaneously: the hot core associated with the water masers and the ultracompact HII region associated with the OH masers. The C¹⁷O emission demonstrated that the hot core is still embedded in the dense molecular cloud core, whereas the UC HII is sited at the edge of this core suggesting a disruption of the cloud by the HII region. The mass of the hot core was estimated to be 10 M_⊙ from both the C¹⁷O line and the dust continuum observations. A total bandwidth of 1.5 GHz was covered with the observations containing ~ 30 lines from 10 molecular species. While oxygen bearing complex molecules are found towards both the hot core dust continuum and the ultracompact HII region, nitrogen bearing complex molecules originate from a position close to but offset by about 1100 AU from the dust peak. The reason for this is still unclear and higher angular resolution is required to clarify the nature of these nearby sub-sources and their different chemical state. It has been shown that the orientation and spatial extent of the maser emission found in this region are intimately related to the observed molecular thermal emission. In particular, the correspondence between methanol thermal and masering emission extending over the whole western side of the UC HII is within 0''.2, so that the estimated temperature of 185 K for the thermal methanol emission and the lower limit of $3 \cdot 10^{-6}$ for the methanol abundance can be used to characterize the physical conditions in the masering region.

In the second part of the thesis, the utility of the carbon recombination line as a tracer for the physical conditions and the morphology of photon dominated regions has been investigated. In contrast to observations of far infrared fine structure lines to trace the ionized carbon, which are still limited in their angular resolution and are difficult to resolve spectroscopically, observations of carbon radio recombination lines lead directly to stringent limits on the temperature in the emitting regions. In particular, the new detection of the C91 α recombination line in NGC 7023 lead via its observed very small linewidth of 0.85 km s⁻¹ to an upper limit of 190 K in this photon dominated region. In the discussion of the results of carbon recombination and carbon monoxide lines towards NGC 2023, several geometrical models have been used to lead to the conclusion that the observed emission is due to high density gas ($\sim 10^5$ cm⁻³). Using the high resolving power of the Very Large Array interferometer, we would be able to test these models and to study the stratification in the photon dominated region by direct comparison with existing high resolution H₂* images. The observations of the C91 α line towards the Orion Bar described in Chapter 9 have shown that such high angular resolution observations of PDRs are indeed possible. These observations with the best spatial resolution (0.02 pc) to date of the ionized carbon layer in a PDR, show that the ionized carbon is in a thin, clumpy layer sandwiched between the ionization front and the molecular gas. A natural continuation of this study will be the addition of still higher resolution C-array VLA data, which will allow for the first time the analysis of the structure of a PDR on a scale of 1000 AU similar to that available in the NIR H₂ data.

Appendix A

30-m line parameters

In the following tables the observed intensities, frequencies, quantum numbers, upper energies, and line strengths of all identified lines from Chapter 4 and 5 are given. For details about the HC₃N frequencies refer to Chapter 4. All other frequencies are taken from the JPL catalog (Poynter & Pickett 1985; Pickett et al. 1996). For line blends the individual components are given together with the total intensity of the blended feature.

Table A.1: Observed HC₃N(17–16) intensities. Note that the v_7 and v_6 lines at 155035 MHz are blended and the total intensity is given.

ν (MHz)	Vib. state	$\mu^2 S$ (D ²)	E_{up} (K)	Source	$\int T_{\text{MB}} dv$ (K km s ⁻¹)
154657.281	(0,0,0,0)	237	67	G10.47	43.0±1.0
				G10.62	46.0±0.4
				G29.96	22.6±0.4
				G31.41	37.5±0.9
				G34.26	49.6±0.9
				W3(H ₂ O)	13.1±0.2
154910.969	(0,0,1,0) ¹⁻	237	785	G10.47	6.6±0.7
				G10.62	0 ±0.2
				G29.96	0.6±0.1
				G31.41	1.7±0.4
				G34.26	1.7±0.3
				W3(H ₂ O)	0.1±0.05
155032.734	(0,0,1,0) ¹⁺	237	785		
155037.359	(0,0,0,1) ¹⁻	238	387	G10.47	23.2±0.5
				G10.62	0.5±0.2
				G29.96	6.1±0.3
				G31.41	11.0±0.3
				G34.26	5.5±0.7
				W3(H ₂ O)	2.6±0.1

Table A.2: Observed HC₃N intensities in G10.47+0.03

ν (MHz)	Transition	Vib. state	E_{up} (K)	$\mu^2 S$ (D ²)	$\int T_{\text{MB}} dv$ (K km s ⁻¹)
HC ₃ N					
36534.1	4–3	(0, 0, 0, 1) ¹⁺	324	55	1.5
109182.9	12–11	(0, 1, 0, 0) ¹⁻	988	167	2.0
109244.0	12–11	(0, 1, 0, 0) ¹⁺	988	167	2.4
109306.7	12–11	(1, 0, 0, 1) ¹⁻	1627	167	0.6
109352.8	12–11	(0, 0, 1, 0) ¹⁻	751	167	3.7
109438.7	12–11	(0, 0, 1, 0) ¹⁺	751	167	3.2
109442.0	12–11	(0, 0, 0, 1) ¹⁻	354	167	7.1
109469.4	12–11	(1, 0, 0, 1) ¹⁺	1627	167	0.6
109522.5	12–11	(0, 0, 2, 0) ⁰	1469	167	0.7
109549.5	12–11	(0, 1, 0, 1) ⁰⁺	1308	167	1.1
109552.1	12–11	(0, 1, 0, 1) ²⁺	1308	167	1.3
109558.0	12–11	(0, 1, 0, 1) ⁰⁻	1308	167	1.3
109563.7	12–11	(0, 1, 0, 1) ²⁻	1308	167	1.4
109598.8	12–11	(0, 0, 0, 1) ¹⁺	354	167	7.9
109616.3	12–11	(0, 0, 2, 0) ²	1469	336	1.1
109862.8	12–11	(0, 0, 0, 2) ⁰	674	168	4.5
109866.1	12–11	(0, 0, 0, 2) ²⁻	674	168	2.4
109870.3	12–11	(0, 0, 0, 2) ²⁺	674	168	4.7
109990.0	12–11	(0, 0, 1, 2) ¹⁻	1391	168	1.4
110035.6	12–11	(0, 0, 1, 2) ⁻¹	1391	168	1.8
110051.0	12–11	(0, 0, 0, 3) ⁻	994	168	2.7
110097.6	12–11	(0, 0, 1, 2) ³	1391	336	1.3
110148.8	12–11	(0, 0, 1, 2) ⁻¹⁻	1391	168	1.2
110189.8	12–11	(0, 0, 1, 2) ¹⁺	1392	168	1.8
110211.4	12–11	(0, 0, 0, 3) ³	994	336	2.2
155037.4	17–16	(0, 0, 0, 1) ¹⁻	387	237	15.4
219173.8	24–23	(0, 0, 0, 1) ¹⁺	451	335	17.3
228303.2	25–24	(0, 0, 0, 1) ¹⁻	462	349	18.8
HCC ¹³ CN					
154259.6	17–16	(0, 0, 1, 0) ¹⁻	784	237	1.9
154365.8	17–16	(0, 0, 0, 1) ¹⁻	386	238	3.8
154370.6	17–16	(0, 0, 1, 0) ¹⁺	784	237	2.4
154969.9	17–16	(0, 0, 0, 2) ⁰	706	238	1.2
HC ¹³ CCN					
154383.2	17–16	(0, 0, 1, 0) ¹⁺	784	237	2.0
154387.2	17–16	(0, 0, 0, 1) ¹⁻	386	238	4.1
154943.8	17–16	(0, 0, 0, 2) ⁰	706	238	1.3
154954.5	17–16	(0, 0, 0, 2) ²⁻	706	238	1.2
154966.8	17–16	(0, 0, 0, 2) ²⁺	706	238	1.6

Table A.3: Observed vibrationally excited CH₂CHCN intensities in G10.47+0.03. Note that all lines are blends of two transitions with different K_b but only one transition is given in the table. $\mu^2 S$ is the sum of both transitions.

ν (MHz)	Transition	Vib. state	E_{up} (K)	$\mu^2 S$ (D ²)	$\int T_{\text{MB}} dv$ (K km s ⁻¹)
219027.1	23 _{7,17} – 22 _{7,16}	v_{11}	574	565	5.68
219077.1	23 _{9,14} – 22 _{9,13}	v_{11}	642	527	4.71
219099.1	23 _{5,18} – 22 _{5,17}	v_{11}	523	527	5.81
219125.8	23 _{10,13} – 22 _{10,12}	v_{11}	682	505	3.46
218719.6	23 _{8,15} – 22 _{8,14}	v_{15}	756	547	3.23
218728.9	23 _{5,18} – 22 _{5,17}	v_{15}	670	593	4.15
218830.5	23 _{10,13} – 22 _{10,12}	v_{15}	835	505	3.57
218841.6	23 _{4,20} – 22 _{4,19}	v_{15}	650	302	3.31
218878.6	23 _{4,19} – 22 _{4,18}	v_{15}	650	302	3.28

Table A.4: Observed CH₃CH₂CN intensities

ν (MHz)	Transition	E_{up} (K)	$\mu^2 S$ (D ²)	$\int T_{\text{MB}} dv$ (K km s ⁻¹)					
				G10.47	G10.62	G29.96	G31.41	G34.26	W3(OH)
215039.7	24 _{9,15} – 23 _{9,14}	218	305						
215039.7	24 _{9,16} – 23 _{9,15}	218	305						
215041.9	24 _{10,14} – 23 _{10,13}	240	293						
215041.9	24 _{10,15} – 23 _{10,14}	240	293	24.1	2.49	5.22	15.9	15.8	3.34
215088.2	24 _{12,12} – 23 _{12,11}	288	266						
215088.2	24 _{12,13} – 23 _{12,12}	288	266	15.5		2.31	8.46	7.00	1.26
215109.0	24 _{7,18} – 23 _{7,17}	183	325						
215109.0	24 _{7,17} – 23 _{7,16}	183	325	19.7	3.25	4.82	12.5	10.7	2.40
215119.2	25 _{0,25} – 24 _{0,24}	135	369	16.5		4.22	12.6	11.3	2.25
215126.7	24 _{13,11} – 23 _{13,10}	316	251						
215126.7	24 _{13,12} – 23 _{13,11}	316	251	10.0		1.66	6.56	4.87	0.82
215400.8	24 _{5,20} – 23 _{5,19}	156	340	17.6		3.44	11.8	9.20	1.69
215428.0	24 _{5,19} – 23 _{5,18}	156	340	19.0	1.67	3.88	12.8	11.9	1.85

Table A.5: Observed CH₂CHCN intensities

ν (MHz)	Transition	E_{up} (K)	$\mu^2 S$ (D ²)	$\int T_{\text{MB}} dv$ (K km s ⁻¹)	
				G10.47	G31.41
227897.6	24 _{7,18} – 23 _{7,17}	242	297		
227897.6	24 _{7,17} – 23 _{7,16}	242	297	13.1	6.58
227906.7	24 _{6,19} – 23 _{6,18}	214	304		
227906.7	24 _{6,18} – 23 _{6,17}	214	304	10.3	6.88
227918.7	24 _{8,16} – 23 _{8,15}	274	288		
227918.7	24 _{8,17} – 23 _{8,16}	274	288	9.17	3.33
227960.2	24 _{9,15} – 23 _{9,14}	311	279		
227960.2	24 _{9,16} – 23 _{9,15}	311	279	7.23	3.03
227966.0	24 _{5,20} – 23 _{5,19}	190	310		
227967.6	24 _{5,19} – 23 _{5,18}	190	310	19.1	6.87
228017.4	24 _{10,14} – 23 _{10,13}	352	268		
228017.4	24 _{10,15} – 23 _{10,14}	352	268	10.2	3.44
228087.3	24 _{11,13} – 23 _{11,12}	396	256		
228087.3	24 _{11,14} – 23 _{11,13}	396	256	6.96	0.91
228090.5	24 _{3,22} – 23 _{3,21}	156	319	8.89	5.45
228104.6	24 _{4,21} – 23 _{4,20}	171	315	11.9	5.46
228160.3	24 _{4,20} – 23 _{4,19}	171	315		
228160.3	24 _{4,20} – 23 _{4,19}	171	315	16.7	7.03
154027.1	2 _{2,1} – 1 _{1,0}	10	2	4.68	2.64
154724.5	16 _{1,15} – 15 _{1,14}	65	215	9.77	5.75
140429.5	15 _{0,15} – 14 _{0,14}	54	202	8.45	2.20

Table A.6: Observed CH₃OCH₃ intensities

ν (MHz)	Transition	E_{up} (K)	$\mu^2 S$ (D ²)	$\int T_{\text{MB}} dv$ (K km s ⁻¹)			
				G10.47	G29.96	G31.41	W3(OH)
140163.0	24 _{5,20} – 23 _{6,17}	308	82	3.91			
140226.2	18 _{2,17} – 17 _{3,14}	159	35	3.28		2.47	
140441.9	27 _{12,15} – 28 _{11,18}	546	16				
140441.9	27 _{12,16} – 28 _{11,17}	546	9				
140442.7	27 _{12,15} – 28 _{11,17}	546	26				
140442.8	27 _{12,16} – 28 _{11,18}	546	26				
140443.5	27 _{12,15} – 28 _{11,17}	546	6				
140443.6	27 _{12,15} – 28 _{11,18}	546	9				
140443.6	27 _{12,16} – 28 _{11,17}	546	3				
140443.7	27 _{12,16} – 28 _{11,18}	546	6	1.35		0.50	
154311.5	14 _{8,6} – 15 _{7,8}	185	40	4.27	0.73	2.24	0.28
154456.5	11 _{1,10} – 10 _{2,9}	62	77	14.8	2.27	7.49	2.54

Table A.7: Observed CH₃CH₂OH intensities

ν (MHz)	Transition	E_{up} (K)	$\mu^2 S$ (D ²)	$\int T_{\text{MB}} dv$ (K km s ⁻¹)	
				G10.47	G31.41
86133.0	18 _{4,14} – 18 _{3,16}	218	9	0.01	0.19
86311.3	5 _{2,4} – 4 _{2,3}	73	13		0.42
87716.1	5 _{2,4} – 5 _{1,5}	17	10		0.68
87959.0	9 _{0,9} – 9 _{1,9}	97	29		1.18
109394.9	19 _{4,15} – 18 _{5,14}	180	11	0.17	0.41
112269.2	9 _{1,8} – 8 _{0,8}	95	5	0.13	0.62
112434.2	14 _{9,5} – 14 _{9,5}	247	19		0.75

Table A.8: Observed CH₃CHO intensities

ν (MHz)	Transition	E_{up} (K)	$\mu^2 S$ (D ²)	$\int T_{\text{MB}} dv$ (K km s ⁻¹)			
				G10.47	G29.96	G31.41	W3(OH)
154159.2	8 _{6,3} – 7 _{6,2}	114	45				
154160.5	8 _{5,4} – 7 _{5,3}	89	63	4.28	0.43	1.90	0.29
154198.1	8 _{4,5} – 7 _{4,4}	69	39				
154198.7	8 _{4,4} – 7 _{4,3}	69	39	4.90	0.81	2.53	0.37
154273.2	8 _{3,6} – 7 _{3,5}	53	44	5.43	0.75	3.07	0.37
154321.1	8 _{3,5} – 7 _{3,4}	53	44	bl.	bl.	bl.	bl.
112248.7	6 _{1,6} – 5 _{1,5}	21	37	2.28	0.60	2.17	0.57

Acknowledgements

In particular, I would like to thank my adviser Malcolm Walmsley for his great guidance during the course of this work, no difference whether he was just around the corner on the same floor in Cologne or 1000 miles away in Florence. I am grateful to Gisbert Winnewisser for his support and helpful discussions about molecular spectroscopy.

Without Peter Schilke and his clever CSO line catalog extensions to CLASS many weak spectral line features detected in this thesis may have been remained unidentified. Moreover, I would like to thank Peter for the opportunity to assist him on an observing run at the CSO in January 1997 and for the longest New Year's Day I ever had. Peter Hofner has been a great room and tennis mate during his time in Cologne and taught me a lot about the VLA.

Many thanks to Xander Tielens for his help with PDR models. I could also benefit a lot from Jörn Wink's knowledge of the IRAM Plateau de Bure interferometer and would like to thank IRAM Grenoble for the hospitality during a data reduction stay. Thanks to Gordon Stacey and Dan Jaffe for supplying the numerical data from the [C II] 158 μm observations of Orion A and B, respectively.

Carsten Kramer helped a lot during the acquisition of the 30-m data on Pico Veleta. Thanks also to my colleagues Nicola Schneider, Robert Simon, and Johannes Staguhn for the enjoyable atmosphere in the astrophysics group.

This research was supported by the Deutsche Forschungsgemeinschaft with grant number SFB 301 "Die Physik und Chemie der interstellaren Molekülwolken".

Finally, I'm very grateful to Tanja for being my lucky star.

Ich versichere, daß ich die von mir vorgelegte Dissertation selbständig angefertigt, die benutzten Quellen und Hilfsmittel vollständig angegeben und die Stellen der Arbeit – einschließlich Tabellen, Karten und Abbildungen –, die anderen Werken im Wortlaut oder dem Sinn nach entnommen sind, in jedem Einzelfall als Anlehnung kenntlich gemacht habe; daß diese Dissertation noch keiner anderen Fakultät oder Universität zur Prüfung vorgelegen hat; daß sie – abgesehen von unten angegebenen Teilpublikationen – noch nicht veröffentlicht worden ist sowie, daß ich eine solche Veröffentlichung vor Abschluß des Promotionsverfahrens nicht vornehmen werde. Die Bestimmungen der Promotionsordnung sind mir bekannt. Die von mir vorgelegte Dissertation ist von Prof. Dr. C.M. Walmsley und Prof. Dr. G. Winnewisser betreut worden.

Teilpublikationen:

Wyrowski F., Walmsley C.M. 1996, “ $^{15}\text{NH}_3$ towards ultracompact HII regions”, A&A 314, 265

Wyrowski F., Hofner P., Schilke P., Walmsley C.M., Wilner D.J, Wink J.E 1997, “Millimeter interferometry towards the ultracompact HII region W3(OH)”, A&A 320, L17

Wyrowski F., Walmsley C.M., Natta A., Tielens A.G.G.M. 1997, “The photon dominated regions associated with NGC 2023 and S 140”, A&A 324, 1135

Wyrowski F., Schilke P., Hofner P., Walmsley C.M. 1997, “Carbon recombination lines in the Orion Bar”, ApJ 487, L171

Lebenslauf

Persönliche Daten:

Name: Friedrich Wyrowski
Anschrift: Vorgebirgstrasse 50
53119 Bonn
Geburtsdatum: 28.02.1967 in Duisburg
Staatsangehörigkeit : deutsch

Schulbildung:

1973–1975 Grundschule Duisburg–Hochfeld
1975–1977 Gemeinschaftsgrundschule Wesel–Büderich
1977–1986 Andreas-Vesalius-Gymnasium Wesel
Abschluß: Abitur

Zivildienst:

01/1987–08/1988 Rettungshelfer beim Arbeiter Samariter Bund Bonn

Studium:

10/1988–09/1993 Studium der Physik an der
Rheinischen Friedrich-Wilhelms-Universität Bonn
09/1993–10/1994 Diplomarbeit: “Physikalische Bedingungen in und um
kompakte HII Regionen” am Max-Planck-Institut für
Radioastronomie, Bonn
Abschluß: Diplom-Physiker

Promotion:

11/1994– Aufnahme der Dissertation im 1. Physikalischen Institut der
Universität Köln
11/1994– Wissenschaftliche Hilfskraft/Mitarbeiter am 1. Physikalischen
Institut